INFORMATION TO USERS

This manuscript has been reproduced from the microfilm master. UMI films the text directly from the original or copy submitted. Thus, some thesis and dissertation copies are in typewriter face, while others may be from any type of computer printer.

The quality of this reproduction is dependent upon the quality of the copy submitted. Broken or indistinct print, colored or poor quality illustrations and photographs, print bleedthrough, substandard margins, and improper alignment can adversely affect reproduction.

In the unlikely event that the author did not send UMI a complete manuscript and there are missing pages, these will be noted. Also, if unauthorized copyright material had to be removed, a note will indicate the deletion.

Oversize materials (e.g., maps, drawings, charts) are reproduced by sectioning the original, beginning at the upper left-hand corner and continuing from left to right in equal sections with small overlaps.

Photographs included in the original manuscript have been reproduced xerographically in this copy. Higher quality 6" x 9" black and white photographic prints are available for any photographs or illustrations appearing in this copy for an additional charge. Contact UMI directly to order.

Bell & Howell Information and Learning
300 North Zeeb Road, Ann Arbor, MI 48106-1346 USA

UMI®
800-521-0600

A Micromachined Silicon Vibrating-Beam Angular Rate Sensor: A Design and Implementation Study

Behrouz Nikpour

A Thesis
in
The Department
of
Electrical and Computer Engineering

Presented in Partial Fulfillment of the Requirements
for the Degree of Doctor of Philosophy
Concordia University
Montreal, Quebec, Canada

January 1998

ABSTRACT

A Micromachined Silicon Vibrating-Beam Angular Rate Sensor:
A Design and Implementation Study

Behrouz Nikpour

Design and Implementation of a Silicon-Beam Angular Rate Sensor is studied. The sensing device is designed based on a micromachined single crystal silicon beam. Electromagnetic actuation supplies the reference vibration, and the Coriolis-induced vibration is sensed by a capacitor plate in close proximity to the vibrating beam. Beams with precise dimensions, and vertical side walls are fabricated using wet anisotropic etching of Si{100} wafers in TMAH 25%. Several issues essential for a successful design are discussed. The required circuitry for actuation of the beam and detection of the Coriolis induced vibrations are discussed. A complete model for the mechanical and electrical components of the sensor is built in HSPICE and used to simulate the basic operation of the sensor. To improve the mismatch between beam resonant frequencies, a scheme of novel Concave Corner Compensation Patterns is devised to substantially reduce the size of the residual {111} flanges at both ends of the beams. The design principles are explained in detail and a numerical simulation program is developed to track the etch progress of the corner compensation patterns. The etch progress in patterns is simulated using a graphical simulation tool and tested experimentally. Experimental results are matched with simulation results. Several test beam structures have been fabricated and tested. Some critical mechanical characteristics of the beam structures are measured and satisfactorily compared with the results from theory and Finite Element Model simulation. Functional sensor structures are fabricated and characterized. The effect of concave corner compensation on mismatch is shown both using the Finite Element Model simulation and experiment.

To my wife Suzan for her endless true love and continued support

Acknowledgements

I would like to thank my supervisor Dr. L. M. Landsberger for his guidance, advice, and support during this work. I would also like to thank Dr. M. Kahrizi for his advice, help, and support in all aspects of this work. I am thankful to Dr. B. Haroun for his advice and support during the first two years of this project. I would also like to thank Dr. Ion Stiharu, and Dr. M. Paranjape for their frequent comments and advice.

Many thanks to Dr. Ted Hubbard from Technical University of Nova Scotia for his invaluable support and co-operation by providing the graphical simulations and FEM simulations. I would also like to thank Dr. J. F. Currie, Mr. A. Lecours, and Mr. P. Boudreau of Laboratoire d'Intégration des Senseurs et Actuateurs of École Polytechnique de Montreal for help in fabrication of electrical test structures.

Special thanks to undergraduate students Z. Kahric, A. Iftimie, F. Quan, and K. Al-Sheraidah for their help during the experiments of this project. Thanks to Mr. A. Pandy for scanning the micrographs of this thesis.

My special thanks to all of the students in Microelectronics Lab for providing such a warm and friendly environment.

TABLE OF CONTENTS

7. Summary of Contributions and Future Work

LIST OF TABLES

LIST OF FIGURES

CHAPTER 1

Introduction

1.1 General View

The rapid progress made in the area of microelectronics over the past three decades has had a revolutionary impact on many aspects of technology. Microcomputers are now used in most instrumentation and control applications. Very large scale integrated (VLSI) systems on a chip play a central role in the implementation of many complex systems including designs associated with most consumer products.

However, microelectronics by itself can only process information as electrical signals. Input/output provides the conduit whereby this enormous computing power becomes useful to aid human life. Thus many new rewards of high-technology are enabled by the recent expansion in the field of sensors.

Sensors provide the interface between any automated system and the outside world. An outside physical quantity such as temperature, humidity, light, force, acceleration, etc. must first be converted into an equivalent electrical signal (using a sensor), before it can be used by the automated systems. Sensing and data acquisition have become critical issues in many systems, often more critical than information processing. At present, sensors are more expensive than many microcomputers and may be more limiting in terms of system performance.

Micromachined silicon sensors were born as an attempt to overcome the above mentioned problems. These sensors are low-priced, small, batch-fabricated, and low-powered. The research field is still in its early stages and growing very fast. In a few areas such as pressure sensors and accelerometers, microsensors have already been established as a

fully commercialized product. In other areas, it will take a few years before they find their way to commercial markets.

Gyroscopes, or angular-rate measurement sensors, are one of the most important components in inertial navigational systems. Small inexpensive micromachined gyroscopes have application in automobile safety systems (airbags, anti-skid systems), machine control and robotics, and global positioning systems. A popular type of gyroscopes, called vibratory gyroscopes, can be successfully miniaturized and implemented using micromachining techniques. Micromachining of mono-crystalline silicon using wet anisotropic etching with Tetra-Methyl Ammunium Hydroxide (TMAH) provides a cost-effective and precise technique to fabricate micromachined structures. Silicon is also compatible with integrated circuit fabrication technology, which creates the opportunity of integrating the sensor and its detection circuitry on one chip.

The design and implementation of a Vibrating-Beam Angular Rate Measurement Sensor using anisotropic etching of Si{100} in TMAH is the subject of this thesis.

1.2 Contents of the Thesis

In Chapter 2, the background of vibratory angular rate measurement sensors, their operation principles, different types of angular rate measurement sensors and fabrication techniques used to fabricate these sensors are presented. Current and future applications of these sensors, design issues such as the type of structural materials used and the operational environment of the sensor are also discussed. Several design examples of the research done so far in development of such sensors are also covered in this chapter. The chapter finishes with a brief introduction to the proposed design of the sensor in this thesis.

Design and Modeling of the vibrating beam angular rate measurement sensor is discussed in Chapter 3. Fabrication issues are discussed first including the overall fabrication

process steps, and the development of a method to etch square-cross-section beams in Si{100} using anisotropic etching in TMAH. The overview of sensor's operation and the mass-spring model of the sensor are discussed next. Important design issues that have to be carefully considered in the design of the sensor (such as actuation frequency and amplitude, sensitivity, sense vibration, damping, and coupling) are discussed, followed by sensor operation issues, which includes the actuation mechanism and circuitry, detection mechanism and circuitry, and non-ideal effects. A tuning-fork-based design is also briefly discussed at the end of this chapter as an improved structure that could be considered in the future for the sensor.

Simulation of the basic sensor operation is presented in Chapter 4. The model developed in Chapter 3 is implemented in HSPICE and tested in this chapter. The steady state response of the sensor, spring softening effect, amplitude stiffening effect, and the transient response of the sensor are tested based on the simulation results and compared with the theory.

A concave corner compensation technique is presented in Chapter 5 as a fabrication technique that can enhance the performance of the sensor. First the problem of non-ideal clamping of the beams fabricated using anisotropic etching of Si{100}, which results in large flanges at the two ends of the beam, is discussed. Then a novel concave corner compensation technique, using a precisely-designed set of mask patterns to substantially reduce the size of the flanges, is discussed in detail. A numerical simulation program that has been developed to design such patterns is discussed next. The etch profile of patterns designed using this technique are then simulated using a graphical simulation tool and the results are compared with the predicted results of numerical simulation. A secondary set of patterns is introduced to enhance the reduction ratio of the flanges.

Experimental fabrication, and testing results are discussed in Chapter 6. The fabrica-

tion procedure used to fabricate test beam structures with precise dimensions and vertical sidewalls is presented and experimentally tested. The concave corner compensation patterns are experimentally tested and the results are compared with simulation results from Chapter 5. Fabrication of beam test structures is explained next, followed by test procedures to test the mechanical characteristics of the beams. The operational test results of the fabricated beams in regular air pressure and reduced pressure are discussed and compared with the results from theory and simulation. The fabrication process used to fabricate complete sensor structures is explained next followed by experimental results of testing these samples. The results from these experiments are then related back to the model developed in Chapter 4 and the model is simulated again to predict the response of the sensor considering all of the experimental factors.

Conclusions and future directions for the research are discussed in Chapter 7.

CHAPTER 2

Background

2.1 Introduction

Micromachined accelerometers in silicon are commercially available. These inertial sensors have shown that micromechanical structures are well qualified as inexpensive, small and reliable sensors. A complete inertial system also needs information about the angular velocity or angular position. New automotive industry and consumer applications constantly increase this need for small and inexpensive angular rate sensors. Conventional gyroscopes which work based on conservation of angular momentum of a spinning rotor are too expensive, too large, or have too short a reliable life time for most new applications. Fiber-optic and laser gyroscopes have excellent performance but are too expensive for many applications where low cost is essential.

Another class of successful gyroscope designs, known as vibrating gyroscopes, use vibrating mechanical elements to sense rotation. These devices are not as well-known as the others but they are very suitable for applications in the medium-performance range (Accuracy of 0.2 ^{o} per second (^{o}/s) to 10 ^{o} per second (^{o}/s)). Almost universally, when low cost is the goal, rotation rate sensing devices are based on vibrating mechanical elements due to their simple structure. Since vibratory gyroscopes have no rotating parts that require bearings, they can be miniaturized and batch fabricated using micromachining techniques to produce a low-cost device. With the precision of micromachining techniques, it is possible to produce a medium to high performance device with smaller size.

In this chapter the concepts of operation, suitability for micromachining technology, and applications of vibratory gyroscopes are discussed. Some examples of the research

done so far in this area are presented next, followed by an overview of the design investigated in this thesis.

2.2 Vibratory Gyroscope Principles

To sense rotation, vibratory gyroscopes use Coriolis acceleration that arises in rotating reference frames. To understand how vibratory gyroscopes use Coriolis acceleration we first examine a simple vibratory device which is known as Foucault Pendulum.

The Foucault Pendulum is shown in Fig.2.1. The pendulum's swing is initially aligned with the x-axis. At this time all the energy or amplitude of vibration is stored in the first normal mode. As the earth rotates under the pendulum the Coriolis acceleration transfers energy between the two normal modes, causing the pendulum to precess. Solving the normal mode equations for the case of constant rotation shows that the pendulum would precess at a constant rate equal to the rotation rate. This principle of the transfer of energy between the two vibration modes of a structure is the basic operating principle of all vibrating gyroscopes [1].

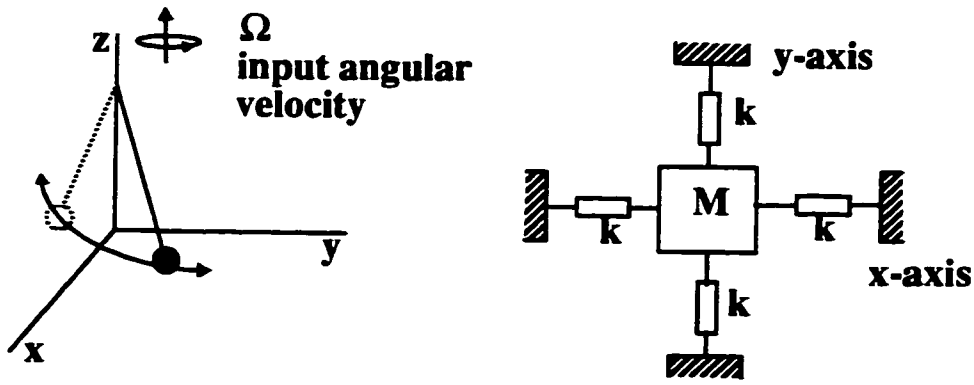

Fig. 2.1: Foucault pendulum and normal model (redrawn from [1]).

To measure the rotation rate, the pendulum would be continuously driven to a fixed

amplitude in the first vibration mode along the X-axis. Under rotation, the Coriolis acceleration will cause energy to be transferred from the first mode to the second mode. In the open-loop mode of operation the second-mode amplitude is measured as a parameter which is proportional to the rotation rate. In the force-to-rebalance mode of operation the secondary vibration amplitude is monitored and continuously driven to zero by applying the necessary force along the Y-axis. In this method the force is considered as a parameter which varies proportionally to the rotation rate. The type of operating mode used in a particular vibratory gyroscope depends on the application and specific characteristics of the design.

All of the vibratory gyroscopes are based on rotation-induced transfer of energy between two vibration modes of the structure. The highest performance for vibratory gyroscopes is obtained when these two vibration modes have the same natural frequency and a high quality factor. When this is the case, the response to the very small Coriolis acceleration is amplified or multiplied by the quality factor of the resonance. Matching the vibration mode frequencies is most easily obtained in symmetric structures that naturally have two identical modes of vibration such as Foucault Pendulum or the vibrating shell or vibrating ring discussed later [2,3]. High quality factor is obtained by using isolated structures that do not radiate acoustic energy and are fabricated from low-loss materials. Also, the damping time is increased as the resonant frequency of the structure is lowered. So lower natural frequency structures are desirable. However, the natural frequency of the structure should be kept above the environmental noise to improve vibration sensitivity.

2.3 Types of Vibratory Gyroscopes

Vibratory Gyroscopes generally fall into one of these six classes: Vibrating Beams, Tuning Forks, Single or Dual Accelerometers, Vibrating Shells, Surface Acoustic Wave,

and Rotating Piezoelectric Crystals. Among these classes the Rotated Piezoelectric Crystal gyroscopes use bearings that are currently unavailable in Micromachining technology, so this class of devices will not be discussed further.

2.3.1 Vibrating Beams

In these vibratory gyroscopes the two identical primary bending modes of a beam are used to sense the rotation (Fig.2.2). The beam is driven to vibration in one mode and the Coriolis force induced in the second mode is measured.

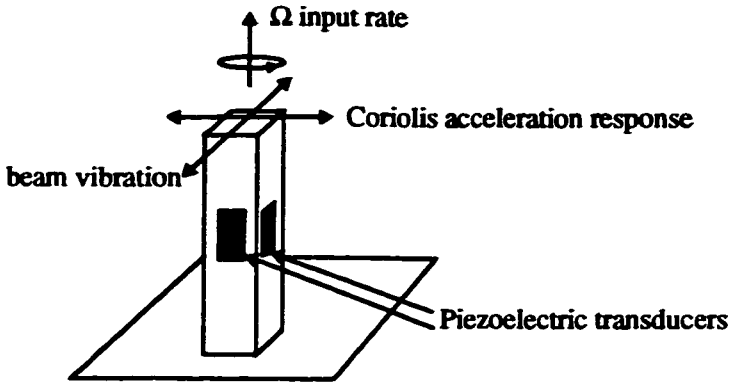

Fig. 2.2: Vibrating Beam (redrawn from [1]).

2.3.2 Tuning Forks

Tuning Forks are well-known as very good resonators which makes them a suitable choice for vibratory gyroscope designs. The tines of a tuning fork are differentially driven to a fixed amplitude and, when rotated, the Coriolis acceleration causes a differential sinusoidal force to develop on the individual tines orthogonal to the main vibration (Fig.2.3). This force is then detected either as differential bending of the tuning fork tines or as a torsional vibration of the tuning fork stem.

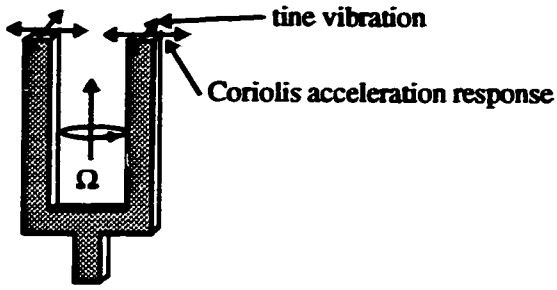

Fig. 2.3: Tuning fork vibrating gyroscope (redrawn from [1]).

2.3.3 Single and Dual Accelerometer

Dual-Accelerometer gyroscopes are essentially tuning fork gyroscopes whose tines are constructed from identical accelerometers. In these devices the accelerometer's proof masses are vibrated anti-phase in one plane and the resulting differential Coriolis acceleration is measured in an orthogonal plane (Fig.2.4).

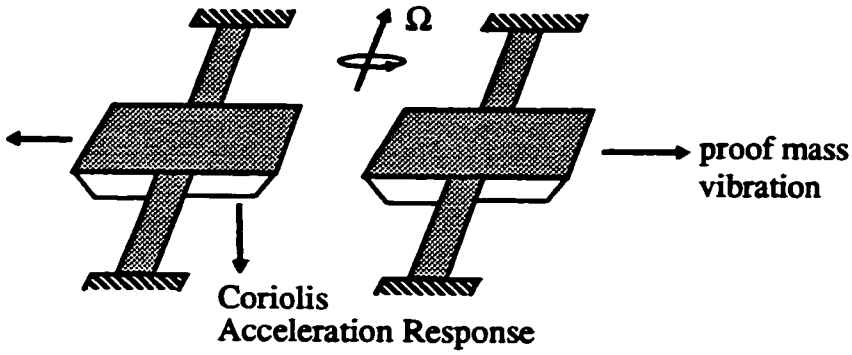

Fig. 2.4: Dual accelerometer vibrating gyroscope (redrawn from [1]).

2.3.4 Vibrating Shells

Vibrating Shell gyroscopes transfer energy between two identical modes of a structure. Because of their shape, vibrating shells have two identical modes of vibration with nominally equal resonant frequencies. They may be shaped like a glass [2], like a cylinder [3], or like a ring [1] (Fig.2.5).

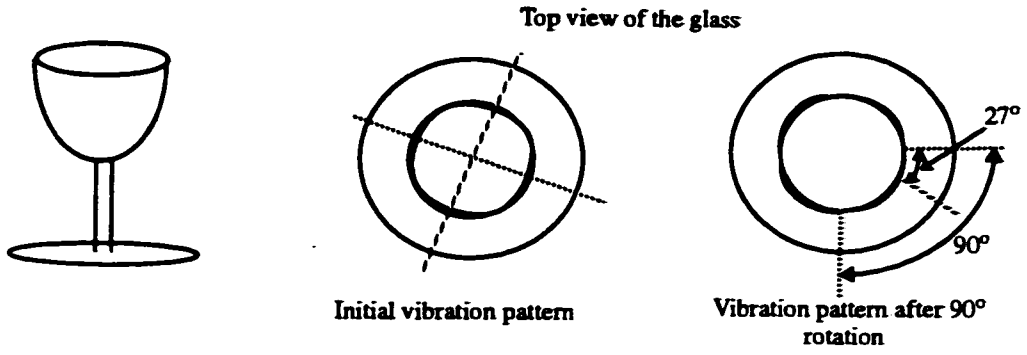

Fig. 2.5: Vibrating shell gyroscope (redrawn from [1]).

2.3.5 Surface Acoustic Wave

In a Surface Acoustic Wave (SAW) gyro, a standing wave is generated on an elastic material surface by combining two SAWs propagating in opposite direction (Fig.2.6). The Coriolis force acts on vibrating particles when the sensor is rotated as shown in Fig.2.6. This force generates a secondary SAW in the orthogonal direction of the primary standing wave. The amplitude of this secondary wave is proportional to the angular velocity.

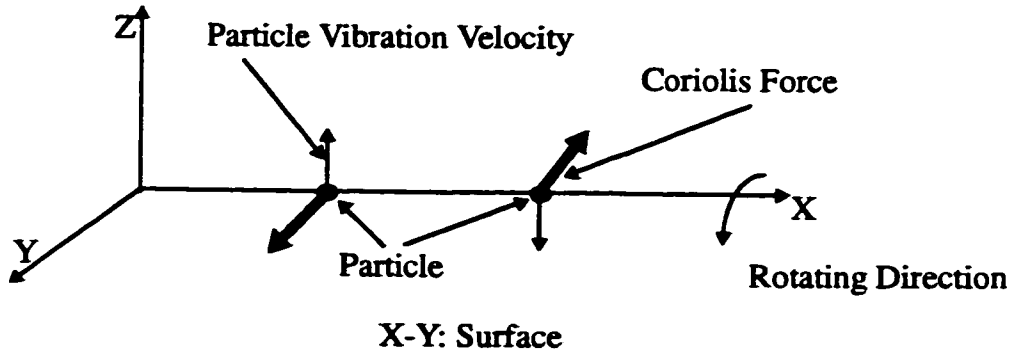

Fig. 2.6: Coriolis forces acting on particles (redrawn from [4]).

2.3.6 Types of Fabrication Techniques

Micromachined vibratory gyroscopes may also be categorized based on the micromachining technique used in their implementation. Two general fabrication techniques of Bulk Micromachinig and Surface Micromachining are normally used. In Bulk Micromachining the structural material of the sensing element is usually the single crystal silicon or quartz substrate. Wet anisotropic etching or special dry etch techniques are used to etch the required structure. Much of the recently published research uses this technique to make angular rate sensors [5-15].

In surface micromachining the structural layer is formed by thin layers of materials such as polysilicon, metals like nickel, or oxide deposited on the substrate. The structural material is then patterned using dry etching and released by sacrificial etching of a spacer layer for surface micromachinig. This technique is also heavily used in research to fabricate angular rate measurement sensors [16-23].

The first successful vibrating angular rate sensor, the Gyrotron, was developed in England in the 1950s, by the Sperry Gyroscope Company [24]. The electromagnetic actuation and detection used in Gyrotron was replaced with piezoelectric means in 1960s when General Electric developed VYRO [25]. Angular Rate Sensors, in which the sensor element itself consisted of a piezoelectric material, were tested in 1980s (Ceramic PZT: Watson Ind. [26]; Monocrystalline Quartz: PTI/Systron Donner Corp. [27]).

The main trend in the 1990s is to develop vibrating angular rate sensors with micromachined bulk or film structures as the sensing element. This allows the possibility of using existing semiconductor manufacturing equipment to build both the sensor and its signal detection and signal processing circuitry.

2.4 Applications of Vibratory Gyroscopes

Some new applications that need small or inexpensive gyroscopes are summarized in Fig.2.7. Most of these applications can not successfully use conventional gyroscopes based on conservation of angular momentum. These applications require gyroscopes with low-cost and small size that have to be batch-fabricated. Angular rate sensors have a wide variety of applications in the automobile industry [28]. They may be used in ABS systems, Anti-Skid systems, motion control, and active suspension for improved comfort and safety. The most important characteristics for angular rate sensors in these automotive applications are reliability and low cost. The small change of the rate signal with temperature and time is often of less importance, since only more rapid changes are of interest.

Another potential application of angular rate sensors is in satellite based GPS systems. In GPS systems, updates of position can only be obtained at a few minutes intervals. Ground interference from tall buildings, mountains, tunnels, etc. can prolong this time. There is a need for an additional navigation system that can give the position in between the updates. New micromachined accelerometers and angular rate sensors will make such systems economically available.

Gyroscopes may also be used in robotic systems as a part of an Inertial Measurement System (IMS) to measure the position of a robotic arm [29]. Anti-Jitter compensation for video cameras, Free Space Pointers (Mice) for computers or virtual reality systems are among other applications of low-cost angular measurement sensors. In addition, the largest area of applications for inexpensive angular rate sensors might turn out to be toys, games and sports equipment. Only the imagination limits the number of applications in these areas.

Area	Example of Applications	Range	Accuracy
Automotive safety			
reliable, inexpensive,	improved controls for airbags	50 g, 200°/s	500 mg, 10°/s
lifetime,	anti-collision systems	100°/s	1°/s
rough environment	active suspension	50°/s	2°/s
	anti-skid	100°/s	1°/s
Consumer			
inexpensive,	free-space pointers (small computers)	100°/s	1°/s
small, lifetime,	remote control devices (TV-controls)	100°/s	2°/s
low_power	video cameras (anti-jitter compensation)	50°/s	0.5°/s
	navigation (complement to GPS)	50°/s	0.5°/s
	toys and sports equipment	varies	varies
Industrial			
reliable, small,	machine control	10°/s	0.01°/s
low-power	angular vibration measurement	varies	varies
	attitude control of flying objects	20°/s	0.02°/s
	automatic guided vehicles	50°/s	0.2°/s
	robotics	20°/s	0.2°/s
	stabilized platforms	10°/s	0.01°/s
Medical			
reliable, small,	monitoring of body-movement	10 g, 100°/s	100 mg, 1°/s
low-power	vibration diagnostics	0.1 g, 50°/s	1 mg, 0.5°/s
	controls for paralysed patients	2 g, 100°/s	20 mg, 2°/s
	surgical instruments	20°/s	0.1°/s
	wheel-chairs	2 g, 50°/s	20 mg, 0.2°/s
Military			
reliable, small,	new weapon systems		
rough environment	smart ammunition		

Fig. 2.7: New applications that need smaller or inexpensive micromachined inertial sensors, including estimate of typical required performance (adapted from [30]).

2.5 Design Issues in Vibratory Gyroscopes

Most of the vibratory angular rate sensors (with the exception of vibrating shells) use two perpendicular vibrations. The amplitude of the Coriolis force induced sense vibration is always much smaller than the reference vibration. The ratios are in the order of 15 ppm

for a 1^{o}/Sec angular velocity and 100 Hz bandwidth [30]. Normally the vibration amplitude of the micromachined structures are in the range of a few microns, implying very small sense amplitudes. The consequences are:

(i) The reference and sense vibrations must be very well isolated from each other.

(ii) Vibrationally inactive mounting areas must be used to reduce uncontrolled aging and temperature drift due to changes in surroundings.

(iii) A stable and inert material should be used for the sensor element.

(iv) Stray capacitances and parasitic elements must be small and stable.

The mechanical coupling between the reference and the sense vibration is mainly due to imperfections in the etching and to stress in the mounting. It can be reduced by mechanically balancing the structure by adding or taking away material. A high Q factor for vibrations may be obtained by operating in a vacuum. A high Q is desirable since:

(i) The resonance frequency of the reference vibration is more pronounced.

(ii) The effect of stray capacitances is reduced due to lower activation voltages.

(iii) The phase of the sensor signal becomes more stable since the resonance peaks become sharper.

The best means for detecting very small sense amplitudes are capacitive and piezoelectric. In general, piezoelectric detection is better than capacitive detection for small resonant amplitudes. Piezoresistivity can also be used but with reduced performance [30]. Optical detection is usually not feasible or too expensive. Inductive detection was used in the first macroscopic tuning fork in the Gyrotron, but is rarely used in micromechanical structures.

A few different material combinations have been used in angular rate sensors:

(i) Metal with piezoceramics mounted to the surface with adhesive.

(ii) Piezoceramics

(iii) Piezoelectric monocrystals such as Quartz.

(iv) Monocrystalline Silicon

(v) Polysilicon

(vi) Electroplated Metals such as Nickel

In 1980's different types of vibrating gyroscopes have been designed using metals and piezoceramics [31]. None of these device types takes advantage of micromachining technology, mostly because of the materials used in their structure.

Piezoceramics have also been used in some vibrating gyroscope designs [32]. A disadvantage with ceramics is that today's manufacturing methods are not well suited for the high precision needed for accurate rate sensors. Also, the aging of today's ceramics is more than metal or monocrystals. It is not possible to use ceramics in today's micromachining technology, so none of these sensors are micromachined.

Price, size and performance indicate that micromachined batch-fabricated gyroscopes will be frequently used in many applications mentioned in Fig.2.7. None of the above mentioned gyroscopes can be classified as micromachined. Further development of the LIGA process might resolve the problems for the metal-ceramic combinations in the future.

Choices for materials in micromachined gyroscopes are currently limited to piezoelectric monocrystals, monocrystalline Silicon, polysilicon, or electroplated metals.

2.6 Design Examples

The increased need for small and inexpensive new vibratory angular rate measurement sensors has initiated a growing number of research and development projects at

many places during the past few years. A few examples of the recent research in this field are briefly explained here.

2.6.1 A Quartz Tuning Fork Angular Rate Sensor [30]

This gyroscope is designed based on a single-ended tuning fork made out of monocrystalline quartz (Fig.2.8). The reference electrodes are used to create the electric field that activates the in-plane resonant flexural reference vibration. The sense electrodes detect the current generated piezoelectrically by Coriolis-induced out-of-plane flexural sense vibration. The detected current is in the range of 50 pA/°/sec. The frequency of operation of the device is 35 KHz. This device operates in an open-loop configuration and at atmospheric pressure. The reported resolution is around 1°/sec for a 40 Hz bandwidth.

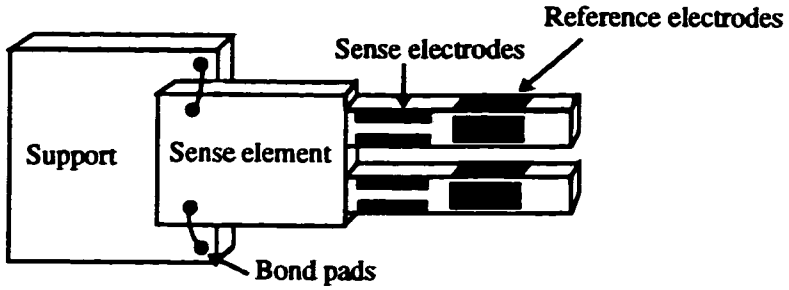

Fig. 2.8: Overview of the quartz gyroscope (redrawn from [30]).

2.6.2 Micromachined Vibrating Ring Gyroscope [1, 16]

This device is designed based on the vibrating ring structure discussed before. The device measures rotation angle by monitoring the position of node lines in a vibrating ring. To sense the rotation, the ring is electrostatically forced into an elliptically shaped vibration mode and the position of the node lines are capacitively monitored. When the device is subjected to rotation, the node lines lag behind the rotation due to Coriolis force. The readout circuitry detects this lag and develops the output signal of the sensor.

This device is fabricated using a process based on metal electroforming techniques that allow large amounts of circuitry to be included with the sensor. The structure of the vibrating ring and capacitive pickup and drive elements are shown in Fig.2.9. The entire ring and also the capacitive drive and pickup electrodes is made out of electroplated nickel. The ring has a diameter of 1 mm, a thickness of 19 μm, a width of 5 μm, with electrode gaps of 7 μm. On-chip CMOS circuitry is used to detect the Coriolis induced vibration in the ring.

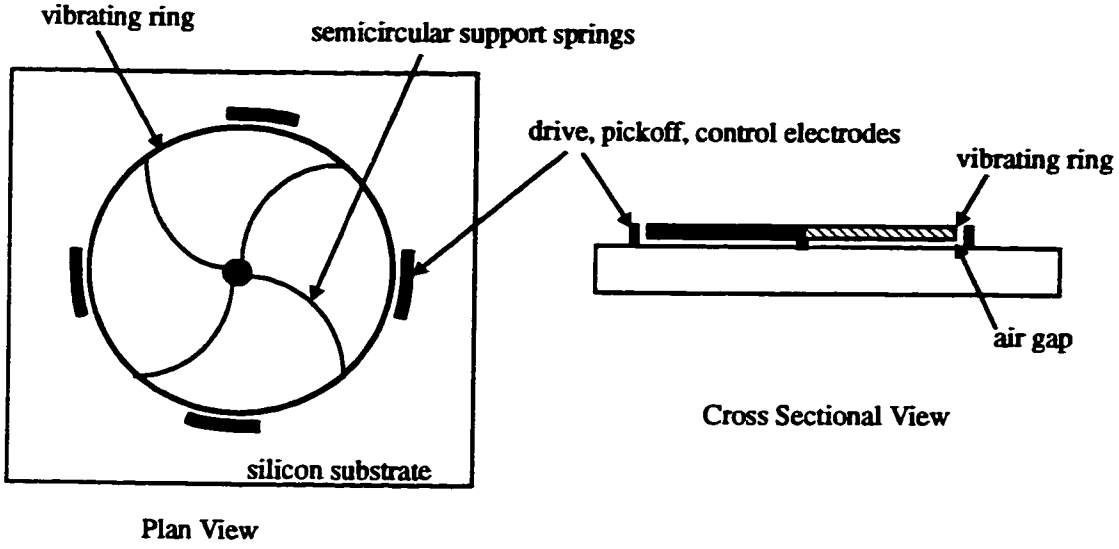

Fig. 2.9: Plan and cross-sectional views of ring gyroscope (adapted from [1]).

Two main advantages of the design are its compatibility with CMOS fabrication process and the vibrating ring structure used as sensing device. As mentioned before, vibrating shell structures have two identical modes of vibration with nominally equal resonant frequencies which makes them a very good choice for a vibratory gyro.

The major drawback of this design is the type of material used as the sensing element. Electroplated Nickel exhibits creep, fatigue and long term drift problems. It also has a rea-

sonably low intrinsic Q which will limit the performance of sensor. Voltage levels applied to the capacitor driving elements should be as high as 60 V in order to generate the required amplitude of vibration in the ring. The whole structure is very compliant and therefore it can not withstand rough environments.

The reported sensitivity is 0.5^{o}/S in a 10Hz bandwidth. A quality factor of 4000 is reported for the device operating in a vacuum.

2.6.3 A Surface Micromachined Tunable Vibratory Gyroscope [17]

This design is based on surface-micromachined comb drive structures [33-36]. The schematic drawing of the design is shown in Fig.2.10 The comb drives actuate the plate in the x direction and the Coriolis induced vibrations along the z direction are sensed by detecting the variations in capacitance between the plate and another polysilicon plate located underneath. The structural layer is 7.5μm thick LPCVD-deposited polysilicon with phosphorus doping. The structure is released by sacrificial etching of 1.5μm thick APCVD (Atmospheric Pressure Chemical Vapor Deposition) phospho-silicate glass (PSG) under the plate.

The gyroscope is intentionally designed to have a higher resonant frequency in the detection mode than in the actuation mode. The resonant frequency in the detection mode can be shifted down using spring-softening effect by applying a DC voltage between the plate and detection electrode. The mismatch between the two natural frequencies could be adjusted this way. The noise equivalent rate (minimum detectable rate) for this device is reported to be 0.1 ^{o}/sec at 1Hz bandwidth.

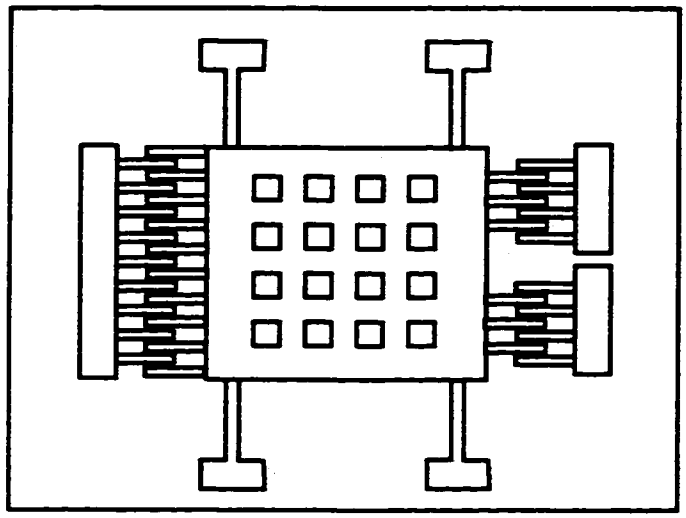

Fig. 2.10: Schematic drawing of the gyroscope (adapted from [17]).

2.6.4 Micromachined Dual Input Axis Angular Rate Measurement Sensor [18,21]

This design is based on angular resonance of a rotating rigid rotor suspended by torsional springs. The rotor is suspended using 4 torsional springs as shown in Fig.2.11. These beams provide a torsional suspension for the rotor allowing it to move about three mutually perpendicular axes. The rotor is driven at angular resonance about the Z-axis using the specially designed comb drives. A rotation about the x axis induces a Coriolis angular oscillation about the y axis and vice versa. Sensing these coriolis oscillations and relating them to the original input rates forms the foundation of angular rate sensor operation.

The micromachined structure is fabricated using a thick (2μm) polysilicon layer released using sacrificial etching of PSG oxide underneath. Electrostatic comb drive is used to actuate the structure and capacitance detection is used to detect vibration in sense direction. Minimum detectable input is reported to be 1.2 ^{o}/sec at 25Hz bandwidth.

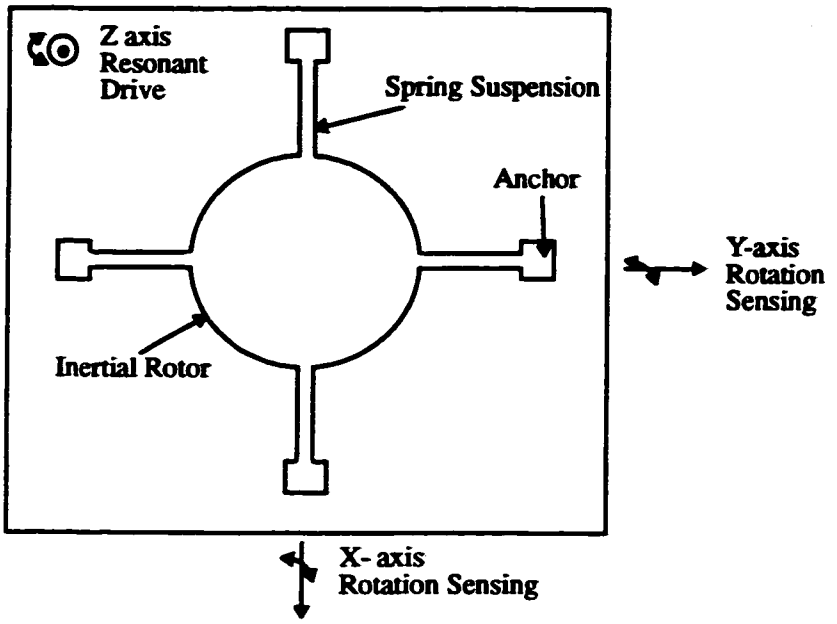

Fig. 2.11: Conceptual illustration of dual axis rate sensor (adapted from [21]).

2.6.5 Silicon Angular Rate Sensor Using Anisotropic Etching Technology [10,11]

This gyro is based on an oscillating bar made by anisotropic etching of silicon. The structure is shown in Fig.2.12. The silicon rate sensor is formed of an oscillation bar and detection electrodes on a glass base. The oscillation bar and detection electrodes are simultaneously formed by a silicon anisotropic etching of a <110> wafer. The oscillation bar is vibrated at its resonance frequency by a piezo-actuator. The applied angular rate generates the Coriolis force which deviates the bar from its normal orbit of the vibration. The deviation is then detected by monitoring the capacitance between the oscillation bar and the detection electrodes. The resolution obtained for this device is 3 ^{o}/sec in a 30 Hz bandwidth. The detected voltage is in the range of $30\mu V_{mean}$ for $1\frac{rad}{sec}$ input angular rate.

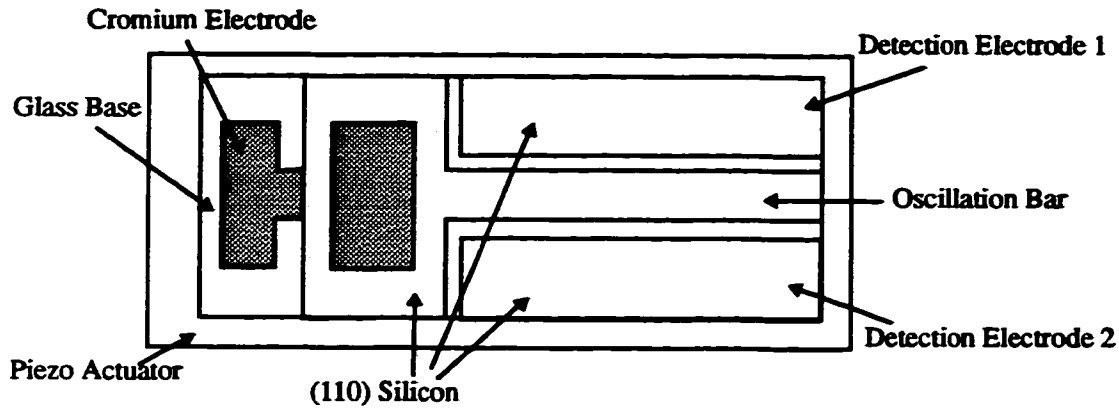

Fig. 2.12: Structure of silicon rate sensor (adapted from [11]).

2.7 The Proposed Design

The design of a vibrating beam micromachined sensor will be discussed in the following chapters of this proposal. The beams are formed using bulk micromachining of silicon, same as is done in [11]. However, <100> wafers are used as the structural material and beams with smooth and vertical side walls are achieved by wet etching in Tetra-Metyl Ammonium Hydroxide (TMAH). This creates the opportunity of integrating circuitry with the sensor on one chip. A clamped-clamped beam or double sided tuning fork is used for the vibrating structure. Electromagnetic coupling is used to actuate the beams. Larger amplitudes of vibration are possible this way, compared to the vibrations induced by a piezoelectric actuator through the base.

CHAPTER 3

Design and Modeling

3.1 Introduction

The Angular Rate Measurement sensor is designed based on a vibrating beam structure. Fabrication of beams with highly accurate dimensions is possible using anisotropic etching of silicon. Mono-crystalline silicon is an excellent structural material [37]. It does not suffer from creep, fatigue and drift problems which are always present in metals. It has very low internal damping and a very high intrinsic Q. Internal stress, which is an ever-present problem in deposited materials, such as polysilicon, is not present in mono-crystalline silicon. Silicon is also compatible with integrated circuit fabrication technology, which creates the opportunity of integrating the sensor and its detection circuitry on one chip. Thus monocrystalline silicon is chosen as the structural material for the sensor.

The fabrication process of the sensor is discussed first, followed by an overview of the sensor operation and modeling. Design issues such as actuation frequency and amplitude, sensitivity, sense vibration, damping, and coupling are discussed next. The operation issues of the sensor including the design of the required circuitry for actuation and detection of the vibrations and non-ideal effects are discussed in the rest of the chapter followed by introduction of a tuning fork structure as an improved structure.

3.2 Sensor Structure and Fabrication Process

A test structure for the silicon-beam micro-sensor is designed and shown in Fig.3.1. It consists of two pieces: (1) a beam formed by anisotropic etching of a silicon wafer and (2)

a glass plate with a cavity, and metal at the bottom of the cavity. The Si wafer is bonded to the glass plate such that the cavity with metal is located under the beam. The sense and detection electrodes are formed by metal deposited on the beam and on the glass. Two ohmic contacts to the substrate are formed at the two ends of the beam.

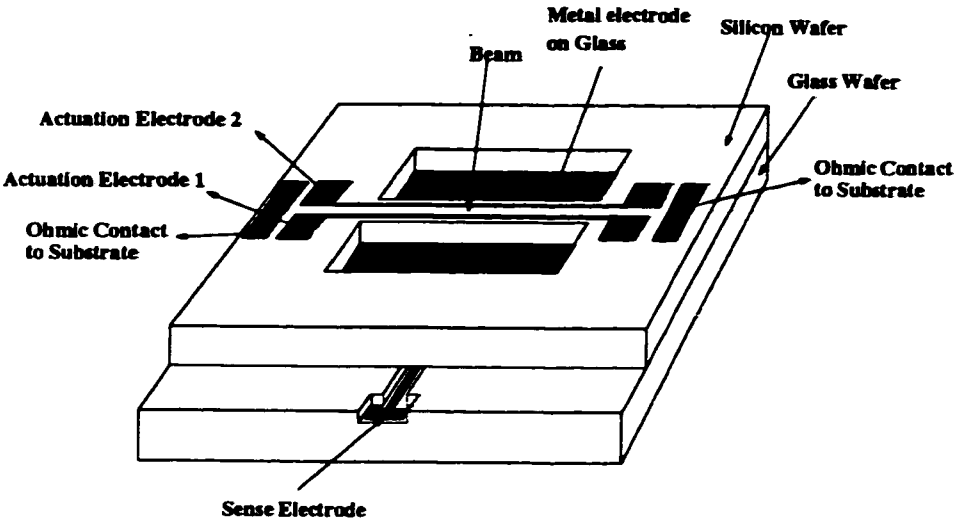

Fig. 3.1: Structure of the vibrating beam gyroscope.

The fabrication process steps are shown in Fig.2.2.

(a) The processing of the silicon wafer.

1- The process starts with a <100> double side polished P-type silicon wafer with the required thickness T.

2- An oxide layer with thickness of 5000 Å is thermally grown on the sample, and patterned to open the windows for Boron diffusion required for ohmic contact to substrate.

3- A layer of borosilica gel is spined on the sample, followed by a drive-in step for 1 hour at 1100°C to form the P^{++} region at the contact areas.

4- The borosilica layer and the thermal oxide are etched off the sample.

5- Another layer of oxide with the thickness of 1200 Å is grown by wet oxidation at 950°C.

6- The oxide is patterned to open the etch windows, and contact windows. The etch windows are opened on both sides of the sample.

7- A stack of two metal layers is then deposited on the sample. The first layer is Chromium with the thickness of 1000 Å and the second layer is Gold with the thickness of 2000 Å.

8- The metal layers are patterned to form the electrodes

9- The sample is etched in TMAH to form the beam. Overhanging oxide layers are removed by a short etch in BOE (Buffered Oxide Etchant).

(b) The processing of the glass plate:

10- A #7740 Pyrex glass is chosen because its thermal expansion coefficient matches silicon at temperatures between 300°C to 400°C where the anodic bonding is done. The glass is then coated with a stack of two metal layers: 1000 Å Chromium and 2000 Å Gold.

11- The metal layers are patterned and the glass is etched in 49% HF to form the cavity.

12- The remaining metal layers are removed and another stack of Chromium and Gold layers (1000 Å Cr and 2000 Å Gold) deposited on the glass. The metal layers are patterned inside the cavity to form the electrode.

(c) The combined process

13- The silicon wafer is bonded to glass plate using anodic bonding (as explained in Sec.6.2.3).

The metal used in this process to form the electrodes on the beam and on the glass is exposed to TMAH for a long time during the etch process (step 9). Therefore it has to be resistant to this etchant. Gold is used for this purpose, because it stays very well in TMAH (unlike Aluminum which is etched quickly as soon as it is exposed to the fresh 25% TMAH which is required for this work) and it is a very good conductor. A layer of Chromium is used as an adhesion layer between the gold and SiO_2 or glass. Chromium has very good adhesion to both SiO_2 and glass, it is easy to pattern, and it is resistant to TMAH.

The metal used in this process should also be resistant to HF so that it stands the final step of the beam's process which is a short etch in BOE. Both Gold and Chromium have very good resistance to etching in HF. For the same reason, they are used for patterning the glass in steps 10 and 11.

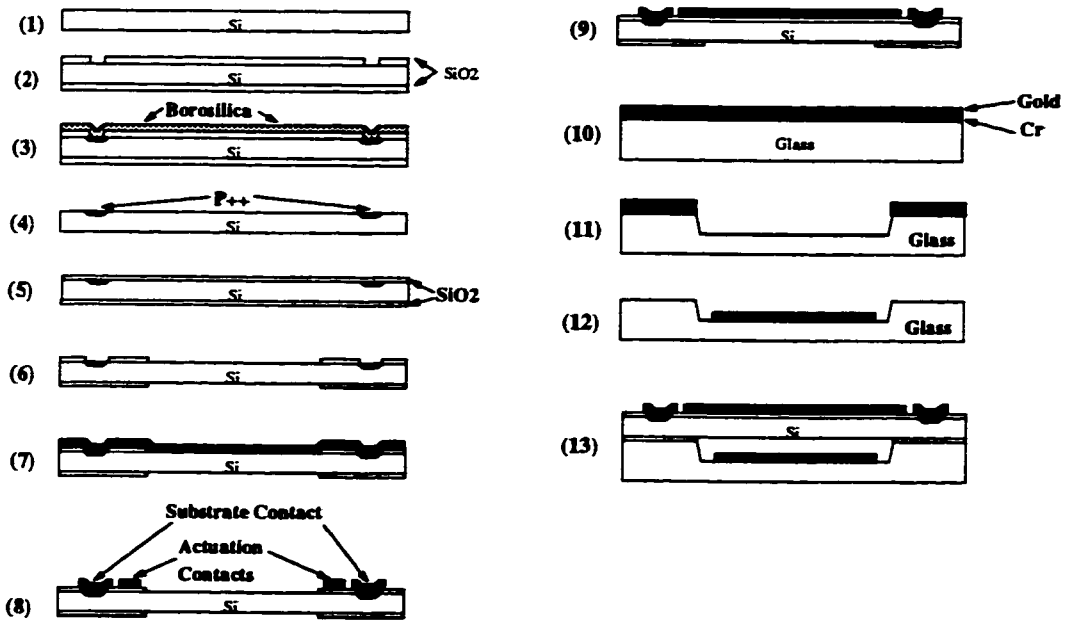

Fig. 3.2: Fabrication Process.

3.2.1 Square-Cross-Section Beam by Anisotropic Etching of Si [38]

One of the most important steps in the device fabrication process is anisotropic etching. As mentioned in previous chapter, closely matched resonance frequencies in two modes of vibration are desirable in order to increase the sensitivity. The beam should have a square-shaped cross section (equal width and thickness) in order to achieve equal (or near equal) resonance frequencies in both vertical and horizontal vibration modes.

Anisotropic etching of silicon takes advantage of the different etch rates of the silicon crystal in different directions. {111} planes in Si have the slowest etch rate among all planes when it is etched in any of the common Si anisotropic etchants. Therefore, {111] planes act as etch-stop surfaces when silicon is etched. Starting from a <100> wafer, it is not possible to achieve vertical side walls if the pattern is aligned with a <011> direction as is usually done in semiconductor process technology. Fig.3.3 shows the relationship among various directions on a Si{100} wafer (one of the <100> family of directions).

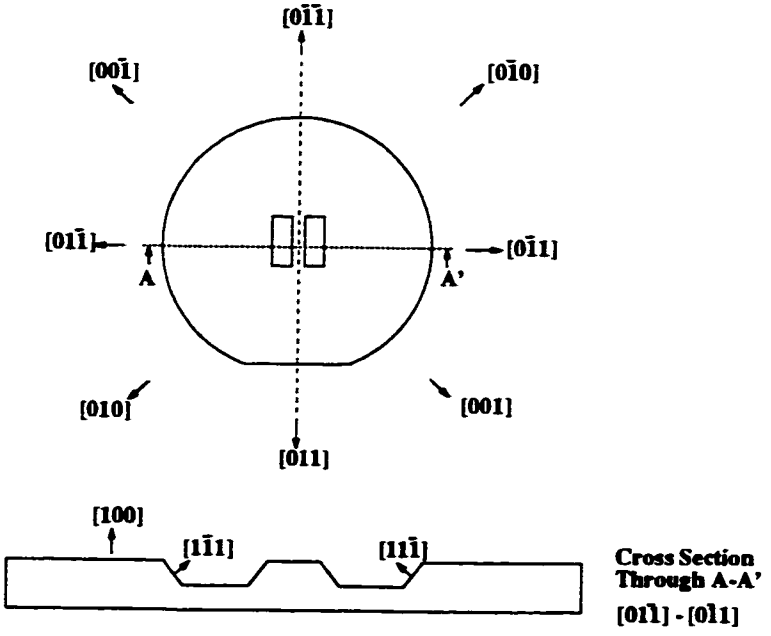

Fig. 3.3: Shape of the side walls generated by TMAH etch when the pattern is aligned parallel or perpendicular to a <011> direction.

The under-etch-rates of silicon are shown in Fig.3.4 for different mask-edge angles, at different temperatures. The inclination angles of the emerging planes are also shown in Fig.3.5 [39]. As shown in the figures, at a deviation angle of 0^o the underetched plane is a vertical [010] plane. Also, the etch rate has a local minimum at the <100> direction. So it is possible to achieve vertical sidewalls by carefully aligning the mask. The mask has to be aligned such that no other plane with a lesser etch rate is exposed to the solution. In order to do this, the mask has to be rotated by 45^o with respect to the <110> directed wafer flat, as shown in Fig.3.6. In this configuration, only {100} planes are exposed at the sidewalls of the beam so the etch rate would be equal in both vertical and lateral directions. It is possible to achieve reasonably flat and uniform vertical sidewalls using this configuration [40,41]. However, this method results in substantial lateral etch at the sides of the beam which leave overhanging SiO_2 strips at the sides of the beam. These need to be removed after the etch. This is done by another etch in BOE after the anisotropic Si etching.

As shown in Fig.3.4, the etch rate changes by almost an order of magnitude as the temperature varies from 80^oC to 50^oC but a substantial local minimum with vertical underetched planes always exists at the intersection of (100)-(001) planes. This local minimum allows smooth vertical sidewalls to be formed on {100} planes regardless of the etching temperature. We can take advantage of this fact in order to achieve more precise dimensions using a timed etch.

Because of the large lateral etch rate, the lateral dimension of the beam is dependent on both the mask size and the etch time. If the sample is taken out of etchant as soon as it is etched through in the mask openings, the lateral size of the beam can be defined as:

$$W = W_m - T \qquad \text{Eq.3.1}$$

In which W_m is the width of beam's pattern on the mask and T is the thickness of the wafer. As mentioned before, the beam has to have a reasonably good match between its lateral and vertical dimensions. We can use a two-step timed etch to achieve more precise dimensions as follows:

1- The mask is designed such that $W_m=W+T+\delta$ in which δ is a safety margin to make sure that when the wafer is etched through, the beam's lateral dimension will still remain larger than the required width W. All of the tolerances mentioned in the following steps should be taken into account and included in the safety margin δ.

2- A double-side polished wafer with the required thickness may be purchased from a suitable vendor. The exact thickness of each wafer should be measured (using a micrometer) and recorded. The wafers usually have some tolerance in their thickness, for example a wafer with the thickness of 100μm may have a tolerance of $\pm 5\mu m$, therefore a measurement of the exact thickness of the wafer is required.

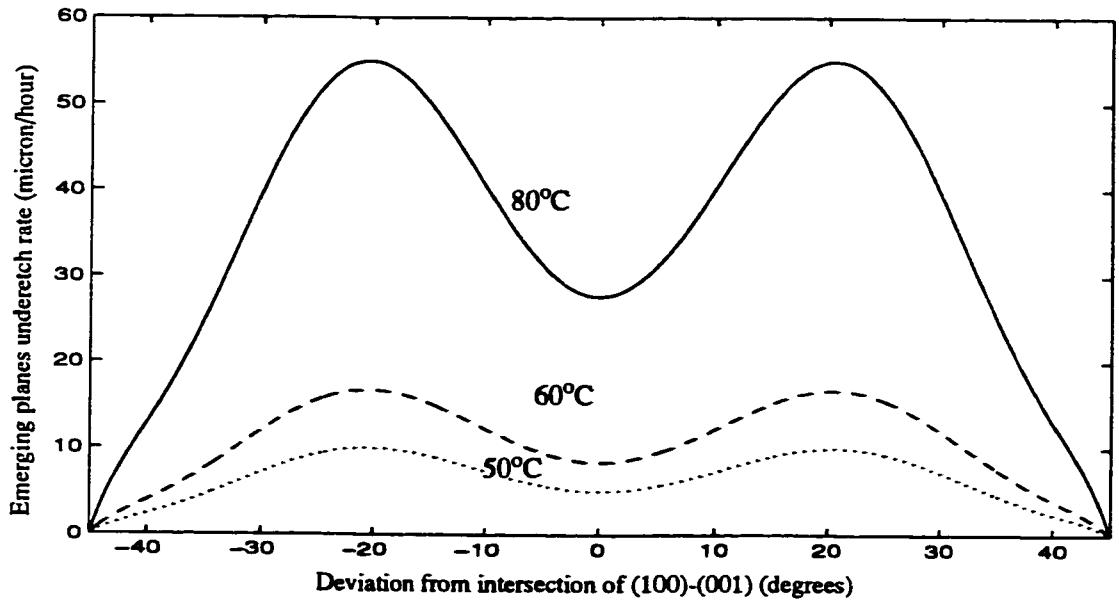

Fig. 3.4: Variation of underetch rate of the emerging planes in Si {100} etched in fresh TMAH 25 wt. % [39].

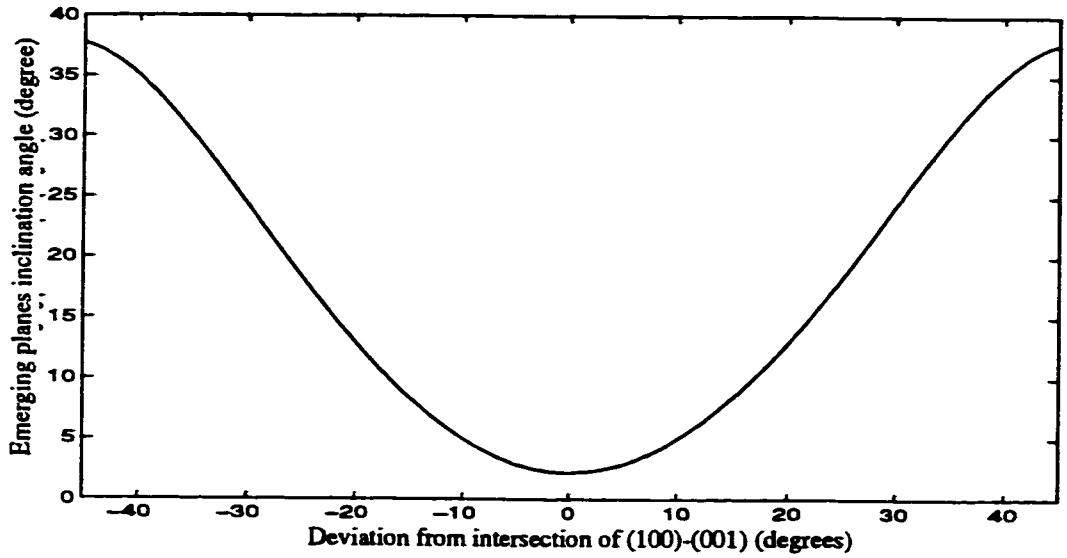

Fig. 3.5: Slope of emerging planes in Si {100} etched in TMAH 25 wt.% at 80°C [39].

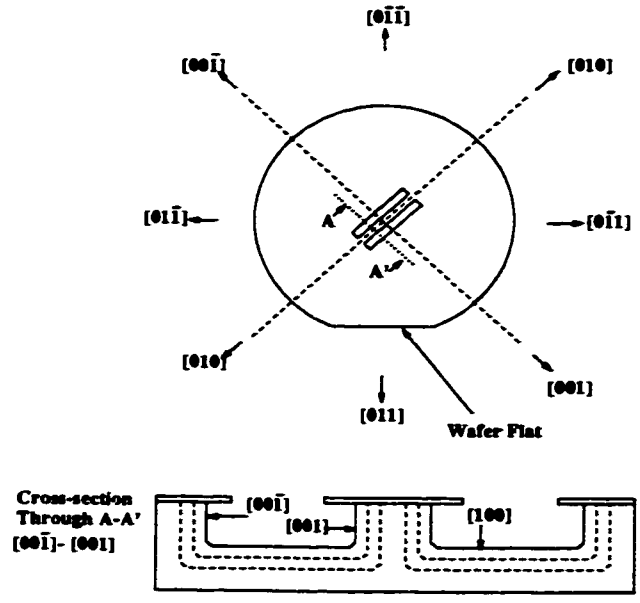

Fig. 3.6: Vertical side walls obtained when the pattern is by rotated by 45^0 from the [011] wafer flat.

3- The wafer is processed according to steps 1-8 in Sec.3.2. As mentioned before, the pattern is aligned by 45° from the <110> direction in order to achieve vertical sidewalls [41]. The wafer is then etched in TMAH at 80°C until it is completely etched through in the mask openings. The required etch time can be calculated knowing the etch rate of silicon at 80°C [39]. The wafer may also be monitored frequently during the etch and taken out as soon as it is etched through. Our experiments found that the width of the beam at the end of this long etch step at 80°C is controllable with a tolerance of better than $\pm 10\mu m$, on a wafer of 100μm thickness.

The width of the beam is measured at this point (using an optical microscope) and a second etch is performed at a lower temperature. The etch rate of silicon in TMAH reduces to $7.9\frac{\mu m}{hr}$ at 60°C. By performing a second etch at this temperature it is possible to control the final width of the beam with a very good accuracy. The required time for the second etch step is calculated using the etch rate of silicon at 60°C. The samples are then etched and frequently monitored during the etch until the required thickness is achieved. Accuracies as good as $\pm 2\mu m$ are achieved in our experiments this way.

Small <111> flanges are formed at the intersection of (010) and (001) planes at both ends of the beam, which contribute to the increase of mismatch between the two natural frequencies of the beam. This problem and a method to substantially reduce the size of these <111> flanges will be discussed in detain in Chapter 5.

Another way of achieving vertical side-walls is to use a <110> wafer. There are problems involved with using <110> wafers. It is not possible to obtain rectangular cavities in <110> wafers. The top view of the final etched cavity in a <110> wafer is always a parallelogram, with angles between edges equal to 70.5° and 109.5°. <110> wafers are not used in standard fabrication industry. Moreover, using a <100> wafer would be beneficial for

adapting the design to a standard process technology in the future.

3.3 Overview of Sensor Operation

The operating principle of the angular rate sensing device is shown in Fig.3.7. The beam is inserted in a constant and uniform magnetic field $\vec{B}$ by placing two permanent magnets around the chip[1]. A sinusoidal current *i(t)* is then applied to the metal electrodes to actuate the beam. The electromagnetic coupling between the electric current and magnetic field will cause the beam to vibrate in the plane of the wafer. The amplitude of the vibrations in the actuation direction is kept constant by feedback. A voltage *E(t)* is induced by the movement of the beam in the B-field. This *E(t)* is measured by an external circuit, and the actuation current *i(t)* is varied accordingly. When the sensor is rotated around its sense axis with angular rate Ω, the Coriolis acceleration will induce another vibration normal to the plane of the wafer. Vibration of the beam normal to the surface will cause a change of capacitance between the beam and electrode deposited at the bottom of the cavity on the glass plate. The variations in capacitance *C(t)* will then be detected as the output signal, which is proportional to the angular velocity.

3.4 Mass-Spring Model of the Vibrating Beam

A simulation model is necessary in order to investigate and predict the dynamic behavior and response of the sensor. The beam may be modeled as a Mass-Spring system shown in Fig.3.8. This system is defined using the following system of differential equations [10]:

---

1. The magnetic field was experimentally estimated to be ~0.25 Tesla (see Chapter 6).

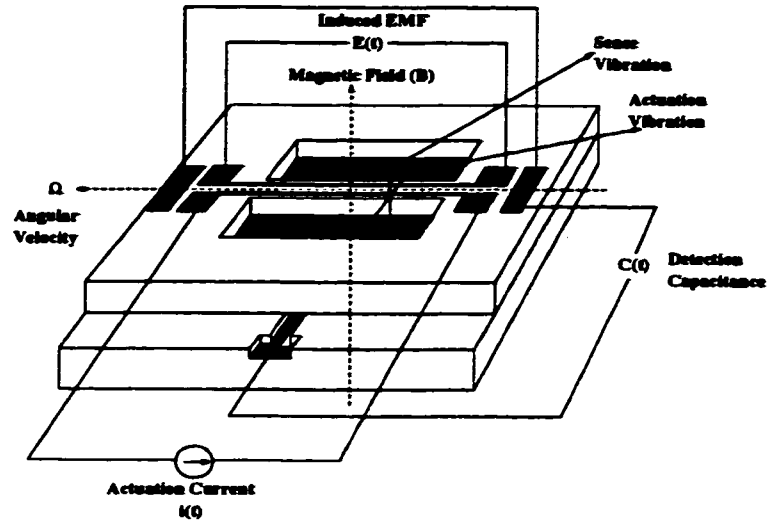

Fig. 3.7: Principle of device operation.

$$m_0\frac{d^2x(t)}{dt^2}+\mu_x\frac{dx(t)}{dt}+K_x x(t) = F_0 COS(\omega t) \qquad \text{Eq.3.2}$$

$$m_0\frac{d^2y(t)}{dt^2}+\mu_y\frac{dy(t)}{dt}+K_y y(t) = 2m_0\Omega\frac{dx(t)}{dt} \qquad \text{Eq.3.3}$$

where x and y are the actuation and sense directions respectively and m_0, μ_x, μ_y, K_x, K_y are equivalent masses of the beam, damping coefficients in x, y directions, and beam stiffness coefficients in x, y, directions respectively. $F_0 COS(\omega t)$ is the actuation force and $2m_0\Omega\frac{dx(t)}{dt}$ is the Coriolis force applied to the mass, due to externally applied rotations.

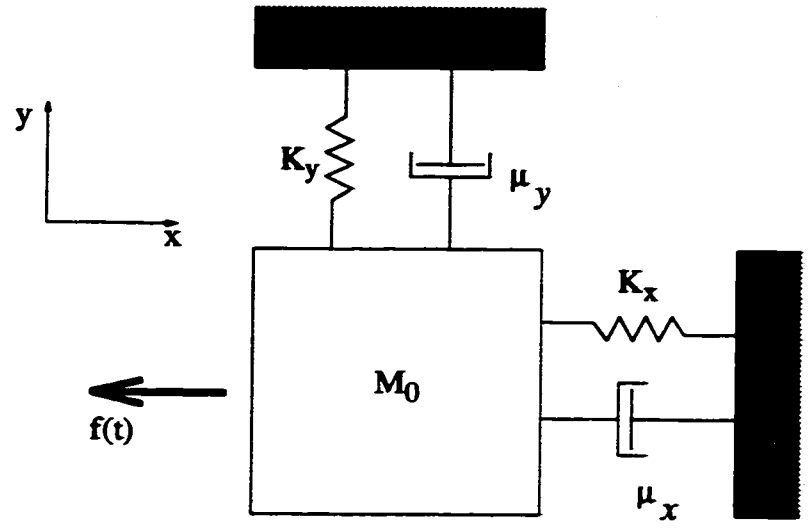

Fig. 3.8: Mass-Spring model of the beam.

The steady-state solution for deflection in the x direction may be found as [42]:

$$x_p(t) = XCOS(\omega t - \phi_x) \qquad \text{Eq.3.4}$$

$$X = \frac{\delta_{st}}{\sqrt{\left[1 - \left(\frac{\omega}{\omega_{nx}}\right)^2\right]^2 + \left[\frac{1}{Q_x}\frac{\omega}{\omega_{nx}}\right]^2}} \qquad \text{Eq.3.5}$$

$$\phi_x = tan^{-1}\left(\frac{\frac{\omega}{Q_x\omega_{nx}}}{1 - \left(\frac{\omega}{\omega_{nx}}\right)^2}\right) \qquad \text{Eq.3.6}$$

where ω_{nx}, Q_x are the natural frequency of the beam and its quality factor in the x direction. δ_{st} is the static deflection in the middle of the beam as a result of the applied force F_0. We have:

$$\omega_{nx} = \sqrt{\frac{K_x}{m_0}}, \qquad \text{Eq.3.7}$$

$$Q_x = \frac{m_0 \omega_{nx}}{\mu_x} \qquad \text{Eq.3.8}$$

$$\delta_{st} = \frac{F_0}{K_x} \qquad \text{Eq.3.9}$$

By solving Eq.3.3 for y we have:

$$y_p(t) = YCOS(\omega t - \phi_y) \qquad \text{Eq.3.10}$$

$$Y = \frac{2\omega\Omega X}{\omega_{ny}^2 \sqrt{\left[1 - (\frac{\omega}{\omega_{ny}})^2\right]^2 + (\frac{\omega}{Q_y \omega_{ny}})^2}} \qquad \text{Eq.3.11}$$

$$\phi_y = \phi_x - \frac{\pi}{2} + tan^{-1}\left(\frac{\frac{\omega}{Q_y \omega_{ny}}}{1 - (\frac{\omega}{\omega_{ny}})^2}\right) \qquad \text{Eq.3.12}$$

where Ω is the input angular rate and Q_y, ω_{ny} are beam's quality factor and natural frequency in y direction.

These equations may be used to investigate the response of the sensor and the influence of different parameters on the output signal. The simple modeling used to derive the equations is based on approximations and allows estimation of the physical values.

A more accurate value for the natural frequency of the beam may be calculated using the Rayleigh method [42,43]. The natural frequency of the beam is defined as follows according to the Rayleigh method[42]:

$$\omega_n^2 = \frac{\int_0^L EI\left(\frac{d^2\phi(x)}{dx^2}\right)^2 dx}{\int_0^L \rho A(\phi(x))^2 dx} \qquad \text{Eq.3.13}$$

where L, E, I, ρ, A are length, Young's modulus, moment of inertia, density, and cross-sectional area of the beam respectively. $\phi(x)$ is the deflection shape of the beam for the fundamental resonance mode. Generally, the static equilibrium shape is assumed for $\phi(x)$. The natural frequency of the beam based on this assumption may be found as [44, 45]:

$$\omega_n = \left(\frac{4.77}{L}\right)^2 \sqrt{\frac{EI}{\rho A}} \qquad \text{Eq.3.14}$$

This method is used in our simulation programs in this work to calculate the resonant frequency of the beam.

3.5 Design Issues

To successfully design an angular rate measurement sensor, several key parameters have to be considered. These parameters stem from the basic mechanical principles of the operation of the device and are applicable to any type of vibrating gyro design.

The first and most important goal in designing such a device is to maximize the amplitude of vibrations induced in the sense direction due to the coriolis acceleration raised from angular velocity. The amplitude of the output vibrations may be defined as:

$$Y = S_b \times X \times \Omega \qquad \text{Eq.3.15}$$

where Y, X, S_b, Ω are the amplitude of output vibrations, amplitude of actuation vibrations, sensitivity of the beam, and angular velocity, respectively. Therefore, to increase the amplitude of vibrations in the sense direction, S_b and X should be maximized.

The actuation of the beam is the first issue that has to be considered. The frequency and amplitude of the actuation vibrations are the issues that have to be addressed. The most practical choice for the actuation frequency is the natural frequency of the beam in the X direction. This allows for an oscillator circuit to be built using the beam as a tuned element to sustain vibrations with constant amplitude in the beam. The amplitude of actuation vibrations can not be increased indefinitely. The response of the beam becomes nonlinear at higher amplitudes as a result of amplitude stiffening effect [46]. Also the power consumption of the device is another factor that limits the maximum amplitude of the actuation.

Sensitivity is the other issue that has to be addressed. It can be increased by reducing the mismatch between the two natural frequencies but this will result in a lower bandwidth (and therefore a more oscillatory response) for the entire sensor, because the bandwidth of the sensor's output is directly proportional to the mismatch between the two natural frequencies.

The sense vibrations is another issue that has to be considered. The sense mechanism that is used to convert the vibrations to an electrical signal may have an effect on the mechanical behavior of the beam. If capacitive detection is used, such as our case, the amplitude softening effect arising from the variation of electrostatic force between the capacitor plates with distance between the plates should be considered [47]. This effect results in reduction of the natural frequency of the beam in the sense direction, and therefore the mismatch between the two natural frequencies.

Air damping is the other issue. High Q is required in both X and Y direction to

enhance the vibration amplitudes. However, high Q is not achievable at atmospheric pressure, especially in the case where the element is vibrating perpendicularly to another planar surface, at a very close distance to that planar surface. A reduced-pressure environment is required for the operation of the sensor.

Coupling between the two modes of vibration is also an issue, it results in Zero-Rate-Output which is a major problem in vibrating gyros. It also affects the natural frequencies and increases the mismatch between them.

These issues are discussed in detail in this section below.

3.5.1 Actuation Vibration

The frequency and amplitude of the actuation vibrations are among the important issues that have to be considered in the design of the device.

3.5.1.1 Actuation Frequency

The response of the beam to actuation inputs in a range of frequencies should be considered. In order to predict the frequency response of the beam, an ideal beam having a width of W=105μm, a height of H=100μm, and length of L=1cm was considered. As mentioned before, a perfect match between the width and thickness of the beam is not achievable, and there are also other non-ideal effects which contribute to increase the mismatch between the two natural frequencies. A reasonable estimate for the mismatch, and Q, according to fabrication technology and procedures, is considered here (based on experimental results in Chapter 6).

The response of the beam to actuation currents with different frequencies (frequency response) is shown in Fig.3.9, and Fig.3.10 respectively. The actuation vibrations have a distinct peak at the natural frequency of the beam in the actuation direction as shown in

Fig.3.9 (which is a typical response for a second order system with high Q). The two peaks in the sense vibration correspond to the resonance frequencies in X and Y directions. Due to the unavoidable mismatch present between the two natural frequencies, two peaks are present in Fig.3.10. The larger peak happens at the resonance frequency in the X direction where the amplitude of actuation vibrations is the maximum. The smaller peak happens at the resonance frequency of the beam in Y direction where the vibrations in sense directions have the highest sensitivity to the input. For the sensor structure shown in Fig.3.1, the Q is lower for sense vibrations compared to the actuation vibrations (as will be discussed in Sec.3.5.4). Therefore, the second peak at the Y resonance frequency has a smaller amplitude compared to the first peak at the X resonance frequency. So a larger output is obtained by actuating the beam at its natural frequency in actuation direction. During the device operation, the beam will be kept in resonance with a constant amplitude in the X direction. The response in the X direction with a high Q can be used to build an oscillator circuit to sustain the vibrations in the beam as will be explained in Sec.3.6.1.

With the actuation frequency set at the natural frequency of the beam in the X direction, the overall phase shift between the actuation current and output sense voltage can be found. Assuming the actuation current to be:

$$i(t) = I\cos(w_{nx}t) \qquad \text{Eq.3.16}$$

and considering Eq.3.10, Eq.3.12 the total phase shift is:

$$\phi_y = tan^{-1}\left(\frac{\frac{\omega_{nx}}{Q_y\omega_{ny}}}{1-\left(\frac{\omega_{nx}}{\omega_{ny}}\right)^2}\right) = tan^{-1}\left(\frac{-1}{2Q_y\Delta}\right) \qquad \text{Eq.3.17}$$

where Δ is the mismatch between the two natural frequencies:

$$\Delta = \frac{\omega_{nx} - \omega_{ny}}{\omega_{nx}} \qquad \text{Eq.3.18}$$

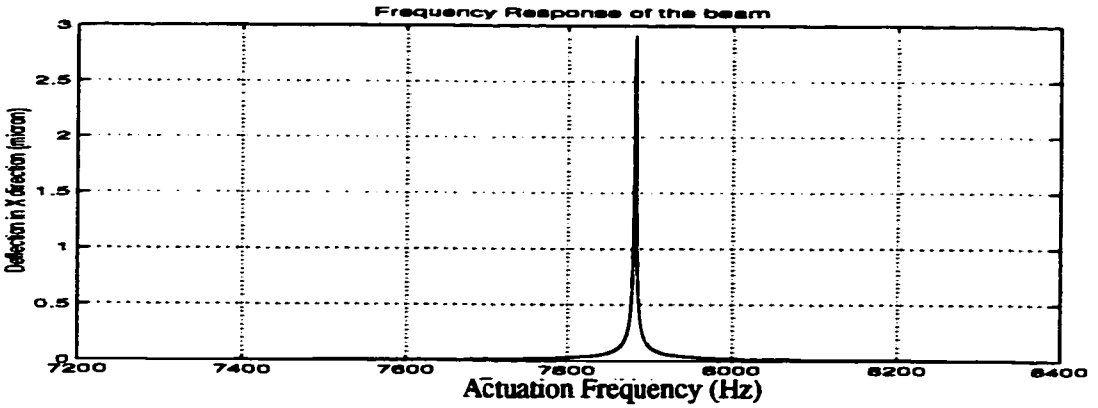

Fig. 3.9: Frequency response in actuation direction. B=0.2 Tesla, Q_x=5000.

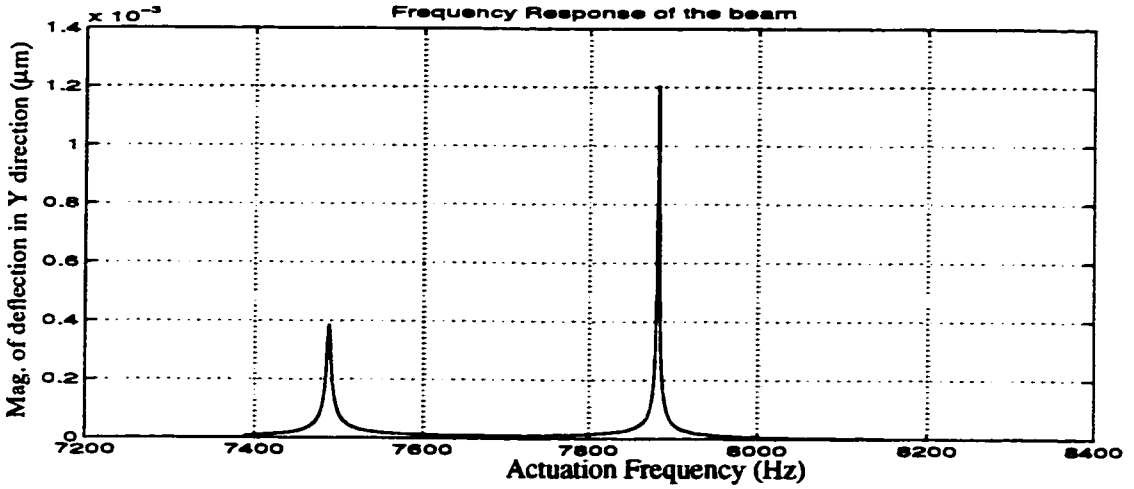

Fig. 3.10: Frequency response in sense direction. B=0.2 Tesla, Q_x=5000, Q_y=1500, 5% mismatch between the two natural frequencies, and $\Omega = 1 \frac{rad}{sec}$.

Thus the overall phase difference between output and actuation input is a function of both Q_y and mismatch between the two natural frequencies. The phase shift is plotted ver-

sus mismatch for different Q_y values in Fig.3.11. As seen in the figure for large Q values and in cases where two natural frequencies are not too close to each other, the phase lag is very small. The phase shift is important in detection of the output signal as will be discussed in Sec.3.6 and it is favorable to keep it as small as possible.

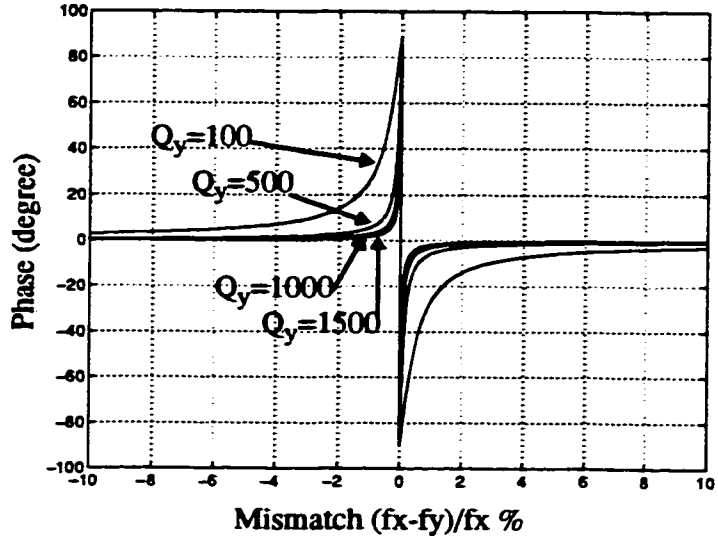

Fig. 3.11: Variation of phase shift between actuation and sense signals with Q and mismatch.

3.5.1.2 Actuation Amplitude

The amplitude of the reference vibration may be increased by increasing the actuation current, by increasing the magnetic field, or by modifying the beam's dimensions such as decreasing the beam's width or increasing its length.

The behavior of a vibrating beam is not perfectly linear. The stiffness of a clamped-clamped beam possesses nonlinear stiffness coefficients as well [48,49]. The differential equation for the actuation direction Eq.3.2 may be modified as follows to include the effect of non-linear stiffness [50]:

$$m_0\frac{d^2x(t)}{dt^2}+\mu_x\frac{dx(t)}{dt}+K_x x(t)+\eta x^3(t) = F_0 COS(\omega t) \qquad \text{Eq.3.19}$$

$$\eta = \frac{EA\pi^4}{8L^3} \qquad \text{Eq.3.20}$$

This differential equation is a form of the Duffing equation [50]. η is the cubic stiffness coefficient of the mechanical system, and E, A, L are the Young's Modulus of the Si, cross-sectional area of the beam and length of the beam respectively.

The Duffing non-linearity results in amplitude-stiffened behavior of the beam. For a beam that is vibrating with amplitude X_{max}, the fundamental resonant frequency may be found as [51]:

$$\omega_n = \frac{k^2}{\sqrt{12}}\frac{h}{L^2}\left[\frac{E}{\rho}\left(1+\gamma\varepsilon\frac{L^2}{h^2}+\beta\left(\frac{X_{max}}{h}\right)^2\right)\right]^{\frac{1}{2}} \qquad \text{Eq.3.21}$$

where E is the Young's Modulus, ε, h, L, and ρ are beam's strain, thickness in the direction of vibration (width), length, and density respectively. The constants k, γ, β can be calculated from the beam's mode shape (k=4.730, γ=0.2949, and β=0.528). Thus the natural frequency of the beam varies with vibration amplitude. This will result in a non-linear behavior of the beam for large amplitudes of vibration. The variation of vibration amplitude vs. frequency is plotted in Fig.3.12 for large vibration amplitudes. The curve is plotted by substituting ω_{nx} from Eq.3.21 into Eq.3.5. The resulting multi-valued function may be solved and plotted as shown in the figure. In real life the oscillations follow the hysteresis path shown in Fig.3.13 [46,49]. Starting from low frequency and low amplitudes, the amplitude of oscillations grows at the same time with the frequency of resonance in the beam until it reaches the peak point A. At this point it suddenly falls to point

B at which the resonance amplitude is very small. As the frequency of oscillations are lowered at this point, it follows a hysteresis path back to point C where it jumps back to the previous curve at point D.

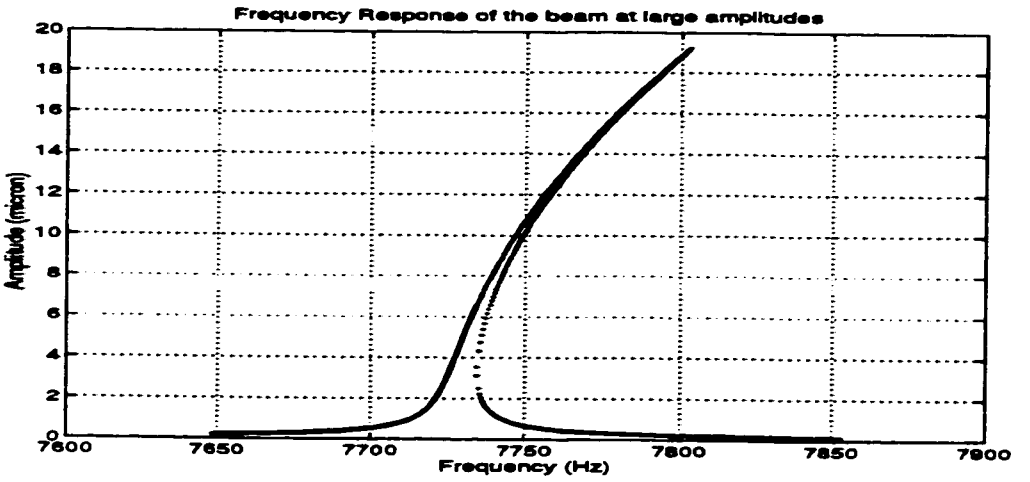

Fig. 3.12: Frequency response of the beam for large vibration amplitudes

The amplitude of oscillations should be kept small enough in order to avoid this non-linear effect. A less extreme example is shown in Fig.3.14. The response of the beam is symmetric for small amplitudes but it starts to become unsymmetrical as the amplitude grows. This is due to variation of natural frequency with amplitude. The hysteresis effect starts appearing as soon as the increase in natural frequency becomes larger than half of the bandwidth of the oscillations [49].

$$(\Delta\omega = \omega_n - \omega_{n0}) \geq \frac{BW}{2} \qquad \text{Eq.3.22}$$

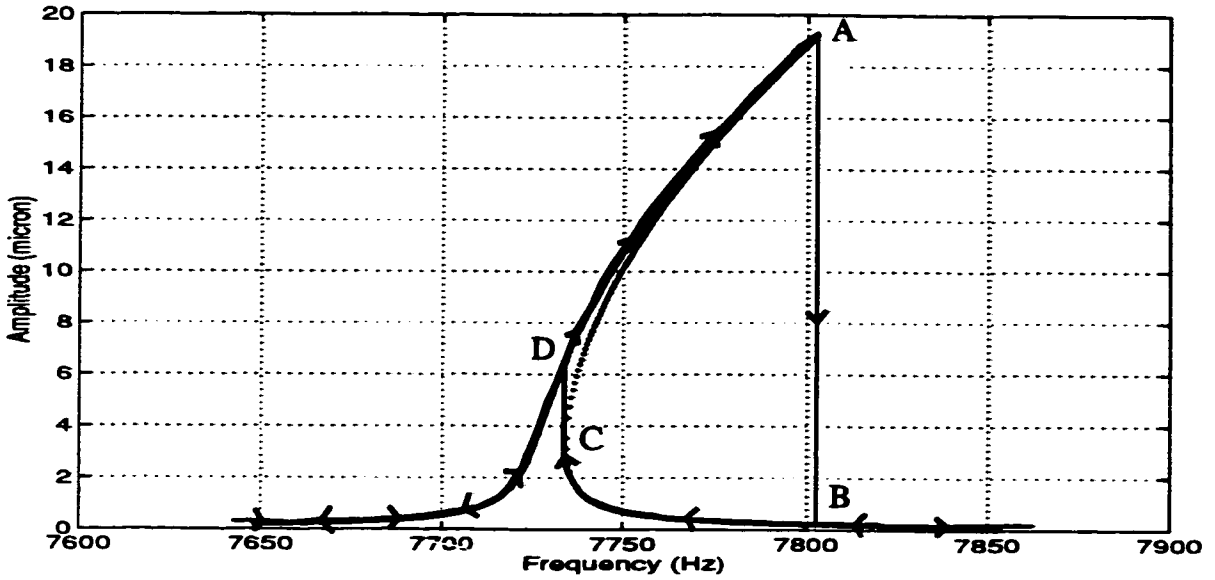

Fig. 3.13: The hysteresis characteristic of the beam for large vibration amplitudes.

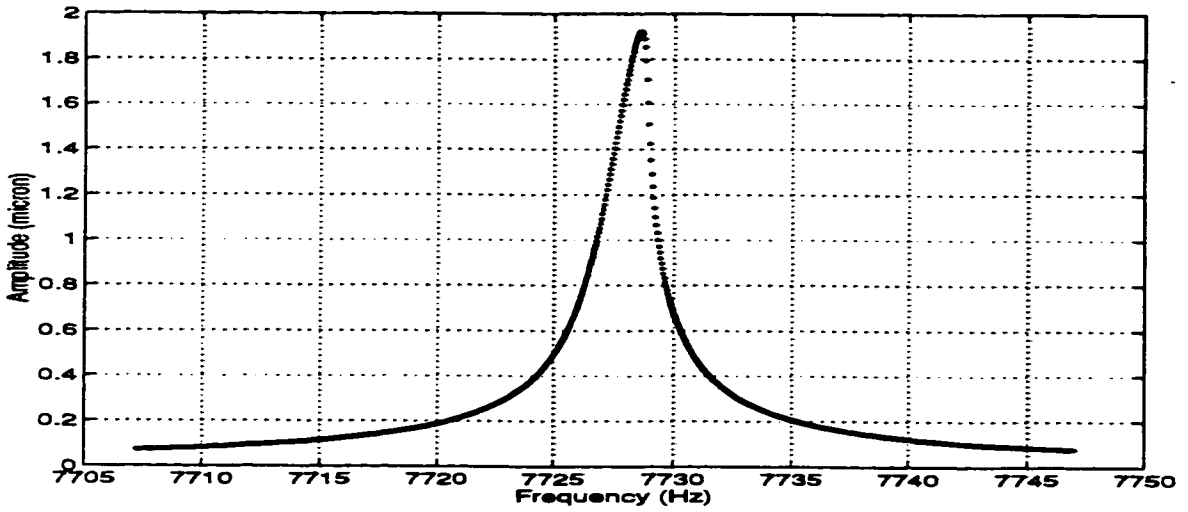

Fig. 3.14: The frequency response of the beam for small vibration amplitudes.

where ω_n , ω_{n0}, BW are natural frequency for large amplitudes, initial natural frequency and bandwidth of the beam respectively. By substituting Eq.3.22 in Eq.3.21 we have [46]:

$$x_{max} = h\sqrt{\frac{\left(1+\gamma\varepsilon\frac{L^2}{h^2}\right)}{\beta Q}} \qquad \text{Eq.3.23}$$

where x_{max} is the maximum amplitude before appearance of the hysteresis effect and Q is the quality factor of the first mode of vibrations ($Q = \frac{\omega_n}{BW}$). If the stress in the beam is negligible, the above equation may be simplified as:

$$x_{max} = \frac{h}{\sqrt{Q\beta}} \qquad \text{Eq.3.24}$$

The variations of maximum oscillation amplitude with the beam's dimensions is shown in Fig.3.15. The maximum amplitude changes linearly with dimension of the beam. Therefore, it is advantageous to use thicker beams. It should also be taken into consideration that it is more difficult to induce vibrations with the required amplitude in thicker beams. The thicker the beam, the larger the current and magnetic field required to actuate the beam. This will be investigated in more detail later in this chapter. The size of the beam has to be chosen based on the value of magnetic field available by permanent magnets and the value of the driving current.

Based on the above-mentioned considerations, a thickness of 100 μm has been chosen for the beam. At this thickness, and in a magnetic field with the approximate value of 0.2 to 0.3 Tesla achievable using small strong permanent magnets, it is possible to generate oscillations in the beams having amplitude ~2 μm, by passing a current of ~0.3 mA, while avoiding the amplitude-stiffening problem (Fig.3.15).

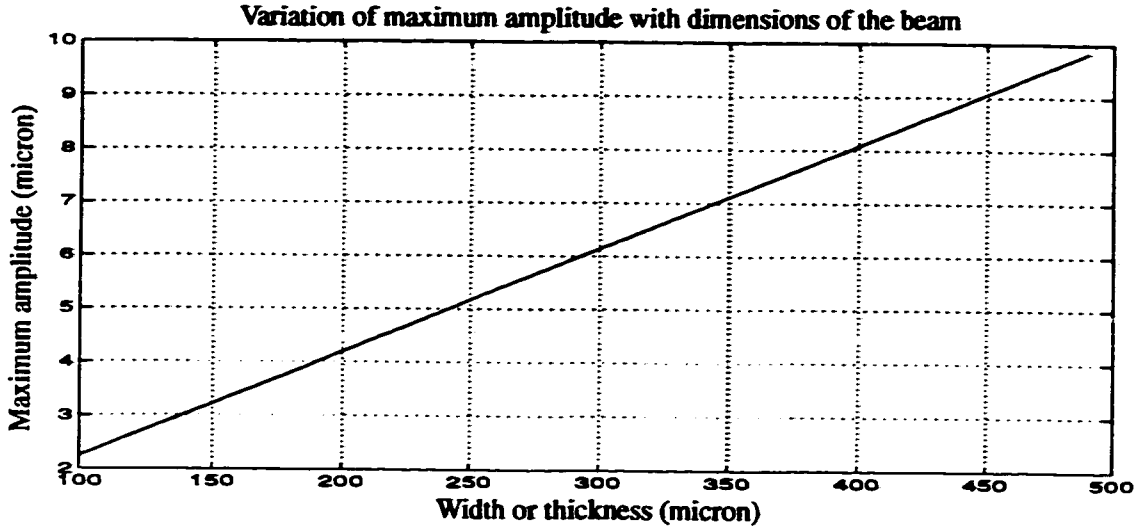

Fig. 3.15: Variation of maximum vibration amplitude with beam's dimensions (L=1 cm, Q=5000).

3.5.2 Sensitivity

The sensitivity S_b of beam vibrations in the sense direction (Y) with respect to vibrations in the actuation direction (X) may be found using Eq.3.11:

$$S_b = \frac{Y}{\Omega X} = \frac{2\omega_{nx}}{\omega_{ny}^2 \sqrt{\left[1 - \left(\frac{\omega_{nx}}{\omega_{ny}}\right)^2\right]^2 + \left(\frac{\omega_{nx}}{Q_y \omega_{ny}}\right)^2}} \qquad \text{Eq.3.25}$$

Variation of sensitivity with the mismatch between the beam's natural frequencies in horizontal and vertical directions (f_h, f_v) is shown in Fig.3.16. As shown in the figure, sensitivity decreases rapidly as the mismatch between two dimensions increases. Equation Eq.3.25 may be simplified to show a more clear relation between mismatch and sensitivity, as follows:

$$S_b \approx \frac{2}{\sqrt{4\Delta w^2 + \left(\frac{w_{ny}}{Q_y}\right)^2}} \qquad \text{Eq.3.26}$$

where:

$$\Delta w = |w_{nx} - w_{ny}| \ll w_{nx}, w_{ny} \qquad \text{Eq.3.27}$$

Assuming the bandwidth of the response in the Y direction to be $BW_y = \frac{w_{ny}}{Q_y} \ll \Delta w$, Eq.3.26 may be further simplified as [21]:

$$S_b = \frac{1}{\Delta w} \qquad \text{Eq.3.28}$$

Thus, since sensitivity is inversely proportional to the mismatch between the two natural frequencies, it is desirable to keep the mismatch as small as possible in order to increase the sensitivity of the beam. Better control over the width (W) and height (H) of the beam will result in a better match and higher sensitivity. Reduction of the size of <111> flanges formed at the two ends of the beam can also contribute greatly in reducing the mismatch and thus increasing the sensitivity as will be discussed in Chapters 5 and 6.

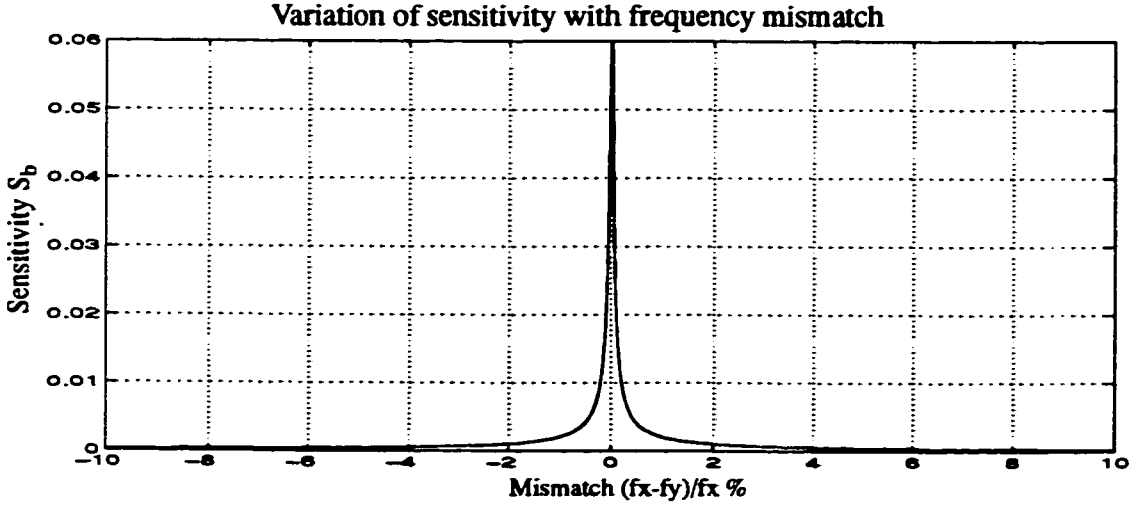

Fig. 3.16: Variation of sensitivity with frequency mismatch. B=0.2 Tesla, Q_x=5000, Q_y=1500.

Variation of sensitivity with the beam's length is shown in Fig.3.17. Longer beams are desirable since sensitivity increases with length of the beam. However, fabrication of beams with very large ratio of length to width is difficult because of potential problems with uniformity of photolitographic process steps. It is also desirable to keep the final device size as small as possible. Therefore the fabrication process and also the final size of the microsensor are factors that limit the beam's length.

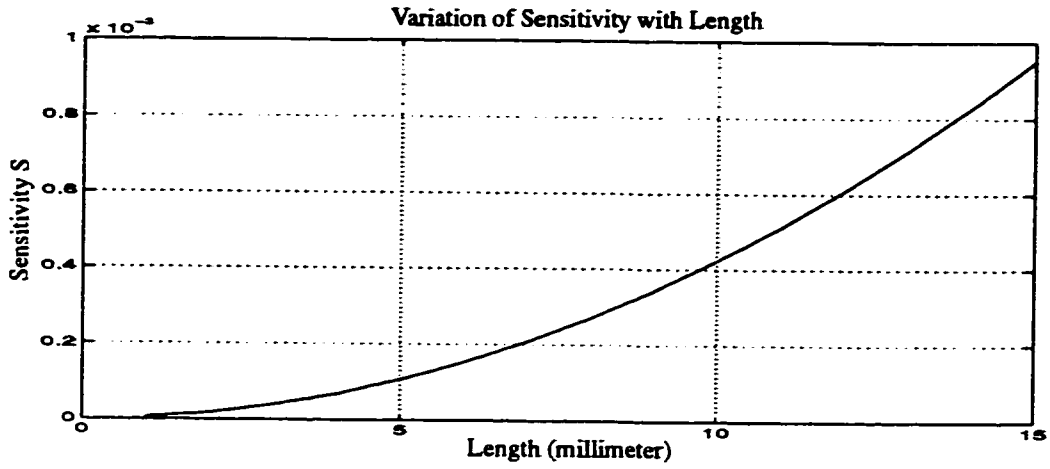

Fig. 3.17: Variation of sensitivity with beam's length. B=0.2 Tesla, Q_x=5000, Q_y=1500, mismatch=5%.

3.5.3 Sense Vibration

In the vertical (sense) direction, the beam is placed at a close proximity to the detection electrode located at the bottom of a cavity in the glass substrate (Fig.3.18). As will be mentioned later (Sec.3.6.2), in order to detect the variation in capacitance between the beam and the electrode, a DC voltage should be applied between them. The DC voltage (V_0) applied across the detection capacitor will result in an electrostatic force which varies

non-linearly with the variation of distance between the two capacitor plates as the beam vibrates in the sense direction. The electrostatic force may be shown as [17]:

$$F_c(t) = \frac{1}{2}\varepsilon A\frac{V_0^2}{(d-d_0-y(t))} \approx \frac{1}{2}\varepsilon A\frac{V_0^2}{d^2}(1+2\frac{y(t)}{d}) \qquad \text{Eq.3.29}$$

assuming: $d \gg d_0$, $d \gg |y(t)|$

where d, d_0 are the initial distance between the two electrodes and the static deflection of the beam due to voltage V_0.

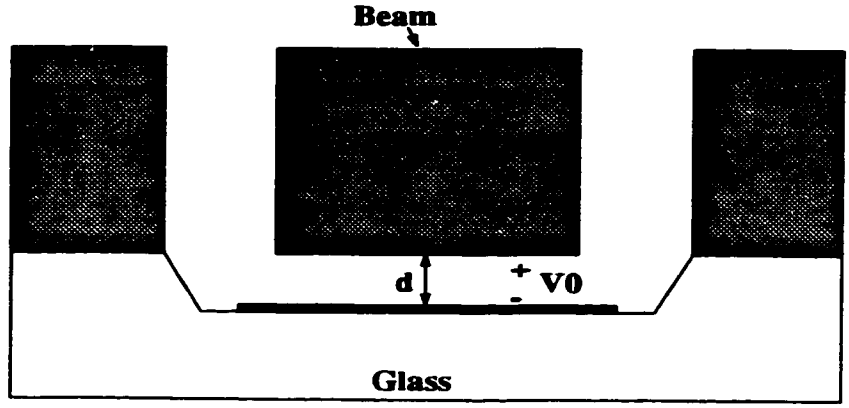

Fig. 3.18: Sense Capacitor formed between the beam and the electrode on the glass.

Therefore the extra electrostatic force generated due to the applied DC voltage, includes a first order term that varies linearly with y(t). By adding the force from Eq.3.29 to the differential equation Eq.3.3 we have:

$$m_0\frac{d^2y(t)}{dt^2}+\mu_y\frac{dy(t)}{dt}+\left(K_y-\varepsilon A\frac{V_0^2}{d^3}\right)y(t) = 2m_0\Omega\frac{dx(t)}{dt}+\frac{1}{2}\varepsilon A\frac{V_0^2}{d^2} \qquad \text{Eq.3.30}$$

The second force term, $F_c(t)$, is translated into a negative spring constant that is directly added to the spring constant of the beam in the sense direction. This causes a shift

in the natural frequency of the beam in sense direction. The shift in natural frequency may be calculated as [17]:

$$\Delta w_{ny} \approx -\frac{w_{ny}\varepsilon A}{2K_y d^3} V_0^2 \qquad \text{Eq.3.31}$$

where w_{ny} is the natural frequency of the beam at V_0=0.

Thus the natural frequency of vibrations in the sense direction may be reduced by applying a DC voltage across the sense capacitor. This spring-softening effect should be considered in the model of the system. Under certain design conditions, this effect may be large enough to tune the two natural frequencies of the beam [18].

For beam dimensions W=105μm, H=100μm, and L=1 cm, the following values (shown in Table 3.1) may be found using the above equation for shift in frequency due to the spring-softening effect (assuming V_0 =10V).

Air Gap (d)	Δf_y	$\Delta f_y / f_y$
10 μm	-8.2 Hz	0.11%
5 μm	-65.6 Hz	0.85%
2 μm	-1028 Hz	13.3%

TABLE 3.1: Variation of mismatch with air gap due to spring softening effect considering a DC voltage of V_0=10V.

For small air-gaps or for large values of DC voltage (V_0), the variation of natural frequency due to spring softening is comparable to the natural frequency of the beam (f_{ny}= 7.73kHz in this case). Therefore, matching the two natural frequencies by applying the proper DC voltage is feasible.

3.5.4 Damping

Damping in microstructures is caused by energy dissipation due to airflow force, squeeze force, internal loss, and support loss. Air damping which could be in the form of airflow force or squeeze force damping is the dominant energy dissipation source in microstructures. A cross-sectional view of the beam and the sense capacitor plate is shown in Fig.3.19. The air damping for two modes of vibration may be found as follows.

To develop a simple closed form solution for Q, the beam may be modeled as a plate moving parallel to the glass surface. A model developed by Xia Zhang *et.al.* [52] may be used in order to find the energy dissipation of the vibration in the lateral direction. This model is based on the assumption that the fluid between two parallel plates undergoes Couette flow with a linear velocity profile, and that the motion of the fluid on top of the plate can be modeled as Stokes flow. The quality factor may be calculated as follows [52]:

$$\frac{1}{Q} = \frac{\mu}{\sqrt{E\rho A\left(\frac{W}{L}\right)^3}}\left(\frac{A}{dh}\left(1+\frac{d}{\delta}\right)\right)+\frac{1}{Q_h} \qquad \text{Eq.3.32}$$

Where E, ρ, A, W, L, h are Young's Modulus, density, effective area on top of the beam, width, length, and height of beam respectively. d is the air-gap size between the beam and the bottom of the cavity, and $\mu = 1.8\times10^{-5}Nsm^{-2}$ is the viscosity of the air. δ is the penetration depth, which is the distance at which the motion amplitude of the fluid decreases by a factor of e. It is defined as: $\delta(w) = \sqrt{\frac{2\upsilon}{w}}$, where υ is the kinetic viscosity of the fluid ($\upsilon = 0.15\frac{cm^2}{s}$), and w is the frequency of lateral vibration of the plate.

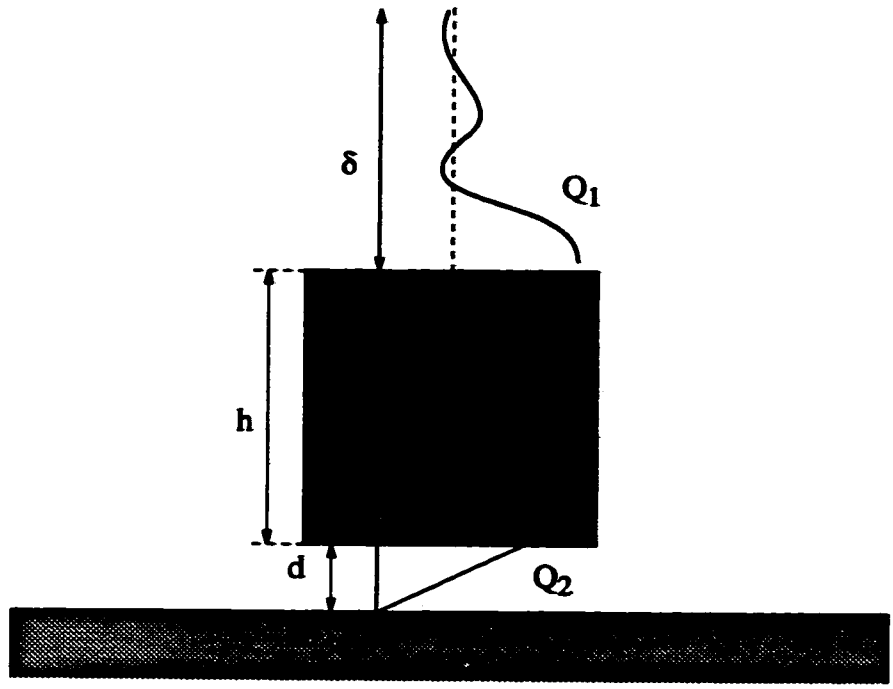

Fig. 3.19: Cross sectional view of the beam and damping models.

Q_h is the term to account for the direct air resistance. Q_h is velocity-squared damping, and is proportional to the density of the fluid and cross-sectional area facing the direction of motion. The proper estimation for Q_h may be found experimentally. Using the above equation, the quality factor of a beam with $100 \times 100 \mu m$ cross-section and 1 cm length with a gap spacing of $10 \mu m$ may be found to be Q_x=686, ignoring the effect of Q_h.

In the second mode of vibration, the sense mode, the beam is moving perpendicularly to a stationary surface located in close proximity. In this case, the damping is further increased due to the pumping action of the air in the intervening space. By using another simple model based on drop in pressure in a viscous fluid flowing through a parallel-walled duct, the value of Q may be found as [53]:

$$Q = \left(\frac{\sqrt{E\rho}W}{\mu}\right)\left(\frac{h}{L}\right)^2\left(\frac{d}{W}\right)^3 \qquad \text{Eq.3.33}$$

For the same beam, the quality factor in the sense direction may be found to be Q_y=9.6. This value shows clearly that sense vibrations will be heavily damped in the presence of the air. Thus the device's operation would be impossible without using vacuum.

As the pressure of the surrounding atmosphere drops, the damping may be analyzed in terms of a simple model in which individual air molecules exchange momentum with the resonator. This damping is proportional to air pressure and yields a Q given by the following equation [53]:

$$Q = 93\left(\frac{h}{L}\right)^2\frac{\sqrt{E\rho}}{P} \qquad \text{Eq.3.34}$$

where P is the pressure in N/m^2.

For a pressure of 0.0003 N/m^2 a quality factor of Q=5360 may be obtained using the above equation. For lower pressures the energy loss due to air damping becomes negligible and energy dissipation due to internal damping of the material and clamping of the structure to the base define the resonator's quality factor.

Monocrystalline silicon is an excellent material as far as the intrinsic damping of the material is concerned. It has shown extraordinarily high Q factor of 6×10^5 in very low pressures for torsional resonators [54]. Energy-loss through the coupling of vibrations to the base is, however, a more important source of damping in silicon resonators at low pressures. This energy-loss may become the dominant parameter which determines the resonator's quality factor at low pressures [55-57].

In order to reduce the energy-loss through coupling, the vibrating structure should be

mechanically isolated from the clamping point. One practical way to overcome this problem is using a tuning fork as the resonant structure [58-60]. A double-ended tuning fork is shown in Fig.3.20. In this structure the tines are actuated in the anti-phase mode so that their torques are cancelled out at both ends. Thus the two ends will always remain as vibration nodes and no vibration energy is coupled to the base through these nodes. This is true only in an ideal situation. In practice, some vibration will be induced in to base due to unavoidable mismatch present between the two tines and also due to the fact that the node is a point, smaller than any physically-realizable area of contact. This structure can be investigated more in the future research as an alternative design to improve the sensor's performance.

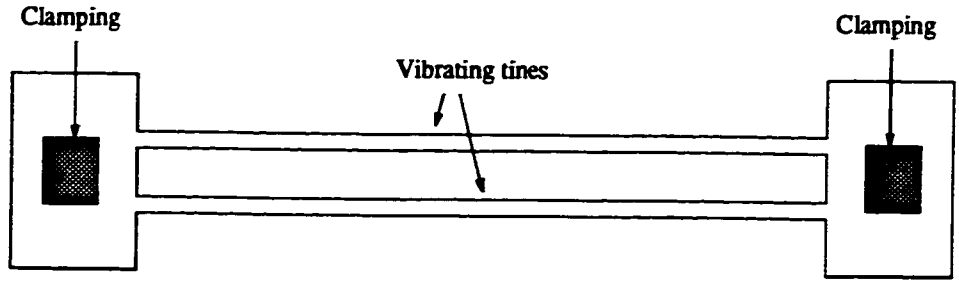

Fig. 3.20: Double-ended tuning fork.

It should be mentioned here that all of the calculations done in this section give us a very rough estimation of the Q factor. More accurate determination of the Q factor may be obtained only by experiment.

3.5.5 Coupled Vibrations

The coupling between base and resonator was mentioned as an unwanted effect which reduces the quality factor in the last section (Sec.3.5.4). Coupling between the two normal modes of vibration should also be considered as yet another unwanted phenomenon. Two adjacent mechanical systems usually affect each other. This is particularly noticeable if

their natural frequencies are almost equal. In our vibrating beam structure, any minor vibration energy that is transferred from actuation to sense direction could generate the coupling effect. This transfer of energy could be through the base or clamped regions, through the imperfections in etching at both ends of the beam or through misalignment of magnetic field. As a result, vibrations will be induced in the sense direction even in the absence of any angular rate inputs. This will result in zero-rate-output (non-zero output with zero input).

The differential equations Eq.3.2, Eq.3.3 may be rewritten as follows considering the effect of coupling and also the effects of amplitude stiffening, and spring softening explained in Sec.2.2.6.

Assuming $|y| \ll |x|$, and $K_c \ll K_x$

$$m_0 \frac{d^2x(t)}{dt^2} + \mu_x \frac{dx(t)}{dt} + K_x x(t) + \eta x^3(t) = F_0 COS(\omega t) \qquad \text{Eq.3.35}$$

$$m_0 \frac{d^2y(t)}{dt^2} + \mu_y \frac{dy(t)}{dt} + \left(K_y - \varepsilon A \frac{V_0^2}{d^3}\right) y(t) = 2m_0 \Omega \frac{dx(t)}{dt} + K_c x(t) + \frac{1}{2} \varepsilon A \frac{V_0^2}{d^2} \qquad \text{Eq.3.36}$$

where K_c is equivalent stiffness due to the coupling. The effect of coupling from sense (y) to actuation (x) direction is ignored because the amplitude of vibrations in the sense direction is very small. The value of K_c maybe obtained experimentally.

The effect of coupling through the base could be reduced by using tuning forks as vibrating structure. This will be considered as an alternative design later in this chapter. Another source of coupling in our design could be the clamping ends of the beam. A view of the beam etched from one side is shown in Fig.3.21. The samples are etched from both sides in TMAH as explained in Sec.3.2, and the {111} sidewalls formed at the two ends of the beam are symmetrical in the y direction as shown in Fig.3.22 [38]. A mechanical cou-

pling is generated between the two modes of vibration of the beam due to the presence of the {111} sidewalls. The length of the sidewalls is much smaller than the length of the beam, therefore, the coupling effect is small. The existing symmetry in the *y* direction is beneficial since any coupling generated by {111} sidewalls, is cancelled out in *y* direction due to the symmetry of the profile.

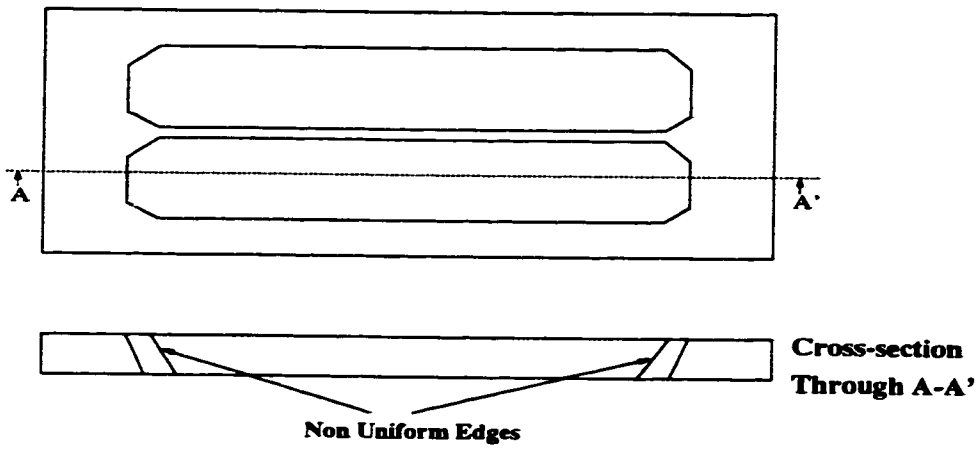

Fig. 3.21: Top and side views of the beam, etched from one side.

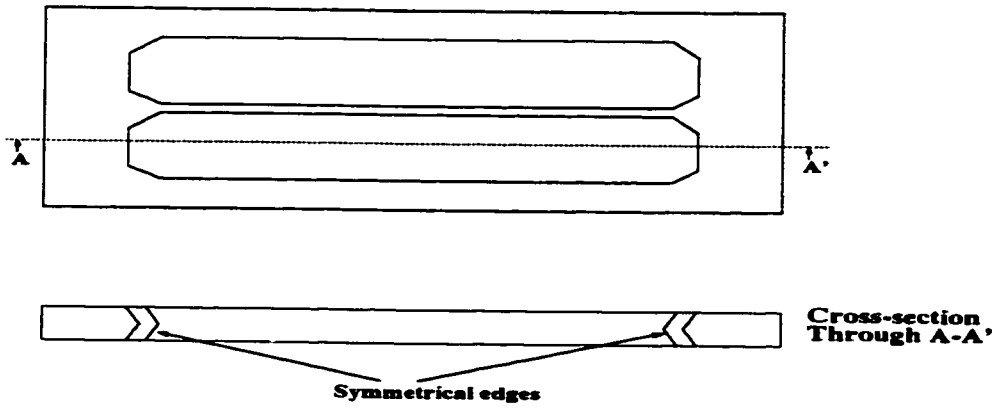

Fig. 3.22: Top and side views of the beam, etched from both sides.

The top view and the cross-sectional view of a beam etched from only one side is

shown in Fig.3.21 for comparison. The absence of symmetry in y direction in this case will result in the presence of some mechanical coupling between the two modes.

Coupling between two modes of operation also affects some important characteristics of the system in both modes of the vibration. The resonance frequencies in both of the actuation mode and the sense mode shift in opposite directions, as shown in Fig.3.23, as a result of coupling [61]. The natural frequency that is already higher is shifted toward the higher frequencies and the one that is already lower is shifted toward the lower frequencies. The frequency shift may be shown as:

$$\omega'_y - \omega'_x = \sqrt{\Delta\omega^2 + K_0^2\omega_0^2} \qquad \text{Eq.3.37}$$

$$\omega_0 = \frac{\omega_x + \omega_y}{2} \qquad \text{Eq.3.38}$$

$$K_0^2 = \frac{K_{coupling}}{K_{coupling} + K_x} \times \frac{K_{coupling}}{K_{coupling} + K_y} \qquad \text{Eq.3.39}$$

where K_x and K_y are the stiffness in actuation and sense directions, $K_{coupling}$ is the equivalent stiffness of coupling, and $\Delta\omega = \omega_y - \omega_x$. K_0 is defined as mechanical coupling coefficient. An interesting observation from Eq.3.37 is that if any coupling exists ($K_0>0$), the two measurable resonance frequencies can never be equal to each other even if a perfect match exists between the two dimensions ($\Delta\omega \neq 0$).

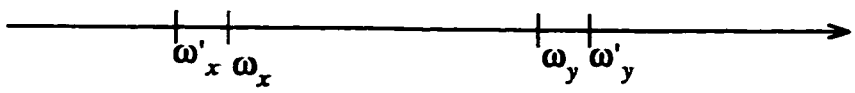

Fig. 3.23: Shift in frequencies as a result of coupling.

Thus coupling increases the mismatch between the two natural frequencies which is another undesirable effect.

3.6 Sensor Operation Issues

The operation of the sensor is based on the actuation of the beam in the actuation direction and detection of Coriolis induced displacement in the sense direction. the circuitry required for generation of sustained vibrations in the actuation direction and detection of small Coriolis induced vibrations in the sense direction need to be designed. The beam is modeled as a parallel RLC circuit and an oscillator feed back loop is built using the beam as the tuned element. A secondary feedback loop may be implemented to keep the amplitude of the vibrations constant. The variations in capacitance between the beam and an electrode located at a close proximity due to Coriolis induced vibrations in the sense direction are detected using a charge detector circuit. The detected signal should then be amplified and demodulated using a synchronous demodulator. The trade-off between sensitivity and bandwidth and also the effect of interconnection wires (connecting the sensor to off-chip circuitry) are considered here. Non-ideal effects such as the effect of beam's weight and linear acceleration are also discussed.

3.6.1 Actuation Mechanism and Circuitry

A simple view of the beam and the actuation electrodes is shown in Fig.3.24. The beam should be kept in oscillation with a constant amplitude in the reference direction. As mentioned before, electromagnetic coupling is chosen as actuation mechanism in this design. By considering the lumped equivalent model for the sensor and for small amplitudes of vibration, the motion in the actuation (X) direction may be modeled as (ignoring the non-linearities) :

$$m_0 \frac{d^2x(t)}{dt^2} + \mu_x \frac{dx(t)}{dt} + K_x x(t) = i(t) BL \qquad \text{Eq.3.40}$$

Where *i(t)* is the excitation current. The motion is monitored by detecting the electromotive force (EMF) which is electromagnetically induced in the secondary electrode. The detected voltage on the secondary electrode is given by:

$$V_{sense}(t) = BL \frac{dx}{dt} \qquad \text{Eq.3.41}$$

using Eq.3.40 and Eq.3.41 the transfer function may be obtained as:

$$\frac{V_{sense}(s)}{i(s)} = \frac{(BL)^2 s}{m_0 s^2 + \mu_x s + K_x} \qquad \text{Eq.3.42}$$

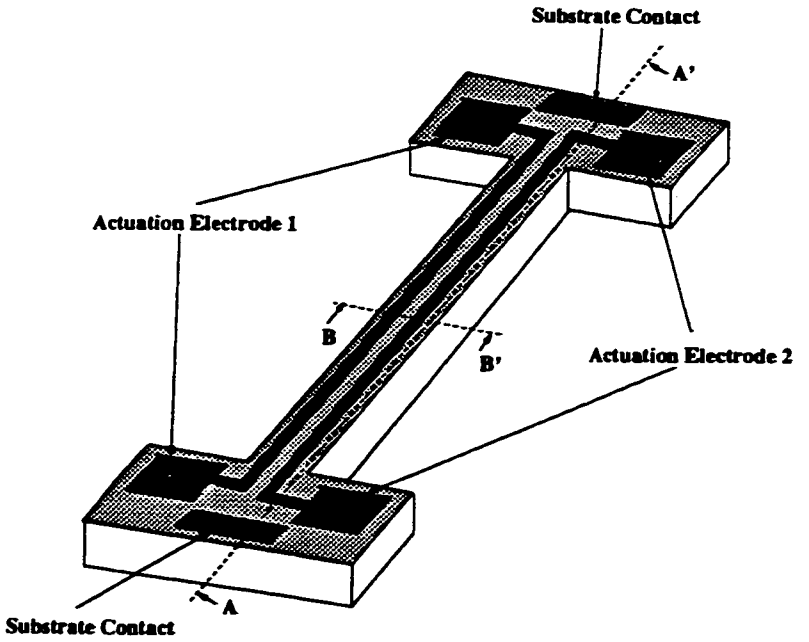

Fig. 3.24: A simplified view of the beam and its actuation electrodes.

This response is similar to that of a parallel RLC tank circuit. By combining this tank circuit with series resistors to model the ohmic losses in the beam, the equivalent circuit may be obtained as shown in Fig.3.25. The back EMF which appears across the detection electrode is represented by coupling the tank voltage from the actuation electrode to the detection electrode. A 1:1 transformer is used to model this. The capacitance present between the actuation electrodes and the beam are modeled by C_p. The resistance of the silicon beam itself is modeled by R_s and R_p.

The values for equivalent parallel RLC circuit representing the tuned mechanical behavior of the beam may be found as:

$$R_m = \frac{Q\,(BL)^2}{mw_{nx}} \qquad \text{Eq.3.43}$$

$$C_m = \frac{m}{(BL)^2} \qquad \text{Eq.3.44}$$

$$L_m = \frac{(BL)^2}{mw_{nx}^2} \qquad \text{Eq.3.45}$$

A cross-sectional view of the beam (view AA' in Fig.3.24) is shown in Fig.3.26. As seen in the figure, the Si substrate is grounded through two contacts at the two ends of the beam. Some current will flow through the beam due to the effect of capacitors C_p formed between actuation electrodes and the silicon beam. Due to symmetry, we can assume that the current flowing through the beam is divided equally between the two substrate contacts. The values of R_s, R_p and C_p may be found experimentally as done in Sec.6.5. The series resistance of each one of the electrodes is shown by R_1, R_2.

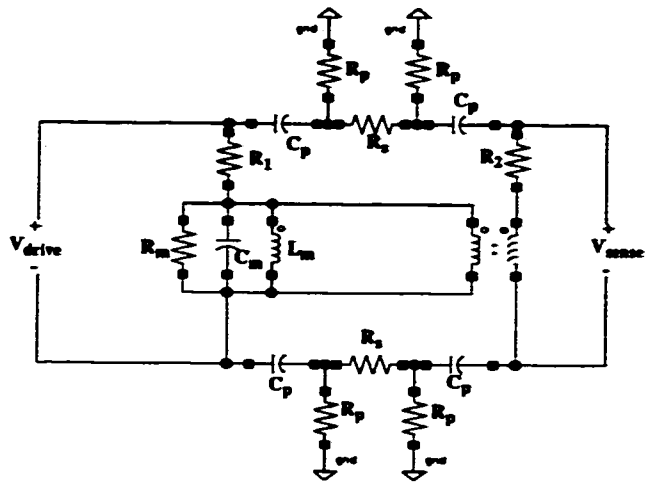

Fig. 3.25: Equivalent circuit of the beam.

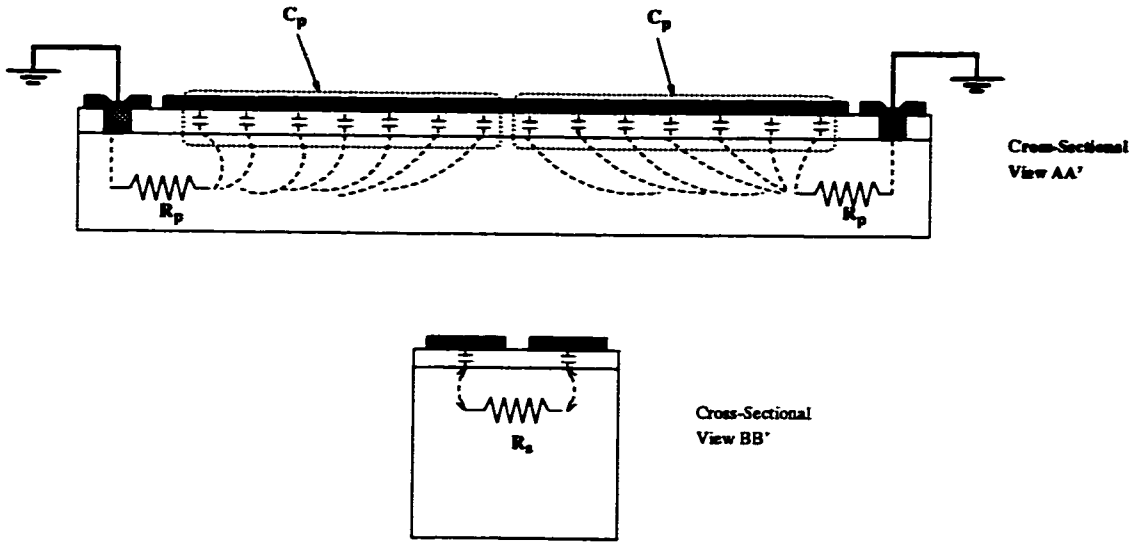

Fig. 3.26: Cross-sectional views of the beam showing the parasitic resistances and capacitances (see Fig.3.24).

Fig.3.27 represents a system which used to excite and detect the oscillation in the beam. The system consists of a low-noise differential sense amplifier, a positive feedback oscillator loop and an Automatic Level Control (ALC) loop. Since the sensed voltage is proportional to the velocity of the beam, the ALC loop amplifies and integrates the sensor

output to create a signal proportional to the beam's oscillation amplitude. The ALC loop maintains a constant oscillation amplitude by adjusting the loop transmission ($LT = K \times G \times T(s)$) of the oscillator to be exactly one. The sensor's transfer function ($T(s)$) can be found as [51]:

$$T(S) = \frac{V_{sense}}{V_{drive}} = \frac{1}{R_1}\left[\frac{L_1 s}{L_1 C_1 s^2 + (\frac{1}{R_1} + \frac{1}{R_2}) L_1 s + 1}\right] \qquad \text{Eq.3.46}$$

When feedback is applied around $T(s)$, the pole locations are given by $1\text{-}LT=0$. For stable amplitude oscillations, the pole locations must be purely imaginary. The value of gain that satisfies this condition is given by [51]:

$$KG = \frac{R_1 + R_2}{R_1} \qquad \text{Eq.3.47}$$

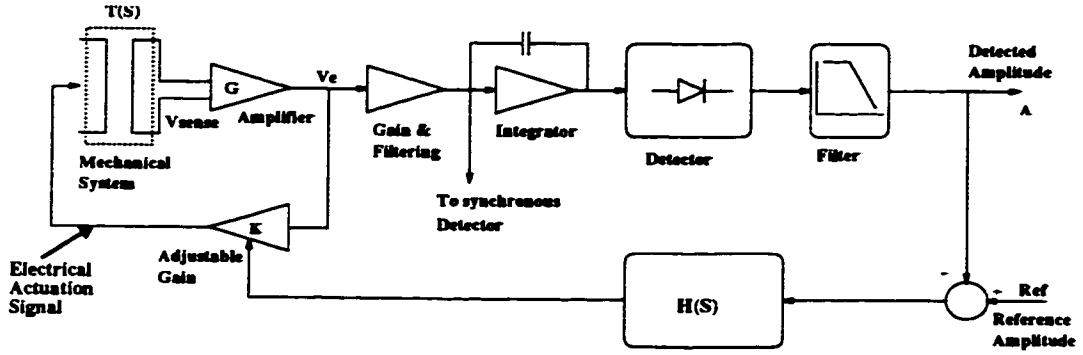

Fig. 3.27: Block diagram of actuation circuitry (redrawn from [51]).

In equilibrium, the ALC loop should maintain this condition; however, if the system is perturbed or a new oscillation amplitude is required, the ALC loop will temporarily increase or decrease the K. A linearized, small signal model of the oscillator amplitude

dynamics as a function of K may be developed to set the bandwidth and ensure the stability of the ALC loop. The small signal response of voltage V_e with respect to K may be calculated as follows [51]:

$$\frac{\Delta V(s)}{\Delta K(s)} = \frac{EG}{2R_2C_1s} \qquad \text{Eq.3.48}$$

Where E is the desired steady-state amplitude of V_e.

The proper loop controller $H(s)$ may be designed to stabilize the system and meet the settling time.

The above mentioned system works well for small amplitudes of oscillation where amplitude stiffened behavior is insignificant. In this design the amplitude of vibration is kept small (below the threshold calculated using Eq.3.24) so that the system operates in its linear region.

The induced emf voltage in the beam as obtained by equation Eq.3.41 is based on the assumption that the entire length of the beam is vibrating with the same amplitude. This is an assumption that simplifies the rest of equations and equivalent circuits. A better approximation for the induced emf voltage may be found by considering the mode shape of the beam at its first resonant mode:

$$V_{sense}(t) = B\left(\int_0^L \phi(z)\,dz\right)\frac{dx(t)}{dt} \qquad \text{Eq.3.49}$$

where $\phi(z)$, L, $x(t)$ are the mode shape function of the beam for its first resonance mode [62], length of the beam, and the amplitude of vibrations at the center of the beam (maximum amplitude). The values of the elements of the equivalent circuit (R_m, C_m, L_m) in Fig.3.25 may also be revised the same way to obtain a better approximation of the real

beam's performance.

3.6.1.1 Actuation System Design Parameters

The important parameters of the actuation system are as follows:

- Sense emf voltage induced in the beam, which is desired to be maximized.
- Power consumption of the sensor (both mechanical and electrical) which should be minimized.
- Maximum induced stress in the beam which should be below the yield stress of the silicon.

A simplified version of the equivalent circuit of Fig.3.25 is shown in Fig.3.28.

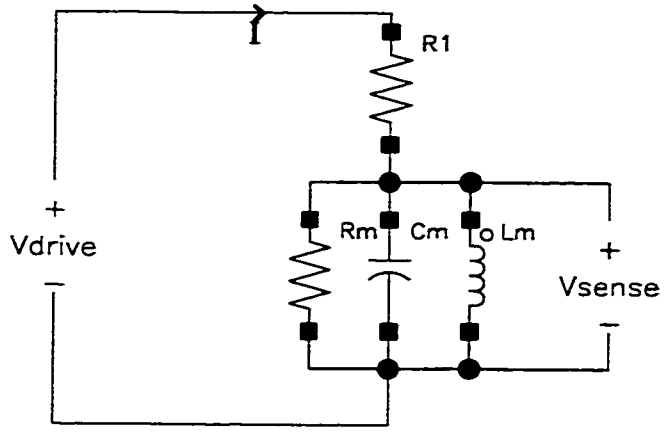

Fig. 3.28: Simplified equivalent circuit for the beam.

At the resonance frequency of the beam we have:

$$I = \frac{1}{R_m} V_{sense} = \frac{m w_{nx}}{B^2 L^2 Q} V_{sense} \qquad \text{Eq.3.50}$$

where V_{sense} and I are the maximum amplitude of the sensed voltage and input cur-

rent respectively. Also using Eq.3.5, at the resonant frequency we have:

$$X = Q\frac{F}{K_x} = Q\frac{ILB}{K_x} \qquad \text{Eq.3.51}$$

Where F, L, K_x are the maximum amplitude of the electromagnetic force applied on the beam, length of the beam and stiffness of the beam in the actuation direction.

To avoid the non-linear effect of the beam, the vibration amplitude should be limited. This will impose an upper limit on the maximum induced voltage in the second electrode. Using Eq.3.51 , Eq.3.50, Eq.3.14, and Eq.3.24 and assuming $Q>>1$ we have:

$$V_{sense} \le C\sqrt{\frac{E}{\rho}}\frac{AB}{L\sqrt{\beta Q}} \qquad \text{Eq.3.52}$$

Where C is a constant (~6.57), ρ is the density of Si, and A is the cross-sectional area of the beam. Therefore, higher magnetic field (B), thicker beam (A), shorter beam length (L), and lower Q will result in higher upper bound for sense voltage. However, the power dissipation in the beam as a result of mechanical power loss and power loss in ohmic resistance in the actuation electrode is:

$$P \le (R_1 + R_m)\frac{K_x^2 h^2}{\beta Q^3 L^2 B^2} \approx R_1\frac{K_x^2 h^2}{\beta Q^3 L^2 B^2} \qquad \text{Eq.3.53}$$

Considering the fact that $R_m << R_1$ the power consumption drastically increases with increasing beam width or height (K_x, h), or with reducing Q, or length of the beam (L). Low power consumption is a critical performance criterion of most microsensors. Therefore, it has to be considered carefully during the design of such a system. The magnetic field (B) is the only parameter whose increase works favorably both in terms of the sensed voltage and dissipated power.

Variation of maximum sensed voltage at resonance with the beam dimensions is shown in Fig.3.29 for different Q values. The variation of power dissipation with beam dimension and Q is shown in Fig.3.30. As shown in the figure, the power dissipation increases rapidly with increase in beam dimensions. In order to keep the power dissipation in a reasonable range the beam's width and height should be kept small. The power dissipation rapidly decreases with increase in Q. Therefore, larger beam dimensions which result in higher sense voltages are more viable if higher Q values are achieved.

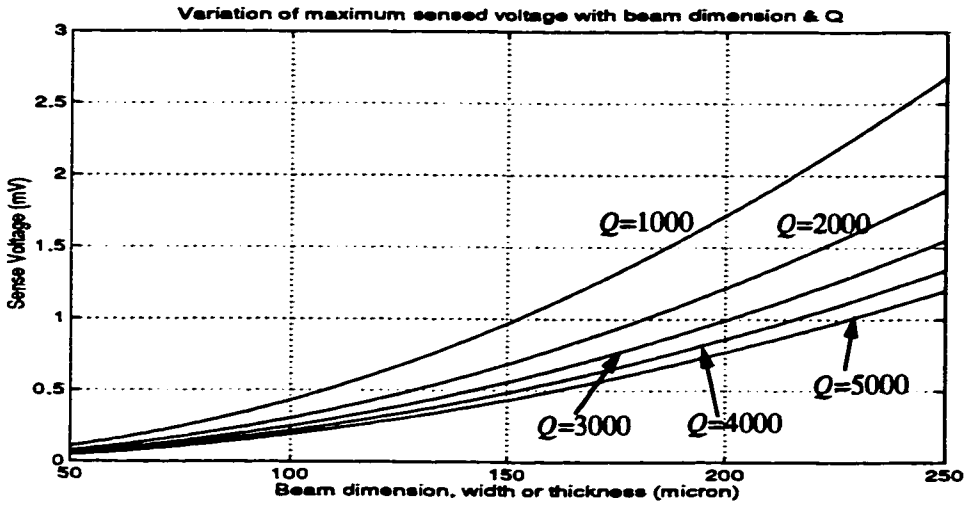

Fig. 3.29: Variation of maximum sense voltage with beam's dimension and Q.

Another limiting parameter could be maximum stress induced in the beam. The maximum stress in a vibrating beam occurs at the two clamping edges and increases with increase in vibration amplitude and also with beam stiffness. Variations of maximum stress induced in the beam with beam dimension is shown in Fig.3.31. The values are well below the yield stress of silicon ($7 \times 10^9 \frac{N}{m^2}$) [37]. So the yield stress of silicon will not be a limiting parameter here.

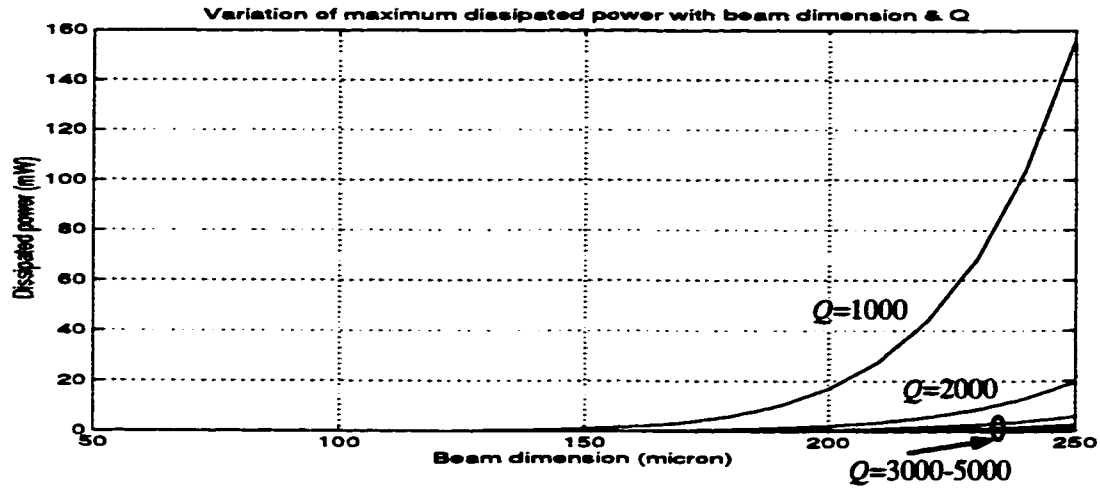

Fig. 3.30: Variation of power dissipation with beam's dimension and Q.

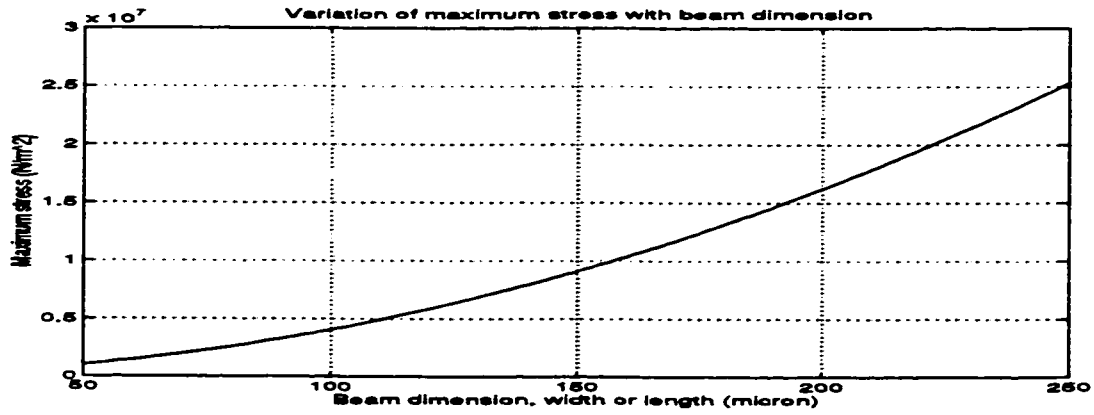

Fig. 3.31: Variation of maximum beam stress with beam's dimension.

3.6.2 Detection Mechanism and Circuitry

Vibrations induced in the sense mode by Coriolis acceleration have to be detected and amplified to give the output signal. Capacitive detection is used to detect these vibrations.

The capacitance between the beam and deposited electrode on glass changes as the beam vibrates in the direction normal to the sensor's plane. The time-varying capacitance may be shown as:

$$C(t) = \int_0^L \varepsilon_0 W \left(\frac{1}{d - Y\phi(x)\,COS(w_{nx}t - \phi_y)}\right) dx \qquad \text{Eq.3.54}$$

In which ε_0, W, d, Y are permittivity of vacuum, beam width, initial gap size, and maximum vibration amplitude in the y direction, respectively. $\phi(x)$ is the first resonance mode shape of the beam [62]. Considering the fact that the amplitude of vibrations induced in y direction due to Coriolis force are much smaller than the initial gap between the beam and the glass plate, the above equation may be simplified as follows:

$$C(t) = C_0 + C_1 COS(\omega_{nx}t - \phi_y) \qquad \text{Eq.3.55}$$

$$C_0 = \varepsilon_0 \frac{WL}{d},\ C_1 = \varepsilon_0 \frac{W}{d^2} Y \left(\int_0^L \phi(x)\,dx\right) \approx \varepsilon_0 \frac{W}{d^2} \frac{X}{\Delta w} \left(\int_0^L \phi(x)\,dx\right) \Omega \qquad \text{Eq.3.56}$$

Where C_0 is the capacitance when the beam is at the rest, X is the amplitude of vibrations in actuation direction, Δw is the mismatch between the two natural frequencies, and Ω is the input angular velocity. Eq.3.55 and Eq.3.56 clearly show that the capacitance varies linearly with the angular velocity.

These changes in capacitance should be detected and buffered through a detection circuit. The detector circuit is shown in Fig.3.32. In this circuit, the upper capacitor plate is clamped to a reference voltage and is kept at $(V_{ref}\text{-}V_T)$. Variations in $C(t)$ due to vibrations will then pump the charges into the non-inverting input of the opamp. Output of opamp

will then be amplified and filtered.

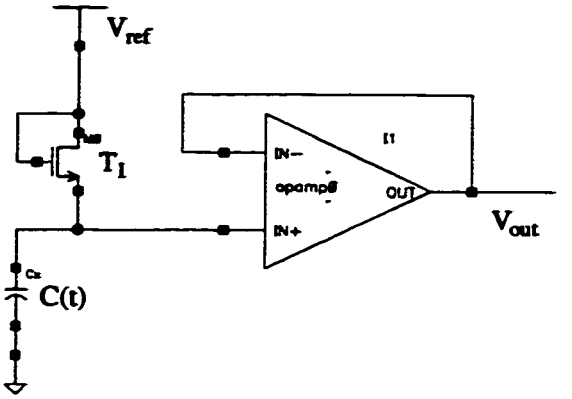

Fig. 3.32: Buffer designed to detect the changes in capacitance.

So far we have considered the angular rate Ω to be constant. In this case the output of the buffer would be a sinusoid with an amplitude that is proportional to the input angular rate. But in real life the angular velocity will be a time varying input $\Omega(t)$. In this case, considering the equation Eq.3.3, the output of the buffer would be an AM modulated signal in which the signal $\frac{dx(t)}{dt}$ is modulated by $\Omega(t)$. A block diagram of the entire system is shown in Fig.3.33. The oscillations in the actuation direction ($x(t)$) are generated by the oscillator, which consists of the oscillator circuit and the beam which acts as a band-pass filter. The output of oscillator block is then fed into the Coriolis Acceleration block where its derivative is modulated with the in-coming angular rate $\Omega(t)$. The output of this block is then fed into a band pass filter which is formed by the beam's frequency response in sense (Y) direction. The output of this block, which is the displacement $y(t)$, causes the variations in output capacitance. These variations are then detected by the detector circuit discussed earlier.

This output should then be filtered and demodulated in order to extract the angular

rate $\Omega(t)$ which is the desired signal. The detected actuation voltage of the beam which is in phase with $\frac{dx(t)}{dt}$ (Fig.3.27) is used to demodulate $\Omega(t)$. At the resonance frequency in X direction, $\phi_x = 90^o$ in equation Eq.3.4, therefore the $\frac{dx(t)}{dt}$ signal would be in phase with the actuation current at the input of the beam, and the phase shift between this signal and the detected output signal would be the same as what is shown in Fig.3.11 for the phase shift between the actuation input and sense vibrations. High Q values for vibrations in vertical direction may be obtained in reduced pressure environment (as explained in Sec.6.3). Also the a mismatch of at least a few percents should always be present to obtain the required bandwidth (as will be explained later in this section). For example for Q_y=1500, and mismatch(Δ)=5%, using Eq.3.18 we have $\phi_y = 0.38^o$.

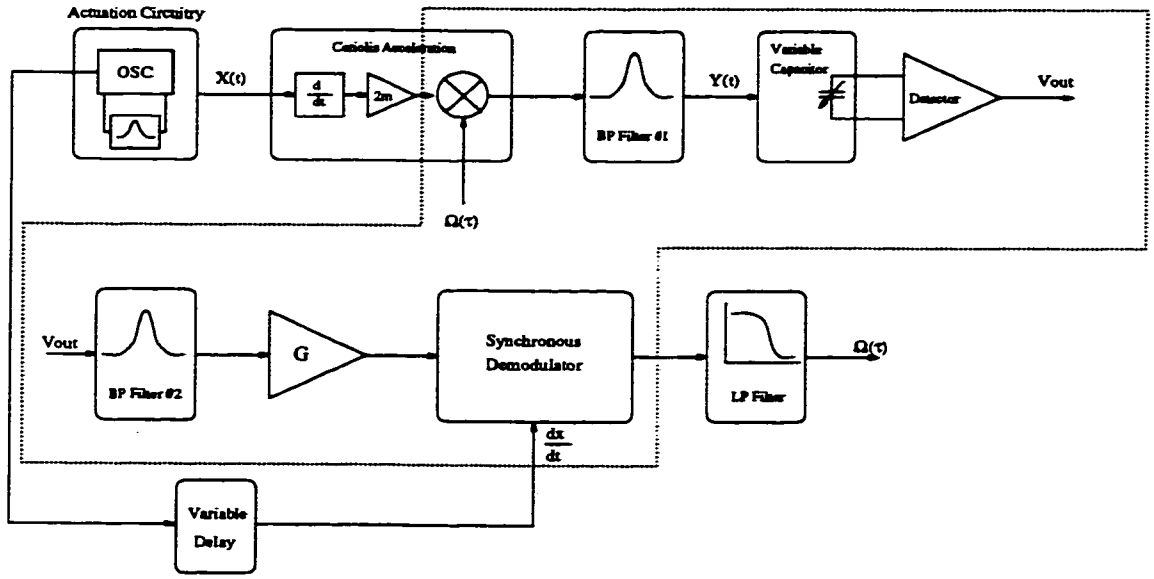

Fig. 3.33: Block-diagram of the overall system

The two signals arriving from two different paths to the demodulator should have the same phase in order to achieve the most effective demodulation. This is achieved by

introducing a variable delay in the path of the $\frac{dx}{dt}$ signal coming from the oscillator. This delay may be set in order to obtain the best performance out of the demodulator. The phase delay should be optimized during the calibration of the sensor, once all of the fabrication and packaging steps are done. The output of this block may be then digitized using an A/D converter.

The central frequency of the modulated signal $2m_0\frac{dx(t)}{dt}\Omega(t)$ is different from the central frequency of the band-pass filter. This difference is due to unavoidable mismatch between the two natural frequencies f_{nx}, f_{ny} (Fig.3.34). Considering the capacitance transducer (Detector), buffer and amplifier (G) to be all linear (as an approximation), an equivalent simplified block diagram may be found for the part of the system contained within the dashed lines in Fig.3.33. This is shown in Fig.3.34. The frequency response of the low-pass filter shown in Fig.3.35 is determined by the frequency response of the mechanical band-pass filter #1, and $\Delta f = f_{ny} - f_{nx}$. The gain G_1 could be found considering the gain in the displacement-to-capacitance transducer, the gain of the buffer, the amplification gain G, and the gain of demodulator.

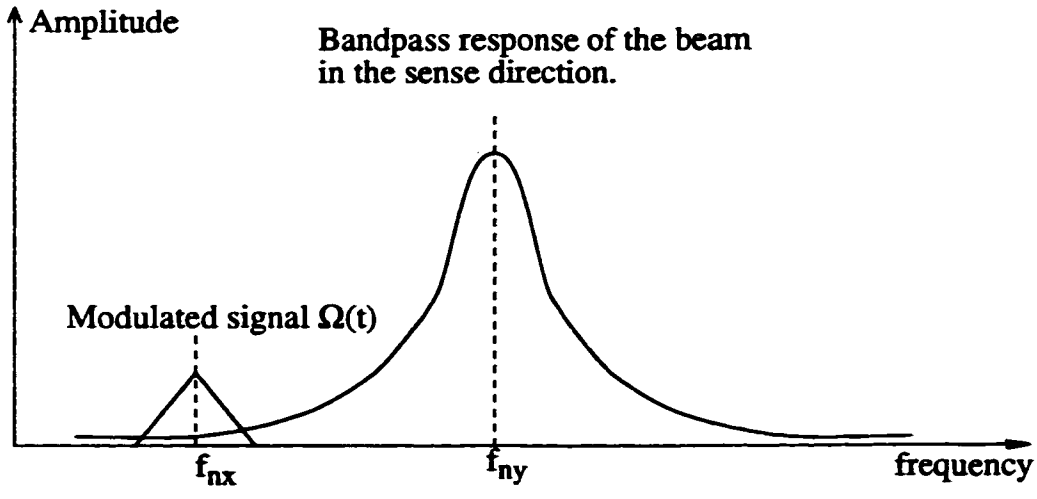

Fig. 3.34: Effect of frequency modulation and band pass filtering with a different central frequency.

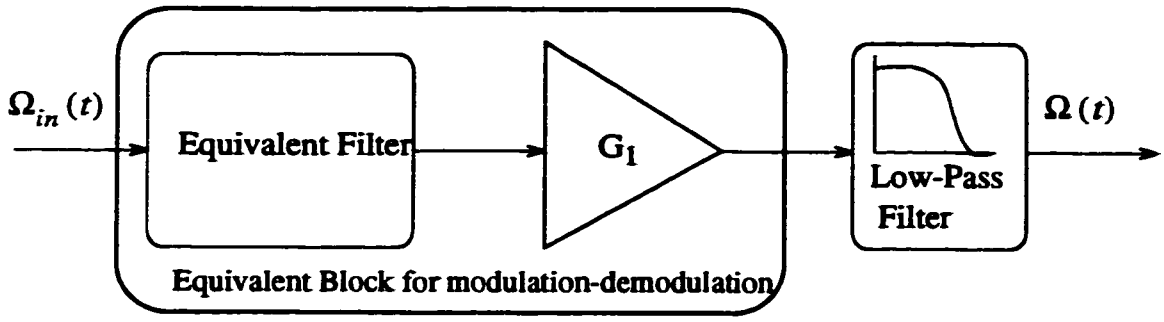

Fig. 3.35: Equivalent block diagram of the system.

A frequency response such as the one shown in Fig.3.36 may be found for the equivalent filter. The response is similar to a band-pass filter with the central frequency of $|f_{nx}-f_{ny}|$. The useful bandwidth of the system should be limited to lower frequencies (below $|f_{nx}-f_{ny}|$) where the frequency response is reasonably flat. To find the effective useful bandwidth, one may limit the variations in gain to 3db which results in a 200 Hz bandwidth for the response shown in Fig.3.36. In later stages and after D/A conversion, it is possible to eliminate the 3db variation of the gain in the passband using DSP techniques.

It can be shown that the bandwidth of this filter is independent of f_{nx} or f_{ny} and is determined only by the difference between the two natural frequencies Δf [30]. Larger mismatch will result in larger bandwidth but it lowers the sensitivity of the sensor according to equation Eq.3.28.

The step response of the equivalent filter is very oscillatory because of the distinct peak at $|f_{nx}-f_{ny}|$. A low-pass filter is required to limit the overall bandwidth to the 3db bandwidth mentioned above and to damp the oscillations in the step response, to achieve the desired settling time.

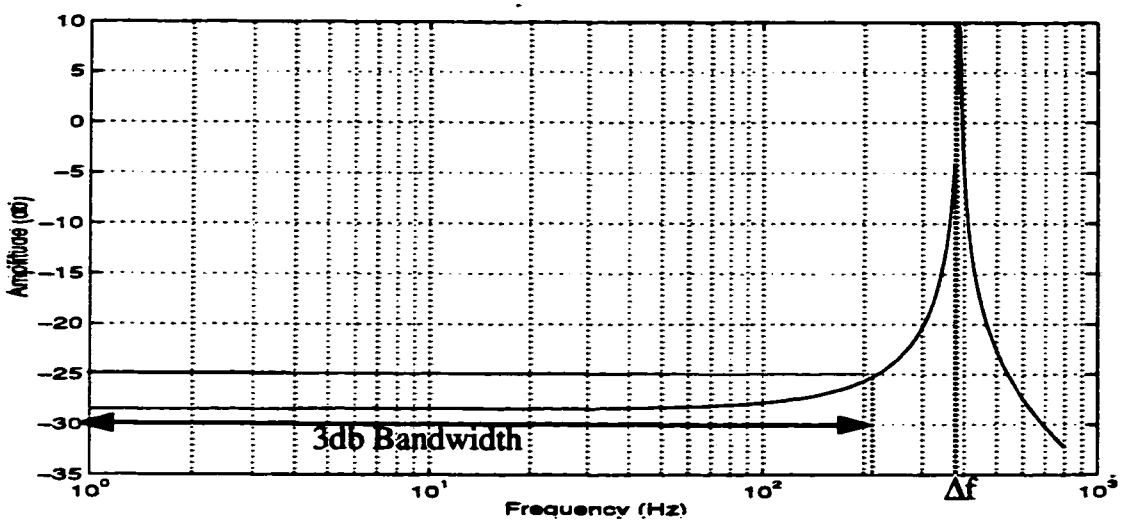

Fig. 3.36: Equivalent frequency response after demodulation (f_{nx}=7875Hz, f_{ny}=7486Hz, Q_x=5000, Q_y=1500).

As mentioned before, this design is not based on a standard fabrication process, therefore it is not yet possible to put both the sensor and its signal processing circuitry on one chip. The solution would be to design a separate chip for circuitry and put it in one package together with the sensor chip. Since the sensor itself is made out of a silicon wafer bonded to glass wafer, it would be possible to use the same glass wafer as a common support for both silicon chips, and make the connections using wire bonding (Fig.3.37).

Wire-bonding would introduce some additional parasitic elements to the detector circuit shown in Fig.3.32. An equivalent capacitance of 0.1pF (C_{b2}) should be considered for each pad. Also an equivalent capacitance of 1pF (C_{b1}) and inductance of 1nH (L_1) should be considered for each wire-bond [63]. The detector circuit could be represented as shown in Fig.3.38 considering the added parasitic elements.

The amplitude of vibrations is not uniform along the beam. The amplitude is maximum at the center and reduces to zero at the two ends. The variation of vibration amplitude along the beam follows the first resonance mode shape function $\phi(x)$ in this case. The dynamic range of variations in capacitance $\frac{C_1}{C_0+C_{b1}+C_{b2}}$ has to be maximized in order to gain the best sensitivity. Both C_1 and C_0 vary by changing the length of the sense capacitor plate (the capacitor electrode deposited on the glass) while C_{b1} and C_{b2} are constant. It is clear that the capacitor plate has to be aligned with the center of the beam where the vibrational amplitude is maximum.

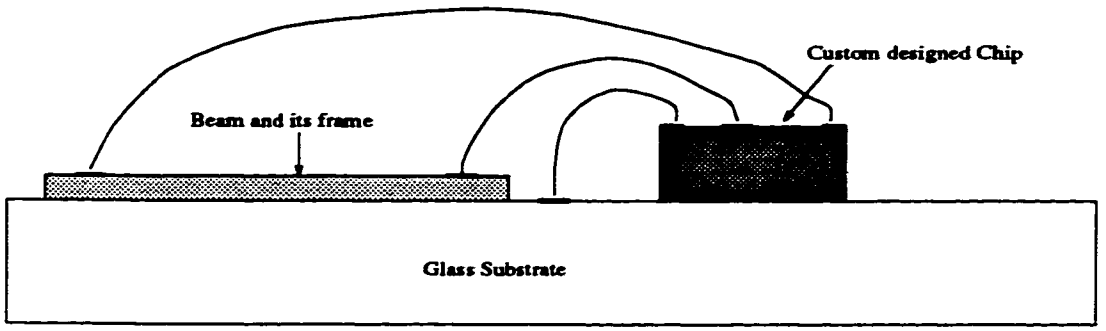

Fig. 3.37: Connection of sensor and its signal processing circuit through wire-bonding.

The variation of dynamic range in capacitance has to be investigated in order to find the optimum length for the capacitor plate considering the parasitic capacitances. The variations of dynamic range with length of the capacitor are plotted in Fig.3.39. The optimum length for the capacitor may be determined from the graph. The value of C_0 and C_1 (in Eq.3.55) are then calculated for the optimum length. The peak-to-peak amplitude of the output signal may be found by simulating the circuit shown in Fig.3.38 using the optimum $C(t)$. The value of the inductor does not have a noticeable effect on the output since the operating frequency is low.

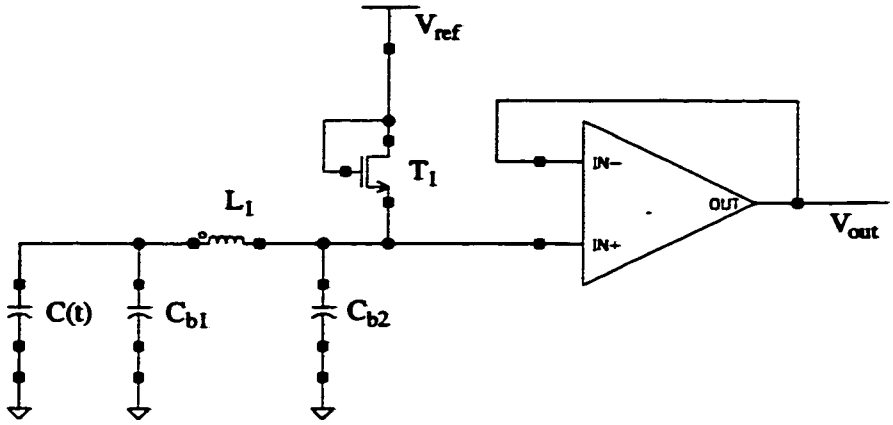

Fig. 3.38: Detection circuit including the parasitic elements.

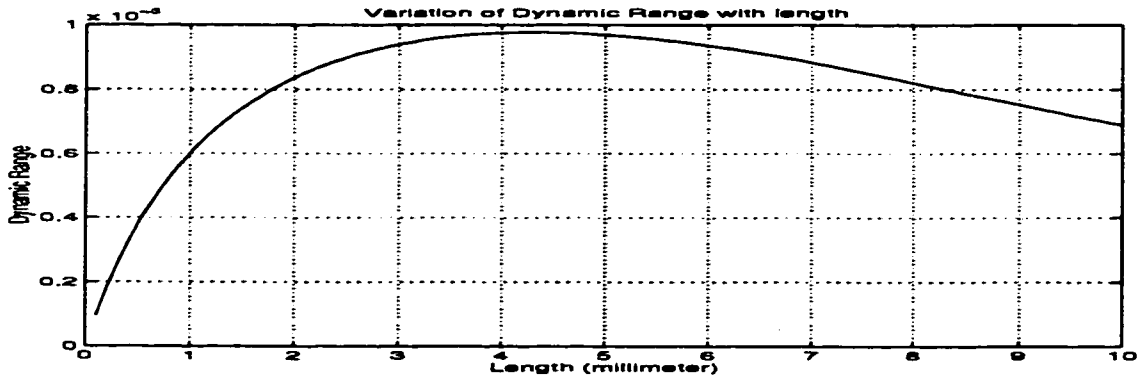

Fig. 3.39: Variation of Dynamic Range with length of the capacitor for wire bonded connection.

3.6.3 Non-Ideal Effects

The effect of the weight of the beam has been neglected in all of the analysis done so far. The beam bends under its own weight, although the deflection induced this way is

very small it may still be comparable to the small sense vibrations induced by Coriolis acceleration. The maximum deflection induced in the middle of a beam with various lengths and $105\mu m \times 100\mu m$ cross-section is shown Fig.3.40. By comparing the deflection obtained from this figure for (length=1cm) with the typical amplitude of vibrations induced in such a beam from Fig.3.10, it is clear that the amplitude of deflections induced by the weight of the beam is even a few times larger than the sense vibrations amplitude. Therefore, this non-ideal effect has to be considered carefully during the modeling and design of the system.

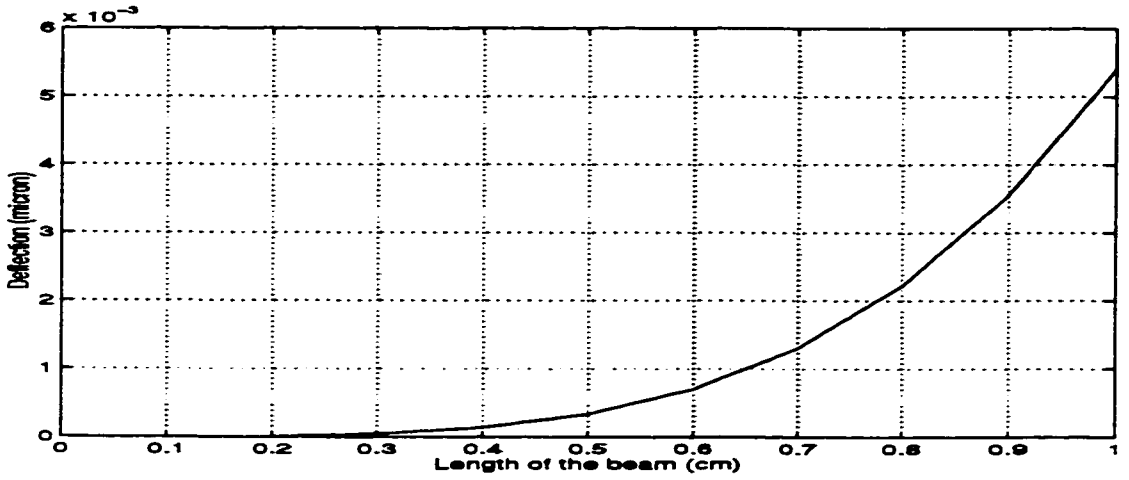

Fig. 3.40: Maximum deflection induced by weight of the beam.

As a result of beam's deflection under its own weight the actuation vibration follows an ellipsoidal path instead of a straight line (the mechanical coupling effect discussed in Sec.3.5.4 will contribute to the same effect as well). This is shown in Fig.3.41. The cross-section of the beam follows the ellipsoidal path instead of the straight line. As the sensor is rotated along its output axis the effective force applied normal to the beam changes, and as a result the deflection induced in the beam varies with angular position. As shown in

Fig.3.42, if the output axis is aligned along x or z axis the component of the weight force applied normal to the sensor's plane varies with the rotation angle, but if the output axis is aligned with the gravity (y axis) the weight will not have any effect on the beam's operation. The vibration induced in sense direction due to beam's weight may be found as:

$$y_w(t) = K_w x(t) \cos(\theta(t)) \qquad \text{Eq.3.57}$$

where K_w, $\theta(t)$ are the coupling coefficient and the angle between the sense vibrations axis and gravity axis.

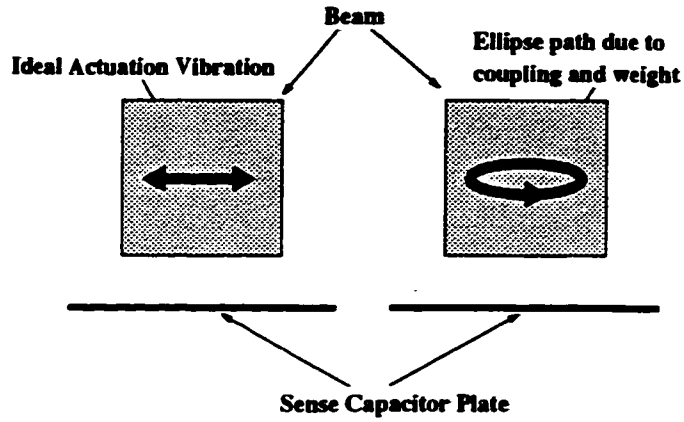

Fig. 3.41: Effect of beam's weight and coupling on actuation vibration.

Fig. 3.42: Cross-section of the sensor while rotating.

Therefore Eq.3.36 may be written in a more complete form as follows:

$$m_0 \frac{d^2y(t)}{dt^2} + \mu_y \frac{dy(t)}{dt} + \left(K_y - \varepsilon A \frac{V_0^2}{d^3}\right) y(t) = \qquad \text{Eq.3.58}$$

$$2m_0 \Omega(t) \frac{dx(t)}{dt} + \frac{1}{2} \varepsilon A \frac{V_0^2}{d^2} + K_c x(t) + K_w x(t) \cos(\theta(t))$$

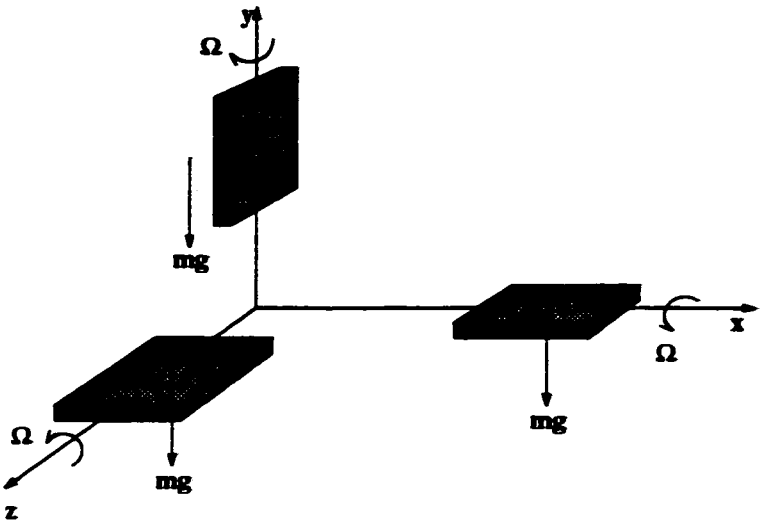

The steady state solution to the above differential equation may be obtained as follows (similar to Sec.3.4):

$$y(t) \approx \frac{X}{\Delta w}\Omega(t)\cos(w_{nx}t-\phi_y) + (E+F\cos(\theta(t)))\sin(w_{nx}t-\phi_y) \qquad \text{Eq.3.59}$$

$$E=\frac{K_c X}{2m_0 w_{nx}\Delta w},\ F\approx\frac{K_w\cos(\theta(t))X}{2m_0 w_{nx}\Delta w} \qquad \text{Eq.3.60}$$

where X is the amplitude of actuation vibrations and ϕ_y is the phase shift between the actuation input and the output as described in Eq.3.16. There is a 90^o phase shift between the desired signal resulted from the Coriolis acceleration and the undesired signal generated due to mechanical coupling and deflection of the beam under its own weight.

After the synchronous demodulation and filtering out the high frequency terms, the output would be:

$$y_{out}(t) \approx \frac{1}{2}\frac{X}{\Delta w}\Omega(t)\cos(\phi_y) + \frac{1}{2}(E+F\cos(\theta(t)))\sin(\phi_y) \qquad \text{Eq.3.61}$$

In an ideal situation where $\phi_y = 0$ the effect of mechanical coupling and weight

of the beam are cancelled out after synchronous demodulation. But in practice there will always be a small phase shift present as shown in Eq.3.16. Based on the comparison we had between Fig.3.10 and Fig.3.40, the absolute value of F would be a few times larger than $\frac{X}{\Delta w}$ for a typical beam, therefore, a very precise control over the phase of the demodulating signal is required to considerably attenuate the undesirable second term of the above equation.

3.6.4 Overall System Sensitivity

The overall system sensitivity may be defined as the output voltage obtained at the output of the sensor vs. input angular velocity:

$$S = \frac{V_{out}}{\Omega_{in}} \qquad \text{Eq.3.62}$$

where V_{out} is the detected output voltage and Ω_{in} is the input angular velocity.

The relation between the overall sensitivity and the beam sensitivity, discussed before in Sec.3.5.2, may be shown as follows:

$$S = S_b \times G_{eq} \qquad \text{Eq.3.63}$$

where G_{eq} is the equivalent gain of the Detector, Gain, Synchronous Demodulator, and LP Filter stages in block diagram in Fig.3.33.

3.7 Tuning Fork Based Design

A tuning fork structure may be used instead of a single beam to improve the performance. This design is based on using a double ended tuning fork, same as the one shown

in Fig.3.20, as the vibrating structure. The structure of the device is shown in Fig.3.43 for this design. The fabrication process for this design would be same as the one described before for the single beam. The two tines of the tuning fork are driven in anti-phase by passing anti-phase currents through the electrodes. Since the tines are moving in anti-phase, the Coriolis Acceleration defined by $2m_0\Omega\frac{dx(t)}{dt}$ would also be in anti-phase. The induced sense vibrations are then detected for each beam and subtracted from each other in order to generate the differential output signal (Fig.3.44).

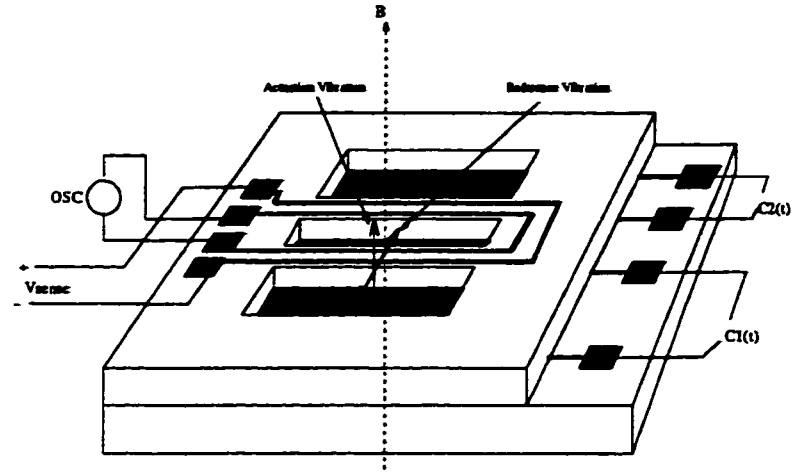

Fig. 3.43: The tuning fork structure.

In the vibration direction, the X direction, the voltages induced in the two sense electrodes located on two tines are added to each other to generate a larger voltage.

The advantages of this structure are as follows:

1- Since the two beams are vibrating in anti-phase their torques are cancelled out at the two ends. The two ends will act as vibration nodes and no vibrational energy will be transferred to the base through them. Higher Q values are achievable this way.

2- The magnitude of the output signal will be doubled since the differential output is

measured.

3- Effect of the noise would be reduced since the output is a differential signal.

4- The effect of linear acceleration and beam's weight would be cancelled out. These effects will contribute to generation of a common mode signal that will be cancelled out when the differential signal is generated.

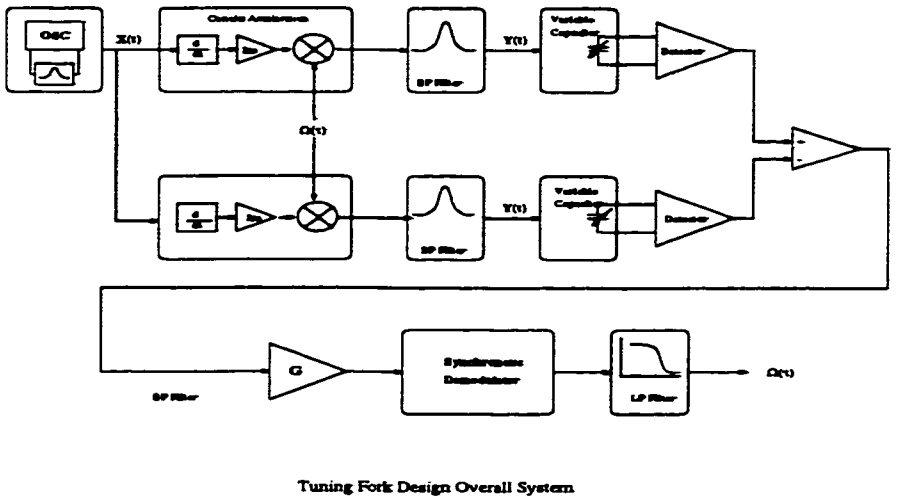

Fig. 3.44: Block-diagram of the system with tuning fork structure.

All of the calculations and models discussed before are applicable to each one of the beams in this structure.

3.8 Chapter 3 Summary (Contributions indicated by *)

. An angular rate sensing device was designed based on a bulk-micromachined single-crystal silicon beam having square cross-section. Electromagnetic actuation using a small permanent magnet supplies the reference vibration, and the Coriolis-induced vibration is sensed by a capacitor plate in close proximity to the vibrating beam.

. The fabrication process is based on wet anisotropic etching of {100} silicon, and uses the specific anisotropy of TMAH at 25% to obtain vertical beam sidewalls, by orienting the mask-edge at 45° to the wafer-flat and using a two-step etch process (at two different temperatures). The fabricated silicon beam/support is anodically bonded to glass, on which the metal sense capacitor is located.

* This design allows beams to be obtained with precisely matched dimensions, square cross-section, vertical smooth sidewalls, and sharp edges on Si{100} wafers using this fabrication process.

. A Mass-Spring model has been provided to simulate the sensor's operation and performance.

. Several issues essential for a successful design have been considered including: actuation frequency and its effect on the output, actuation amplitude and its limitation due to the amplitude stiffening effect, sensitivity of the beam and its relation to the mismatch of horizontal and vertical resonant frequencies, spring softening effect in the sense direction and its effect on reducing the mismatch, air damping, and effect of coupling on increasing the mismatch.

* The amplitude-stiffened behavior of the beam and its effect on limiting the amplitude of the reference vibrations is discussed.
* The sensitivity of the device and its variations with different design parameters is explained.
* The spring-softening effect in the vertical direction and its possible application in tuning the mismatch between the two natural frequencies is explained.

* The damping by the air or coupling through the base is discussed and the necessity of reduced pressure environment for the operation of the device is shown.
* The effect of coupling between the two vibration modes and its effect on shifting the natural frequencies (increasing mismatch) is explained.

. The required circuitry for actuation of the beam and detection of the Coriolis induced vibrations was discussed, and some non-ideal effects, such as the effect of beam's weight and linear acceleration on the response, were presented.

* An equivalent electrical circuit model is presented for the actuation of the beam, including a tuning circuit to represent the mechanical response and the parasitic capacitors and resistors.
* Design parameters regarding the actuation system including the dissipated power in the actuation electrode, the maximum obtainable value for the induced emf in the beam, and the maximum induced stress in the beam are discussed.
* The detection circuit required to convert the variations in capacitance in the sense direction to a voltage is explained.
* The overall block diagram of the required circuitry to detect, amplify, and recover (demodulation) the coriolis induced signal at the output is explained.
* The relation between mismatch between the two natural frequencies and the bandwidth of the sensor is explained and its is shown that in an open-loop operation configuration the bandwidth is inversely proportional to the sensitivity.
* Non-ideal effects such as the effect of linear acceleration and the weight of the beam on the output signal is discussed. It is shown that a precise phase match is required at the demodulator in order to eliminate the non-ideal effects.

. A tuning fork structure was mentioned to potentially improve the performance of the sensor.

. A simulation model will be implemented in Chapter 4 based on the various principles and equations explained in this chapter. The response of the sensor and several issues such as spring softening, amplitude stiffening and the trade-off between the bandwidth and mismatch will be investigated using the developed model.

. Several experimental samples are fabricated and tested in Chapter 6 using the fabrication process developed in this chapter. The samples are tested and the results are compared with the theory explained in this chapter.

CHAPTER 4

Simulation of Basic Sensor Operation

4.1 Introduction

The commercially available electronic simulation package (HSPICE) offers multi-dimensional controlled sources with polynomial non-linearity. Therefore, analog computer elements like summers, multipliers, dividers and integrators can be constructed and used in conjunction with other elements to solve differential equations [64]. All of the parameters may be defined as voltages and voltage sources in order to do a transient time simulation.

A simulation model is built and tested using HSPICE in this chapter to concurrently simulate both the mechanical and electrical aspects of the sensor. The overall block diagram of the HSPICE simulation model is discussed first. A typical sensor structure is modeled next, and the steady-state and transient time responses of the model are compared with the theory. Nonlinear aspects of the response of the model, such as spring softening and amplitude stiffening effects, are also compared with the expected results from theory.

4.2 Simulation Model in SPICE

To simulate the sensor in a numerical simulation tool such as HSPICE, the following two non-linear differential equations which describe the response of the system in the most general form, must be solved simultaneously.

$$m_0\frac{d^2x(t)}{dt^2}+\mu_x\frac{dx(t)}{dt}+K_x x(t)+\eta x^3(t) = F_0 COS(\omega t) \tag{4.1}$$

$$m_0\frac{d^2y(t)}{dt^2}+\mu_y\frac{dy(t)}{dt}+K_y y(t) = 2m_0\Omega\frac{dx(t)}{dt}+K_c x(t)+ \tag{4.2}$$

$$K_w x(t)\cos((\theta(t)))+\frac{1}{2}\varepsilon A\frac{V_{dc}^2}{(d-d_0-y(t))}$$

The overall block diagram of the model built in HSPICE is shown in Fig.3.1 (see Appendix I). The model consists of the following blocks:

- The response of the beam in the actuation direction is modeled in the "X Response" block. The actuation voltage applied to one of the actuation electrodes is input to the block. The outputs are the actuation displacement *x(t)* and the sense voltage (emf) induced in the second actuation electrode *e(t)*. The two capacitors (C_p) and resistor ($R_p/2$) model the electrical coupling between the two actuation electrodes as mentioned in Sec.3.6.1.

A more detailed view of this block is shown in Fig.4.2. This block solves the nonlinear differential equation numerically. Constants C_1 to C_5 may be found from the differential equation.

- The Coriolis force arising from the angular velocity $\Omega(t)$ is simulated by the "Coriolis" block.
- The coupling forces generated by mechanical coupling and deflection of the beam under its own weight are simulated by gains K_c and K_w.

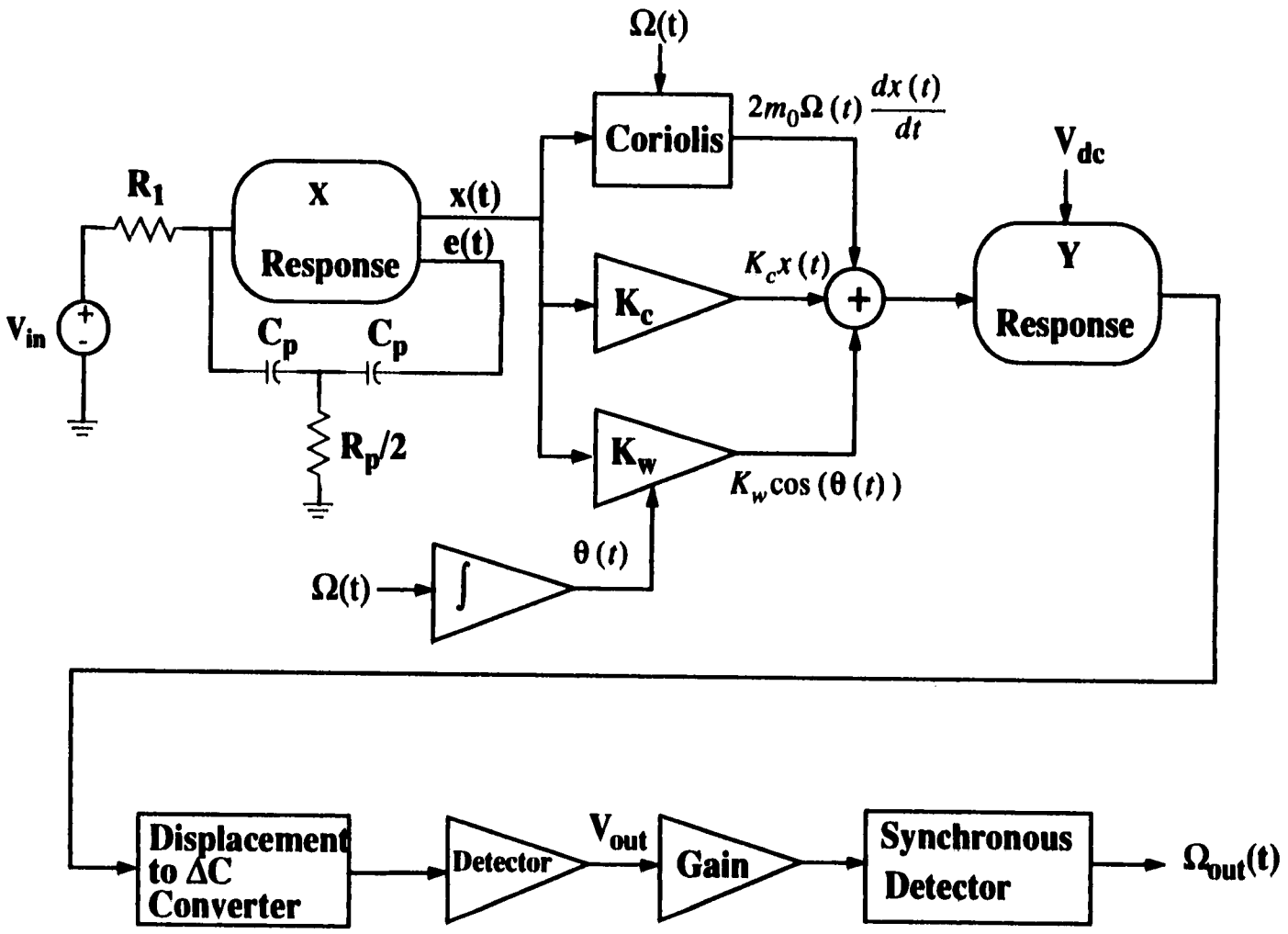

Fig4.1: Overall block diagram of the HSPICE simulation model.

- The response of the beam in the vertical or sense direction is modeled in Y response block. This block solves the differential equation Eq.4.2 numerically. The total force generated by Coriolis acceleration and coupling in the sense direction is input to this block, the output is the displacement in the y direction *y(t)*. A more detailed view of this block is shown in Fig.4.3. Constants C'_1 to C'_4 may be found from the differential equation Eq.4.2. Constant C'_4 and input V_{dc} are used by the block to generate the variable term in differential equation that varies with the dc voltage applied across the beam.

- The variations in capacitance may be found using Eq.3.56. This is done in the block labelled "Displacement to ΔC converter".

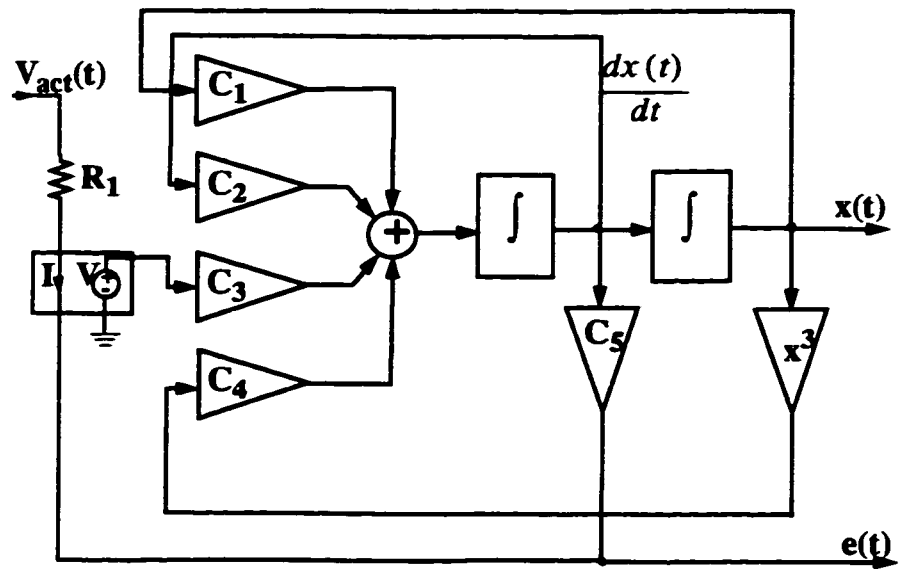

Fig. 4.2: Detailed Block Diagram of the "X-Response" block.

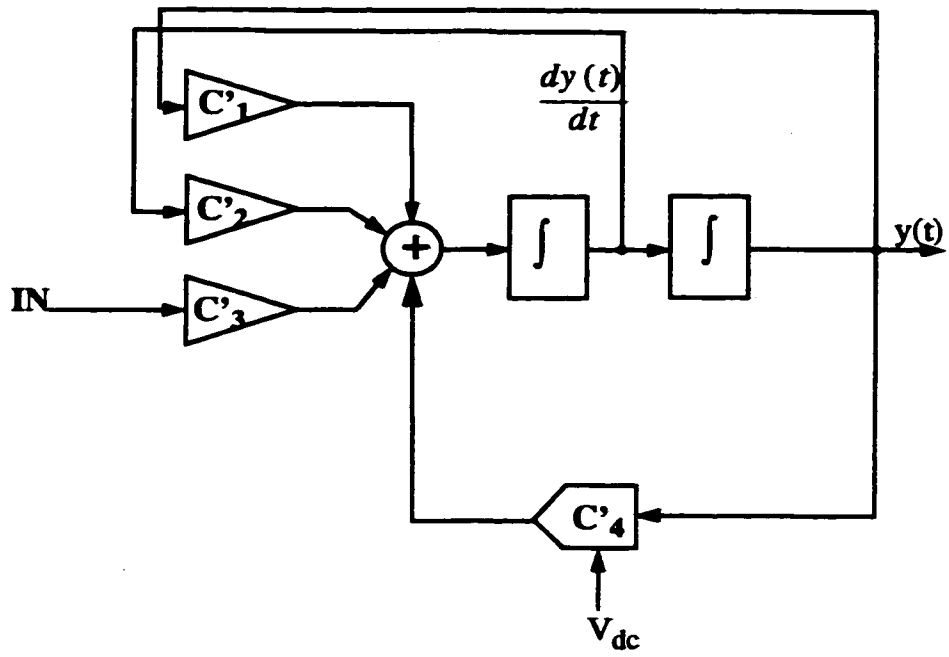

Fig. 4.3: Detailed block diagram of the "Y-Response" block.

- The Detector Circuit explained in Sec.3.6.2 is used to convert the variations in capacitance to voltage. This signal is then amplified by a gain stage.
- The synchronous detector is performing the synchronous demodulation task. The original actuation voltage is used as a reference signal to recover $\Omega_{out}(t)$. A variable delay stage is used to match the phase of the reference signal with the in-coming modulated signal.

4.3 Simulation Results

The HSPICE model developed may be used to simulate the response of the system to a variety of inputs. A beam with the following basic characteristics is considered in the rest of this chapter for the simulations:

Beam width=105μm, Beam height=100μm, mismatch=5%, Beam length=1cm, Q_x=5000, Q_y=1500, Resistance of the actuation electrode $R_1 = 23\ \Omega$.

4.3.1 Steady State Response

The model is actuated by a sinusoidal input with a frequency set to the natural frequency of the beam in the actuation mode (f_x). The amplitude of the input is set such that the amplitude of vibrations in the actuation direction remains within the linear region. Fig.4.4 shows the simulation results for a constant angular rate input of $\Omega = 1 rad/\text{sec}$. The input actuation voltage, actuation vibrations, induced voltage in the second actuation electrode of the beam and the Coriolis-induced vibrations induced at the output are shown in Fig.4.4. The beam is actuated with an input voltage of 20mV as shown in Fig.4.4 (a). The amplitude of vibrations resulted from this actuation input is ~2.35μm as shown in Fig.4.4 (b). The induced EMF in the beam is shown in Fig.4.4 (c) which has an amplitude of ~230μV. The sense vibrations obtained when the beam is actuated with a constant angular rate of 1 rad/sec is shown in Fig.4.4 (d) which has an amplitude of 11Å.

The variation in output (sense) capacitance and the detected output voltage for the same beam is shown in Fig.4.5. The sense vibrations with an amplitude of 11Å shown in Fig.4.4 (d) results in variation in capacitance with the amplitude of 0.33 fF peak-to-peak (p-p) as shown in Fig.4.5 (b). This will result in a detected voltage of ~0.15 mVp-p at the output of the detector circuit as shown in Fig.4.5 (b). The simulation results are compared with the theory from Chapter 3 in Table 4.1.

	X amplitude	Y amplitude	Induced EMF	Change in Capacitance
Simulation	2.35 μm	11 Å	0.23 mV	0.33 fF p-p
Theory	2.36 μm	9.48 Å	0.229 mV	0.36 fF p-p

TABLE 4.1: Steady state simulation results compared with theory.

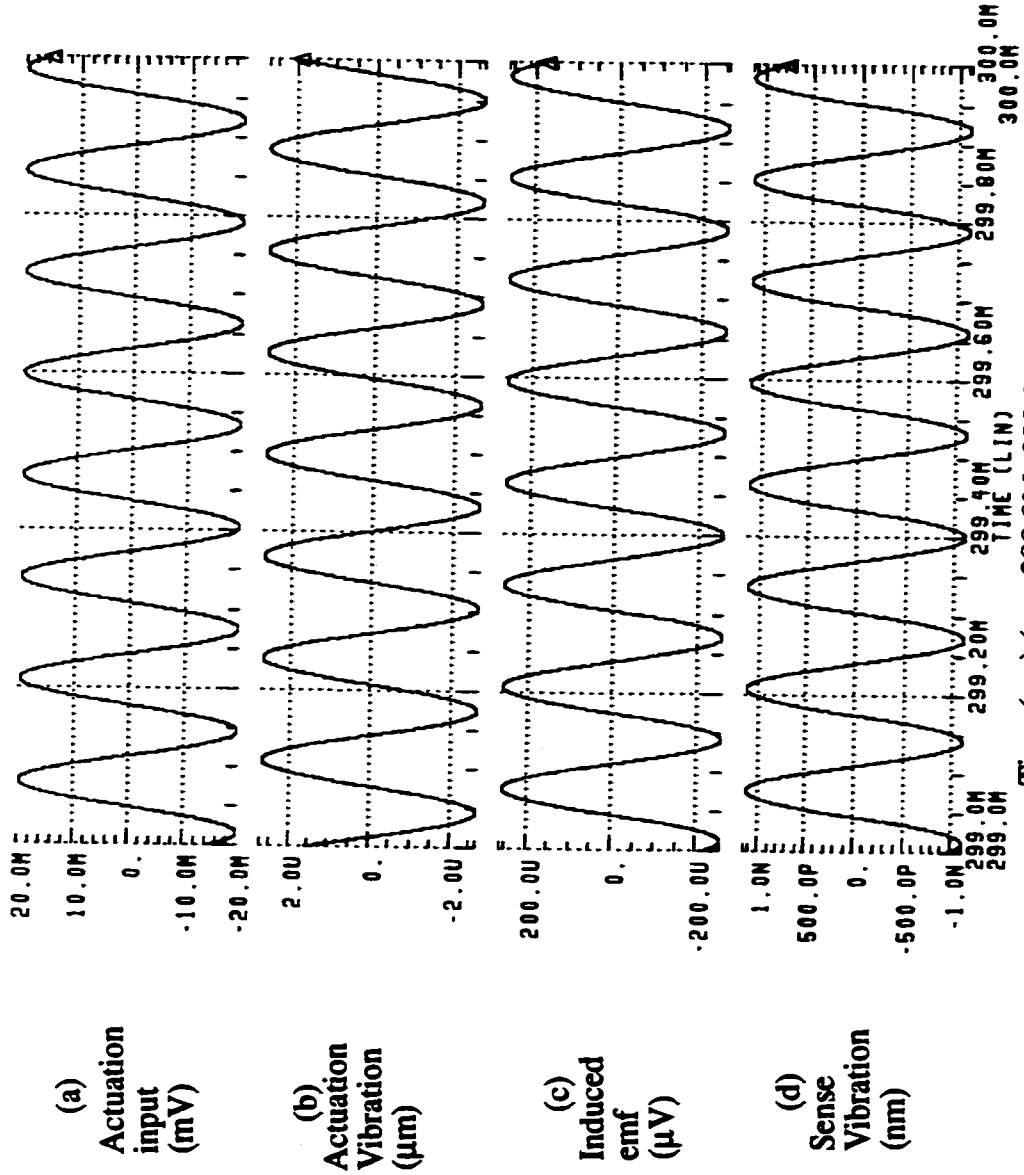

Fig.4.4: Steady state response to the input of Ω=1rad/sec in the modeled beam:
(a) actuation input (b) actuation vibration (c) induced emf (d) sense vibration
M: milli (e.g. 10.0M=10.0mV), U: micro (e.g. 2.0U=2.0μm), N: nano (e.g. 1.0N=1.0 nm)
P: pico (e.g. 500.0P=500.0pm)

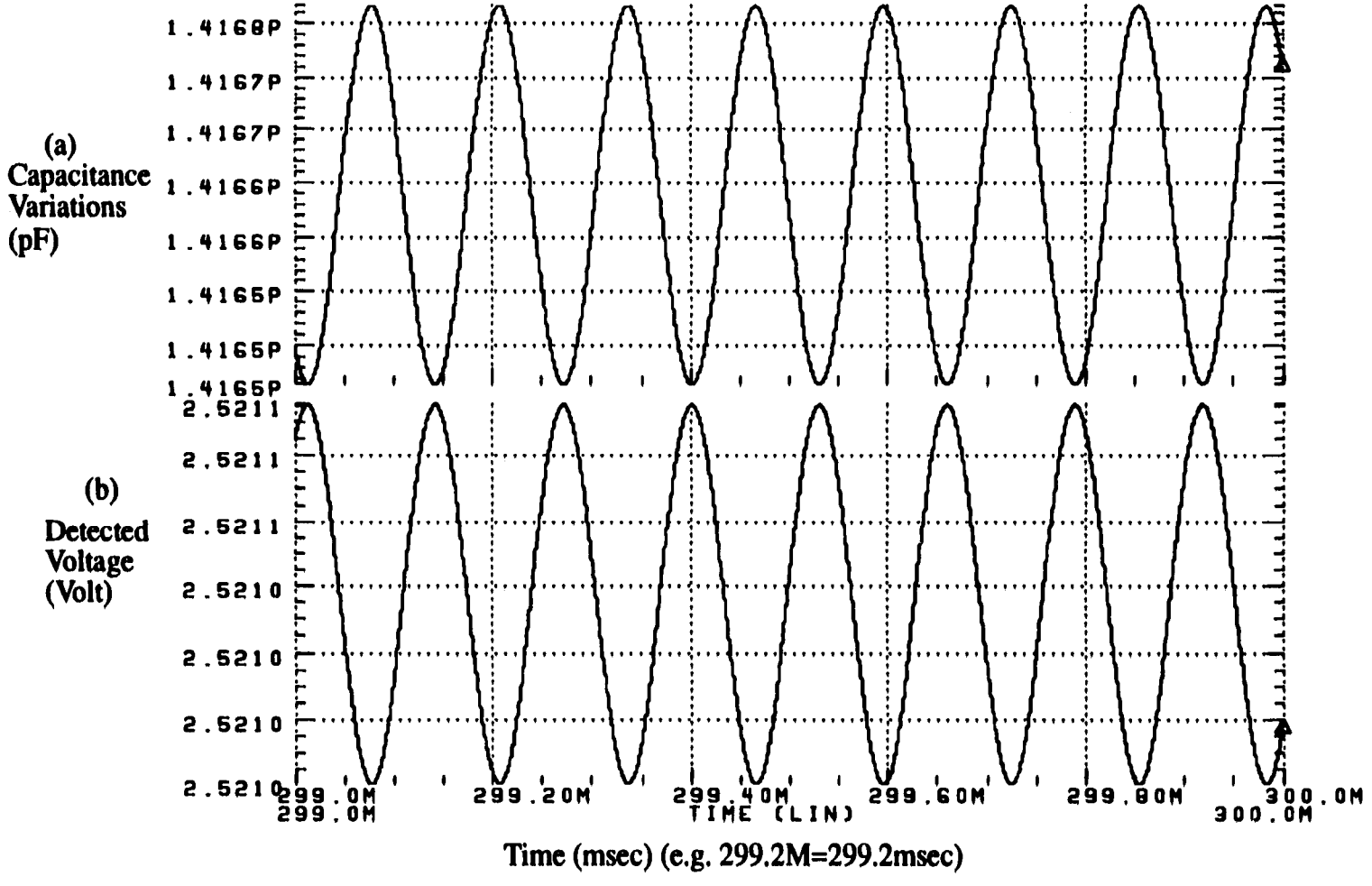

Fig.4.5: Steady state response for the same beam as Fig.4.4 :
(a) Capacitance variations (b) Detected Voltage

4.3.1.1 Spring Softening

As mentioned before in Sec.3.5.3, variations in the dc voltage applied across the detection capacitor plates affect the mismatch between the two natural frequencies due to the spring softening effect. Provided that the original design is made such that the natural frequency in the sense mode is higher than the natural frequency in the actuation mode, this effect may be used to reduce the mismatch. This is verified by considering a beam with the following conditions: original mismatch=5%, $f_x<f_y$, Capacitor air gap=5μm. The actuation input and amplitude of vibrations in the sense direction are simulated for V_{dc}=7V, V_{dc}=14V, V_{dc}=21V, V_{dc}=28V in Fig.4.6. The sense amplitude increases as the applied voltage is increased, as a result of the decrease in mismatch. The results are compared with the theoretical calculations in Table 4.2. The shift in natural frequency in the sense direction (Δf_y) obtained from equation Eq.3.31 in Sec.3.5.3, and the amplitude of the vibrations in the sense direction obtained from equation Eq.3.11 in Sec.3.4 are compared with the results obtained from simulation.

	Sense Amp. Theory	Sense Amp. Simulation	Δf_y Theory	Δf_y Simulation
V_{dc}=7 V	10.1 Å	9.9 Å	18 Hz	16.5 Hz
V_{dc}=14 V	11.7 Å	11.6 Å	72 Hz	70 Hz
V_{dc}=21 V	16.5 Å	17 Å	163 Hz	164 Hz
V_{dc}=28 V	42.3 Å	47 Å	292 Hz	295 Hz

TABLE 4.2: The sense amplitude and Δf_y due to spring softening obtained from theory and simulation for various applied dc voltages.

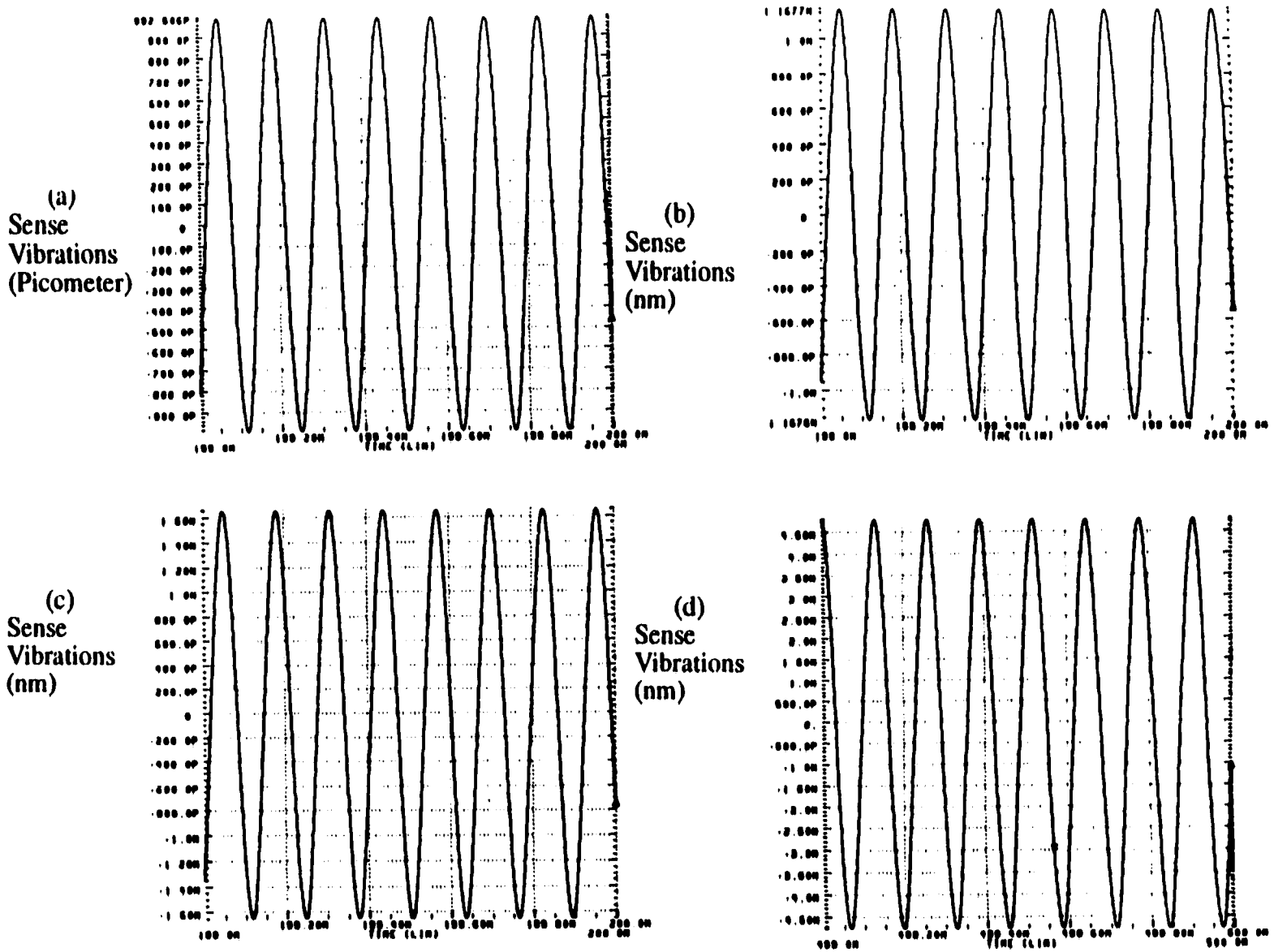

Fig. 4.6: Simulated sense vibrations for an angular rate input of Ω=1rad/sec, when various dc voltages applied across the sense capacitor: (a) V_{dc}=7V, (b) V_{dc}=14V, (c) V_{dc}=21V, (d) V_{dc}=28V. The time axis unit is (ms) (e.g. 199.0M=199.0msec). On vertical axis: N: nanometer (nm) (e.g. 1.0N=1.0nm), P: picometer (e.g. 100.0P=100.0pm)

4.3.1.2 Amplitude Stiffening

The frequency response of the beam in the actuation direction and its non-linear characteristics are an important parameter of the sensor's operation. To obtain the frequency response of the model in the actuation direction, inputs with different frequencies are applied to the model and the amplitude of the steady state response is measured for each input. The frequency response obtained from the model for two different inputs of V_{act}=18mV and V_{act}=100mV are shown in Fig.4.7 and Fig.4.8 which indicate a typical linear and nonlinear response of the model. The limit for the maximum vibration amplitude (where the hysteresis response begins) is found from simulations to be 2.7μm. This matches well with the amplitude 2.4μm that is found from theory (equation Eq.3.24 in Sec.3.5.1.2) for the same beam.

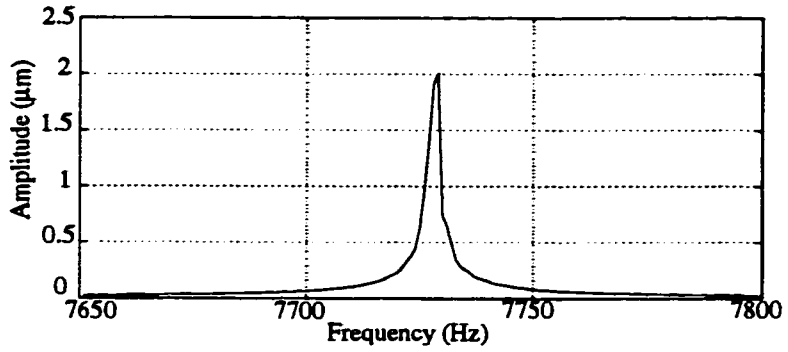

Fig. 4.7: Linear response of the beam for V_{act}=18mV.

4.3.2 Transient Response

The response of the beam to a step angular rate input with the amplitude of *1rad/s* applied at t=150ms is shown in Fig.4.9 for beams with 5% and 2.5% mismatch. The amplitudes of output vibrations decay exponentially to their final settling values. The time constant τ may be measured from the graph by considering the time it takes for the vibrations to reach to *1/e* of their original amplitude. The settling time may be considered as

5τ. As seen from the figure, the settling time and the amplitude of the output become smaller as the mismatch is increased.

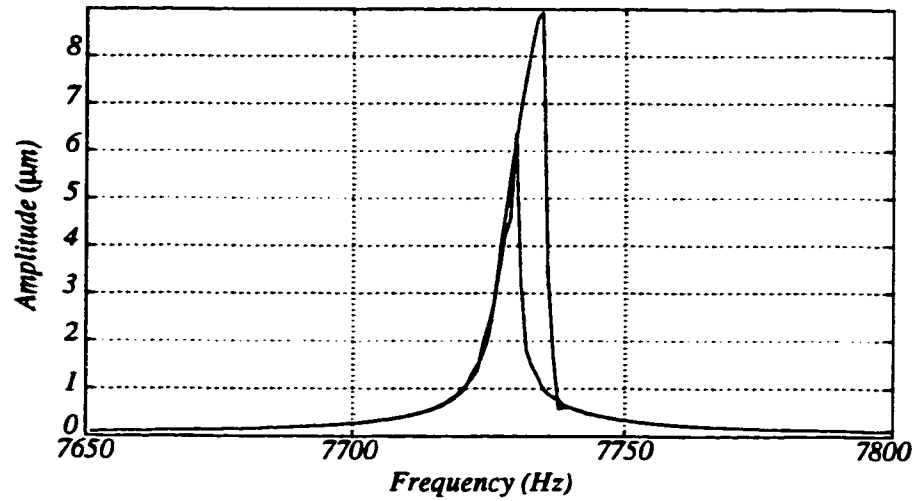

Fig. 4.8: Simulated response of the beam to an actuation input of V_{act}=100mV.

Sense vibrations are simulated for a beam with a range of mismatch values (from 1% to 10%) and the time constant and the settling time of the response are compared in Table 4.3. As seen from the table, increasing mismatch results in reduction in both sensitivity (output amplitude) and settling time. The oscillatory response is similar to the response of a band-pass filter with central frequency of $\Delta f=f_x-f_y$ and damping of $Q=Q_y$, which concurs with the model shown in Fig.3.35 in Sec.3.6.2.

The force-to-rebalance method may be used to eliminate the dependency of the sensitivity on bandwidth. In this method, the beam is constantly driven back to its steady state position using a feedback loop. The position of the beam is constantly monitored and a force is applied to cancel the effect of Coriolis acceleration and bring the beam back to its steady state position. The amount of the force required to rebalance the beam is proportional to the input angular rate [1].

Mismatch	Δf	Time constant τ	Settling time ~5τ	Sense Amplitude
1%	80 Hz	~190 ms	~950 ms	~70 Å
2.5%	201 Hz	~80 ms	~400 ms	~25 Å
4%	322 Hz	~55 ms	~280 ms	~15 Å
5%	402 Hz	~40 ms	~200 ms	~11 Å
7.5%	604 Hz	~32 ms	~160 ms	~8.4 Å
10%	804 Hz	~23 ms	~115 ms	~5 Å

TABLE 4.3: Simulated variation of time constant and settling time of sense vibrations with mismatch. These cases were all simulated with an actuation voltage of 20mV.

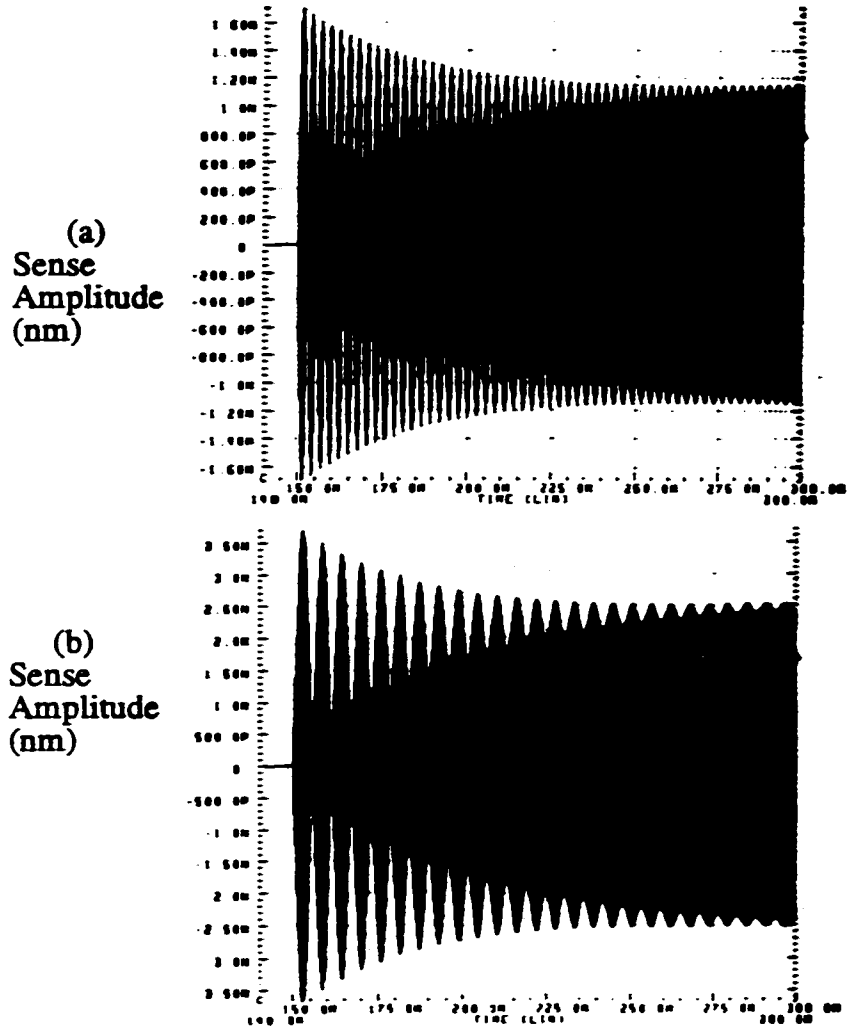

Fig. 4.9: The sense vibrations in response to a step input for a beam with (a) 5% mismatch (b) 2.5% mismatch. The time axis unit is (msec) and M: msec on this axis: P: picometer (pm) (e.g. 200.0P=200.0pm), N: nanometer (nm) (e.g. 1.0N=1.0nm).

The step output after detection, synchronous demodulation, and filtering is shown in Fig.4.10 for a beam with a mismatch of 5%. The detector circuit is implemented using the cells (opamp, NFET) available in the Mitel 1.5 micron CMOS technology and considering the parasitic elements shown in Fig.3.38. The Gain and the Synchronous Detector stages (see Fig.4.1) are implemented using the ideal behavioral elements in HSPICE. The overall gain of the Gain and Synchronous Detector stages is ~115. The filter used in this simulation is a 5th order Butterworth filter with a cut-off frequency of 100 Hz. The oscillatory response in sense vibrations has been filtered out, but the bandwidth is limited to 100 Hz. A total settling time of ~35mS is measured from the simulations.

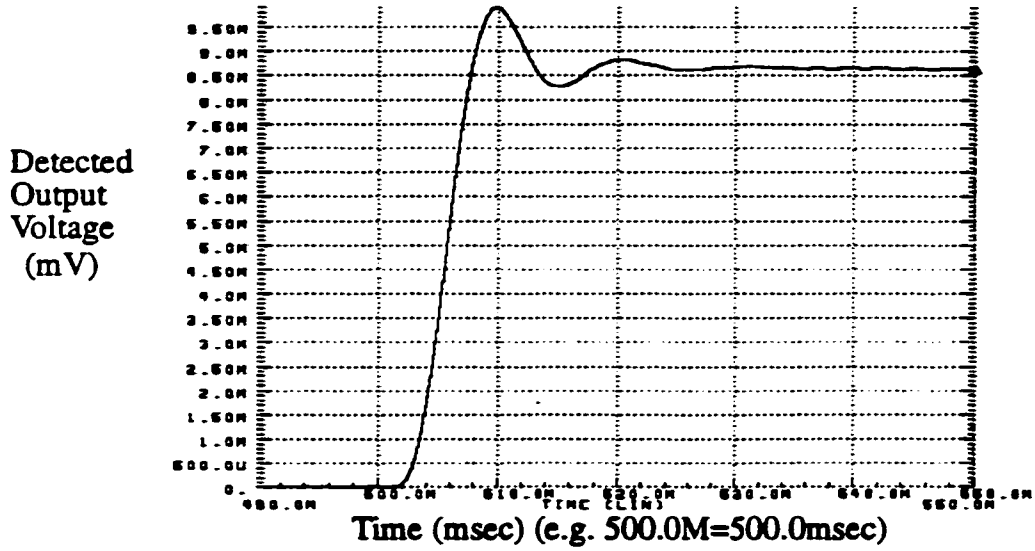

Fig. 4.10: Step response of the sensor to a step input (applied at t=500 msec) with amplitude of 1 rad/sec. On vertical axis: M: mV (e.g. 1.0M=1.0mV) and U:μV (e.g. 600.0U=600.0μV).

4.4 Overall Important Parameters

Several critical parameters that have to be considered carefully while designing an angular rate sensor, such as the ones discussed in this thesis, are shown in Table 4.4. The value of some of the parameters is not defined at this point, they will be defined after considering the experimental results in Chapter 6 (see Table 6.11).

Reference Section	Parameter	Simulation
Beam & Glass Dimensions		
Sec.3.5.1.1	Beam Length	1 cm
Sec.3.5.1.1	Beam Width	105 μm
Sec.3.5.1.1	Beam Height	100 μm
Sec.3.5.4	Air Gap	5 μm
Mechanical Parameters		
Sec.6.3.3	Air Pressure	----------
Sec.3.5.4, Eq.3.32 & Eq.3.34	Q_x	5000
Sec.3.5.4, Eq.3.33 & Eq.3.34	Q_y	1500
Sec.3.4, Eq.3.14	f_x	8114 Hz
Sec.3.4, Eq.3.14	f_y	7728 Hz
Sec.3.5.1, Eq.3.18	Mismatch	~5%
Sec.3.6.2, Fig.3.36	3db Bandwidth	~200 Hz
Sec.3.5.2, Eq.3.28	Sensitivity (1/rad/sec)	0.0004
Sec.3.5.3, Eq.3.31	Spring Softening	16.5 Hz
Sec.6.5.5	K_c (N/m)	----------
Sec.6.5.5	K_w (N/m)	----------
Sec.3.5.1.2, Eq.3.24	Threshold of Hysteresis-Free Actuation Amplitude	2.4 μm
Operational Parameters		
Sec.3.4, Eq.3.5	Actuation Amplitude	2.35 μm
Sec.3.6.1, Eq.3.49	Induced EMF	0.23 mV
Sec.3.6.1.1, Eq.3.53	Dissipated Power	0.86 μW (rms)
Sec.3.4, Eq.3.11	Sense Amplitude	11 Å
Sec.3.6.2, Eq.3.56	ΔC	0.33 fF p-p
Sec.3.6.2	Detected Voltage (1 rad/sec input)	0.15 mV p-p
Sec.6.7, Eq.6.6	Phase Delay	----------
Sec.3.6.3, Eq.3.61	Zero-Rate-Output	----------
Sec.4.3.2, Sec.6.7	Output/Input (V/rad/sec)	8.7 mV/rad/sec

TABLE 4.4: List of critical parameters that need to be considered during the design of the sensor, simulated from HSPICE simulation model. The actuation voltage is chosen as V_{act}=20 mV.

4.5 Chapter 4 Summary (Contributions indicated by ❋)

. A model is built using HSPICE to concurrently simulate both the mechanical and electrical elements of the sensor.

❋ The model includes many relevant non-linear and non-ideal effects of the mechanical behavior of the sensor and allows both the mechanical and electrical parts of the sensor to be simulated in an interrelated manner.

. A typical sensor structure is modeled and simulated using the developed model in HSPICE to find the steady state and transient response to input angular rates.

. The steady state response of the model is compared with the results from theory (Chapter 3). A sense vibration peak amplitude of ~10Å, and capacitance variation of 0.33fF p-p is obtained in response to an angular rate input of 1rad/sec.

❋ The resulting actuation amplitude, output sense vibration amplitude, induced EMF, and variations in capacitance obtained from the model match well with the theory outlined in Chapter 3.

. The non-linear behavior of the model including the spring-softening and amplitude- stiffening effects are compared with the expected results from theory.

❋ The model follows the expected behavior of the beam in the non-linear region within acceptable tolerances.

. The transient response of the sensor to a step input is investigated using the model and the results are compared for various mismatch values to show the trade-off between mismatch and settling time (bandwidth).

❋ The trade-off between the bandwidth and sensitivity is shown using the HSPICE model and compared with the theory.

CHAPTER 5

Concave Corner Compensation

Design and Simulation

5.1 Introduction

Mismatch between the two natural frequencies of the beam is one of the critical parameters in the performance of the rate sensor. Lower mismatch is desirable to increase the sensitivity of the sensor. The fabrication of vibrating beams in this research is based on anisotropic etching of <100> silicon wafers with the patterns aligned at 45° with respect to the <110> wafer flat. This results in the formation of <111> flanges on both ends of the beam (Fig.5.1), which contribute to the increase of mismatch between the two vibration modes of the beam. By reduction of the size of <111> flanges, the mismatch between the natural frequencies may be reduced. The point of this development is modulation of the mismatch to get it into an acceptable range. This will relieve some of the other constraints on other techniques, such as the spring-softening method explained in Sec.3.5.3 (so that wider air gaps would be allowed).

This chapter presents a concave corner compensation technique, to substantially reduce the residual {111} flanges between two vertical (010)-(001) planes, underetched on a (100) silicon wafer [65,66]. A carefully-planned set of rectangles is used, oriented parallel or perpendicular to the wafer flat, at 45° to the desired underetched vertical (010) and (001) planes. The set of rectangles is designed based on several principles, and the behavior during etching is graphically and numerically simulated.

The formation of the flanges at the two ends of the beam during the fabrication of the beam is discussed first. Design of the concave corner compensation patterns is discussed

next. Then the design principles are explained in detail and the numerical simulation program is developed to track the progress of the etch front through the patterns. The etch progress in the patterns is simulated using a graphical simulation tool and the results are compared with the numerical simulation results.

5.2 Flange Formation

Wet anisotropic etching of bulk silicon is a very important technique in the fabrication of micromachined devices. As discussed in the previous chapter, while the prevalently-used {111} planes are the slowest-etching planes in silicon, under certain conditions {100} planes have also a local minimum in etch rate [40,67]. This can be used beneficially to achieve quite flat vertical (010) and (001) planes on a (100) wafer.

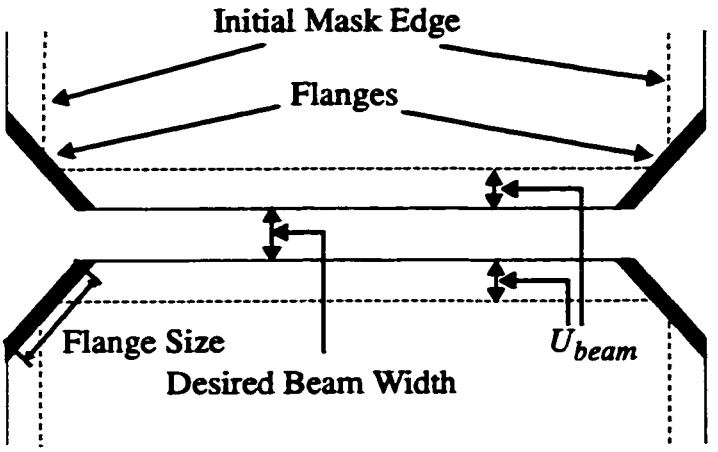

Fig. 5.1: Plan view of the <111> flanges.

Anisotropic etching of silicon is used in an unusual way in this research to achieve beams with square cross-section and flat sidewalls. As discussed in Sec.3.2.1, the pattern is aligned by 45° from the <110> direction to achieve this. The top view of a beam formed this way is shown in Fig.5.1. Since the pattern is rotated by 45° from <110> wafer flat, only the (010) and (001) planes are exposed on all of the sides of each opening in oxide.

The (010) and (100) planes have a local minimum underetch rate (Fig.3.4). Therefore the etch front always terminates at these planes, as long as no other planes with a lower etch rate are exposed. This results in flat, and smooth (100) sidewalls on all of the edges of the etched cavity. However, at the corners where the two (010) and (001) planes intersect, a (111) plane is exposed which has the lowest etch rate (much lower than (100)). Therefore, as shown in Fig.5.1, as the (010) and (001) planes progress in underetching the oxide, a flange-shaped residual mass of Si is left over on both sides of the beam, extending symmetrically on both sides from the original mask corners.

Each flange is formed by slowest-etching (111) planes, extending from the surface of the wafer to the bottom of the cavity. The flange width is a function of the total underetch distance on the sides of the beam and may be calculated as:

$$FlangeWidth = \frac{2U_{beam}}{\cos(45^o)} \qquad \text{Eq.5.1}$$

where U_{beam} is the extent of underetch of the oxide on the sides of the beam. If the wafer is etched from only one side (top or bottom), a {111} flange will be extended outward beginning at the etched side. However, if the beam is etched from both top and bottom simultaneously, a convex edge is formed at the intersection of the {111} planes which extend from top and bottom of the wafer, as soon as the cavity is etched through from both sides (see Fig.5.2a, Fig.5.2b). This convex edge then etches quickly and, provided that sufficient time is allowed, the shape would transform a convex edge, to a vertical wall, and eventually to a concave edge as shown in Fig.5.2b. Therefore the final shape of the flange in this case would be dependent on the etch time after the time the cavity is etched through. The final flange would look like Fig.5.2c provided that sufficient time is allowed for the turned-in (inverted) concave configuration to form.

The total time required for the final inverted edge to form is:

$$T_{total} = \frac{d}{2Rate\{100\}} + \frac{d}{\tan(54.7^{o})}Rate\{011\} \qquad \text{Eq.5.2}$$

where *d, Rate{100}* are the thickness of the wafer and the etch rate of the {100} planes, respectively.

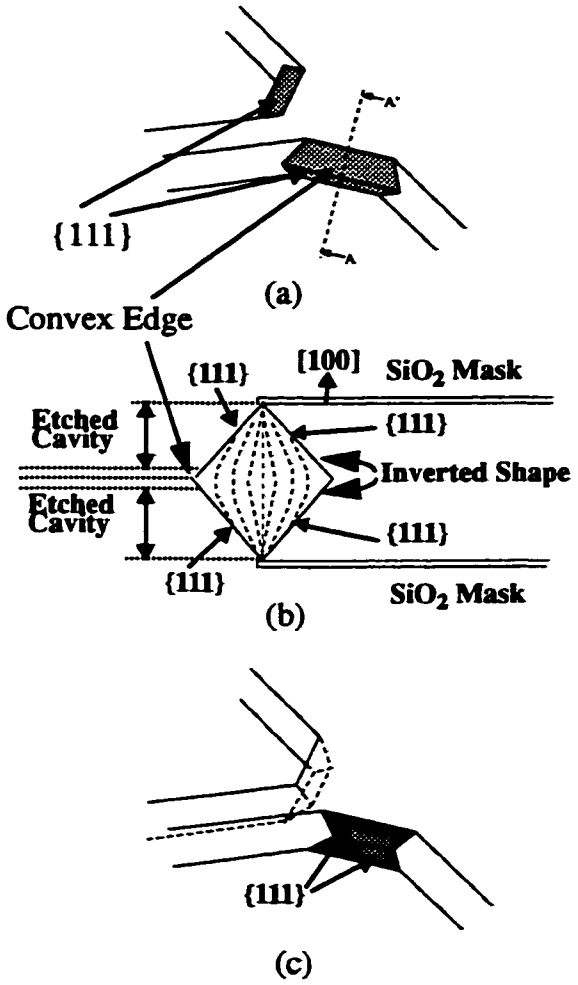

Fig. 5.2: (a) {111} flanges which require compensation. The flanges shown result from etching the wafer from both top and bottom simultaneously. (b) A-A' cross-sectional view of a flange being etched, beginning just before the main cavity is etched through, terminating at the final re-entrant shape bounded by (different) {111} planes. (c) Final inverted edge formed.

Si{110} wafers may be used to achieve beams with vertical side walls [12], but unsymmetric flanges are formes at the two ends of the beam in this case. Although some of the {111}-family planes are perpendicular to the {110} wafer surface, others are inclined at ~35° to the surface, and cause unavoidable unsymmetrical clamping at the two ends of the beam. Even though on a (100) wafer, slowest-etching {111} planes must appear at concave intersections between faster-etching (010) and (001) planes, these {111} flanges subtended from the concave corners at the ends of the beam are symmetric, and can be reduced symmetrically. In order to advance the implementation of the angular rate measurement sensor based on such a silicon beam, a *concave corner compensation technique, to substantially reduce the residual {111} flanges* between two vertical (010)-(001) planes, underetched on a (100) silicon wafer is presented in the rest of this chapter.

5.3 Design and Simulation of Concave Corner Compensation Patterns

Fig.5.3 shows the basic geometry which requires the use of concave corner compensation. The strategy is to design mask patterns which guide the etch-front into the concave corner at the correct rate. A simple representative pattern is depicted in Fig.5.4. A carefully-planned set of rectangles is used, oriented parallel or perpendicular to the wafer flat (parallel or perpendicular to the intersection of {111} planes with the wafer surface), at 45° to the desired underetched vertical (010) and (001) planes. The set of small rectangles is arranged in columns to control the progression of the etch front at the concave corner between the two desired vertical planes. As an example of the time sequence, the boundaries of the underetched regions are simulated in Fig.5.4 as a function of etch time in 25wt% TMAH, using the previously-developed tools of Hubbard *et al* [68,69][1].

1. The graphical simulations were done courtesy of Dr. Ted Hubbard, Dept. of Mech. Eng. of Technical University of Nova Scotia.

At the beginning of the etch, each closed rectangle is etched to termination at intersecting {111} planes. While the sides of the main beam ((010) or (001)) are underetched, the main etch front also progresses into the rectangle pattern by underetching convex corners, beginning with the convex mask corners at points A, B, C, D in Fig.5.5. Because of overlap (Δ) between the rectangles in adjacent columns, the etch sequentially opens each rectangle to the main cavity.

The success of the technique is sensitively dependent on the precise dimensions and placement of the rectangles, which must be designed using exact knowledge of the etch anisotropy of the particular etchant used, in this case TMAH at 25wt%. Critical parameters in designing the pattern are:

. underetch rates of {111} ($U\{111\}$) and {100} ($U\{100\}$) planes,

. angle of deviation, (ϕ), of fast-etch planes from the wafer flat,

. underetch rate of fast-etch planes ($U\{\phi\}$),

. length (L), width (W), row and column separations (S_r) and (S_c),

. length (L_1) and width (w_1) of the last rectangle,

. overlap (Δ) between the rectangles in adjacent columns,

. initial distance (M) from the main etch cavity to the first closed rectangle.

The timing of the progression into the concave corner is controlled based on several principles, outlined below.

(i) When the etch front reaches the base vertices on the outside of a rectangle on an outer column such as points E, F, G in Fig.5.5, it immediately begins to underetch a (010) or (001) plane. Since (010) or (001) etch-fronts at these points will continue to be etched at the same etch rate as the main beam-side, the dimensions must be arranged such that the main etch-front does not reach point F before the point H, does not reach point G before

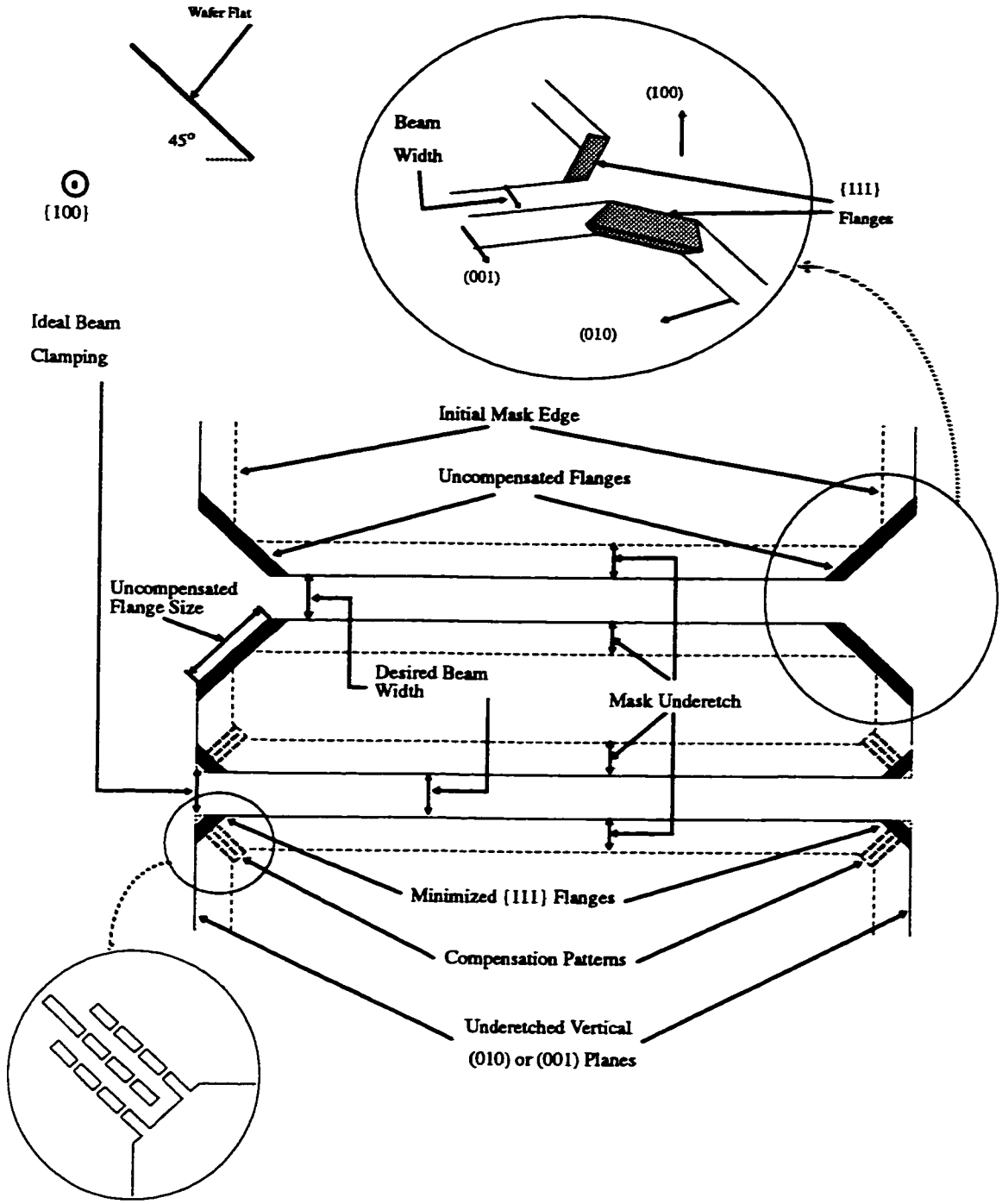

Fig. 5.3: Top : Plan view of {111} flanges (without masking film).
Middle : Top view of uncompensated {111} flanges.
Bottom : Reduced {111} flanges, which require compensation patterns.

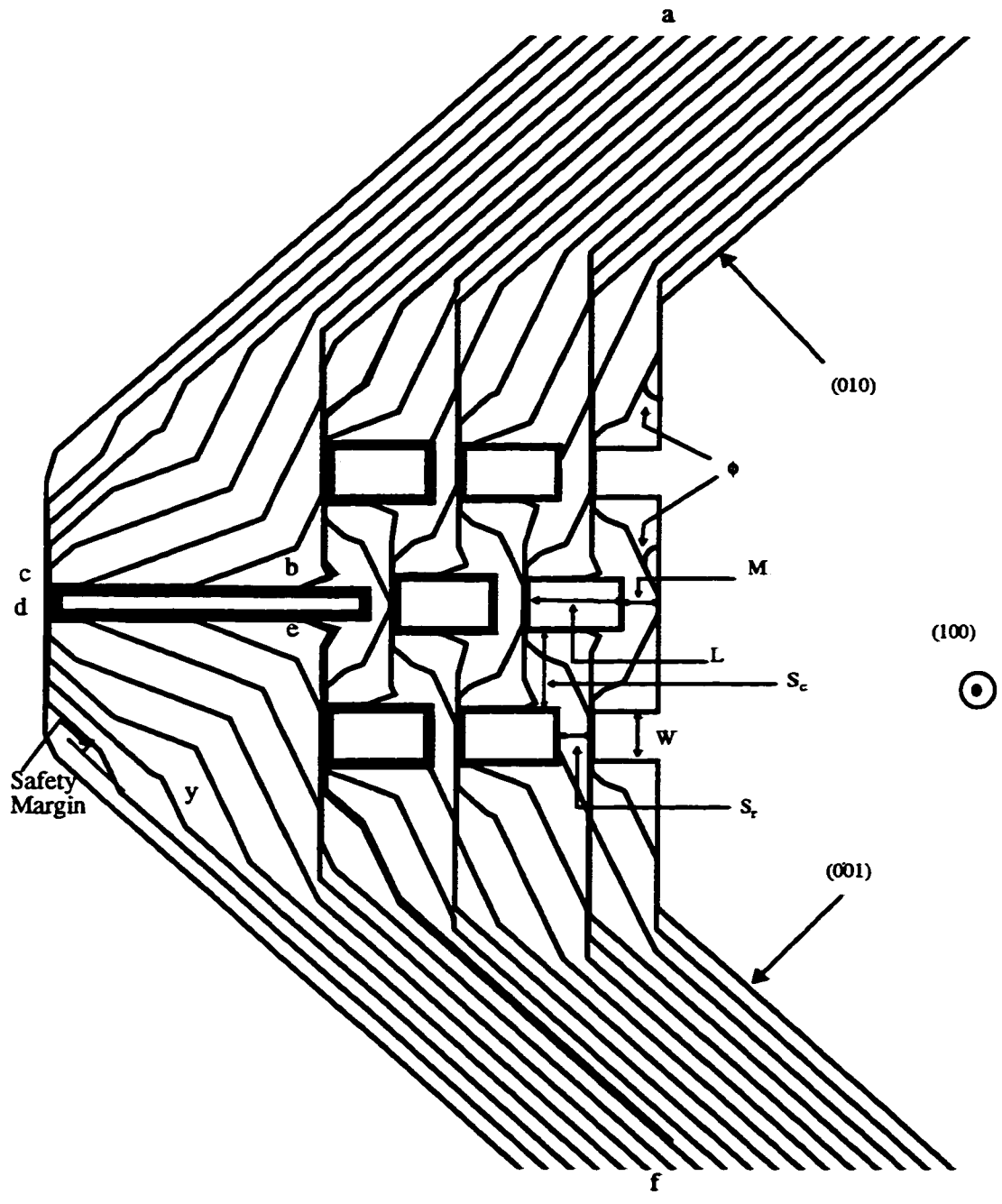

Fig. 5.4: Simulation of etch progress in a representative pattern.

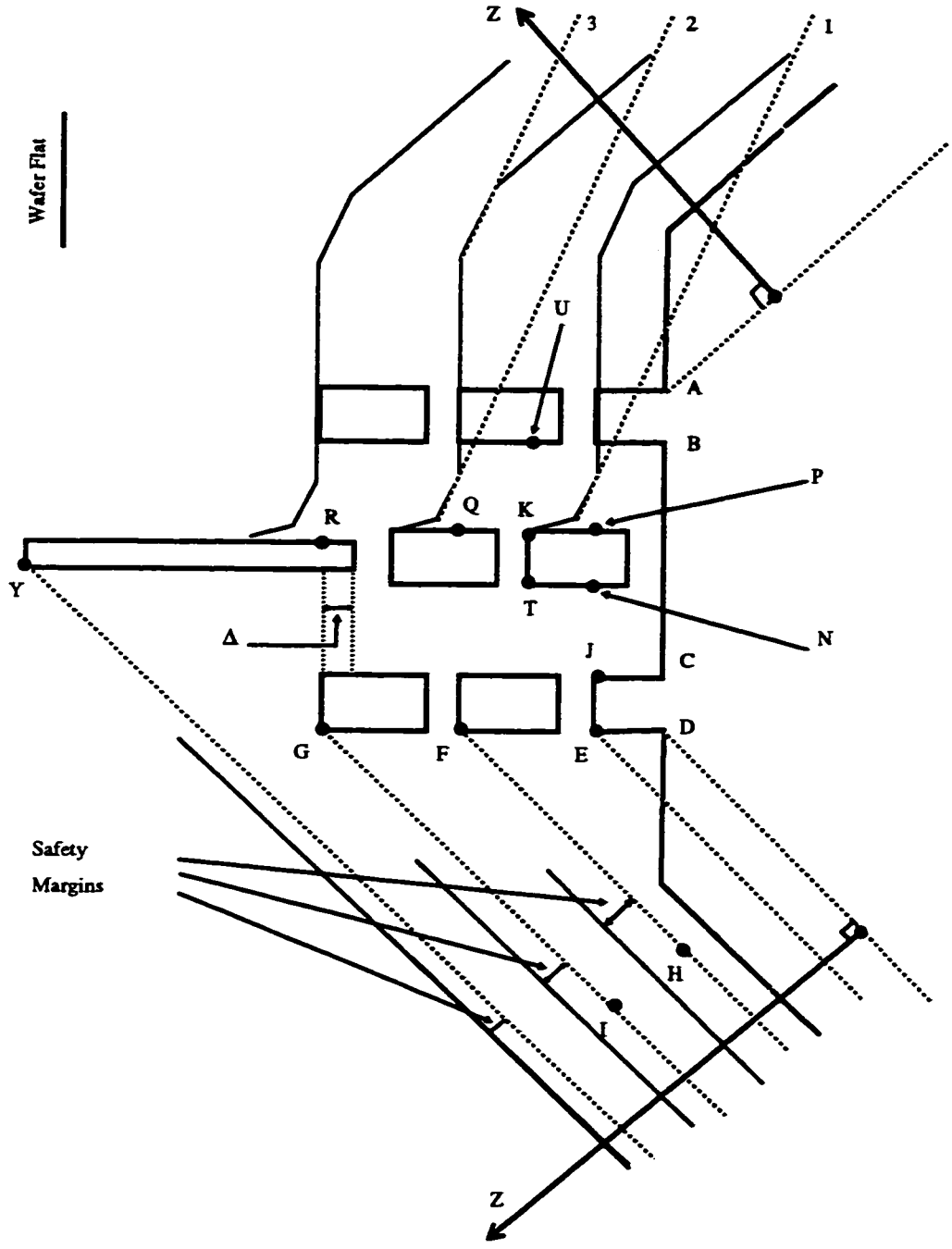

Fig. 5.5: Illustration of pattern design principles.

point I, and so on. The simulation of etch progress in Fig.5.4 shows that the pattern in Fig.5.4, Fig.5.5 satisfy this principle.

(ii) When the etch front reaches the base of any rectangle, it stops at a {111} plane (for example lines EJ or KT). Because they are very slow-etching, such exposed {111} planes widen rapidly, as seen in the sequence in Fig.5.4, but the etch front does not pass this {111} plane until after it has reached the rectangle in an adjacent row, at points such as N, P, Q, R, U in Fig.5.5. For example, JE widens until point N is reached. This timing controls the delay between the opening of each subsequent rectangle.

(iii) When points such as N, P, Q, R, U are reached, convex corners are generated. From these corners, fast-underetch planes proceed rapidly down the sides of the rectangles, and then along the {111} planes at the base of the rectangle, toward the adjacent column. In this way the auxiliary (010) and (001) planes, mentioned in (i) above, are removed.

(iv) After points on the central column such as N, P, Q, R (not U) are reached, the progress of the fast-etch planes indicated by dashed lines 1, 2, 3 at the top of Fig.5.5 is critical. The fast-etch planes progressing outside the outer column must stay ahead of the new fast-etch planes created at the center column. For example, plane 2 must lag behind plane 3. This condition is satisfied by the pattern in Fig.5.4, and Fig.5.5. The separation between adjacent columns is the most important factor affecting this condition. If the separation between the columns were decreased, this condition could become violated.

(v) As the etch continues, the rectangles grow in size due to non-zero underetch rate of {111} planes. This is represented in Fig.5.4 by the later-reached rectangles becoming larger. As a result, the delay between the opening of subsequent rows reduces with the progression of etching.

5.3.1 Detailed Design of the Patterns

The patterns should be designed according to the above mentioned principles to form the final structure within the specified etch time. Therefore, precise knowledge of the movement of etch fronts and timing of the etch progress is necessary.

The progress of the etch in the {111} direction in Fig.5.4 is mainly determined by the rate at which each of the central column of rectangles is opened to the main cavity. Consider the simplified view shown in Fig.5.6. Two etch fronts are generated at point C at the beginning of etching. The geometry of the design determines which one of the two etch fronts (1 or 2) will reach point p first. To find the time required for the etch front to reach from point C to point p, we should first examine the criteria that determine which one of the two fast-etch fronts reaches point p. To do this, one must consider the trajectory of movement of the intersection of the two fast etch planes as the etching proceeds. Since both of the fast-etch planes are travelling with the same speed ($U\{\phi\}$) the trajectory makes an angle of $\theta_1 = 45^o$ with the {111} wafer flat, while the straight line connecting points C to p makes an angle of $\theta_2 = \text{atan}(M/S_c)$ with the wafer flat (as shown in Fig.5.6). Therefore, depending on the relative values of θ_1 and θ_2, either etch-front (1) or etch-front (2) reaches point p.

Once one of the etch fronts (in this case etch-front (1)) reaches point p, another fast etch plane is generated which travels from point p toward point N. The time required for etch front (3) to travel from point p to N is constant regardless of which etch front that has previously originated it (etch front (1) or (2)).

Using some trigonometry, the total time required to reach from point C to N can be calculated as follows:

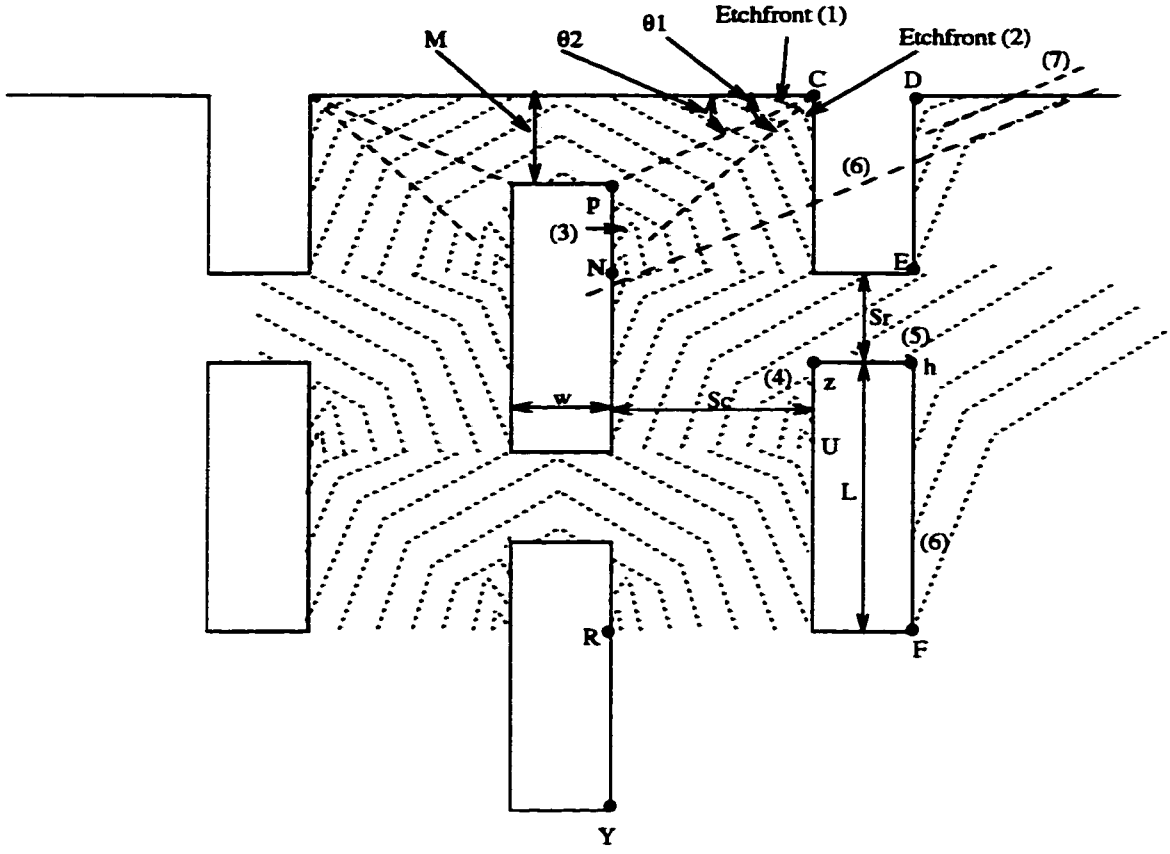

Fig. 5.6: Etch progression of a representative pattern.

For $\theta_1 \geq \theta_2$:

$$Time_{C_P} = \frac{\sqrt{S_C^2 + M^2}\cos\left(\phi - \text{atan}\left(\frac{M}{S_c}\right)\right)}{U\{\phi\}} \qquad \text{Eq.5.3}$$

For $\theta_2 \leq \theta_1$,

$$Time_{Cp} = \frac{\sqrt{S_c^2 + M^2}\sin\left(\phi + \text{atan}\left(\frac{M}{S_c}\right)\right)}{U\{\phi\}} \qquad \text{Eq.5.4}$$

Then for both cases:

$$Time_{pN} = \frac{\frac{L - S_r}{2}\sin(\phi)}{U\{\phi\}} \qquad \text{Eq.5.5}$$

$$Time_{CN} = Time_{Cp} + Time_{pN} \qquad \text{Eq.5.6}$$

Where S_C, M, L, S_r are geometrical values shown in Fig.5.4, and $U\{\phi\}$ and ϕ are the underetch rate of fast etch planes and their deviation angle with {111} plane respectively.

The mechanism of progression of the etch front from one rectangle to another in the adjacent rows, such as point N to z, is the same as mentioned above. At point z, two sets of fast etch planes are generated (4 and 5), which travel toward points U and h respectively. Progression of fast etch plane (4) from z to H is similar to what described above for progression of plane (3) from point p to N. Consequently the required time may be calculated in a similar way. The time required for the etch front to reach from point N to U may be calculated similarly as follows:

For $\text{atan}\left(\frac{S_r}{S_c}\right) \geq \theta_1$

$$Time_{Nz} = \frac{\sqrt{S_c^2 + S_r^2}\cos\left(\phi - \text{atan}\left(\frac{S_r}{S_c}\right)\right)}{U\{\phi\}} \qquad \text{Eq.5.7}$$

For $\text{atan}\left(\frac{S_r}{S_c}\right) \leq \theta_1$

$$Time_{Nz} = \frac{\sqrt{S_c^2 + S_r^2}\sin\left(\phi + \text{atan}\left(\frac{S_r}{S_c}\right)\right)}{U\{\phi\}} \qquad \text{Eq.5.8}$$

Then for both cases:

$$Time_{zU} = Time_{pN} \qquad \text{Eq.5.9}$$

$$Time_{NU} = Time_{Nz} + Time_{zU} \qquad \text{Eq.5.10}$$

Also from the symmetry it is clear that all subsequent etch times from one row to another will be equal to $Time_{NU}$.

Using the above equations it is possible to predict the time at which each one of the rows are opened and therefore the time at which the etch front reaches each of the points C, z,.... To check the first principle, however, we have to find the times when the etch front reaches to points E, F,... Note the etch fronts created at point D. At the same time with progression of etch-fronts (1) and (2) another etch front that is generated at the convex corner at point D will progress toward E. The time required for this fast etch front to reach from D to E may be calculated as:

$$Time_{DE} = \frac{M + \frac{L - S_r}{2}}{U\{\phi\}}\sin(\phi) \qquad \text{Eq.5.11}$$

As the etch continues, and the second row opens up, etch front (5) generated at point z travels toward right until it reaches to point h. From there it generates a new etch front (6) which continues travelling toward right until it reaches the other corner of the rectangle at point F. The time required for the etch front to reach from point z to F may be calculated as follows:

$$Time_{zF} = \frac{w\sin(\phi) + L\sin(\phi)}{U\{\phi\}} \qquad \text{Eq.5.12}$$

The total time required (from the start of etch) for the etch front to reach to point F and generate the second {010} plane can therefore be calculated as:

$$Time_{CF} = Time_{CN} + Time_{Nz} + Time_{zF} \qquad \text{Eq.5.13}$$

Similarly the time at which all subsequent {010} planes are generated may be calculated. Having the above mentioned times at which the {010} planes are generated in a design and knowing the etch rate of the {010} planes, it is possible to compare the relative location of each newly generated {010} plane with respect to the location of the beam's {010} etch front. This may be used to design the patterns such that they satisfy principle (i) in Sec.5.3.

To satisfy the principle (iv) the relative location of fast etch fronts generated at points D, N, R, ... should be checked. Consider the two fast etch planes (6) and (7) shown in Fig.5.6, the principle is satisfied only if fast etch plane (6) generated at point N is ahead of fast etch plane (7) generated at point D as shown in the figure. The same condition

should be true between fast etch plane (6) and the fast etch plane that is generated at point R (not shown on the figure) and so on. The criteria may be formulated as follows:

For the first row:

$$Time_{CN} > \frac{\left(M + \frac{L - S_r}{2}\right)\cos(\phi)}{U\{\phi\}} \qquad \text{Eq.5.14}$$

For the second row:

$$Time_{NR} > \frac{(L + S_r)\cos(\phi)}{U\{\phi\}} \qquad \text{Eq.5.15}$$

The condition is checked for all of the rows the same way. Usually if the condition is met for the second row onward, it will hold for the first row as well. Having the above equations it is possible to design the required set of rectangles such that they satisfy both sets of criteria.

The last rectangle in the center column is designed to bring the etch to its final shape with the smallest possible residual flange. The fast-etch planes (1) and (2) propagating from point e to d in Fig.5.7 must be allowed to die off. During this time the (010) planes are progressing and the {111} plane at the base of the last rectangle is widening. The auxiliary (010) plane generated at the bottom of the last rectangle should be as close as possible to the main beam's (010) plane without falling ahead of it. Therefore, it is brought to within a certain safety margin as shown in Fig.5.4, Fig.5.7. This safety margin is also depicted at the bottom left of Fig.5.5. This case represents the minimum attainable flange width. Of course, the safety margin must be as small as possible because it causes asym-

metry in the fast-etch planes, shown at point *y* in Fig.5.7, which must be allowed to die off, and the {111} flanges widen while this happens. The minimum obtainable flange width depends on ϕ, Δ, $U\{100\}$, $U\{\phi\}$, and the length and width of the cavity of the last rectangle, at the time that the main etch front reaches it. In practice, this will be determined by {111} underetch rate, duration of etch, photolithographic minimum feature size, and alignment accuracy.

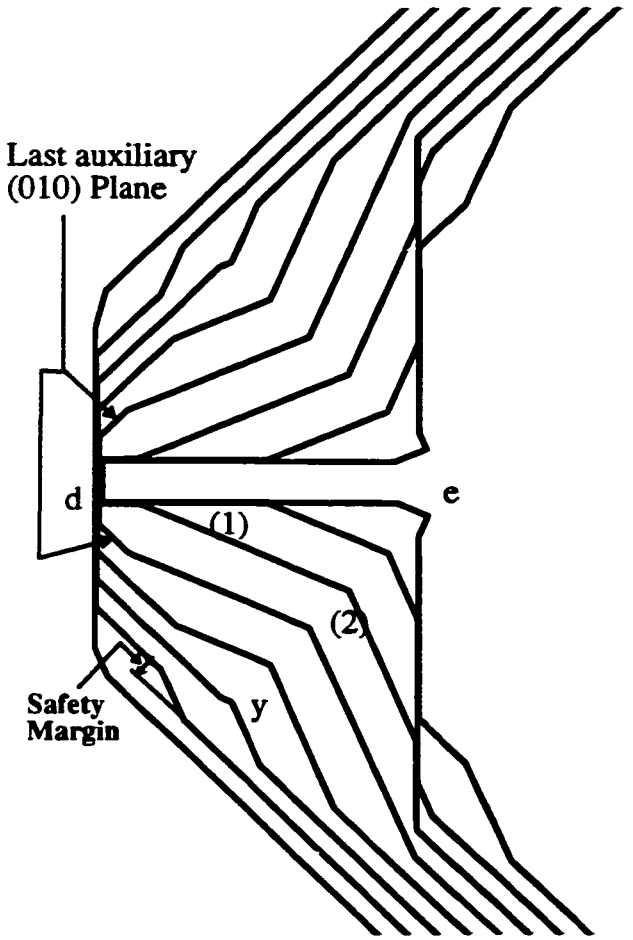

Fig. 5.7: Etch progress from the last rectangle.

The final width may be calculated as follows:

$$W_f = w_1 + 2\left(L_1 - \frac{(L - S_r)}{2}\right) \times \frac{(\cos(\phi) - \sin(\phi))\, U\{100\}}{U\{\phi\} \sin(45^O) - U\{100\} \sin(\phi)} + 2\frac{Margin}{\cos(45^O)} \qquad \text{Eq.5.16}$$

Also the total time from point C to the conclusion of the etch:

$$Time_f = Time_{CR} + \frac{\left(L_1 - \frac{(L - S_r)}{2}\right) \times \sin(45^O) \cos(\phi) - \frac{U\{100\}}{U\{\phi\}} \sin^2(\phi)}{U\{\phi\} \sin(45^O) - U\{100\} \sin(\phi)} \qquad \text{Eq.5.17}$$

Where $Time_f$, W_f, L_1, $Margin$, and $U\{100\}$ are the final time, final width of the {111} flange, length of the last rectangle, last safety margin and etch rate of {010} sidewalls respectively.

One assumption that has been made so far is that the small rectangles will be etched to termination at {111} planes shortly after etch begins and will not etch any further until they are opened to the main cavity. This ideal scenario is true only if the ratio of the etch rates of {100} planes to {111} planes is very high. In other words, the anisotropic etchant should have a very good selectivity for {100} planes vs. the [111} planes. In the case of TMAH 25%, which is the etchant used in this research, this is barely true. The etch rate ratio $ER\{100\}/ER\{111\}$ is around 1/23 [67] which is not negligible for the geometries used in this research. As a result of the non-zero etch rate for {111} planes, the rectangles grow in size as the etching proceeds, thus shortening the spacing between them and consequently the time required for the etch front to travel from one column to the next. To take this into account the spacing between the rectangles (S_c, S_r) and also the size of the rectangles (w, L) are recalculated after each row of rectangles is opened (For example, there are 4 rows of rectangles depicted in Fig.5.6). Then the required time to open the next row is calculated using these new parameters. We have:

$$S_{r_{i+1}} = S_{r_i} - 2Time_i \times ER(111)$$

$$S_{c_{i+1}} = S_{c_i} - 2Time_i \times ER(111)$$

$$w_{i+1} = w_i + 2Time_i \times ER(111)$$

$$L_{i+1} = L_i + 2Time_i \times ER(111)$$

Where S_{r_i} and S_{c_i} specify the separation between the rows and columns for ith row, $Time_i$ is the time required to open ith row, and L_i and w_i are the length and width of the rectangles in ith row respectively.

5.3.2 Numerical Simulation

A numerical simulation program has been implemented (see Appendix II), using geometrical relations based on the above principles and equations, to predict the progression of the etch for a given set of rectangles. Fig.5.8 is a sample output, which shows the timing of the main etch front reaching certain points in Fig.5.5. The vertical axis gives the position of various points in the etch projected onto one of the axes marked Z in Fig.5.5, perpendicular to the (010) or (001) planes. The dashed straight line in Fig.5.8 represents ideal timing such that these points are reached in synchrony with the main etch front. The actual timing must not cross above this line due to principle (i). Therefore some tolerance must be designed into this pattern, to account for non-idealities such as etchant concentration, photolitographic line width and alignment tolerances, and patterning defects, which may lead to uncertainty in actual etch timing. The above outlined principles are used to bring the etch front to the line *abcdef*, which is highlighted in Fig.5.4. The last rectangle is designed to obtain the optimum safety margin.

Different available parameters may be changed and the results checked until the desired curve, which results in the required final beam size and satisfies all criteria, is

obtained. Once the desired design is obtained, the program generates an standard CIF file for the layout of the patterns. This file may be imported into other tools to generate the actual mask.

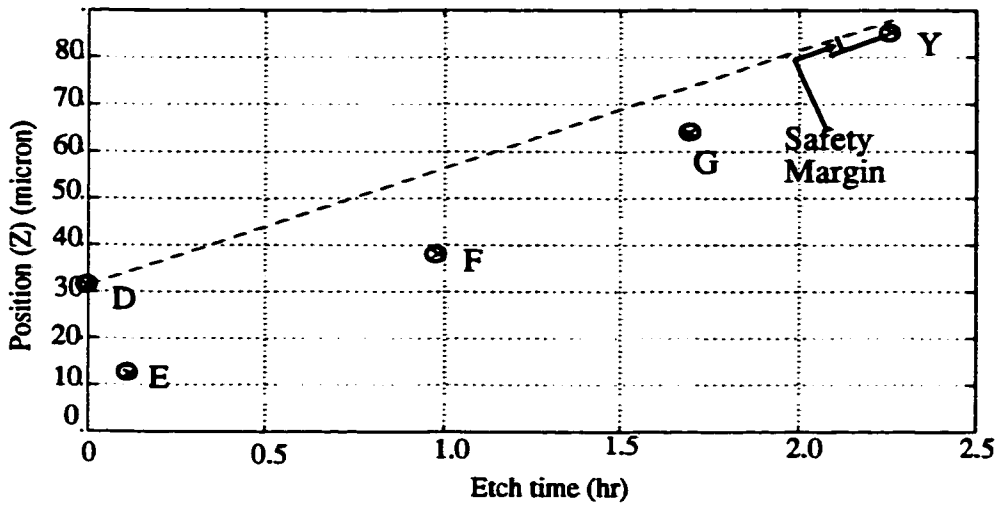

Fig. 5.8: Numerical simulation of etch progress

5.3.3 Graphical Simulation

Graphical simulation of the patterns were done courtesy of Dr. T. Hubbard (see footnote of page 102) using a simulation program [68,69]. Fig.5.9 shows a full graphical simulation of an optimized pattern, using a minimum feature size (rectangle width) of 5 μm, to underetch a distance of 100 μm in the (010) and (001) directions. The {111} flange width has been reduced from ~290 μm to ~40 μm, a factor of ~7.25 times smaller.

Results obtained from graphical simulation matches the predicted results of the numerical simulation with a good accuracy. The time at which each of the rectangles are opened up to the main front etch (points D,E,F,G, and Y), and the total etch time required

for the beam to form are predicted with an accuracy of better then 0.2 hr. The final flange size is also predicted with an accuracy of better than 15μm.

The results obtained from numerical simulation are compared with the graphical simulation for the design simulated in Fig.5.8 in Table 5.1. The time at which each of the points D, E, F, G, Y are reached during the etch are compared for Numerical and Graphical simulations. The underetch of the main beam at any time is also shown in the table. The total time required for the etch to conclude is compared in the last row for numerical and graphical simulations. The predicted final flange size by numerical simulation is 60.3 μm which matches with the value of ~75 μm obtained from the graphical simulation within acceptable tolerances.

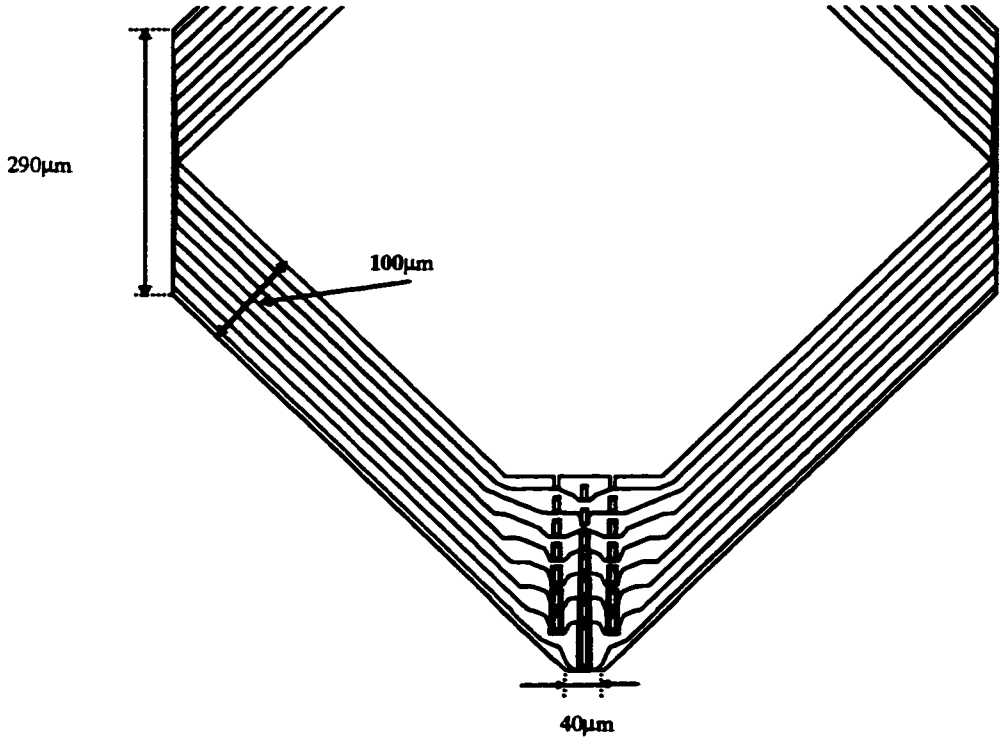

Fig. 5.9: Optimized 5μm pattern simulated.

Points	Time Num. Sim.	Time Graph. Sim.	Under Etch
D	0	0	0
E	0.12 hr	0.15 hr	3 μm
F	0.99 hr	1.1 hr	24 μm
G	1.70 hr	1.8 hr	41 μm
Y	2.26 hr	2.45 hr	55 μm
Conclude	3.23 hr	3.41 hr	77 μm

TABLE 5.1: Numerical and graphical simulation results compared.

5.3.4 Secondary Patterns

If lithography and process constraints allow, one can improve the pattern by adding a secondary set of smaller rectangles at the tip of the concave corner. These smaller rectangles replace the last long rectangle in the optimum pattern described above.

The secondary set should in general be designed following the same principles as outlined above. However, in practice this may be more difficult, due to the following constraints:

(1) the obtainable residual flange is smaller than with the larger patterns, and thus there is less design flexibility in the choice of spacings (S_r, S_c).

(2) Due to the non-zero under-etch rate of {111} planes, the actual sizes of the rectangles grow larger than the designed sizes during the etch. This limits the effective minimum size of the rectangles at the time that the main etch front reaches them.

(3) The etching of the smaller rectangles (from when they are first opened to the main cavity until the completion of the etch) occurs very rapidly. Therefore satisfying some of the design principles is more constrained.

The graphical simulation of the etch progress of a sample pattern is shown in

Fig.5.10. The design shown in Fig.5.10 is graphically simulated in Fig.5.11 with a secondary set of patterns replacing the last rectangle. In this design, the feature size for the small rectangles was limited to 2.5 micron. As seen in the figure, the fast etch plane created by the first row of the secondary patterns is not removed as the etch continues. The reason is that principle (iv) (Sec.5.3) could not be satisfied for the secondary patterns due to above mentioned limitations. In this case the final flange size and the completion of etch is limited by the movement of this fast etch plane. However, the resulting final flange size is smaller than the original design by a factor of x1.5 in this case.

Equations Eq.5.16 and Eq.5.17 may be revised to predict the total etch time and the final flange size for this kind of design:

$$t_f = \frac{U\{100\}\,T_d \sin(\phi) - \sin(45^o)\cos(\phi)\,L_2}{U\{100\}\sin(\phi) - \sin(45^o)\,U\{\phi\}} \qquad \text{Eq.5.18}$$

$$w_f = w_2 + 2(t_f - T_d)\frac{U\{100\}}{\sin(45^o)} + 2\frac{Margin}{\cos(45^o)} \qquad \text{Eq.5.19}$$

where T_d is the total time delay between the time when the fast etch plane is generated (etch front at point A in Fig.5.11) and the time when the last auxiliary (010) plane is generated (etch front reaches point B in Fig.5.11). L_2 is the vertical distance between the two points A and B, and w_2 is the width of last rectangle on the secondary patterns.

The numerical simulation program checks the validation of principle (iv) for each row of the secondary design to find point A at which this principle is violated. Then the values of L_2 and T_d can be calculated.

The optimum pattern shown in Fig.5.9 may also be improved by adding a secondary

set of smaller rectangles at the tip of the concave corner. An example of such a design is shown in Fig.5.12a, and is simulated in Fig.5.12b. The smallest rectangles are 1x1 μm in size in this case and the {111} flange has been reduced to ~18μm for a reduction of ~16 times (and an improvement of x2.21 compared to the original pattern). As seen in Fig.5.12b, in an etch of such a substantial duration, with a {111} underetch rate of ~1 μm/ hr, the cavities of the smaller rectangles have noticeably widened by the end of the etch, significantly affecting the minimum attainable flange width.

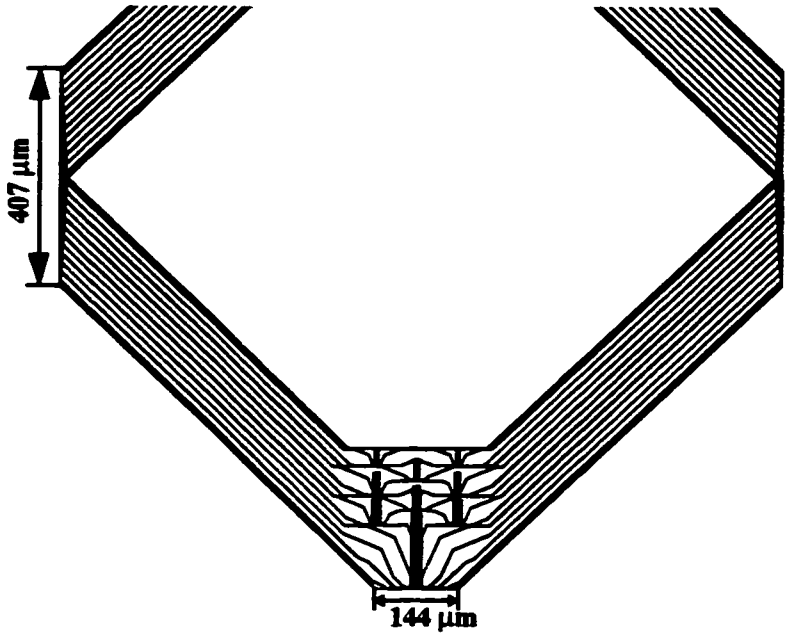

Fig. 5.10: Simulation of the etch progress for a design with one set of patterns.

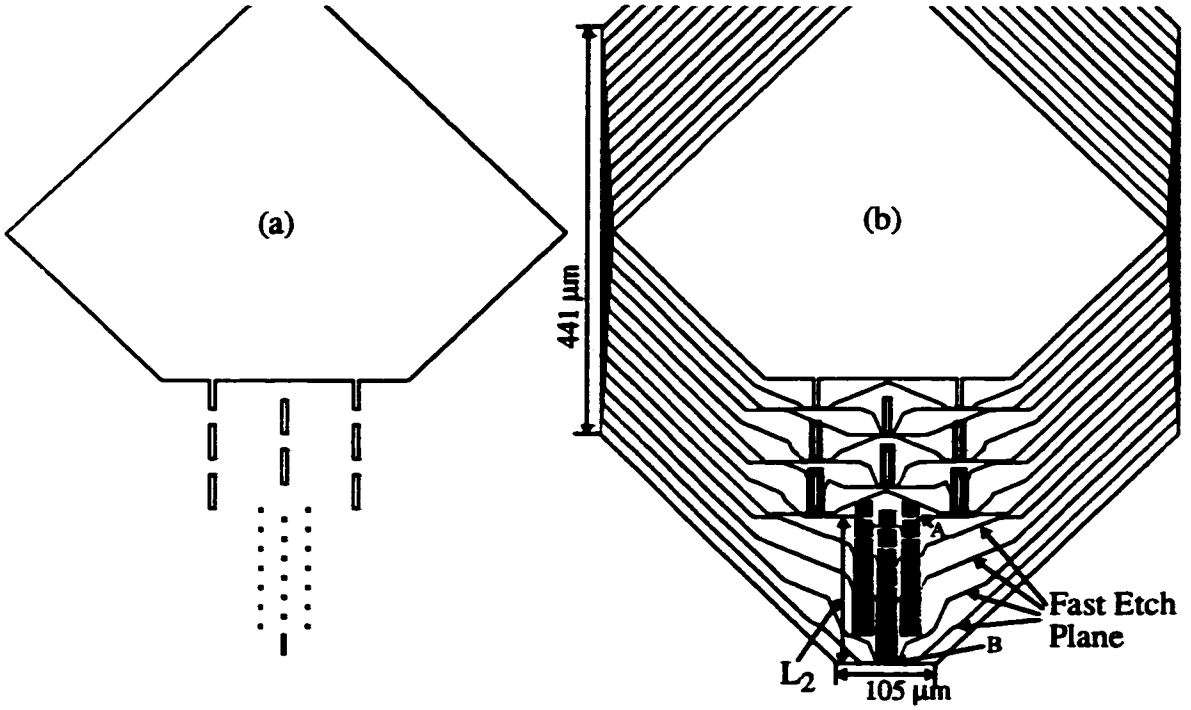

Fig. 5.11: (a) Design of Fig.5.10 modified by removing the last rectangle and adding a secondary set of rectangles. (b) Graphical simulation of the etch progress for this modified design.

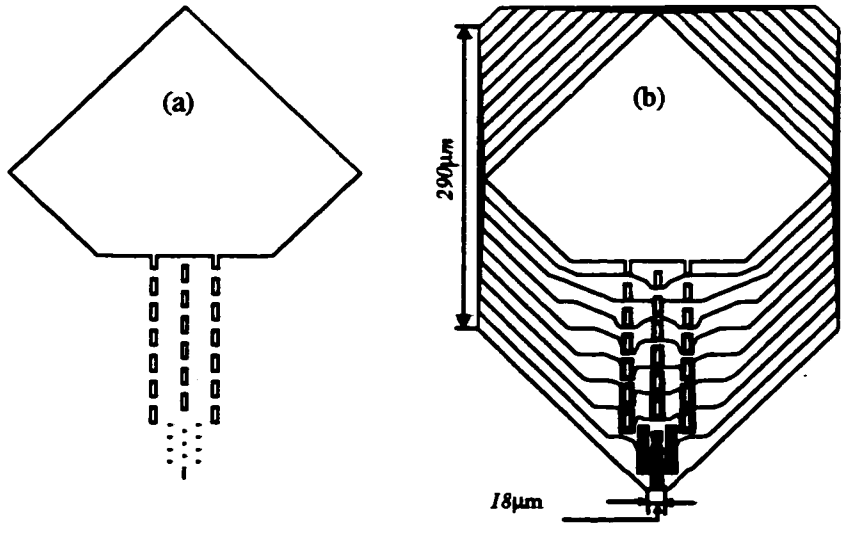

Fig. 5.12: (a) pattern with secondary 1µm set. (b) Simulation of the pattern.

Much better reduction rates may be obtained by using an etchant having better {100}/{111} anisotropy, (lower relative under-etch of {111} planes).

5.4 Chapter 5 Summary (Contributions are indicated by ✱)

. The formation of flanges at the two ends of the beam during the fabrication of the beams is discussed.

✱ A beam with vertical sidewalls is achievable on a Si{100} wafer, but residual {111} flanges are an unavoidable side-effect at the concave corners at both ends of the beam.

✱ By etching from both sides of the wafer these {111} flanges can be turned inward, creating a re-entrant structure, also terminated by {111} planes.

. Concave corner compensation patterns are designed in order to reduce the size of the flanges. The design of the patterns, etch progress of the patterns, and the parameters and principles involved in successful design of such patterns is discussed in detail.

✱ Motivated by the need for symmetric clamping at the ends of the beam, in order to achieve a small enough mismatch between beam resonant frequencies in vertical and horizontal directions, a scheme of concave corner compensation patterns is devised, in order to substantially reduce the size of the residual {111} flanges.

✱ The success of the technique is sensitively dependent on the precise dimensions and placement of the rectangles, which must be designed using exact knowledge of the etch anisotropy of the particular etchant used, in this case TMAH at 25wt%. Critical parameters in designing the pattern are:

. underetch rates of {111} (*U{111}*) and {100} (*U{100}*) planes,

- angle of deviation, (ϕ), of fast-etch planes from the wafer flat,
- underetch rate of fast-etch planes ($U\{\phi\}$),
- length (L), width (W), row and column separations (S_r) and (S_c),
- length (L_1) and width (w_1) of the last rectangle,
- overlap (Δ) between the rectangles in adjacent columns,
- initial distance (M) from the main etch cavity to the first closed rectangle.

* A numerical simulation program is developed to track the progress of the etch through the rectangles. Several sets of patterns were designed using the numerical simulation tool and simulated using a graphical simulation tool.

* The design principles are explained in detail and numerical simulation program is developed to track the progress of the etch fronts through the pattern of rectangles.

* The minimum obtainable flange width depends on width (w_1), Length (L, L_1), safety margin (*Margin*), and separation of rows (*Sr*) in the designed patterns. It also depends on the deviation angle of the fast etch planes (ϕ), and the ratio of the etch rate of {010} planes to the etch rate of fast etch planes ($U\{100\}/U\{\phi\}$) which are properties of the anisotropic etchant used.

* Several types of patterns are examined with a single set of rectangles and improved by the addition of a second set of smaller rectangles.

* The etch progress in the patterns is simulated using a graphical simulation tool

and the results match very well with the numerical simulation results.

* For a beam with dimensions of ~100μm x ~100μm, a minimum flange width of ~40μm (reduction ratio ~7.25) is obtained using a single set of patterns (having a feature size of 5μm) using graphical simulation. This was improved to a minimum flange width of 18μm by using a secondary set of patterns (reduction ratio of ~16) with a feature size of 1μm.

CHAPTER 6

Experimental Fabrication, Testing and Results

6.1 Introduction

The fabrication of the experimental test structures, testing and results are discussed in this chapter. The practical context of the steps to completion of a fully functioning angular rate measurement sensor is discussed first, followed by an overview of the experimental proof of concept tests done in this research. Fabrication of test beam structures with precise dimensions and vertical sidewalls is presented and experimentally tested. The concave corner compensation patterns are experimentally tested and the results are compared with the numerical and graphical simulation results from Chapter 5. The operation of the test beam structures is tested both in regular air pressure and reduced pressure environments. Several important mechanical characteristics of the beams are obtained from the experiments and compared with the predicted results from theory and simulation. The fabrication process of a complete sensor structure is discussed next, followed by the experimental results of the fabricated sensor. The electrical and mechanical characteristics of the sensor structures obtained from theory are then related back to the model developed in Chapter 4 and the model is simulated again to predict the output of the sensor considering all of the measurement results.

6.1.1 The Practical Context: Steps to Completion of a Functioning Micro-Gyroscope Rotation Sensing System.

The achievement of a fully-functioning micro-gyroscope system is a very ambitious project, beyond the scope of this thesis. However, the experiments and analyses done in this thesis should be seen in light of the full practical context of the project. Therefore,

below is listed an outline of the steps that would have to be taken in order to achieve a fully functioning practical micro-gyroscope system.

1- The sensor would have to be designed, considering all different design and operation issues involved.

2- A complete model would have to be built for the sensor to simulate both mechanical and electrical components of the system at the same time. The model should include the linear and non-linear characteristics of the system.

3- The beams would have to be fabricated with excellent match between the two dimensions, with smooth vertical side walls, and with sharp edges. The effects of different etching conditions (temperature, concentration, impurities) on the final results would have to be considered. Different processes (single-sided or double-sided) would have to be investigated in order to find the most suitable process. The non-uniformity of the dimensions along the length of the beam would have to be considered and minimized as much as possible.

4- The beams would have to be characterized in order to find the natural frequency, damping, and coupling.

5- The beams would have to be anodically bonded to the glass and the effects of stresses induced by anodic bonding on the characteristics of the beams would have to be investigated.

6- The sensing mechanism for sensing the vibrations in the actuation direction would have to be tested. The oscillator circuit and the Automatic Level Control (ALC) feed back loop would have to be designed and implemented. This circuit would have to be tested practically with the micromachined beams. Many adjustments would have to be made to the circuit, based on the results of the practical tests. This is because of the uncertainties

that exist in the modeling of the beams. It has been often found in the study of the microstructures that the physical/mechanical properties are different from those that would be predicted from macroscopic studies. This makes the operation of the actual microstructure very hard to model without extensive experimental tests. Factors such as damping, coupling, stresses induced in the structure from clamping points, parasitic capacitances, and noise are usually different in the actual system compared to what is produced in the models.

After optimizing the circuit based on the experimentally characterized system, it should be possible to generate vibrations with the required amplitudes along the actuation direction.

6- The capacitive detection circuitry, required for the detection of the vibrations in the sense mode, would have to be implemented and tested. Again the tests would have to be carried out with the actual fabricated beams in order to take into account all of the parasitic effects, and noise. The noise level at the output of this circuit is the limiting factor which determines the final resolution of the device, therefore it would have to be optimized in order achieve the lowest noise level.

7- The amplifier, A/D converter and digital signal processing circuits required to filter and demodulate the output signal would have to be designed and tested. If the demodulation is done in the analog domain then the required analog filters and demodulators would have to be built and tested.

8- The entire sensing and signal conditioning block (depicted in Fig.3.33) would have to be tested with the beams. Integrating the analog and digital circuits on one chip will introduce additional problems such as additional noise to the analog part that would have to be overcome. As mentioned before, the output signal of the detection circuit has a very low amplitude and therefore is very noise-sensitive. Therefore, any additional noise

induced by other parts of the circuitry would have to be removed as much as possible.

9- The entire gyro, including the actuation and sense circuitry, would have to be tested at stationary conditions. The Zero-Rate-Output of the sensor may be investigated at this step.

10- The sensor would have to be situated on a specially-designed rotating plate with slip rings (in order to maintain electrical contact during the rotation) in order to extract the required signal outputs. The output signal of the sensor may be then monitored as the plate is rotated with various angular rates.

11- Packaging is usually a major problem with any kind of vibrating micromachined sensors (Gyros, Accelerometers, Force sensors, Pressure Sensors) since a vacuum or reduced pressure environment is usually required. Problems with packaging of the sensor would have to be solved. Also, stresses induced in the structure by packaging are among the parameters that would have to be considered.

6.1.2 Proof-of-Concept Experiments

The experimental work done in this thesis consists of experiments and analyses which will be useful within the full practical context outlined above in Sec.6.1.1. The experimental strategy is briefly outlined as follows:

(a) The method explained in Sec.3.2.1 to obtain beams with smooth vertical sidewalls and precise dimensions using anisotropic etching in TMAH is experimentally tested. Beams with very smooth vertical sidewalls, sharp edges, and precisely controlled dimensions are fabricated and characterized.

(b) The concave corner compensation patterns are experimentally tested to fabricate beams with flanges that are substantially reduced in size, to improve the performance of

the sensor.

(c) The fabricated beam structures are bonded to glass using anodic bonding to form test structures. These test structures are then mechanically tested to find parameters such as natural frequency in the horizontal and vertical directions, quality factor in the horizontal and vertical directions, induced EMF, non-linear characteristics, and mismatch both in regular air pressure and reduced air pressure environments. The experimental results are then compared with the results from theory and the simulation model developed in Chapter 3.

(d) Complete sensor structures, same as the one shown in Fig.3.1, are fabricated and tested to find the electrical parameters (the parameters shown in the equivalent electrical model in Fig.3.25) and mechanical parameters. The Zero-Rate-Output of the sensor is then measured under various actuation levels and compared with the results obtained from the simulation in order to find the equivalent coupling factors (K_C and K_W).

(e) The effect of the flange size reduction on mismatch is experimentally tested.

(f) The overall model of the sensor is then reconsidered in light of the experimental results and an approximation for the expected output of the sensor under various angular rate inputs is given based on simulation results.

6.2 Fabrication of Beams with Square Cross-Section

The first step toward the implementation of the designed gyro is the fabrication of beams with closely matched natural frequencies in vertical and horizontal directions using <100> Si wafers. The method explained in Sec.3.2.1 had to be tested and verified experimentally to obtain uniform beams with the desired dimensions, and smooth vertical sidewalls. The fabrication process followed to fabricate experimental beams for this purpose is as follows:

1- A mask was designed for the beams with a length of 1cm and final width of ~100μm (Fig.6.2). The original width of each beam pattern on the mask was chosen as follows (for a process where the wafer is simultaneously etched from both sides):

$$W_m = W + 2\left(\frac{T_{nom} + \Delta T_{max}}{2}\right) + Mask_{tol} = 2\left(T_{nom} + \Delta T_{max}\right) + Mask_{tol} \qquad \text{Eq.6.1}$$

where W_m is the width of the beam pattern on the mask, W is the desired width of the beam, T_{nom} is the nominal thickness of the wafer, ΔT_{max} is the maximum tolerance in the thickness of the wafer, $Mask_{tol}$ is the Maximum tolerance of the in-house mask-making technique used to fabricate the masks.

In order to obtain beams with closely-matched dimensions (width & thickness) the final width of the beams (W) should be set equal to the thickness of the wafer which is $T_{nom} + \Delta T_{max}$ in the worst case. The wafers usually have a tolerance of $\pm 5\mu m$ or $\pm 10\mu m$ ($\Delta T_{max} = 10\mu m$). The in-house process used to build the masks usually has a tolerance $\pm 25\mu m$ which has been considered in designing the mask patterns as $Mask_{tol}$ parameter ($Mask_{tol}$=25μm).

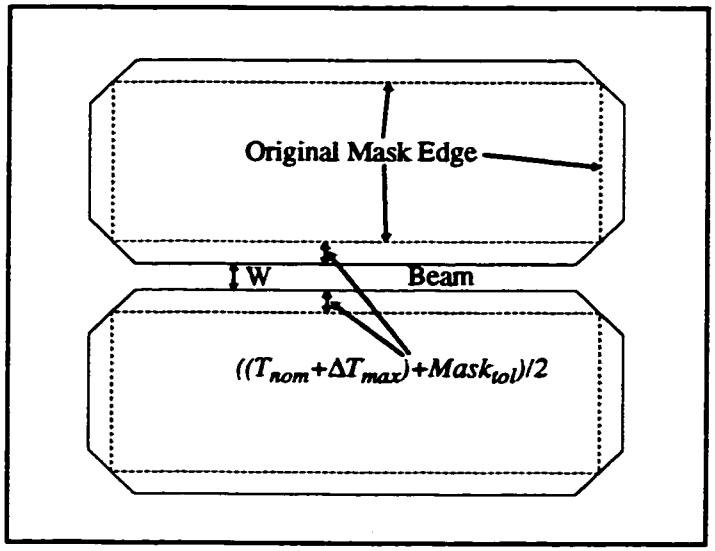

Fig. 6.1: Tolerances considered in the design of the mask pattern.

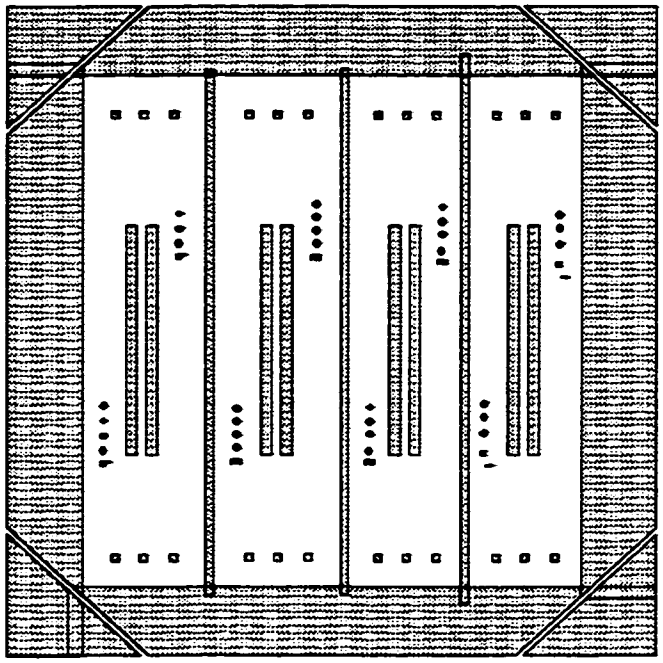

Fig. 6.2: Overview of the mask used to fabricate beams.

2- Several samples were cut out of special double side polished <100> P-type wafers with nominal thickness of 100μm. The samples were cut into squares 25mm x 25mm, with sides aligned parallel or perpendicular to the <110> wafer flat.

3- The samples were cleaned using the cleaning procedure (Appendix III).

4- A thermal oxide layer with the thickness of 1500 Å was grown on the samples by dry oxidation at 1100 ^{o}C.

5- One side of the samples was patterned by photolithography procedure using the previously prepared design mask. The <110> sides of the samples were aligned with 45^{o} with respect to the beam patterns to achieve vertical sidewalls.

6- The second side of the samples was protected by photoresist and then the patterned side was etched in BOE (1 HF : 6 NH_4F).

7- The photoresist was stripped from the samples followed by another cleaning step (without HF dip).

8- The second side of the samples was patterned using the mirror image of the first mask. A double side mask aligner instrument with infrared camera was used to align the pattern with the original pattern on the first side of the sample.

9- The first side of the samples was protected by photoresist and the second side was etched in BOE to open the windows in the oxide.

10- The photoresist was stripped from the samples.

11- The samples were then etched in TMAH 25% using the two step etch procedure explained in Sec.3.2.1 to obtain the beams with required thickness. The two etch steps were performed at 80°C for the first step (etch rate of 24μm/hr) and 60°C for the second step (etch rate of 7.9μm/hr).

12- The oxide left over on the beams was etched away in BOE .

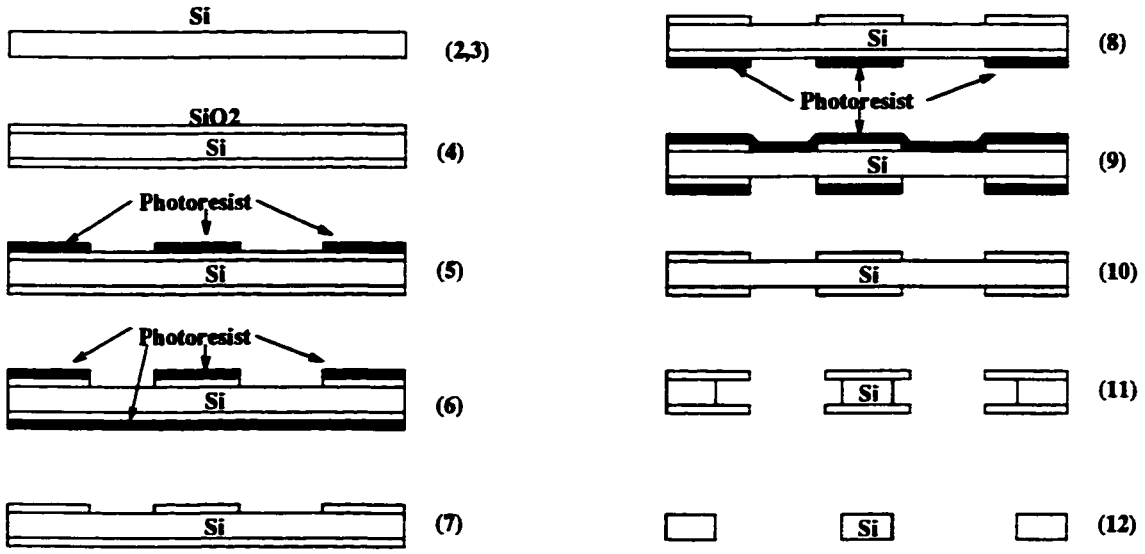

Fig. 6.3: Fabrication procedure for test beam structures.

The thickness of the beams (samples) was measured using a micrometer and the width of the beam was measured and inspected under the microscope. The results of these measurements for some beams are shown in Table 6.1.

Beam No.	Beam Thickness	Beam Width	Beam * Uniformity	Total etch time
1	110μm	108μm	2μm	5:15 hr
2	110μm	105μm	2μm	5:15 hr
3	105μm	107μm	2μm	4:55 hr
4	105μm	109μm	2μm	4:55 hr

* along the length of the beam

TABLE 6.1: Measured characteristics of the fabricated beams.

The table indicates the thickness of the sample (beam), final width of the beams, uniformity of the beam width along the length of the beam, and total etch time. Beams 1 and 2 were located on the same sample (each sample holds 4 beams as shown in Fig.6.2), and beams 3 and 4 on another sample. As seen from the table, there is some difference between the width of the beams located on the same sample.

On average the width and thickness of the beam can be matched with each other within a tolerance of $\pm 2\mu m$. The uniformity along each beam's length is usually $\pm 2\mu m$ on average.

An optical micrograph of part of a fabricated beam using the above procedure is shown in Fig.6.4. The uniformity of the beam's width along its length is clear from the figure. The SEM photograph of a corner of a beam etched from both sides is shown in Fig.6.5. The smooth vertical sidewalls and sharp corners of the beam are seen in the figure. This particular beam has been taken out of the etchant as soon as it has been etched through (as soon as the top and bottom cavities have met). The symmetrical <111> sidewalls extending from top and bottom of the wafer are clearly seen in the picture. The sym-

metry of these sidewalls results in better performance for the sensor as explained in Sec.3.5.5. Another SEM of the same sample is shown in Fig.6.6 showing more clearly the vertical smooth sidewalls of the beam. If the sample is etched for enough time (according to equation.Eq.5.2 in Sec.5.2) after it is etched through, the concave corner will eventually turn inwards and form a symmetric concave corner as shown in the SEM micrograph in Fig.6.7 (see Sec.5.2).

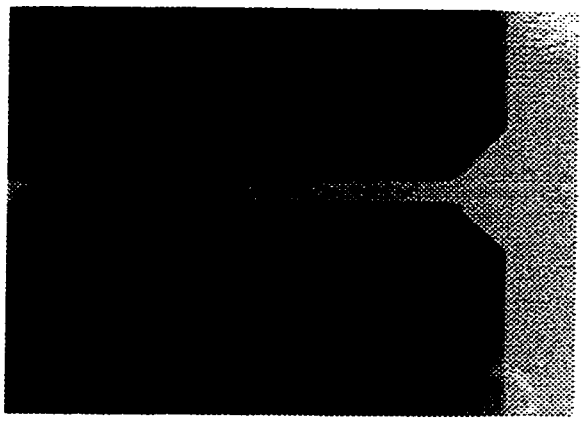

Fig. 6.4: Top view of a fabricated beam after removal of oxide (magnification=50).

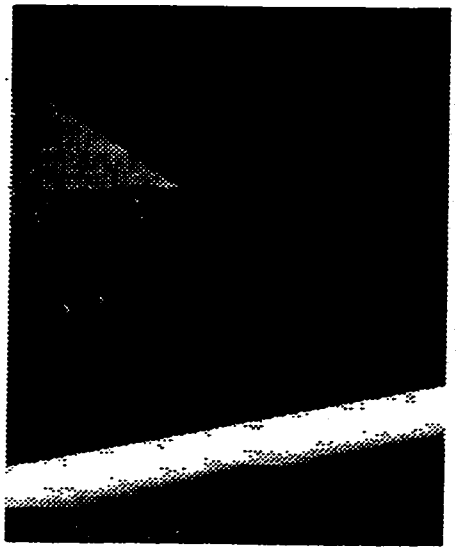

Fig. 6.5: Corner of a fabricated beam showing the symmetrical <111> planes and the smooth vertical sidewall.

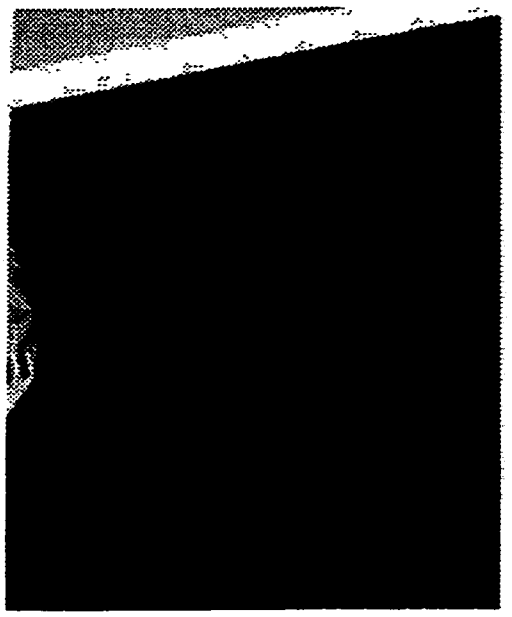

Fig. 6.6: Side wall of a fabricated beam etched in TMAH 25wt% at 80°C, showing the smooth vertical sidewall and sharp edges.

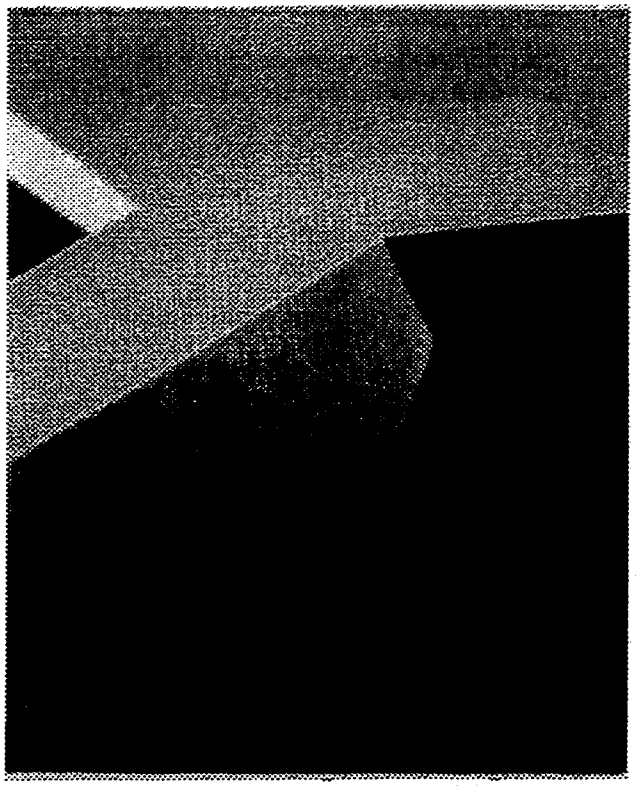

Fig. 6.7: Corner of a fabricated beam where the symmetrical inverted corner is fully formed.

6.2.1 Concave Corner Compensated Beams

A mask was designed to test the principles and simulations discussed in Chapter 5. Several sets of patterns with minimum feature sizes varying from 2.5μm to 15μm were included in the mask. The mask was designed such that individual fabricated beams could be separated and electrically tested afterwards. An overview of the mask is plotted in Fig.6.10. An optical mask of the pattern shown in figure and its mirror image (for double sided patterning) were fabricated.

The samples were prepared as follows:

. The samples were cut out of special double-side-polished P-type wafers with a nominal thickness of 100μm.

. The samples were cleaned using the cleaning procedure (Appendix III) and then a layer of oxide with the thickness of 1500Å was grown on the samples using dry oxidation at 1100°C.

. One side of the samples (first side) was patterned and etched in BOE to open the etch windows while the oxide on the other side (second side) was protected with the photoresist.

. The samples were cleaned and the second side was patterned (with a double side aligner) using mirror image of the mask, and then etched in BOE to open the etch windows while the patterned oxide on the first side was protected using photoresist.

. The samples were then etched at TMAH 25wt% at 80°C for the required time to form the structures.

During the investigation of this technique, the etching of many samples was monitored in detail. This was done by etching the sample for intermediate times, and then periodically removing the sample from the etchant to observe the etch progress, compare to

graphical and numerical simulations, and refine the algorithms. Excellent agreement was finally achieved. For example, Fig.6.8 shows the experimental structure obtained for a test pattern after 1:30 hr etch time which matches very well with the graphical simulation shown in Fig.6.9. This also matches the predicated values of numerical simulation with a 0.25 hr tolerance.

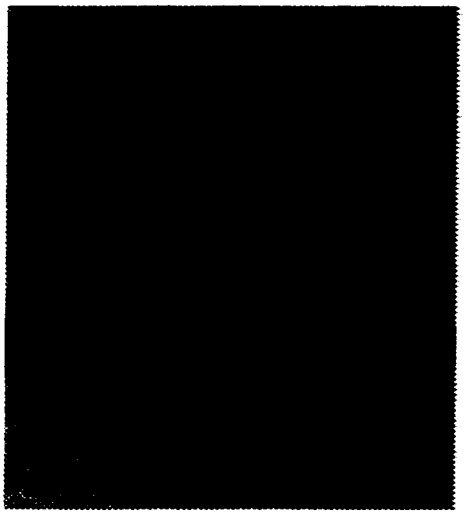

Fig. 6.8: Micrograph of a sample pattern, etched in TMAH 25% for 1hr:30min.

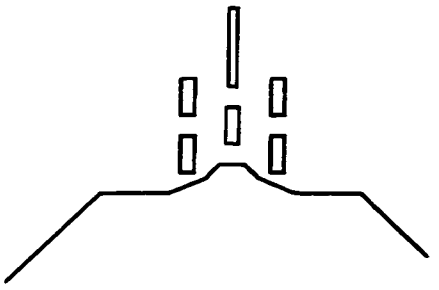

Fig. 6.9: Graphical simulation result for the sample shown in Fig.6.8.

A micrograph of one of the fabricated beams is shown in Fig.6.11. Two beams, one with and one without compensation patterns, are shown in this figure, with a flange reduction ratio of ~3.

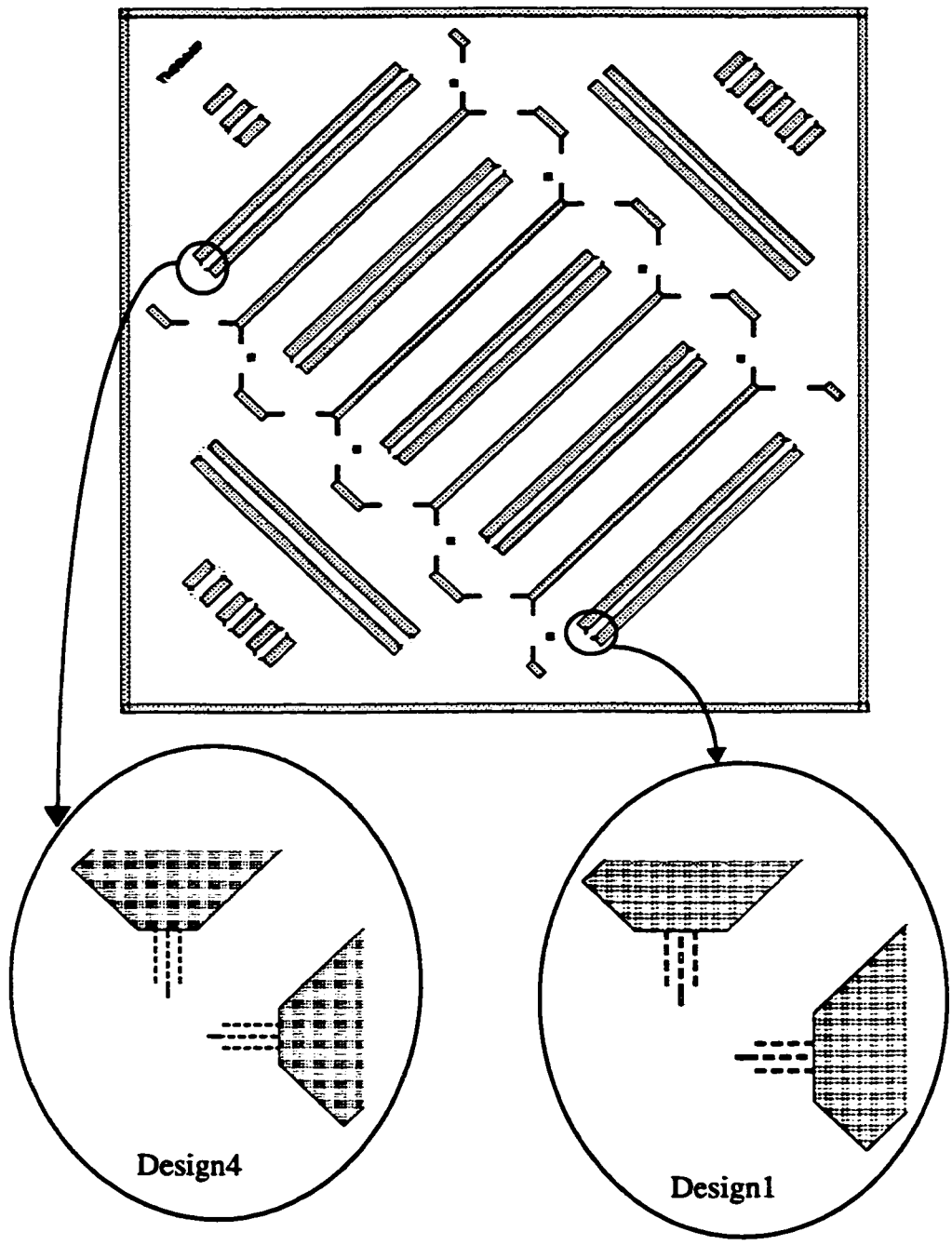

Fig. 6.10: Design of the mask for test of concave corner compensation patterns.

The results obtained for 4 different designs are summarized in Table 6.2. For each design, the total etch time, final beam width after completion of the etch, final reduction ratio of the flange size predicted by numerical simulation program, final reduction ratio obtained using graphical simulator [68], and the final reduction ratio obtained from the experiment are listed on each row of the table.

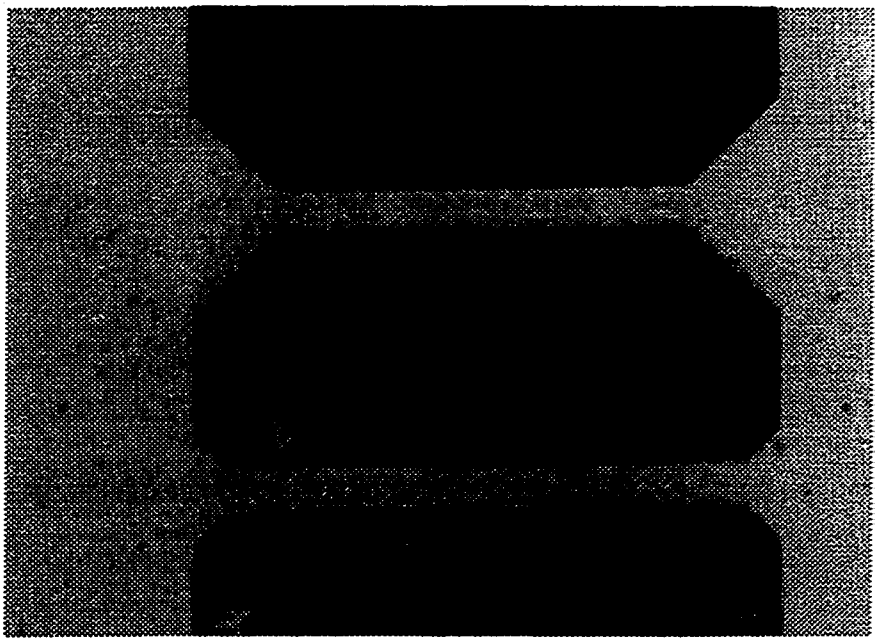

Fig. 6.11: Micrographs of etched beams: (top) a beam without compensation patterns and (bottom) a beam with compensation patterns.

	Design1	Design2	Design3	Design4
Etch Time	4:50 hr	4:50 hr	4:50 hr	5 hr
Final Beam Width	110 μm	110 μm	108 μm	111 μm
Reduction Ratio (Num. Sim.)	3.2	3.0	4.8	5.9
Reduction Ratio (Graph. Sim.)	2.8	2.5	4.0	5.5
Reduction Ratio (Experiment)	2.9	2.7	4.5	5.2
Margin (see Fig.5.5)	7 μm	14 μm	5 μm	1 μm
Min. Feature Size	10 μm	10 μm	5 μm	5 μm

TABLE 6.2: Numerical simulation, graphical simulation, and experimental reduction results for 4 designs.

As seen in the table the experimental results match well (within acceptable tolerance) with the numerical and graphical simulation results. The difference between the simulation and experimental results are mostly due to tolerances in photolitography, patterning, and alignment procedures, and also due to variations of anisotropic etchant (TMAH) properties due to temperature and concentration control, and aging.

The completed beams etched from both sides are shown in micrographs in Fig.6.12 for two of the designs.

6.2.2 Flange Inversion

Formation of an inverted <111>-defined shape was discussed in Sec.5.2 for an uncompensated flange. The inverted configuration is formed provided that there is enough time delay between the time when the wafer is etched through, and the time of completion of the etch.

When compensation patterns are present, the etch progress is more complex, as depicted in Fig.6.13. An upper bound for the time delay required for flange inversion can be approximated using the etch rate of {011} surfaces:

$$Time_{inv} = \frac{d}{2ER\{010\}} + \frac{(E_1 + \frac{d}{\tan(54.7^o)})}{ER\{011\}} \qquad \text{Eq.5.20}$$

where $ER\{010\}$, $ER\{011\}$ and d are the etch rate of {010} planes, etch rate of {011} planes and the thickness of the wafer respectively. E_1 is the distance from the {111}-defined etch front at the time the sample is etched through, to the edge of the last rectangle in the pattern as shown in Fig.6.13.

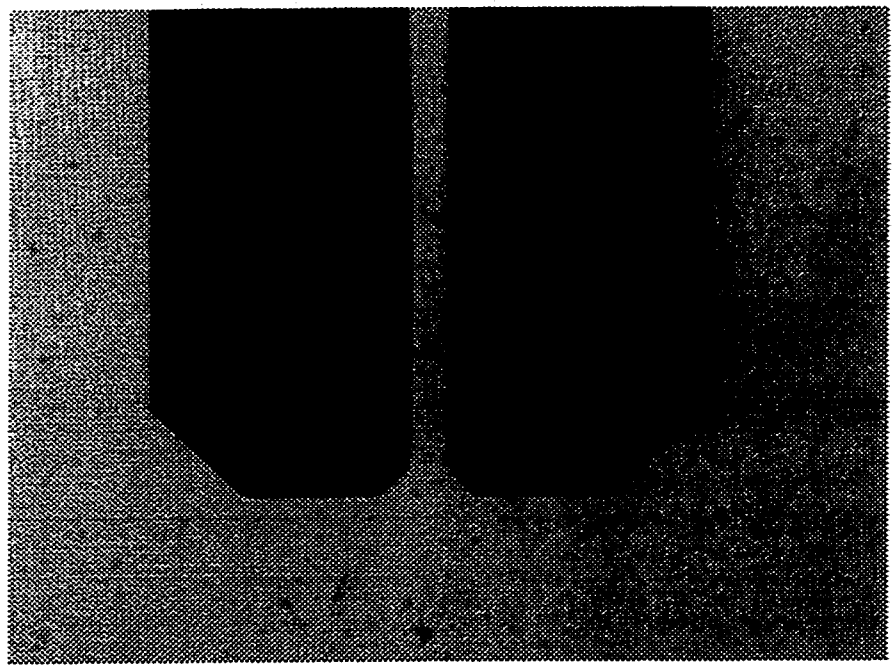

(a)

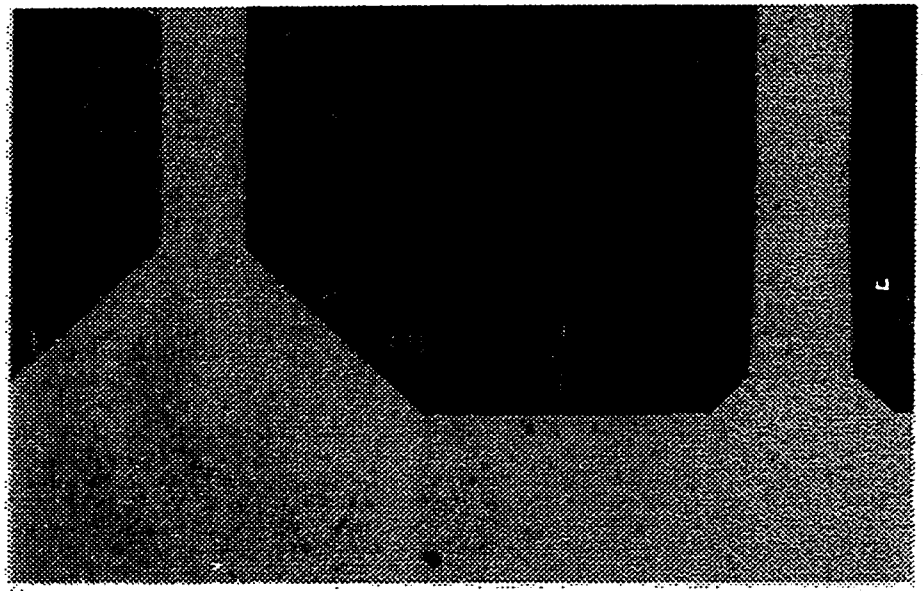

(b)

Fig. 6.12: (a)Micrograph of a fabricated beam corner (design4) showing a reduction of ~5 (b) Micrograph of a fabricated beam corner (design3) showing a reduction of ~4.5.

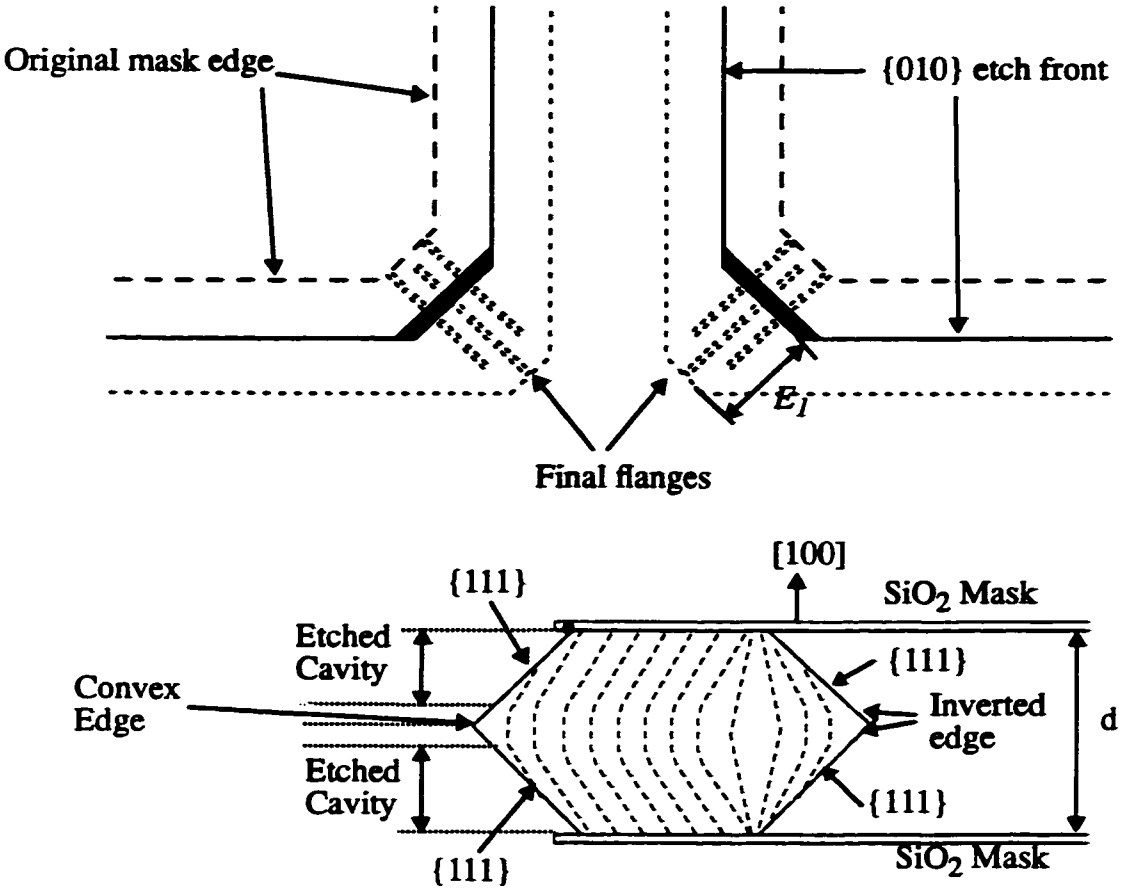

Fig. 6.13: Formation of the inverted flanges in a compensated concave corner.

As long as the wafer is etched through before $Time_f$-$Time_{inv}$, inversion will be complete. Thus, for a given wafer thickness and desired beam width, the mask pattern defining the beam width must be designed to be wide enough to allow for this. Note that a specified beam width can be obtained by a range of (greater) mask widths, simply by designing the compensation patterns to extend the appropriate distance into the concave corner.

The rough near-{011} surface is shown in Fig.6.14. These rough {011} planes rapidly progress into the concave corner as shown in Fig.6.15 and Fig.6.16, where the inverted edge is almost formed and there is only a small {011} plane left at the center of the cavity. A fully formed concave corner is shown in Fig.6.17 and Fig.6.18.

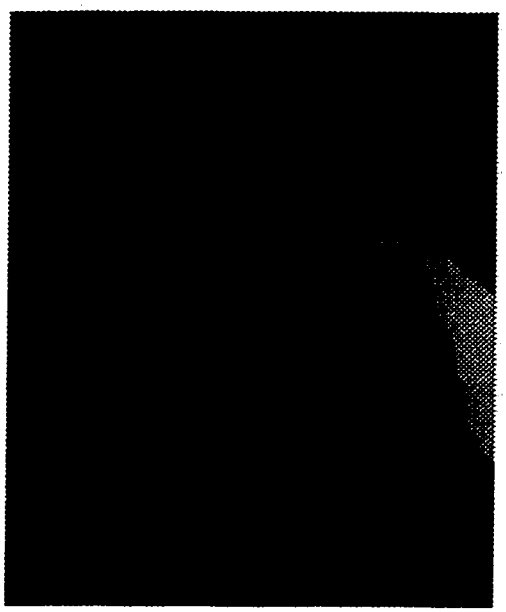

Fig. 6.14: SEM micrograph: the rough near-{011} surfaces progressing into the inverted concave corner.

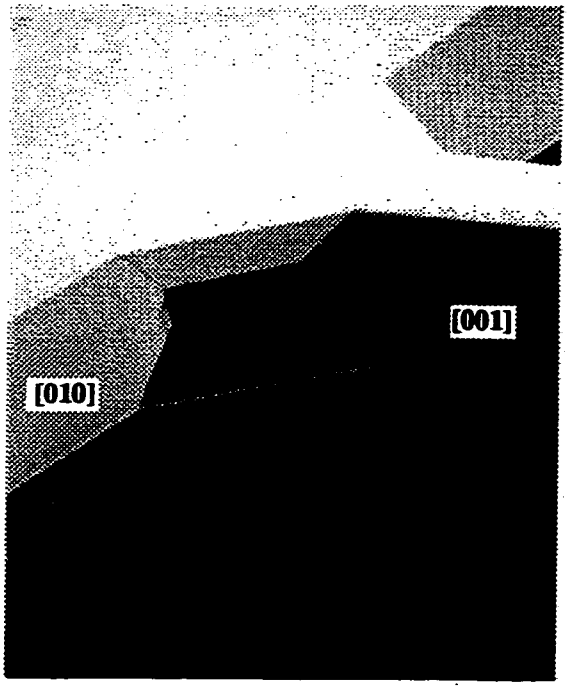

Fig. 6.15: SEM micrograph: smaller near-{011} surfaces, in the inverted corner. Note the very smooth [001] plane formed on the side of the compensated beam.

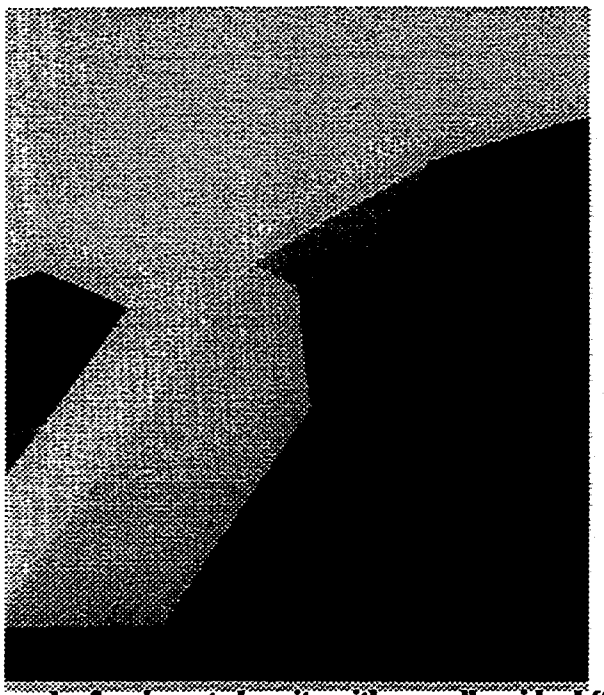

Fig. 6.16: SEM micrograph of an inverted cavity with a small residual {011} surface.

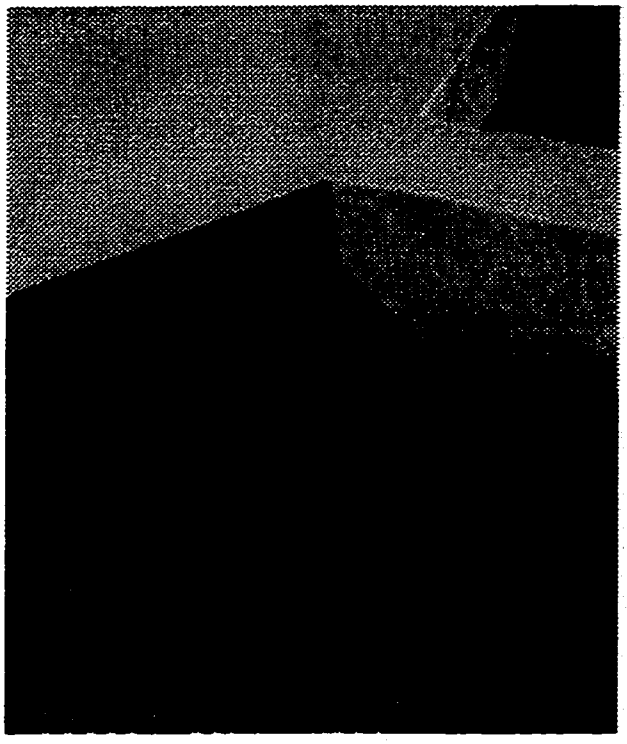

Fig. 6.17: SEM micrograph of a fully formed inverted concave shape.

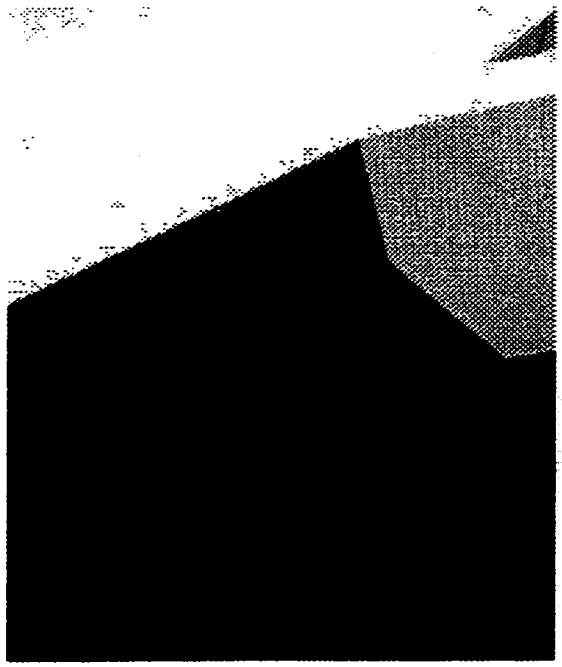

Fig. 6.18: SEM micrograph of the same beam as in Fig.6.17 showing the inverted shape more clearly.

6.2.3 Metallization and Anodic bonding

The fabricated beams should be characterized mechanically to test the natural frequencies in two orthogonal modes, Q and other properties important in the design of the sensor.

The following method was used to prepare the beams for these measurements:

1- Two sides of the frame of each beam were covered with photoresist as shown in Fig.6.19.

2- A layer of Aluminum with thickness of 2000 Å was evaporated on the sample.

3- The photoresist was lifted off in Acetone removing the Al from the two arms of the frame. Thus the only remaining low-resistance Al path connecting the two ends of the frame is the one on top of the beam. The ohmic resistance of the beam was tested at this step. Ohmic resistance in the range of $20 \pm 5\ \Omega$ is obtained for a typical beam.

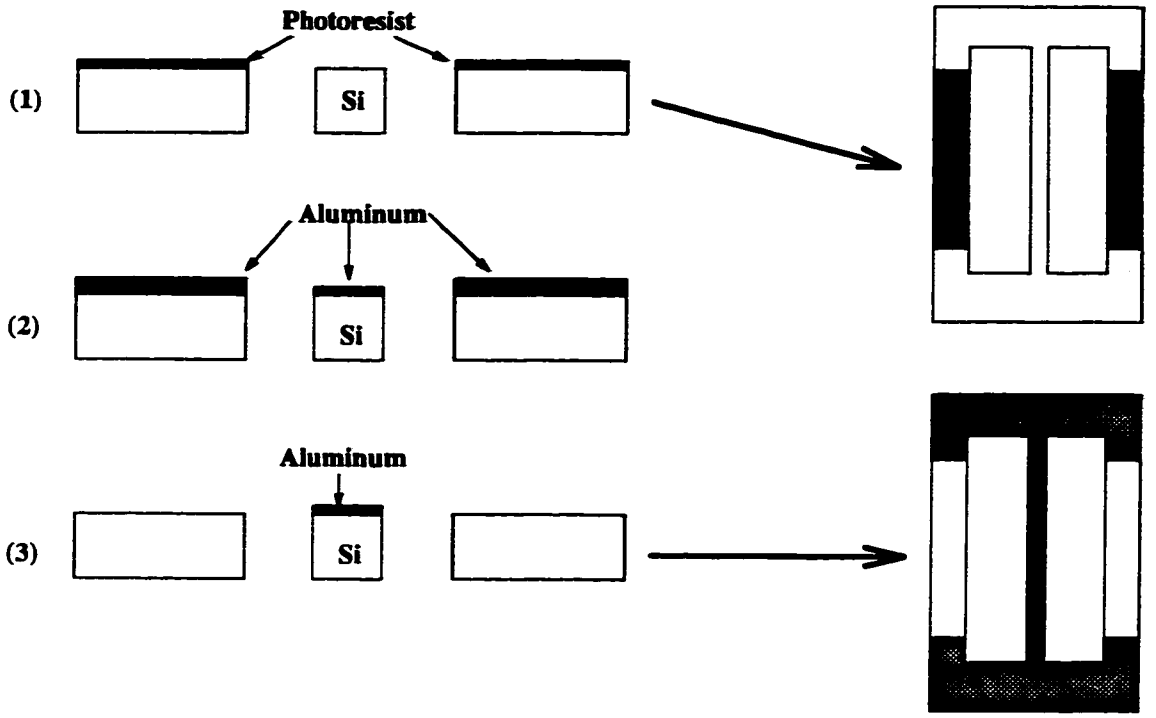

Fig. 6.19: Al evaporation and patterning.

The next step is preparation of a glass substrate with a cavity. Special Pyrex #7740 glass is used because its thermal expansion coefficient matches that of silicon at temperature range between 350°C to 400°C [70]. The preparation procedure for the glass samples is as follows:

1- The samples are cut from the Pyrex #7740 wafers and cleaned using the first two steps of the cleaning procedure.

2- A layer of Chromium with thickness of 1000Å followed by another layer of Gold with the thickness of 2000Å was deposited on the samples.

3- The samples were patterned using normal photolithography procedure.

4- The Gold and Chromium layers are etched away using proper wet etchants to open

the etch windows for cavities.

5- The glass is etched in 49% HF to form the cavity. Etch rate of the pyrex #7740 in 49% HF is about 9μm/hr. The Gold layer protects the glass during this etch step very well. Cr is used as an adhesion layer because it has a very good adhesion to both Gold and the glass, and it is resistant to HF. A Chromium layer may be used alone (without Gold) to protect the glass during the etch but with reduced performance. Usually many pin holes appear on the glass after HF etch if Chromium alone is used as the protective layer. These can affect the strength and even the formation of the bond between the silicon and glass at the later step.

6- The Gold and Chromium layers are etched off the sample. The glass is cleaned once again to prepare for the anodic bonding.

Anodic bonding is a well established and reliable way of making strong bonds between glass and silicon (or metal) at relatively low temperatures. The advantage is that surfaces remain solid during the bonding process, and no adhesives are used [71].

The prepared glass and beam frames are placed on top of each other and aligned carefully using the set up shown in Fig.6.21. The samples are aligned under the microscope then the needle is brought into contact with the glass. The samples are then heated up to the required temperature (~380^{o}C) and a voltage of 1000 V_{dc} is applied between the needle and the plate. The bond formation is usually rapid and the two pieces are bonded in less than a second. Special aligner instruments available by industry may be used to perform the same operation with increased accuracy. A cross-sectional drawing of the final product is shown in Fig.6.22.

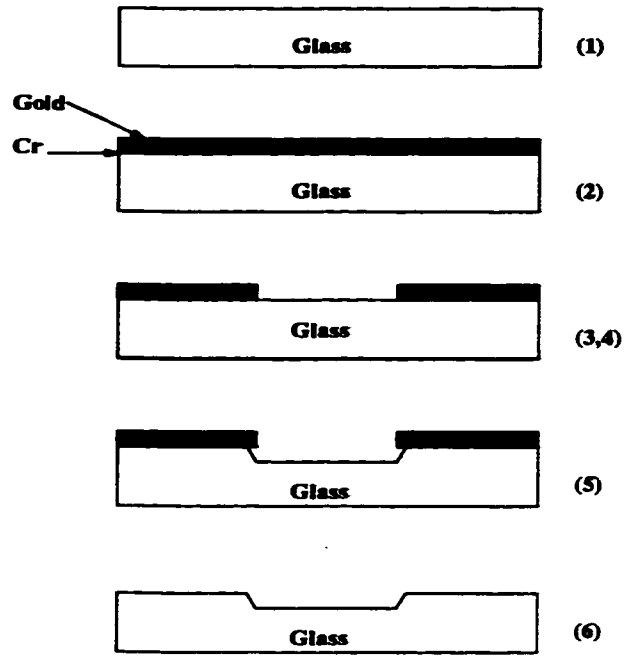

Fig. 6.20: Preparation of glass samples for anodic bonding.

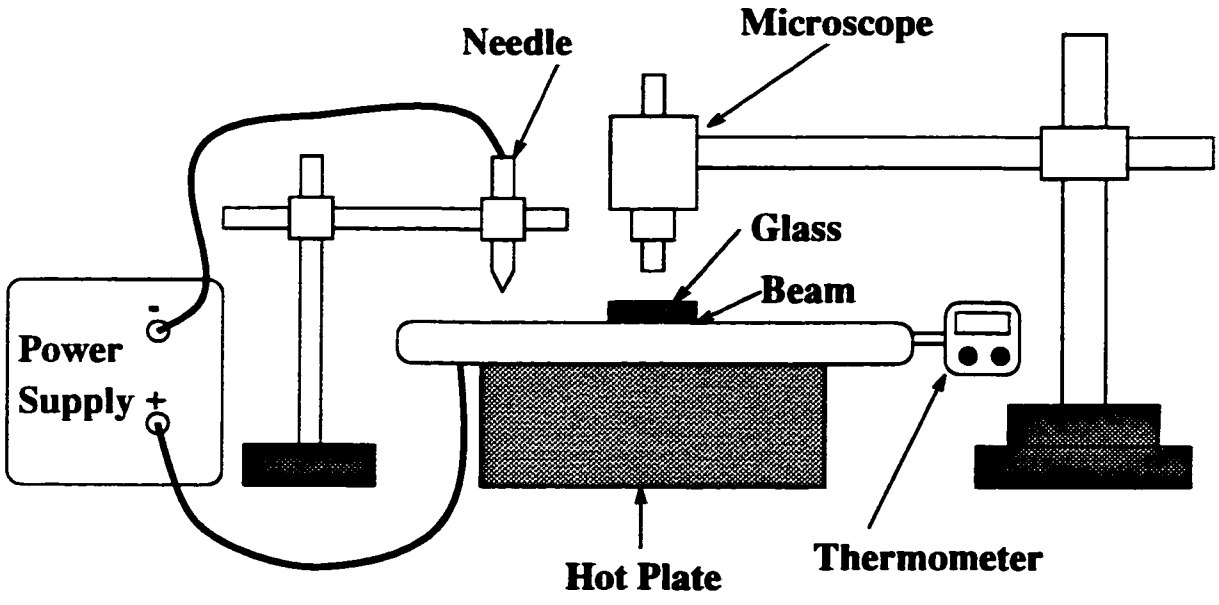

Fig. 6.21: Setup used to perform anodic bonding.

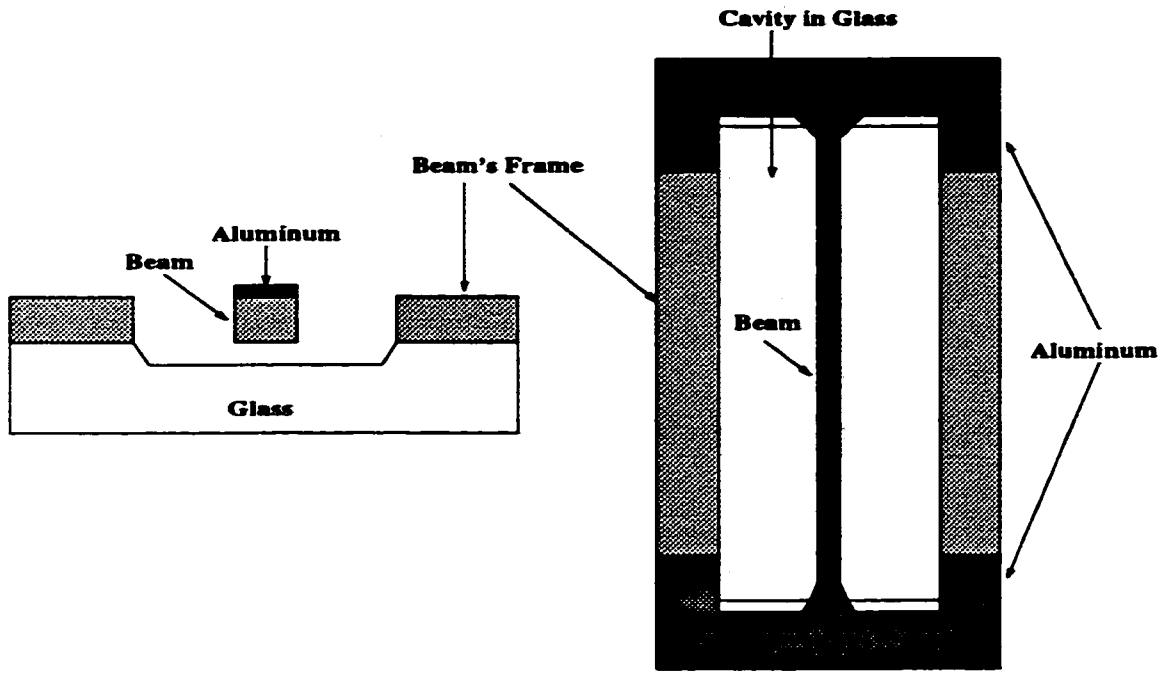

Fig. 6.22: Cross sectional and top view of the final structure of patterned beam bonded over the cavity in glass.

6.3 Test Procedure and Results

The fabricated samples were vibrated in the horizontal (actuation) and vertical (Sense) directions. To do this, a small permanent magnet ($B \approx 0.25 Tesla$) was located in close proximity to the beams in either the horizontal or vertical direction and a sinusoidal voltage signal was applied across the beam. Two different methods were used to find the natural frequency, maximum amplitude of vibrations, Q factor, and hysteresis effect in the beams.

(i) Visual Observation

This method can be used only to test the horizontal response of the beam. The beam is located under the microscope as shown in Fig.6.23. The frequency of the applied actuation voltage is varied and the vibrations induced in the beam are observed under the microscope. An approximate value may be found for the natural frequency and maximum vibration amplitude of the beam in this way.

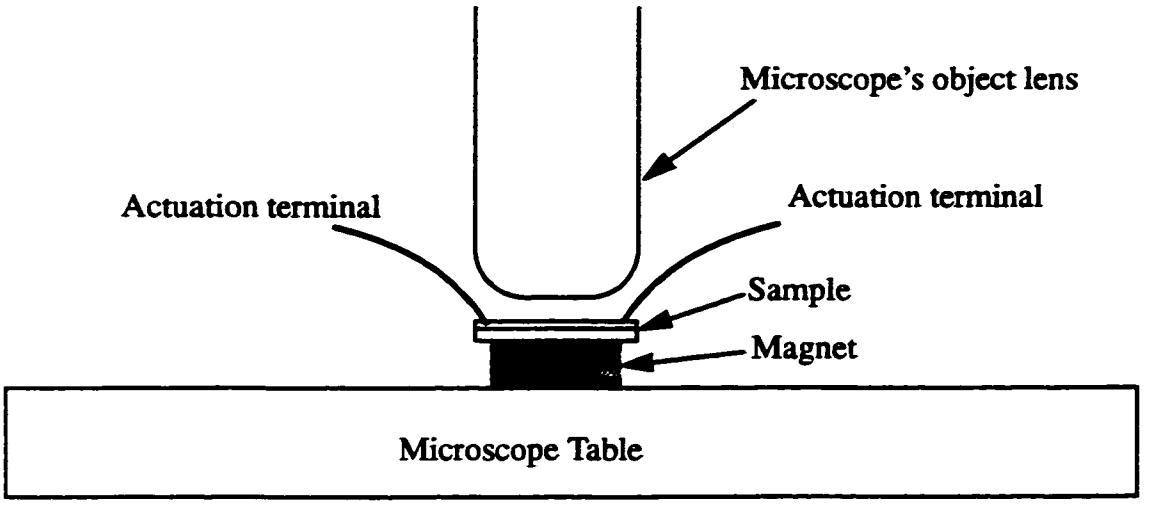

Fig. 6.23: Setup used to measure vibration amplitudes visually.

(ii) Impedance Measurement

In Sec.3.6.2 an electrical equivalent circuit model for the vibrating beam was presented. According to this model, the impedance of the beam measured between the two terminals varies with the actuation frequency and has a peak at the natural frequency of the beam. To test the mechanical and electrical properties of the beam a HP4194 gain-phase analyzer (network analyzer) is used. As shown in Fig.6.24 the beam is actuated by the HP4194 in vertical or horizontal direction at various frequencies and the gain and phase of the impedance between the two actuation terminals is measured at each fre-

quency. A plot of the impedance vs. frequency may be obtained for each beam (see Sec.6.3.1 for results). Using this plot, the natural frequency, Q, and the induced emf voltage in the beam may be measured.

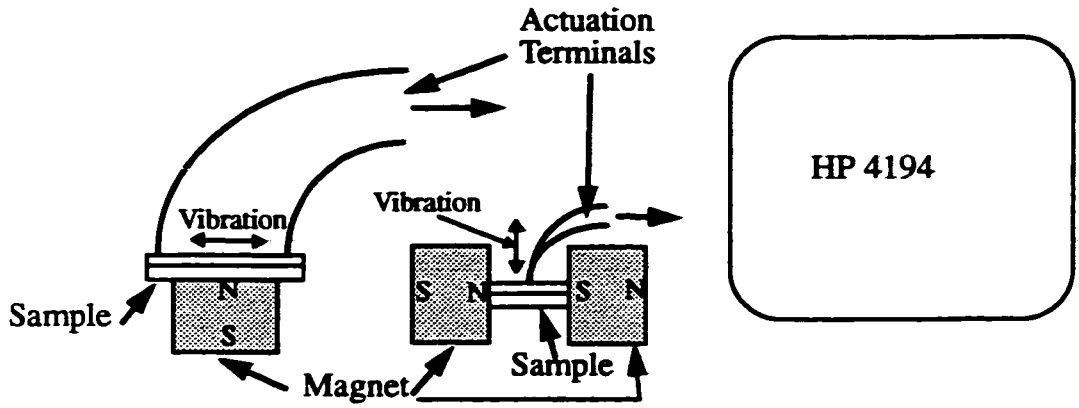

Fig. 6.24: Setup used to measure the response of the beams using HP4194 gain-phase analyzer.

An example of a typical waveform expected for a beam is shown in Fig.6.25. The natural frequency of the beam is simply the frequency at which the peak occurs. The Q may be measured by finding the bandwidth of the response, and using

$$Q = \frac{\omega_n}{BW} \qquad \text{Eq.6.2}$$

where ω_n and BW are the natural frequency and Bandwidth respectively. The induced EMF in the beam may also be measured using the model described in Fig.3.28 in Sec.3.6.2. By using the measured impedance of the beam at its natural frequency, and knowing the value of series ohmic resistance and amplitude of the actuation signal, it is possible to find (using Fig.6.25) the value of the induced EMF at the natural frequency of the beam.

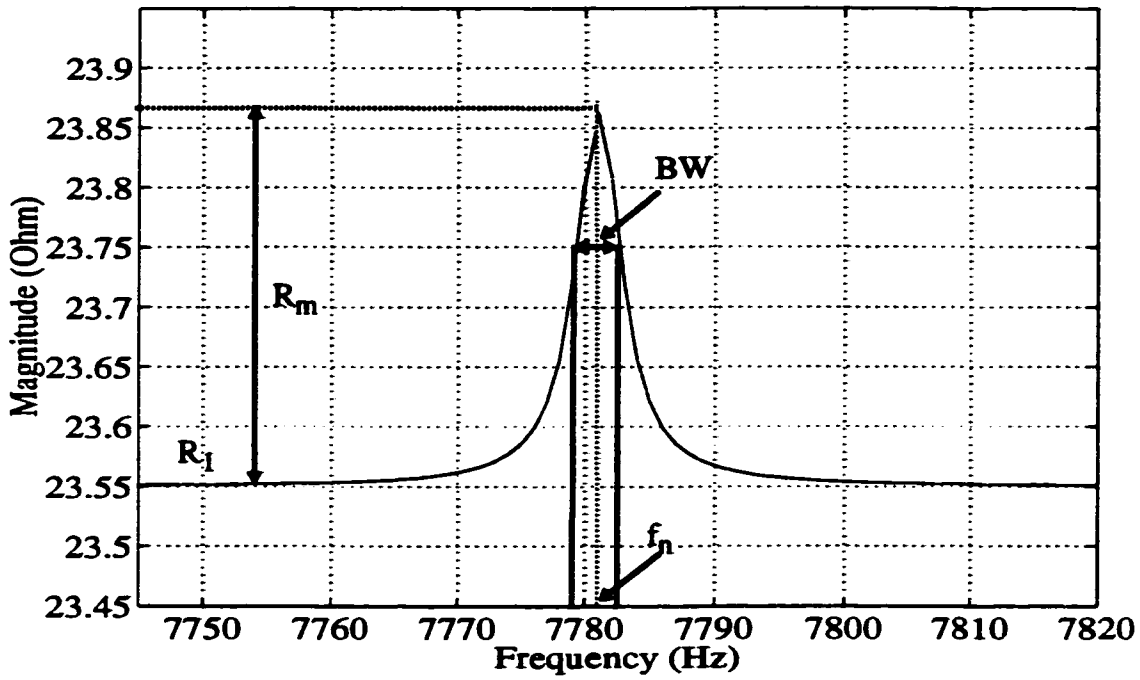

Fig. 6.25: A representative response of a beam and the measured parameters.

At the natural frequency of the beam the impedance is purely ohmic, therefore the equivalent circuit model may be simplified as shown in Fig.6.26. The values of R_1 and R_m may be accurately found from the plotted frequency response, R_s is the internal impedance of the HP4194 which is precisely set to 50 ohms. The amplitude of the driving signal V_{drive} is also accurately set. Thus, the induced EMF at the natural frequency of the beam can be found with very good precision.

The beam response starts to become non-linear as the amplitude of vibrations grows (as explained in Sec.3.5.1). This can be investigated experimentally by increasing the amplitude of vibrations and plotting the frequency response of the beam. The threshold of the maximum driving voltage that can be applied to the beam without driving it into hysteresis can be found experimentally. Also the maximum induced EMF voltage in the beam may be measured by finding the EMF for the maximum driving voltage that can be

applied before driving the beam into hysteresis region.

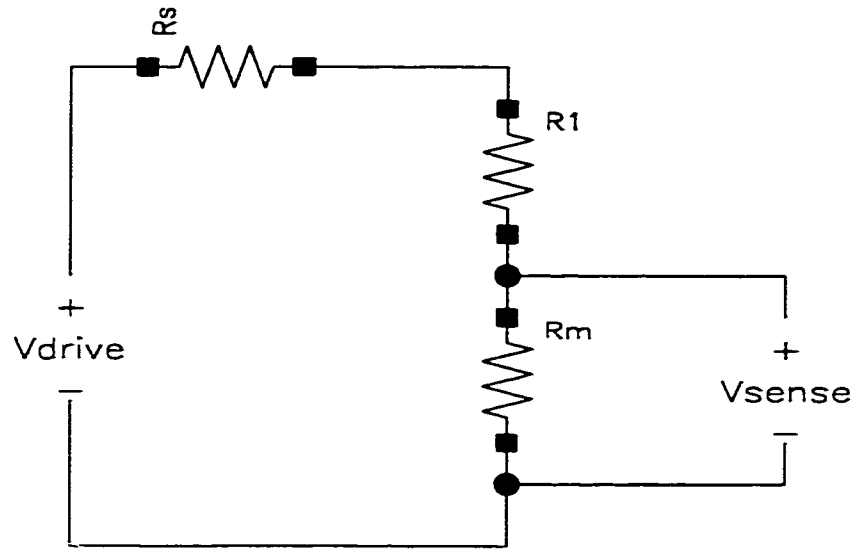

Fig. 6.26: The simplified equivalent circuit model of the beam at its natural frequency.

6.3.1 Test Results

Two fabricated beams with the following characteristics were prepared using the previously mentioned fabrication procedure (Sec.6.2).

Beam #1:

Length=1cm, width=109μm, height=105μm, Cavity depth (in glass)=30μm.

Beam #2:

Length=1cm, width=107μm, height=105μm, Cavity depth (in glass)=30μm.

The two beams were tested both under the microscope and using the HP4194 analyzer. The beams were vibrated horizontally, first at regular atmospheric pressure (no vacuum), and then at reduced pressure.

6.3.2 Regular Atmospheric Pressure

The results of the measurements of horizontal vibrations under the microscope are plotted in Fig.6.27 and Fig.6.28. The accuracy of the measured amplitudes is within $\pm 1 \mu m$. The minimum frequency steps available from the function generator were 10Hz which are large compared to the expected width of the resonance peaks of the vibration amplitude near beam's natural frequency. Therefore, the graphs are not smooth. The beams were first actuated with lower amplitudes where there is no frequency shift due to amplitude stiffening. Then the amplitude was increased until the hysteresis effect became visible. In Fig.6.27 the beams were actuated with an actuation voltage of 20 mV, 70 mV, and 100 mV. At 20 mV and 70mV the response is still symmetric, for V_{act}=100mV, no hysteresis is observed but the resonance is obviously not symmetric, and the peak is shifted toward the higher frequencies due to the amplitude stiffening effect. At higher actuation levels the hysteresis effect becomes obvious. In Fig.6.28, the beams are actuated with an input of 200 mV amplitude, where the hysteresis effect is clearly observed.

A much smoother and more accurate curve for the frequency response of these beams in the horizontal direction was obtained by impedance measurement using the HP4194. The measured frequency response (gain and phase of the beam impedance) for beam #2 are shown in Fig.6.29 for inputs with: V_{act}=20 mV, V_{act}=70 mV, V_{act}=100mV, and V_{act}=200 mV.

The response matches well with the measurements shown in Fig.6.27 and Fig.6.28 for the same beam under the same conditions. At V_{act}=20 mV peak (amplitude=2 μm) the response is perfectly symmetrical, at V_{act}=70 mV (amplitude= 6 μm) the peak is slightly (~4 Hz) shifted toward the higher frequencies, at V_{act}=100 mV (amplitude=7 μm) the response is very close to the transition point to the hysteresis region, and at V_{act}=200 mV (amplitude=18 μm) the hysteresis response is clearly observable. The measured response

of the beam #2 in the vertical direction is also plotted in Fig.6.30. This is measured only using the HP4194 since it was not possible to make this measurement under the microscope.

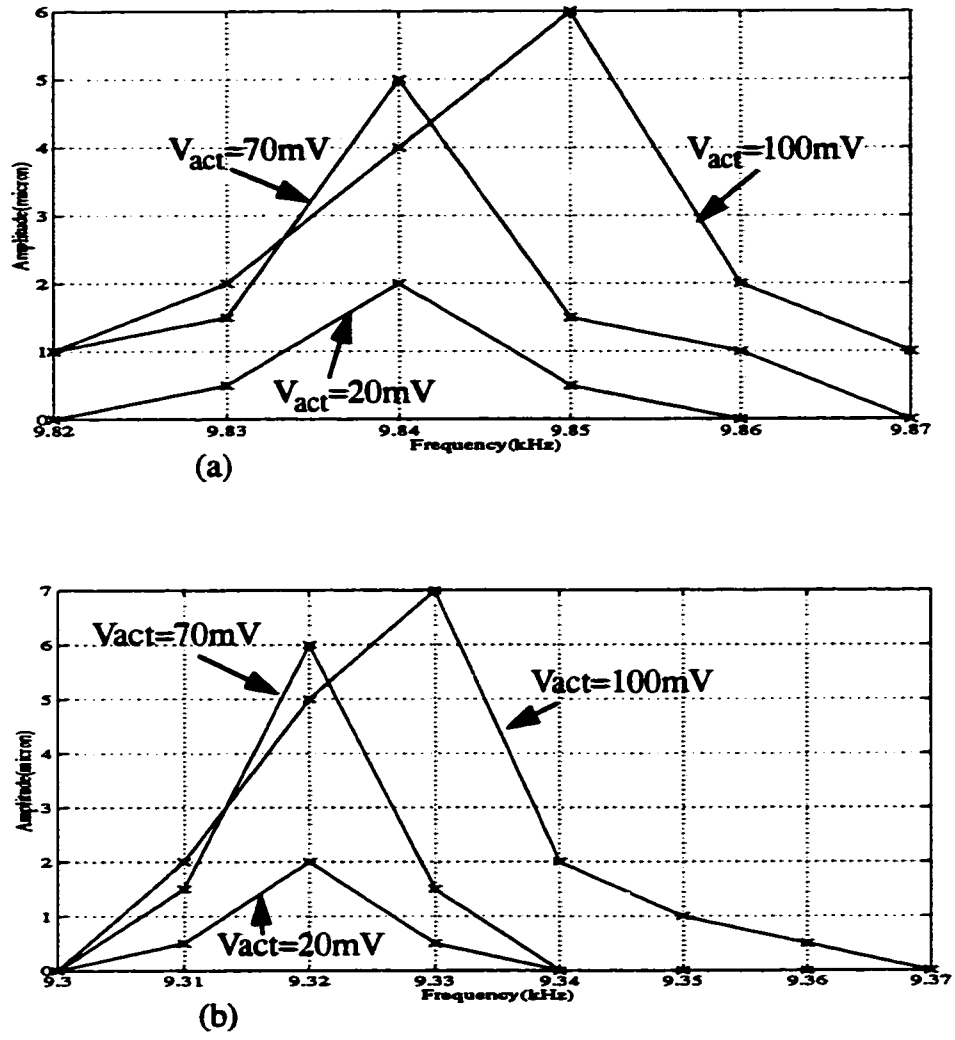

Fig. 6.27: Response measured under the microscope for V_{act} =20 mV, 70 mV, 100 mV peak, for (a) beam #1, (b) beam #2.

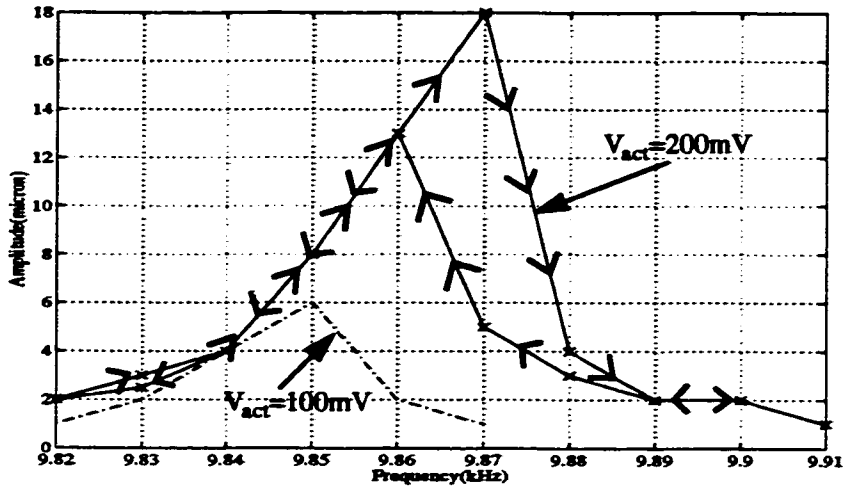

(a)

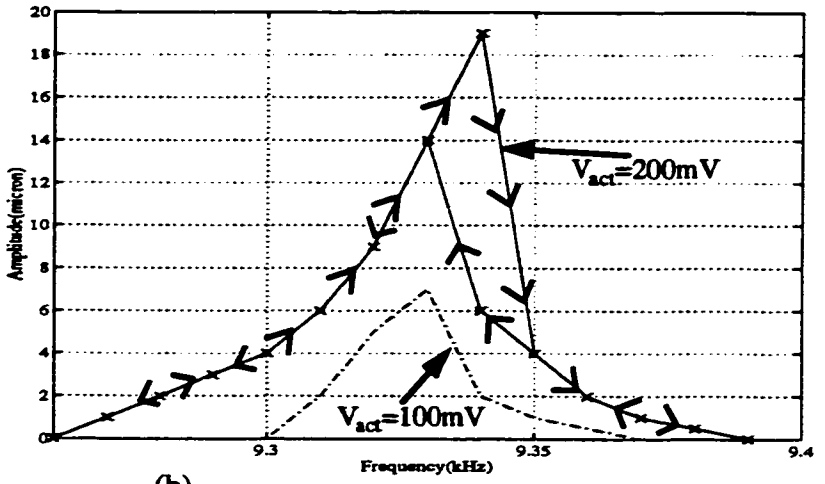

(b)

Fig. 6.28: Response measured under the microscope for V_{act} =200 mV peak, for (a) beam #1, (b) beam #2.

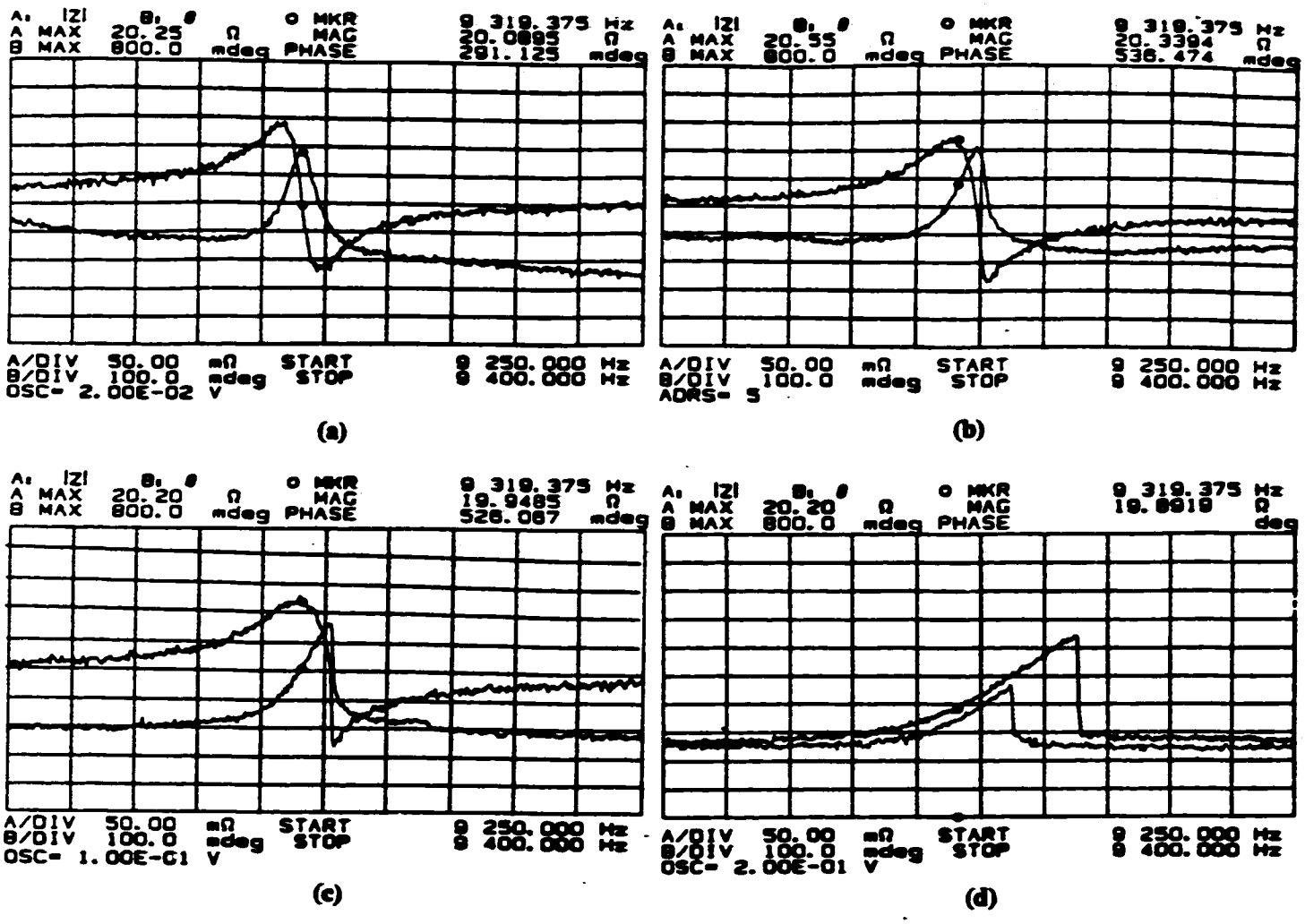

Fig. 6.29: Measured response of the beam#2 in horizontal direction for (a) V_{act}=20mV, (b) V_{act}=70mV, (c) V_{act}=100mV, (d) V_{act}=200mV. The frequency is varying on the horizontal axis from 9250 Hz to 9400 Hz by 15 Hz/div. On vertical axis the impedance is varying by 50 mΩ/div and the phase is varying by 100 mdeg/div.

The response predicted from theory for beam #2 with V_{act}=20 mV, 70 mV, and 100 mV is shown in Fig.6.31. The simulated response of the Beam #2 for V_{act}=20 mV, 70 mV and 100 mV using the model developed in Chapter 4 is also shown in Fig.6.32.

The theoretical response matched well with the experimental results for V_{act}=20 mV and *70 mV* where the beam is not yet deeply into the non-linear region. At V_{act}=100 mV the error between the amplitude obtained from theory and experiments is increased and also the linear model used in theory is not able to predict the noticeable frequency shift due to amplitude stiffening. The simulation model however, tracks both the amplitude and

the frequency shift very well for all different vibration amplitudes.

The experimental results obtained for the two beams are shown in Table 6.3 together with the results from theory and FEM (Finite Element Model) simulation with ANSYS.

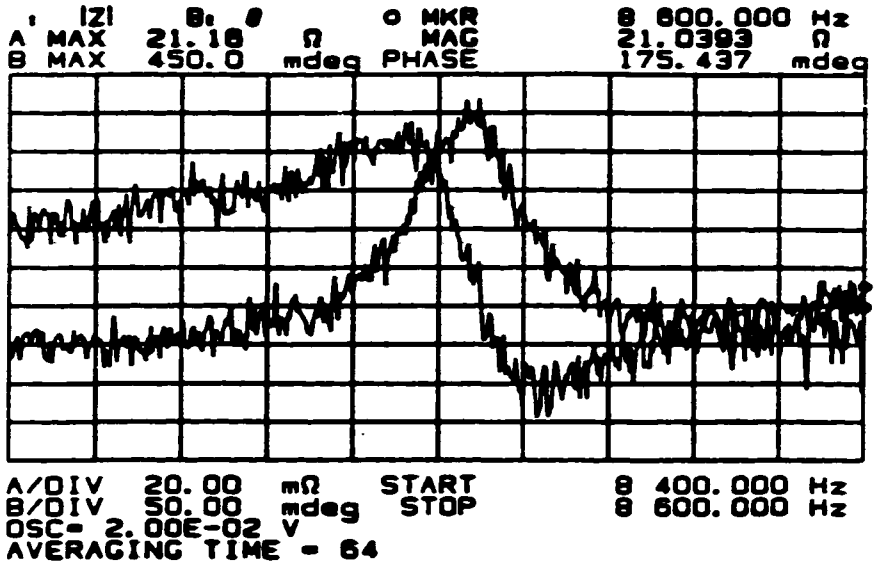

Fig. 6.30: The response of beam#2 in the vertical direction. The frequency is varying on the horizontal axis from 8400 Hz to 8600 Hz by 20 Hz/div. On vertical axis the impedance is varying by 20 mΩ/div and the phase is varying by 50 mdeg/div.

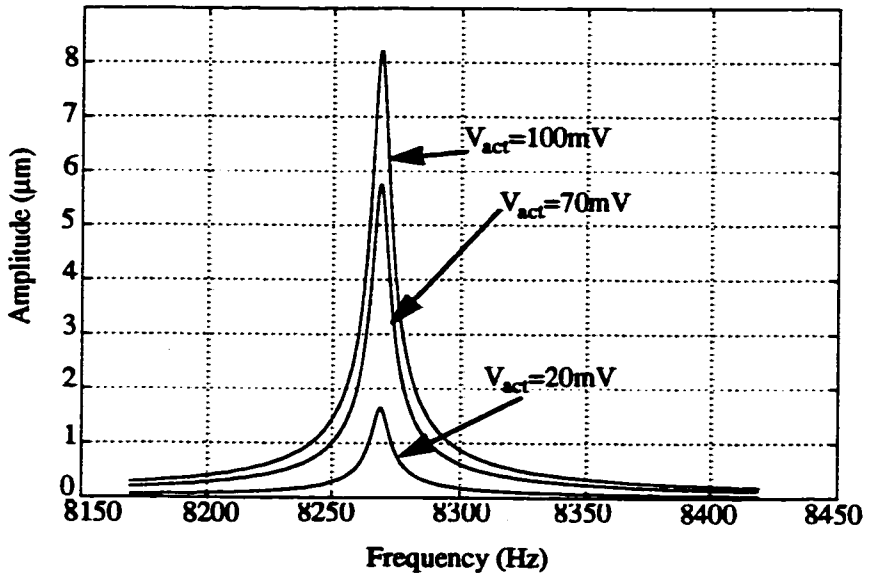

Fig. 6.31: Response of beam #2 to V_{act}=20mV, 70 mV, and 100mV obtained from theory.

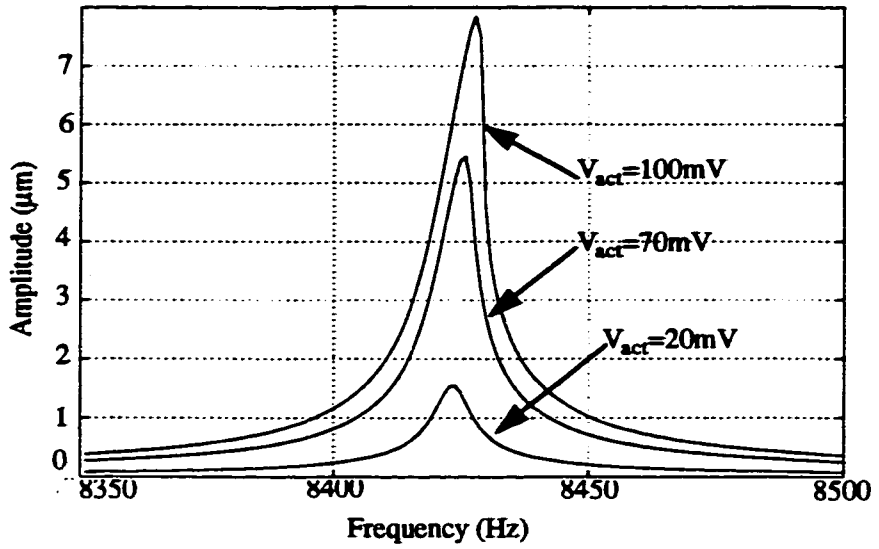

Fig. 6.32: Simulated response of beam #2 for V_{act}=20mV, 70 mV, and 100 mV.

	beam #1		beam #2	
	Horizontal direction	**Vertical direction**	**Horizontal direction**	**Vertical direction**
Natural Frequency (theory) vac	8423 Hz	8114 Hz	8269 Hz	8114 Hz
Natural Frequency (theory stressed)vac	9029 Hz	8741 Hz	8885 Hz	8741 Hz
Natural Frequency (FEM) vac	9470 Hz	8870 Hz	9310 Hz	8870 Hz
Natural Frequency (microscope) air	~9840 Hz	----------	~9320 Hz	----------
Natural Frequency (HP4194) air	9833 Hz	8637 Hz	9319 Hz	8507 Hz
Quality Factor (theory) air	1499	240	1472	250
Quality Factor (experiment) air	1680	341	1553	322
Induced EMF (theory) air	0.21 mV	----------	0.22 mV	----------
Induced EMF (simulation) air	0.20 mV	----------	0.21 mV	----------
Induced EMF (experiment) air	0.15 mV	----------	0.17 mV	----------
Mismatch (theory) vac	3.6%		1.8%	
Mismatch (theory stressed) vac	3.19%		1.6%	
Mismatch (FEM) vac	6.3%		4.7%	
Mismatch (experiment) air	12.1%		8.8%	

"vac" refers to "vacuum"

TABLE 6.3: The theoretical, FEM simulation, and experimental results for the two beams in the air.

The values obtained from experiment for several key parameters such as quality factor, natural frequency, mismatch, and EMF are compared with theory and simulation in the subsequent sections (Sec.6.3.2.1 to Sec.6.3.2.5).

6.3.2.1 Quality Factor (Q)

The quality factor obtained for the beams in horizontal and vertical directions may be checked against the values obtained from theory using equation Eq.3.32 and Eq.3.33 in Sec.3.5.4. The values obtained from theory are compared with experimental values for both beams in Table 6.3. The theoretical and experimental values for the Q_x match reasonably well. However, the results from Q_y have a larger disparity.

6.3.2.2 Natural Frequency

As seen from the figures, the maximum vibration amplitude obtained from the theory, simulations, and experiments are matching within acceptable tolerances, but the natural frequency predicted from theory is considerably lower than the experimental result. The reason for this discrepancy could be associated with the effect of the flanges at the two ends of the beam and the stress induced in the beam due to anodic bonding.

i) Effect of flanges

The top view of a beam and its flanges is shown in Fig.6.33. The following parameters may be extracted from the figure:

L_b: Length of the beam without flanges.

L_f: Projected length of the flanges.

L_u: Undercut in [010] or [001] direction under the mask.

L_m: Length of the beam pattern on the mask.

The natural frequency of the beam shown in Fig.6.33 would be different from a simple clamped-clamped beam with a length of L_m we used to consider so far. Finding a closed form solution for the natural frequency of such a beam considering the effect of flanges would be extremely complicated. A finite-element simulation model may be used to find the natural frequency of the beam [65]. The result may be considered in theoretical calculations to obtain a better approximation for the natural frequency of the beam.

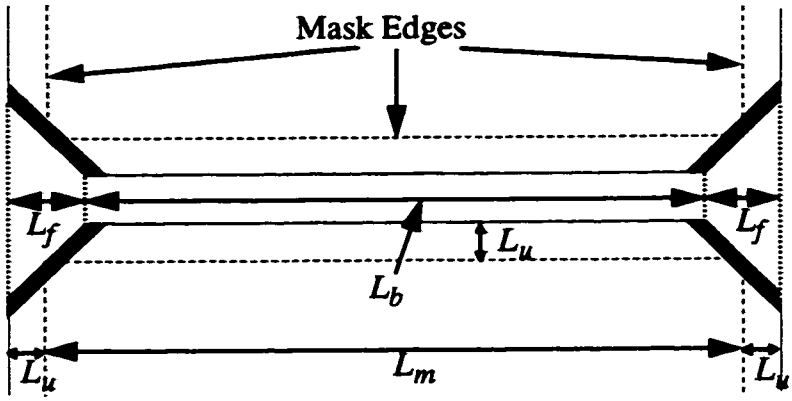

Fig. 6.33: Plan view of a beam and the flanges.

ii) Tensile stress

The natural frequency of a beam changes with stress (strain) as [51]:

$$\omega_n = \omega_{n0}\sqrt{\left(1+\gamma\varepsilon\frac{L^2}{w^2}\right)} \qquad \text{Eq.6.3}$$

where $\gamma = 0.2949$ is a constant, ε is the strain of the beam, ω_{n0} is the natural frequency of the beam without strain, and L and w are the length and width of the beam

respectively.

The thermal expansion coefficients of Pyrex #7740 glass and Silicon are close to each other at temperatures between 300°C to 400°C where anodic bonding is done, but not equal. After the bonding is done at a high temperature and as the beam and glass are cooled down to the room temperature some strain is induced in the beam due to mismatch between the two thermal expansion coefficients. The strain may be found as [70]:

$$\varepsilon = \int_{T_{bond}}^{25^{o}} (\alpha_g(T) - \alpha_{Si}(T))\, dT \qquad \text{Eq.6.4}$$

where T_{bond}, α_g, α_{Si} are the bonding temperature, thermal expansion coefficient of glass, and thermal expansion coefficient of Si respectively. Predefined curves are available that give the amount of induced strain based on bonding temperature between Si and Pyrex #7740 glass [70]. For a temperature of 380°C, at which the bonding was done in this experiment, the induced strain is found to be tensile with the value of $\varepsilon \approx 60ppm$. Better approximations for the natural frequency of the beam may be obtained by substituting this into equation Eq.6.3. This is listed in Table 6.3 as "theory stressed".

Further, a finite element model of the beam using ANSYS may be used to simulate the response of the beam considering both the effect of flanges and stress in the beam [65,66]. The results are also included in Table 6.3. The results obtained from theory (without any stress or flange effects) are compared with the results obtained by considering the effect of stress only, and the results obtained from finite element simulation considering both the effect of stress and flanges. As seen from the Table 6.3, better approximations of the natural frequencies are obtained by considering the effect of the stress in the theoretical calculations, and even better approximations are obtained using the FEM model considering the effect of flanges and stress together.

6.3.2.3 Mismatch

The mismatch obtained from experiment is compared with the results obtained from pre-stressed FEM simulation and theory with or without the stress in Table 6.3. According to the theory for the stressed and unstressed cases in Table 6.3, the stress in the beam changes the mismatch only by a few tenths of percent, it should therefore not be an important parameter in mismatch. The mismatch obtained from FEM simulation indicates that the higher mismatch (compared to theory) must be due to the effect of flanges. The experimental results show an even greater mismatch compared to the FEM simulation. Note that the values for mismatch found from theory and by FEM are very sensitive to the accuracy of the f_x and f_y values predicted by FEM simulation. There is always a few percent error between the predicted natural frequencies and the experimental results which causes an error of about 50% in mismatch. For example, a 3.8% and 0.1% mismatch between the predicted and experimental values of f_y and f_x can caused the FEM predicted mismatch to be almost half of the experimental mismatch for beam#2.

6.3.2.4 Induced EMF

The value of the EMF induced in the beam, obtained from theory and simulation using the model developed in Chapter 4 are compared with experimental values for the two beams in Table 6.3. The EMF measured in practice is lower than the values found from simulation and theory. This discrepancy may be attributed to the non-ideal shape of the beam (the flanges). The presence of the flanges makes the beam stiffer in the horizontal direction, it also changes the mode shape of the beam for the first vibration mode.

6.3.2.5 Non-linear Response

The simulated non-linear behavior of the beam #2 for V_{act}=100 mV was shown in

Fig.6.32. The obtained peak amplitude matches the experimental results in Fig.6.27. Also the shape of the curve and the magnitude of shift in peak frequency due to amplitude stiffening matches the simulation ($\Delta f \approx 8Hz$) and experiment ($\Delta f \approx 7.2Hz$). By increasing the input amplitude beyond the 100 mV the simulation model begins to show a hysteresis. The response of the beam for V_{act}=200 mV is simulated in Fig.6.34. which matches well with the experimental results of Fig.6.28 and Fig.6.29 except for the fact that the frequencies are lower in simulation due to the effects mentioned in Sec.6.3.2.2.

The threshold input voltage beyond which the hysteresis effect appears is compared for both beams in: theory (obtained from equation Eq.3.23 in Sec.3.5.3), simulation and experiments. The values match within acceptable tolerances.

	Theory	Simulation	Experiment
beam #1	4.58 μm	6.2 μm	7 μm
beam #2	4.50 μm	6 μm	7 μm

TABLE 6.4: The hysteresis threshold value obtained from theory, simulation and experiment.

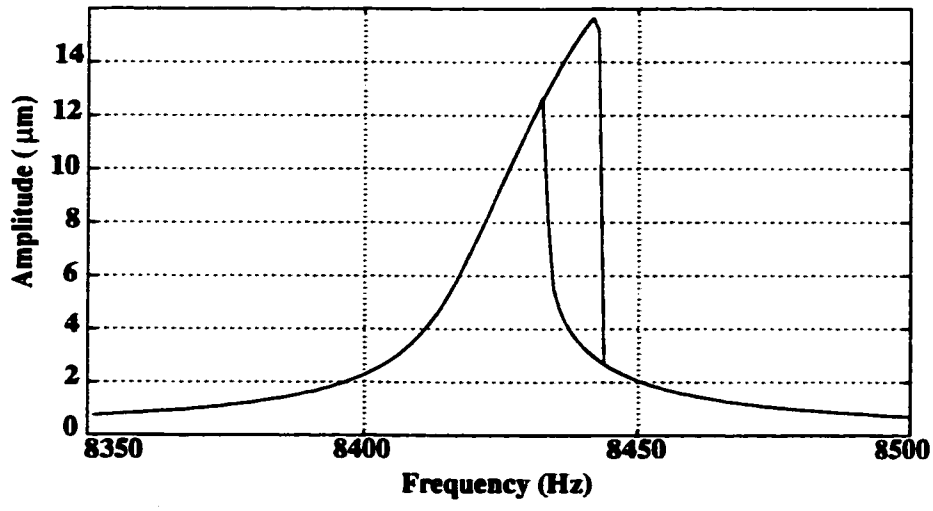

Fig. 6.34: Simulated response of beam#2 for V_{act}=200 mV.

6.3.3 Response in Reduced Pressure

The beams were placed in a Vacuum Jar as shown in Fig.6.35. A partial vacuum was created in the jar using a vacuum pump[1]. The samples were then tested using the HP4194 gain-phase analyzer. An example of experimentally measured responses for beam#2 is shown in Fig.6.36 for vertical and horizontal directions. The values obtained for natural frequencies, quality factors and induced EMF for the two beams are summarized in Table 6.5.

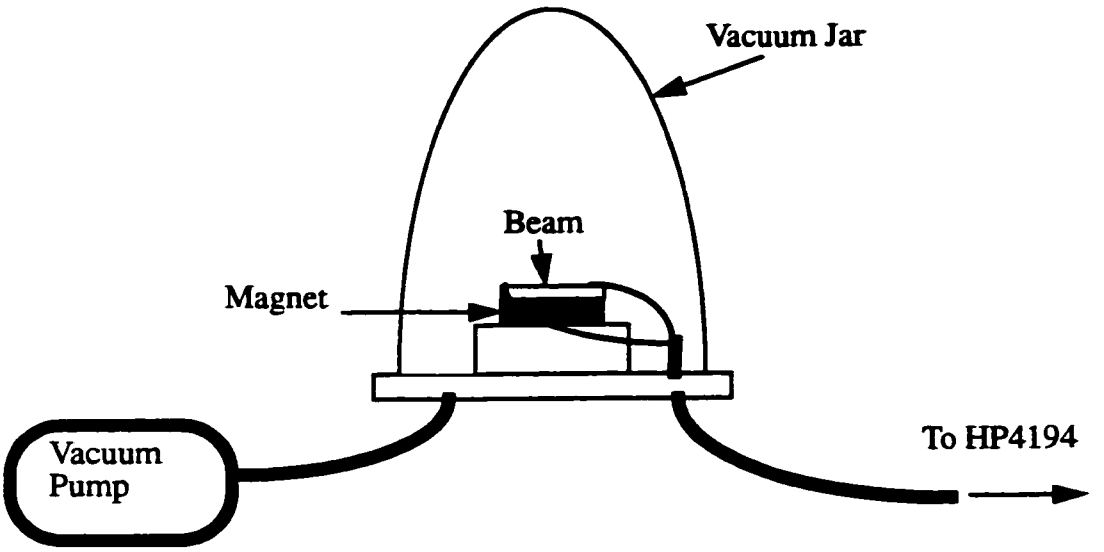

Fig. 6.35: Setup used to test the beams in partial vacuum.

1. Pressure of ~0.1 Torr is estimated for the vacuum jar.

	beam #1		beam #2	
	Horizontal direction	**Vertical direction**	**Horizontal direction**	**Vertical direction**
Natural Frequency (theory) vac	8423 Hz	8114 Hz	8269 Hz	8114 Hz
Natural Frequency (theory stressed)vac	9029 Hz	8741 Hz	8885 Hz	8741 Hz
Natural Frequency (FEM) vac	9470 Hz	8870 Hz	9310 Hz	8870 Hz
Natural Frequency (microscope) air	~9840 Hz	----------	~9320 Hz	----------
Natural Frequency (HP4194) air	9833 Hz	8637 Hz	9319 Hz	8507 Hz
Natural Frequency (HP4194) pvac	9856 Hz	8654 Hz	9344 Hz	8514 Hz
Quality Factor (theory) air	1499	240	1472	250
Quality Factor (experiment) air	1680	341	1553	322
Quality Factor (experiment) pvac	4748	1276	4852	1459
Induced EMF (theory) air	0.21 mV	----------	0.22 mV	----------
Induced EMF (simulation) air	0.20 mV	----------	0.21 mV	----------
Induced EMF (experiment) air	0.15 mV	----------	0.17 mV	----------
Induced EMF (experiment) pvac	0.11 mV	----------	0.12 mV	----------
Mismatch (theory) vac	3.6%		1.8%	
Mismatch (theory stressed) vac	3.19%		1.6%	
Mismatch (FEM) vac	6.3%		4.7%	
Mismatch (experiment) air	12.1%		8.8%	

"vac" refers to "vacuum", "pvac" refers to "partial vacuum"

TABLE 6.5: The theoretical, FEM simulation, and experimental results for the two beams in air and reduced pressure.

Comparison between the natural frequencies obtained for reduced pressure environment in Table 6.5 with those obtained in atmospheric pressure shows a shift in natural frequency due to reduction of pressure. The measured natural frequencies are slightly (~10-20Hz) shifted toward higher frequencies in reduced pressure. This phenomena has been investigated by other researchers ([43,54]) and is attributed to the effect of gas molecules being accelerated by the beam. The effect of gas molecules may be considered as an added mass to the effective mass of the beam. This added mass is varying with variation of air pressure causing a reduction in the effective mass of the beam and thus an increase in nat-

ural frequency. The variation of natural frequency of a resonating microbeam with air pressure is almost linear for the pressure range between 1000mbar (760 Torr) down to 10 mbar (7.6 Torr). A variation of ~1.6 ppm/mbar is predicted for natural frequency of a typical microbeam with pressure in this region. For pressures below 10mbar the natural frequency is almost insensitive to reduction in pressure [43].

(a)

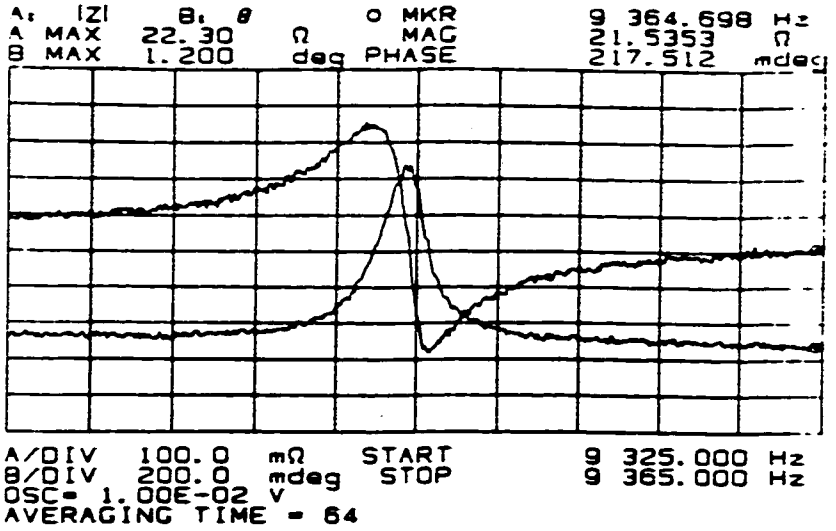

(b)

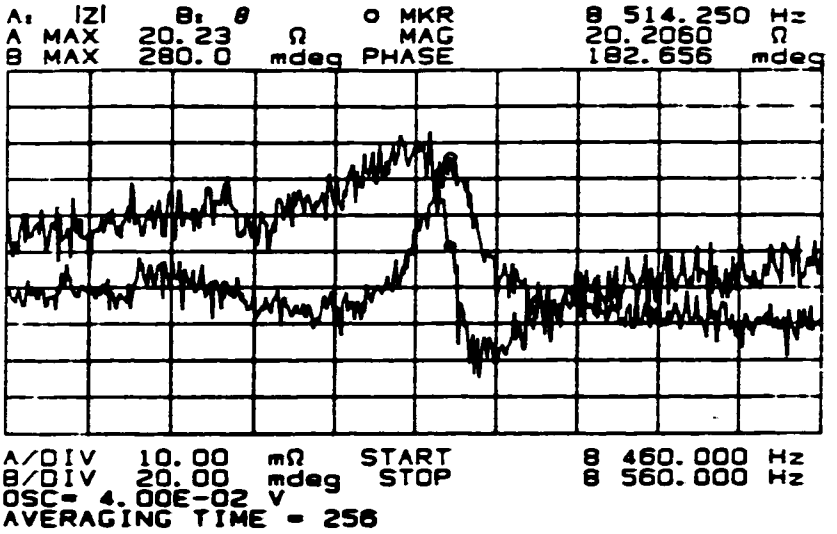

Fig. 6.36: Measured response of the beam#2 in reduced pressure: (a) Horizontal direction (b) Vertical direction. The frequency is varying on the horizontal axis (a) from 9325 Hz to 9365 Hz by 4 Hz/div (b) from 8460 Hz to 8560 Hz by 10 Hz/div. On vertical axis the impedance and phase are varying by (a) 100 mΩ/div and 200 mdeg/div (b) 10 mΩ/div and 20 mdeg/div.

The value of the shift induced in the natural frequency of the beams under the experiment (~2500ppm) indicates that the pressure inside the chamber is well below 10 mbar (7.6 Torr). Based on the nominal characteristic of the vacuum pump used and the amount of time that is allowed for the pump to create the vacuum (~15 hrs) the pressure in the vacuum jar is estimated to be 0.1 to 0.2 Torr.

The value predicted by theory for quality factors of the beam is (equation Eq.3.34, Sec.3.5.4) $Q_x \approx Q_y \approx 5300$, this matches the experimental value obtained in Table 6.5 for Q_x of the beams within acceptable tolerances, but there is a large error between experimental values obtained for Q_y and theory. This should be attributed to the presence of the glass cavity wall in close proximity to the beam. Although the pressure is reduced, the presence of wall still has a potential impact on the damping in the Y direction in this reduced pressure region. The damping of the beam in this region is not accurately predicted by either of the equations Eq.3.34 or Eq.3.33. The experimental value of Q_y is in between the values predicted by the two equations.

The induced EMF in the beams is smaller than the value obtained in atmospheric pressure. From the simplified model in Fig.6.26, the induced EMF is directly proportional to the value of R_m and also to the value of the actuation voltage V_{drive}. The value of R_m is directly proportional to Q_x (according to equation Eq.3.43) and therefore it increases in the reduced pressure environment. But the maximum voltage that can be applied to the beam before driving it into hysteresis decreases gradually in the reduced air pressure, this will reduce the maximum EMF. Therefore, as seen in Table 6.5, the maximum EMF induced in the actuation electrode effectively decreases by reducing the air pressure. This effect is also predicted by equation Eq.3.52, where the maximum sense voltage is inversely proportional to square-root of Q.

6.4 Fabrication of the Sensor

A simple fabrication procedure was used, as explained in Sec.6.2, to build some experimental beams in order to test and measure the basic parameters involved in the operation of the actual sensor, such as quality factor, natural frequency, induced EMF in horizontal direction, mismatch, and hysteresis effects. A complete sensor structure such as the one shown in Fig.3.1 should be fabricated in order to test other characteristics of the sensor, such as the Zero-Rate Output, and Coupling. This structure may also be used to measure the equivalent circuit model parameters shown in Fig.3.25, and also to find the coupling coefficients K_c and K_w in the model shown in Fig.4.1.

The fabrication procedure for the sensor consists of three parts, fabrication of the beam, fabrication of the glass with cavity, anodic bonding. The fabrication process of the beams is shown in Fig.6.37. Two cross-sectional views are shown for all of the steps. The overview of different masks used in the process are shown in Fig.6.39. All of the masks were fabricated using in-house mask fabrication process.

(i) Fabrication of the beam

1. The samples are cut from a special double-side-polished P-type wafer with a nominal thickness of 100μm. The samples are cleaned using the cleaning procedure.

2. A thermal oxide with a thickness of 5000 Å is grown on the samples using wet oxidation at 1100°C.

3. The samples are patterned using Mask#1 to open the ohmic contact windows in the oxide. The contacts are opened by etching the exposed oxide in BOE.

4. The samples are then cleaned using the cleaning procedure without HF dip. A layer of Borosilica gel is then spun on the samples. The drive-in step is then done at 1100°C for one hour.

5. The Borosilica layer and the oxide are removed from the samples in BOE.

6. A thermal oxide layer with the thickness of 1200 Å is grown on the samples by wet oxidation at 950°C.

7. First side of the samples is patterned using Mask#2 to open the etch windows and the contact windows in oxide. Backside of the samples is protected by photoresist and then the windows are opened by etching the samples in B.O.E.

8. A layer of Cr with the thickness of 1000 Å and a layer of Gold with the thickness of 2000 Å are deposited on the first side of the sample.

9. The Gold and Cr layer are then patterned using Mask#3 to form the electrodes and contacts to substrate.

10. The second side of the samples is patterned using Mask#4 which is a mirror image of Mask#2 without the contact windows. The first side of the samples is protected by photoresist while the open windows on the second side are etched in BOE.

11. The samples are then etched in TMAH first at 94°C for 1/4 of an hour, then the temperature is reduced to 80°C until the required width is obtained.

12. The overhanging oxide is removed by a short etch in BOE. The samples are the annealed in the annealing furnace to form the ohmic contact between metal and P++ regions.

(ii) Fabrication of the Glass substrate

The fabrication steps for the glass substrates is shown in Fig.6.38. The first 6 steps required to form the cavity in glass are similar to what mentioned in Fig.6.20 at Sec.6.2.3. (Mask#5 is used to pattern the glass) the rest of the steps are as follows:

7. A layer of Cr (1000 Å) and Gold (2000 Å) are deposited on the glass.

8. The layers are patterned using Mask#6 to from the electrode at the bottom of the

cavity.

(iii) Anodic bonding

The glass substrate and the beam frames are bonded together using field assisted bonding similar to that described in Sec.6.2.3.

The etch step for these samples is slightly different from what has been used for the previous test samples. Recent research has shown that etch rate of silicon in TMAH can be substantially reduced (almost stopped) by covering one side or parts of the sample with a metal like Cr or Gold that is resistant to TMAH [72]. The metal has to be in contact with the Si substrate. A Gold/Cr/Si/TMAH cell, formed by the evaporation of a Gold+Cr layer on the silicon, generates a passivation voltage internally causing the growth of an anodic oxide on the silicon surface. This oxide protects the silicon from being etched by TMAH. This effect may be used in many applications beneficially to produce etch-stop layers for fabricating thin membranes, but in our case this is an unwanted effect that has to be overcome. The etch-stop effect may be overcome by increasing the temperature to above 90°C. The etch rate of the oxide in TMAH increases at these temperatures preventing the formation of the thin anodic oxide layer explained above.

In this research, the samples are etched at 94°C first for about 1/4 of an hour and then the temperature is reduced to 80°C. The experiments show that it is possible to successfully etch the samples this way. The exact nature of the phenomenon is currently under investigation [73], and better understanding of the problem may result in other ways to etch the samples without increasing the temperature of TMAH.

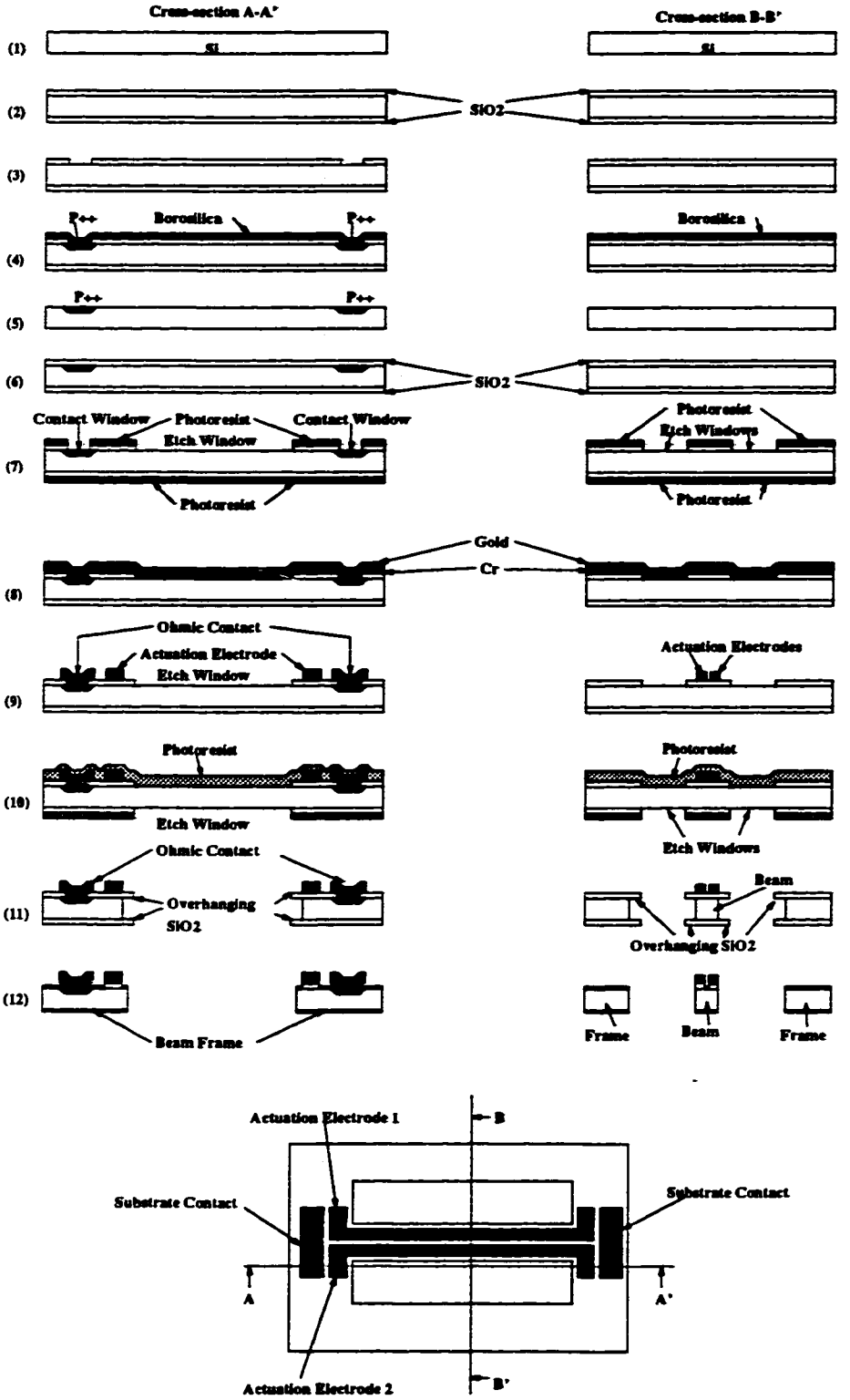

Fig. 6.37: Fabrication procedure for the beam.

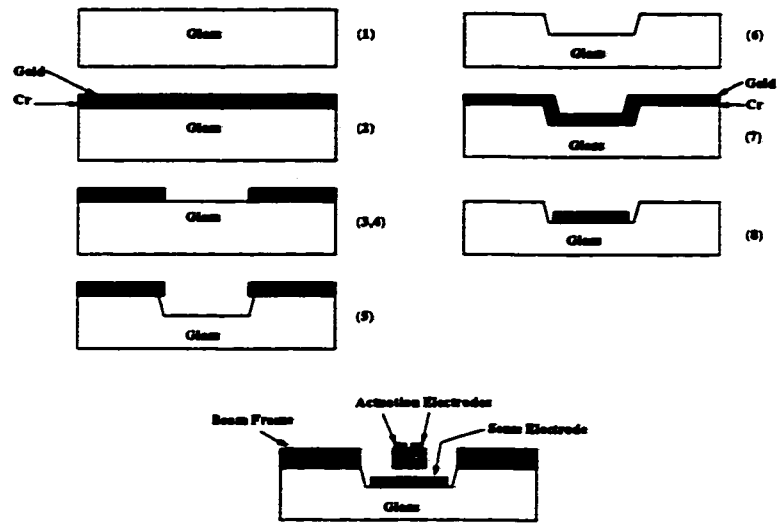

Fig. 6.38: Fabrication process of glass and anodic bonding.

6.5 Test of the Sensor

A sensor structure was fabricated with the following specifications:

Beam: Length=1 cm, Width=107 μm, Thickness=110 μm

Glass cavity depth=5 μm, Length of the capacitor electrode on glass=8 mm

6.5.1 Basic Equivalent Circuit Tests

The fabricated device is first tested to find the electrical parameters shown in the equivalent model of Fig.3.25 in Sec.3.6.1. An overview of the beam and its actuation electrodes together with its equivalent circuit is shown in Fig.6.40.

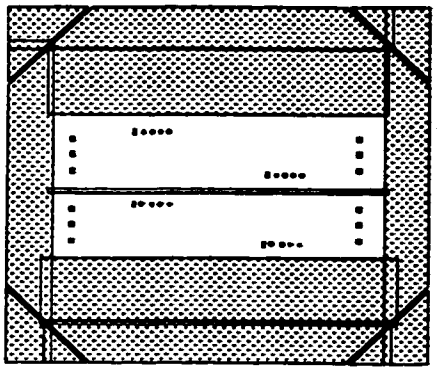

Mask#1

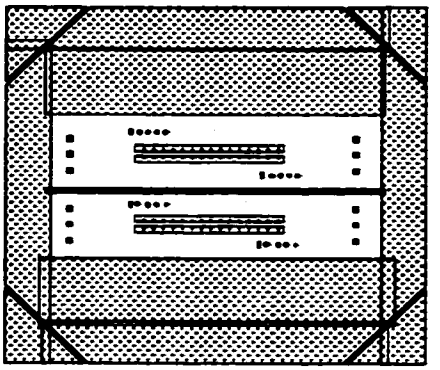

Mask#2

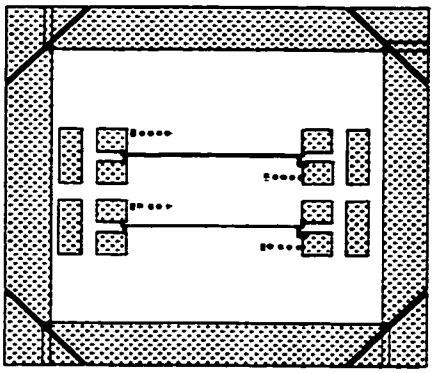

Mask#3

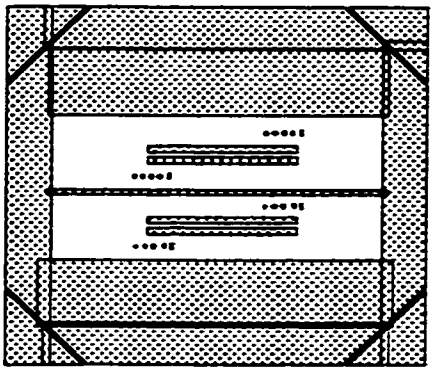

Mask#4

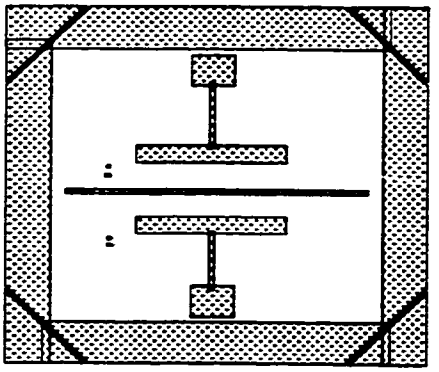

Mask#5

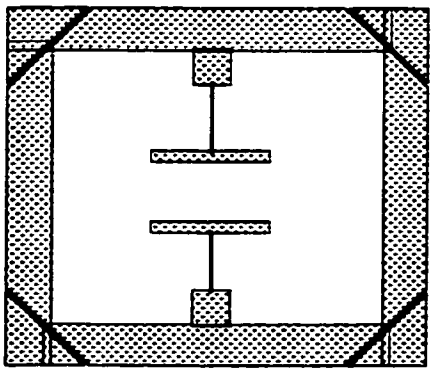

Mask#6

Fig. 6.39: Masks designed to fabricate beams and glass substrates.

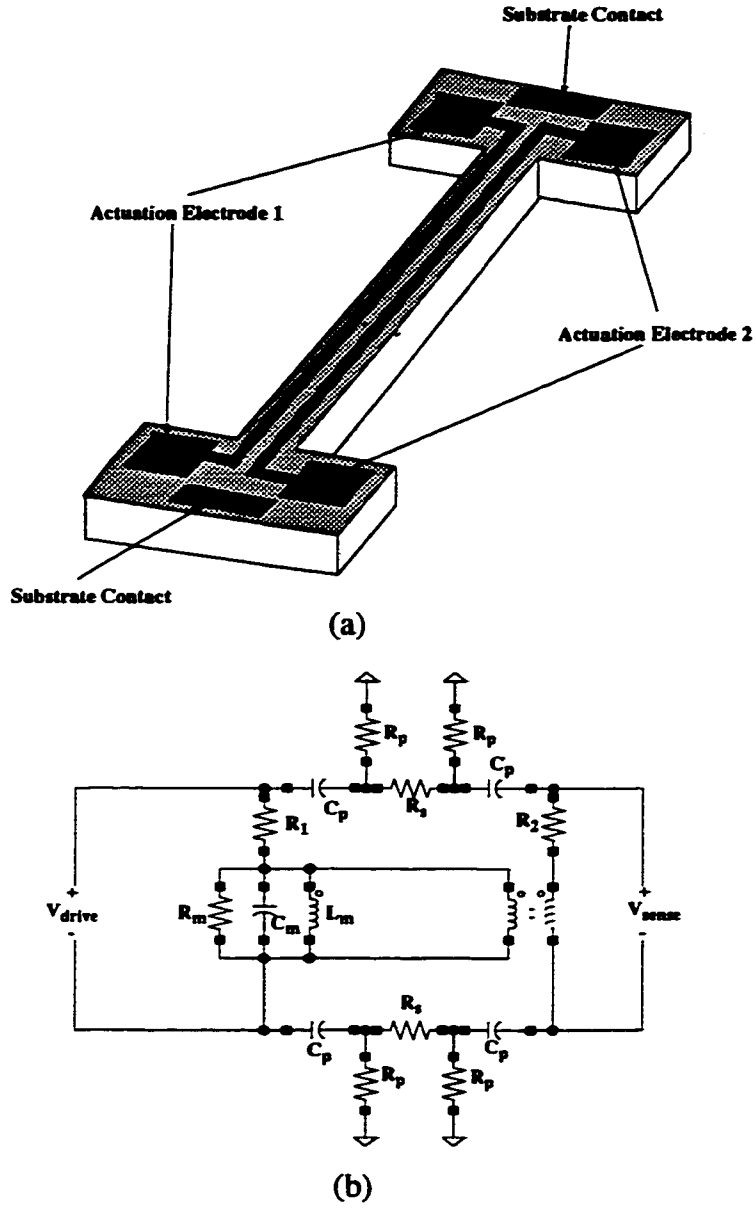

Fig. 6.40: (a) Overview of the beam and its actuation electrodes, (b) equivalent circuit of the beam.

A RLC meter is used to estimate the parasitic resistances (R_s, R_p) and capacitances (C_p) and the series resistance of the electrodes (R_1, R_2). The values of R_p and C_p were estimated by measuring the impedance between each actuation electrode and the substrate contact. The value of R_s was estimated by measuring the impedance between the two actu-

ation electrodes. The series resistances were estimated by measuring the resistance of each electrode. The measured values are:

$$R_1 = R_2 = 27\Omega,\ C_p = 224pF,\ R_s = 185\Omega,\ R_p = 221\Omega$$

The value of C_p is mostly dominated by the contact pads on the two ends of each electrode. The pads had to be made large enough to provide the required area for contacts made using regular wires connected with silver epoxy to the pads. This considerably increases the value of C_p. The value of R_p is mainly dominated by the resistance between the actuation electrode pads and the ground connection pads which are located close to each other.

6.5.2 Basic Mechanical Vibration Tests

The beam was then tested mechanically both in regular atmospheric pressure and in the low pressure environment using the same procedures as described in Sec.6.3.2 and Sec.6.3.3. The actuation input was set at $20mV$ to keep the beam response in the linear regime. The characteristics of the beam, obtained from experiment, are shown in Table 6.6. The value of Q_y is very low for this beam in atmospheric pressure. Therefore it is not possible to obtain the parameters f_y, Q_y, Mismatch.

The experimental values obtained for Q_x and Q_y are compared with the theory in Table 6.7. The value for Q_x predicted by theory using equations Eq.3.32 and Eq.3.33 for this beam in atmospheric pressure are Q_x=471, Q_y=1.2. These values match the experimental results in Table 6.6 within acceptable tolerances (note that the value of Q_y is so low that it can not be measured experimentally). However, the values obtained from theory (Eq.3.34) for reduced pressure environment is Q_x=Q_y=5909 which shows a large error compared to experiment for Q_x and even larger error for Q_y. As explained in Sec.6.3.3 this should again be attributed to the presence of the glass wall at a close proximity underneath

the beam. In this case, since the gap is smaller, both Q_x and Q_y are likely to be affected by the presence of glass wall. For both Q_x and Q_y, none of the equations developed for atmospheric and low pressure regimes can predict the Q accurately and the experimentally-measured value of Q is between the two extreme values obtained from equations (Eq.3.33, Eq.3.34).

	f_x	f_y	Q_x	Q_y	EMF	Mismatch
Air	8754 Hz	--------	562	--------	0.31 mV	----------
Reduced pressure	8764 Hz	8165 Hz	1874	910	0.22 mV	6.8%

TABLE 6.6: Experimentally measured parameters for the beam.

	Experimental		Theory	
	Q_x	Q_y	Q_x	Q_y
Air	562	--------	471	1.2
Reduced pressure	1874	910	5909	5909

TABLE 6.7: Experimental and theoretical values for Q_x and Q_y

6.5.3 Capacitance-To-Voltage Conversion

The sensor was connected according to the configuration shown in Fig.6.41. The simple Capacitance to Voltage converter circuit used in this configuration is shown in Fig.6.42.

A simple C/V converter circuit was built to detect the variation of capacitance at the output. The circuit consists of an FET input opamp (LF441) connected as a non-inverting amplifier with a gain of ~11. One input of the variable capacitance is connected to a DC supply and the other input is connected to the non-inverting input of the opamp. A large resistance is present at the non-inverting input, for dc biasing. A second gain stage with a

gain of 2 follows the first stage which acts as a buffer as well as a gain stage. The parasitic capacitances of this simple circuit due to wiring, resistor, and the opamp itself are reasonably large. The large 8MΩ resistor is also a source of thermal noise. However, for the purpose of finding approximate values for coupling and non-ideal mechanical effects (such as the effect of the beam's weight) this circuit is sufficient.

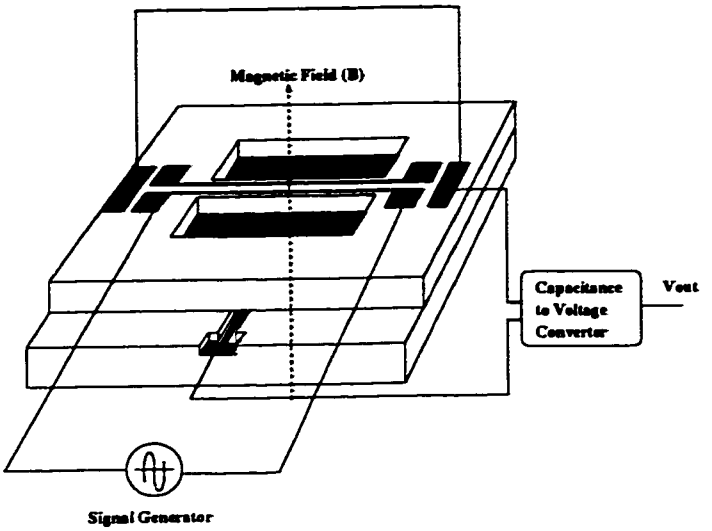

Fig. 6.41: Test setup for the sensor.

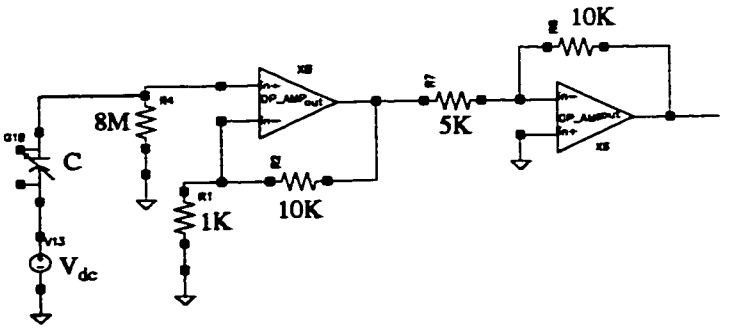

Fig. 6.42: Capacitance to voltage converter.

6.5.4 Zero-Rate-Output Measurements

The sample was placed in a reduced pressure environment in a vacuum jar. Actuation inputs with variable frequency and amplitude were applied to the actuation electrode and the output of the C/V converter was monitored. The sample was first aligned vertically (aligned with the y axis in Fig.3.42) to eliminate the side-effect of the weight of the beam. As the beam is actuated with a frequency close to its natural frequency in the x direction (f_x), a sinusoidal signal with the same frequency as the actuation input is detectable at the output of the C/V converter, due to coupling. This is called the zero-rate-output of the sensor. The measured variation of the output voltage vs. input frequency is plotted in Fig.6.43 for an actuation input level of V_{act}=*50 mV*. As seen from the figure the Zero-Rate-Output peaks at the natural frequency of the beam in the x direction where the amplitude of vibrations in x direction is maximum (The peak is slightly shifted to the right due to the amplitude stiffening effect). A constant output of ~1mV is measured at the output at all frequencies due to electrical feed-through of the signal from input to the output.

6.5.5 Estimation of Coupling Constants

Next the beam was actuated with different actuation amplitude levels. The frequency and amplitude of the measured peak at the output of C/V converter for each case are shown in Table 6.8. To relate these measured output voltages with the variations in capacitance between the beam and the electrode at the bottom of the cavity, a comparison between the measured outputs and the outputs of the HSPICE model of the C/V converter is performed. The HSPICE model of the C/V converter circuit (Fig.6.42) was built using the predefined HSPICE model of the opamps, and also by considering an estimated capacitor at the input of the circuit to account for the parasitic capacitances added by the wiring and the resistor (~2pF). This HSPICE model is simulated for each of V_{act} shown in the

Table 6.8 and the values of variations in C (ΔC) at the input of the model are adjusted to match the output of the simulation with the measured output voltage. An approximation for the variations in capacitance which resulted in the measured output in each case is obtained in this way, and appears in the third column of Table 6.8. Having the approximated variations in capacitance, the amplitude of the sense vibrations are then approximated using Eq.3.56 and appear in the 4th column of the table.

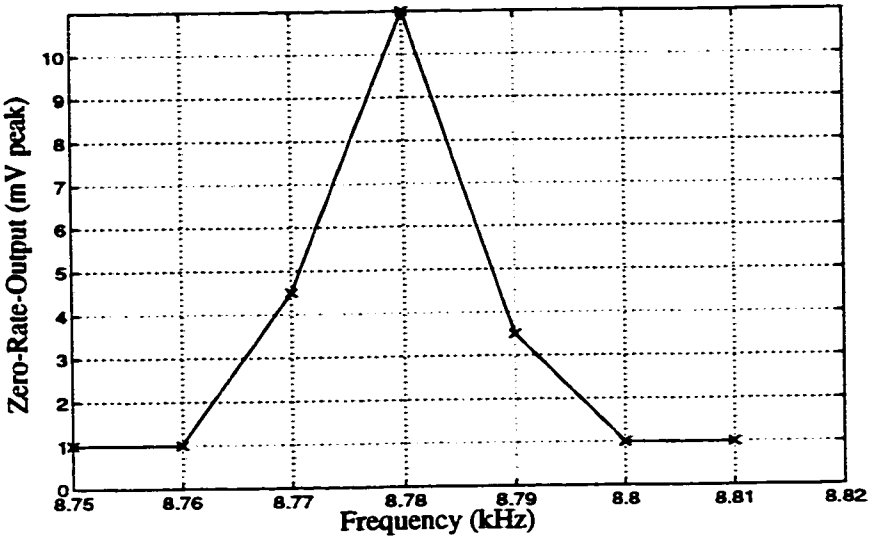

Fig. 6.43: Zero-rate output measured for an actuation input with V_{act}=50 mV peak.

V_{act}	Measured Peak Frequency	Measured Peak Amplitude	Estimated output ΔC	Calculated Sense Amplitude
10 mV	8.77 kHz	5.5 mVp-p	0.11 fF p-p	4.6 Å
20 mV	8.77 kHz	8.5 mVp-p	0.23 fF p-p	9.2 Å
30 mV	8.77 kHz	11.5 mVp-p	0.34 fF p-p	13.8 Å
40 mV	8.77 kHz	15 mVp-p	0.45 fF p-p	18.4 Å
50 mV	8.78 kHz	21 mVp-p	0.67 fF p-p	27.6 Å
60 mV	8.78 kHz	27.5 mVp-p	0.90 fF p-p	36.8 Å

TABLE 6.8: Measured peak output amplitude (zero-rate-output), estimated capacitance variations, and vibration amplitude for different input actuation levels. The beam was oriented vertically with respect to gravity (along the y axis in Fig.3.42).

The sample was then aligned horizontally along the x axis in Fig.3.42 where the effect of the weight of the beam on the zero-rate-output is maximum and the same parameters were measured again as shown in Table 6.9. The zero-rate-output increases drastically as a result of the coupling induced by the weight of the beam as predicted in Sec.3.6.3.

The HSPICE model of the sensor developed and tested in previous chapters may be used to find an approximate value for the total coupling coefficient in the two cases where the beam is placed horizontally and vertically. The characteristics obtained experimentally for the beam at reduced pressure in Table 6.6 are used in the model to have the maximum similarity between the response of the model and the experiment. The value of the K_c (from equation Eq.4.2) is then adjusted such that the output of the HSPICE model matches the output values obtained in Table 6.8 while $K_w=0$. Then the value of K_w is set such that the output of the model best matches with Table 6.9. The average values obtained for coupling coefficients K_c and K_w in this way are $K_c=0.095$ and $K_w=0.59$.

V_{act}	Measured Peak Frequency	Measured Peak Amplitude	Estimated Output ΔC	Calculated Sense Amplitude
10 mV	8.77 kHz	24 mVp-p	0.77 fF p-p	31 Å
20 mV	8.77 kHz	53 mVp-p	1.78 fF p-p	72 Å
30 mV	8.77 kHz	76 mVp-p	2.53 fF p-p	102 Å
40 mV	8.77 kHz	101 mVp-p	3.39 fF p-p	137 Å
50 mV	8.78 kHz	133 mVp-p	4.46 fF p-p	179 Å
60 mV	8.78 kHz	167 mVp-p	5.71 fF p-p	229 Å

TABLE 6.9: Measured peak output amplitude (zero-rate-output), estimated capacitance variations, and vibration amplitude for different input actuation levels. The beam was oriented horizontally (along the x axis in Fig.3.42).

6.6 Measurements Using Concave Corner Compensated Beams

The effect of the reduction of flange size on mismatch may be verified using a Finite-Element Model (FEM) simulation in ANSYS[1]. The effect of flange size reduction on natural frequencies and thus on total mismatch is verified using the FEM model built for beam#2 in Sec.6.3.1. The results of the FEM simulation for this beam are shown in Table 6.10 [65,66]. As seen from the table, a substantial enhancement of the mismatch may be obtained by reducing the flange sizes by ~3, which is a typical reduction ratio easily obtainable using the concave corner compensation technique. The mismatch is reduced even more by a reduction ratio of ~7 which is obtainable using the optimized patterns discussed in Chapter 5.

	f_y	f_x	Mismatch
Uncompensated	8870 Hz	9310 Hz	4.7%
Reduction ~3	8590 Hz	8880 Hz	3.2%
Reduction ~7	8550 Hz	8790 Hz	2.7%

TABLE 6.10: Comparison of the natural frequencies and mismatches obtained for beam#2 from a prestressed FEM simulation.

A beam was fabricated using the concave corner compensation patterns described in Chapter 5 and tested to find the effect of the flange size reduction on the mismatch. The dimensions of the beam are as follows:

Length=1cm, Width=102 μm, Thickness=104 μm, Flange-size reduction ~5x

The beam was bonded to a glass substrate. The sample was then placed in a vacuum jar and tested in order to find the natural frequencies. A plot of the measured mechanical response of this beam showing the two peaks associated with two natural frequencies is

1. Done in collaboration with Dr. T. Hubbard, from Dept. of Mech. Eng. of Technical University of Nova Scotia.

shown in Fig.6.44. The two natural frequencies are at f_x=*8380 Hz* and f_y=*8130 Hz*, respectively, resulting in a total mismatch of 3%. This is a substantial enhancement compared to the results obtained for the uncompensated beams (e.g. 6.8%-12.2% in Table 6.5, Table 6.6).

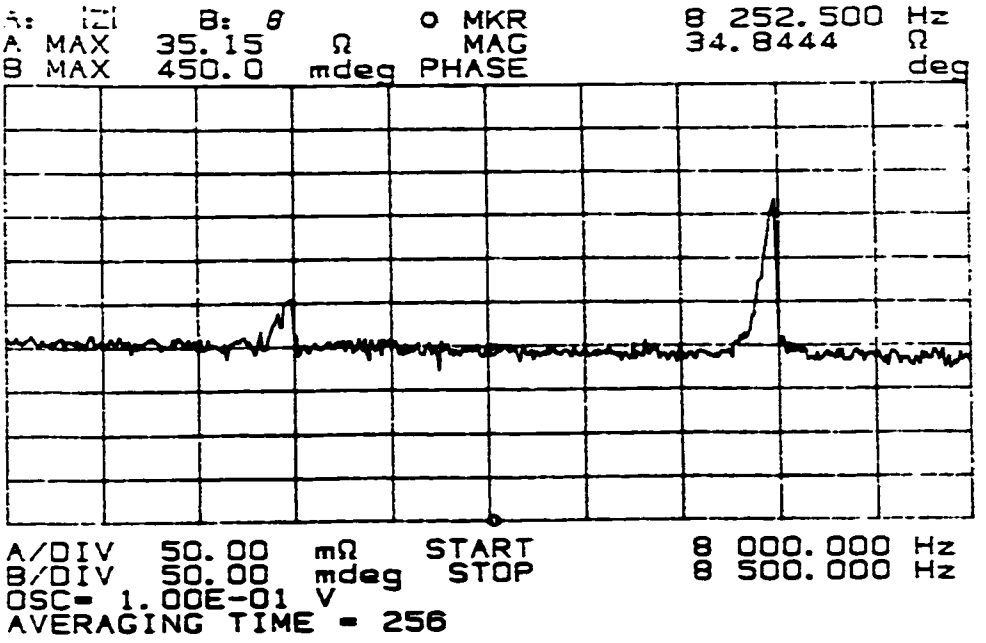

Fig. 6.44: Frequency response of a beam with concave corner compensated flanges with a reduction ratio of ~5x. The frequency is varying from 8000 Hz to 8500 Hz on the horizontal axis (50Hz/div), while the variations in impedance are shown on vertical axis (50mΩ/div). The two peaks f_x=8380 Hz and f_y=8130 Hz are clearly seen on the graph.

6.7 Implications for Overall Sensor Modeling and Performance

The overall model developed in Chapter 4 (see Fig.4.1) for the sensor may be re-simulated after substituting all of the parameters obtained from experiments (Q, natural frequencies, coupling coefficients, parasitic capacitances and resistances) for the fabricated sensor structure. The detector circuit shown in Fig.3.38 is considered in the model using

the available opamp cell from the Mitel 1.5 micron CMOS technology. The parasitic capacitances are modeled as described in Sec.3.6.2. The Gain and Synchronous Detector (see Fig.4.1) stages of the model are implemented using ideal behavioral models available in HSPICE. A 5th-order Butterworth low-pass filter with a cut-off frequency of 100Hz is considered for the Synchronous Detector. The overall gain of the Gain and Synchronous Detector stages is ~115. The model is actuated with an actuation input of 50mV to avoid the hysteresis effect in the actuation direction (due to amplitude stiffening). The simulated amplitude of actuation vibrations is ~3.4 μm and the simulated induced EMF in the beam is 0.25mV peak.

The response of the model to step inputs applied at *t=500ms*, and with amplitudes of 1rad/sec, 0.75 rad/sec, 0.5 rad/sec, and 0.25 rad/sec, is simulated in Fig.6.45. What is seen in Fig.6.45 is the output of the synchronous detector (after demodulation). A Zero-Rate-Output with an amplitude of ~5.4mV is present at the output, as seen in the figure. This Zero-Rate-Output is due to coupling and effect of the weight of the beam (K_c and K_w) and may be related to the previously discussed theory as follows:

Using the approximate sense amplitude found in Table 6.9 and Table 6.9 for V_{act}=50mV and considering Eq.3.61, it is possible to estimate the variables E and F (defined in Eq.3.60) to be: E=27.6Å, F=(179-27.6)=151Å. The amplitude of the Coriolis induced sense vibrations for 1rad/sec input angular rate may also be calculated to be ~9.2Å using the first term of Eq.3.61. Then Eq.3.61 may then be written for an input angular rate Ω=1 rad/sec in this case (V_{act}=50mV) as:

$$y_{out}(t) = \frac{9.2}{2}\cos(\phi) + \frac{(27.6 + 151\cos(\theta(t)))}{2}\sin(\phi) \qquad \text{Eq.6.5}$$

$$\phi = \phi_y + \phi_e \qquad \text{Eq.6.6}$$

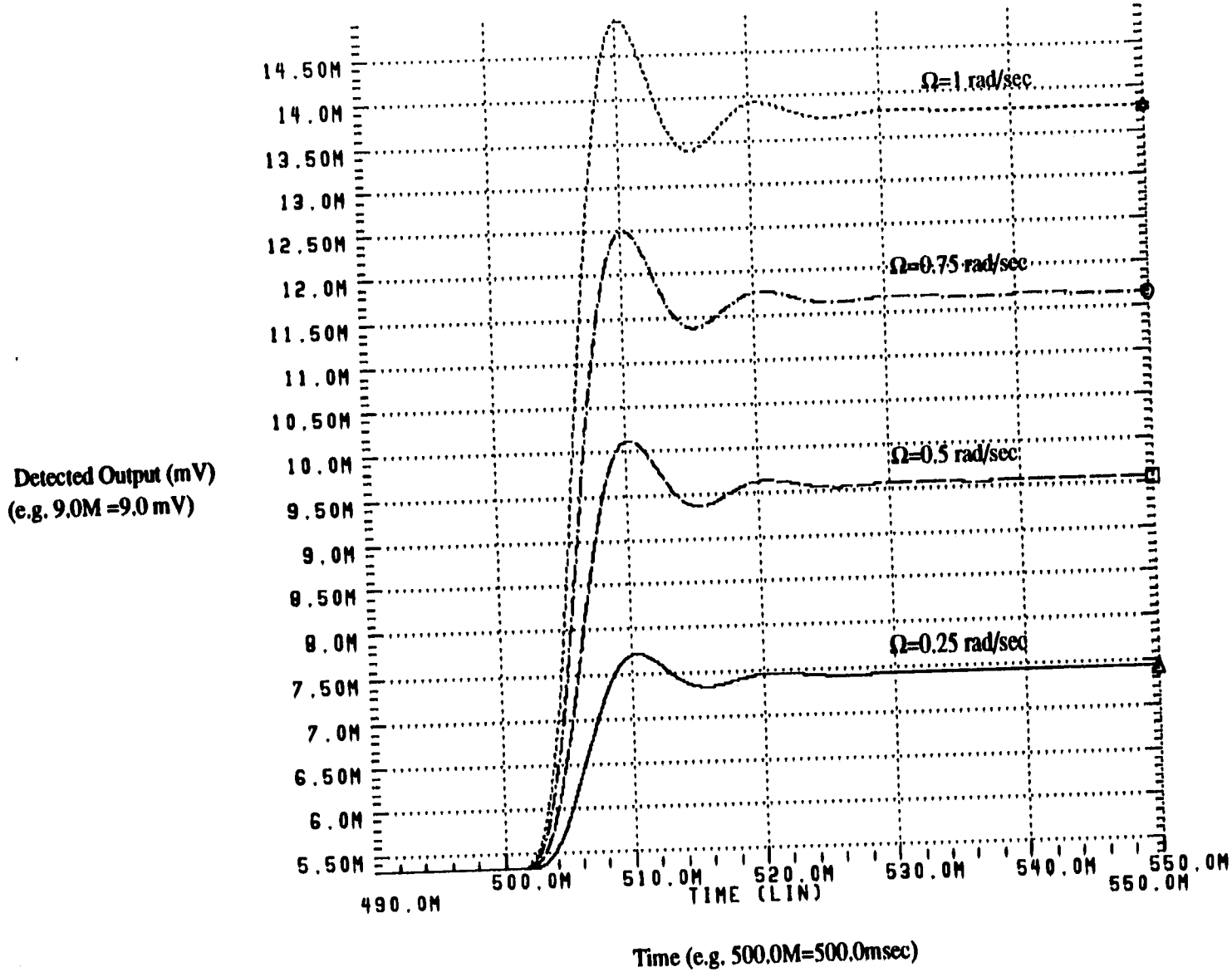

Fig 6.45: Simulated output of the sensor for Ω=1, 0.75, 0.5 , 0.25 rad/sec angular rate inputs.

where ϕ is the total phase delay between the reference signal used to demodulate the output and the sensed output signal (see Fig.3.33), which is composed of the mechanical phase delay of ϕ_y plus the phase delay of the electronic circuitry ϕ_e (detector and gain stages). It can be clearly seen from Eq.6.6 that the total phase delay ϕ must be very small, in order to minimize unwanted Zero-Rate-Output. For example, for a minimum detectable angular rate of 1^o/sec, a total phase delay of less than 0.05^o is required. A variable phase delay should be used to delay the reference signal and match the total phase delay to the above value. The variable phase delay shown in Fig.3.33 should be adjusted to keep the total phase delay ϕ within the required range. This may be very difficult to achieve since the total phase delay allowed between the signals is very small.

The total phase delay in the simulated sample may be found to be 1.83^o from the Zero-Rate-Output measured from Fig.6.45 and using Eq.6.5. In this case, this delay is composed of the mechanical delay and the delay of the detector circuit.

The output voltages obtained for different input angular rates are also shown in Fig.6.46. vs. input angular rates. As seen from this figure, the output varies linearly with input.

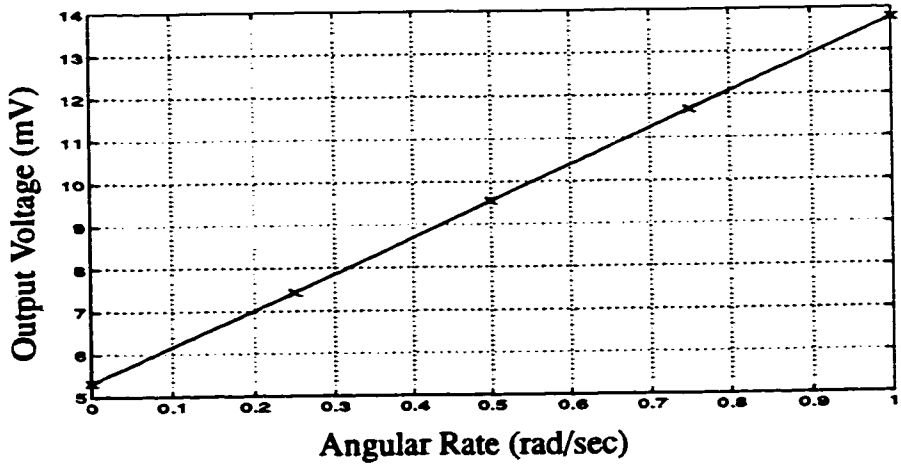

Fig. 6.46: Simulated variation of output voltage with input applied angular rate.

6.7.1 Effect of Concave Corner Compensation

The sample beam simulated in Sec.6.7 is without concave corner compensation patterns. The mismatch obtained for this sample from experiments is 6.8% (see Table 6.6). Experimental results show that it is possible to reduce the mismatch down to 3% using the concave corner compensation technique as discussed in Sec.6.6. The simulated output of the same sensor structure with a mismatch of 3% (instead of 6.8%) is compared with its original response for an angular rate input of 1 rad/sec in Fig.6.47. As seen from the figure, both the Zero-Rate-Output and the amplitude of the step response are increased as the mismatch decreases. This matches well with Eq.3.60 and Eq.3.61, where all of the terms E, F, and $\frac{X}{\Delta w}$ are found to vary inversely with Δw. The output values obtained for both the compensated and uncompensated beams are shown vs. various input angular rates in Fig.6.48.

As seen in Fig.6.47 there is not much difference between the output settling time for the two cases. This is due to the fact that in this case the settling time is limited by the bandwidth of the 100Hz filter which is smaller than the difference between the two natural frequencies for both cases. The relation between the bandwidth of the filter and the difference between the two natural frequencies is shown in Fig.6.49 for both of the compensated and uncompensated beams. As seen from the figure, the frequency response of the system before filtering has a distinct peak at the difference between the two natural frequencies (Δf) (as explained in Sec.3.6.2 and shown in Fig.3.36). The filter must have sufficient attenuation at this frequency to compensate for the high gain at the peak and ensure a flat bandwidth. In this case, as shown in the figure, the cut-off frequency of the filter ($f_{cut}=100Hz$) is small enough to provide the necessary attenuation at the peak frequency for both cases. However, it is clearly seen that by increasing the bandwidth of the filter, higher bandwidths may be achieved for the uncompensated design (compared to the

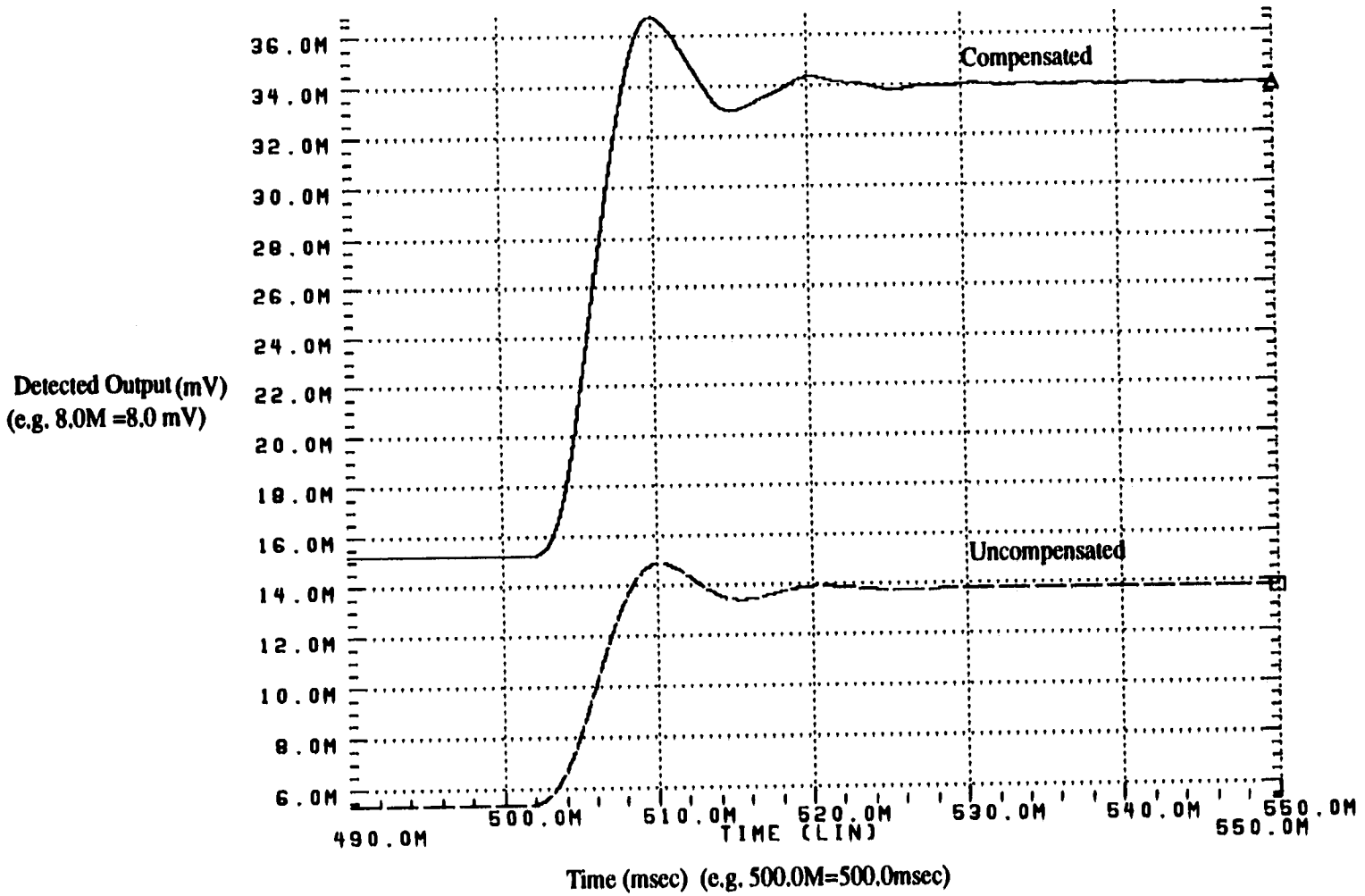

Fig. 6.47: Step responses for an uncompensated beam with a mismatch of 6.8% and a compensated beam with a mismatch of 3%.

compensated design) since the peak is occurring at a higher frequency for this design ($f_{cut1}>f_{cut2}$).

The bandwidth required for the sensor is usually determined by the type of application the sensor is built for. For example in this case were the bandwidth is limited to 100Hz a concave corner compensated beam with a reduced mismatch is certainly a better choice since it provides a better overall sensitivity ($G_3>G_2$) with the same bandwidth of 100Hz. Further reduction of mismatch will result in higher output amplitudes but as the difference between the two natural frequencies approaches the required bandwidth (f_{cut}=100Hz in this case) the constraints on the filter become tighter. The desired mismatch for an application may be found based on the required overall bandwidth and the type (and order) of the filter used in the synchronous demodulator.

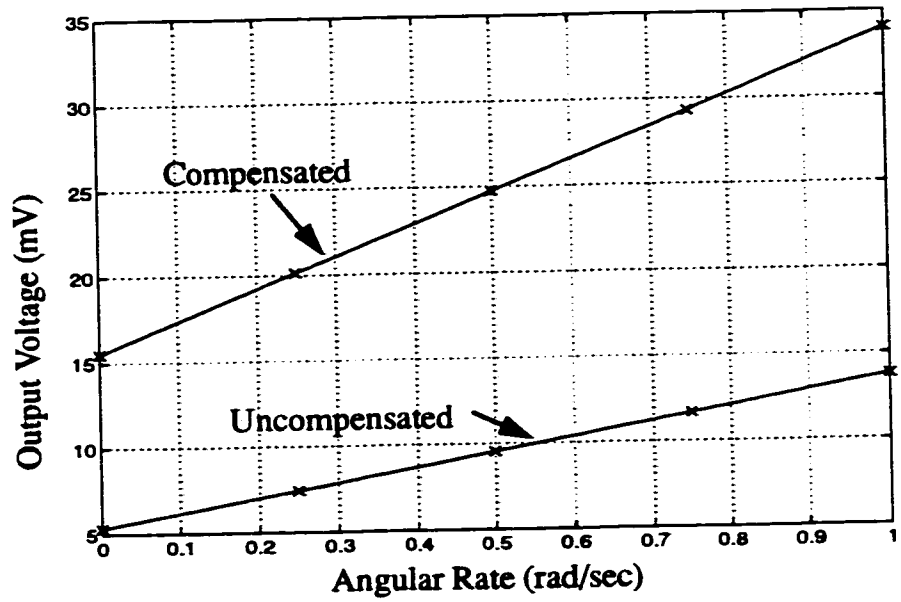

Fig. 6.48: Simulated output vs. angular rate input for uncompensated and compensated beams.

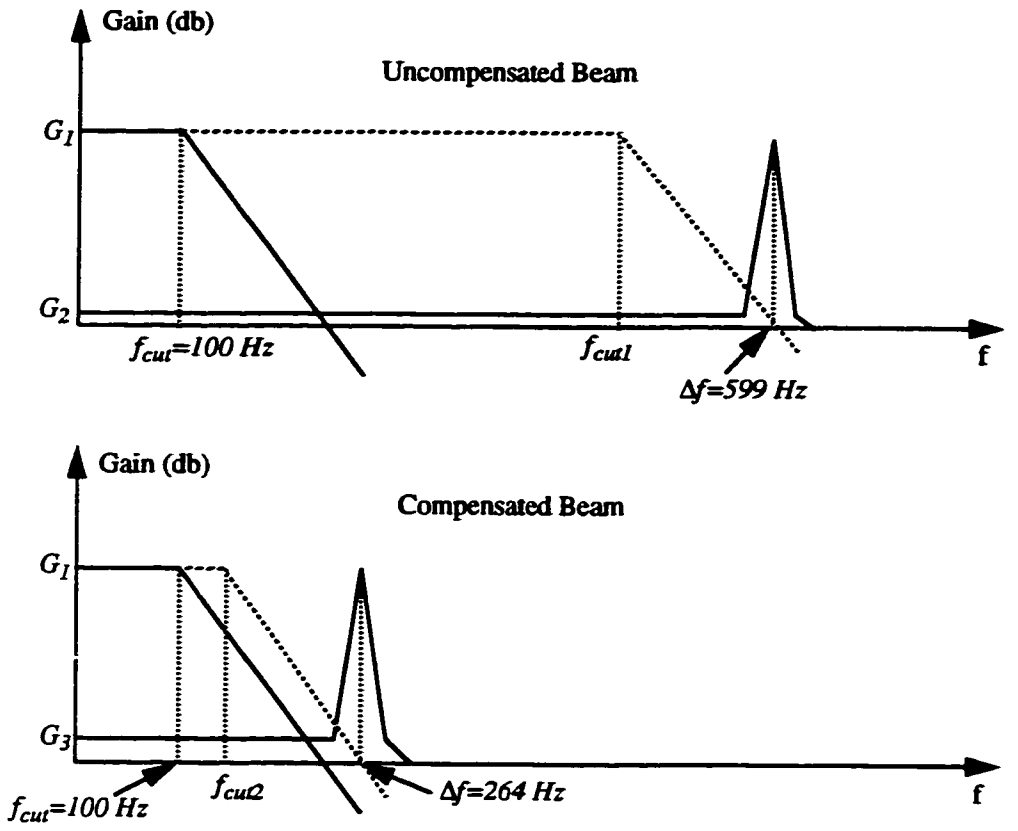

Fig. 6.49: Schematic Relationship between the bandwidth of the demodulation filter and the difference between the two natural frequencies (mismatch).

6.7.2 Overall Important Parameters

Several critical parameters that have to be considered carefully while designing an angular rate sensor, such as the ones discussed in this thesis, are shown in Table 6.11. The parameters considered during the basic sensor operation investigation in Chapter 4 are compared with the parameters obtained from experiments and re-simulation of the model in the light of experimental results.

Reference Section	Parameter	(a) Simulation	(b) Experiment	(c) Re-Sim.
	Beam & Glass Dimensions			
Sec.3.5.1.1	Beam Length	1 cm	1 cm	1 cm
Sec.3.5.1.1	Beam Width	105 μm	107 μm	107 μm
Sec.3.5.1.1	Beam Height	100 μm	110 μm	110 μm
Sec.3.5.4	Air Gap	5 μm	5 μm	5 μm
	Mechanical Parameters			
Sec.6.3.3	Air Pressure	----------	~0.1 Torr	~0.1 Torr
Sec.3.5.4, Eq.3.32 & Eq.3.34	Q_x	5000	1874	1874
Sec.3.5.4, Eq.3.33 & Eq.3.34	Q_y	1500	910	910
Sec.3.4, Eq.3.14	f_x	8114 Hz	8764 Hz	8764 Hz
Sec.3.4, Eq.3.14	f_y	7728 Hz	8165 Hz	8165 Hz
Sec.3.5.1, Eq.3.18	Mismatch	~5%	6.8%	6.8%
Sec.3.6.2, Fig.3.36	3db Bandwidth	~200 Hz	~320 Hz	~320 Hz
Sec.3.5.2, Eq.3.28	Sensitivity (1/rad/sec)	0.0004	0.00027	0.00027
Sec.3.5.3, Eq.3.31	Spring Softening	16.5 Hz	--------	~20 Hz
Sec.6.5.5	K_c (N/m)	---------	~0.09	~0.09
Sec.6.5.5	K_w (N/m)	---------	~0.59	~0.59
Sec.3.5.1.2, Eq.3.24	Threshold of Hysteresis-Free Actuation Amplitude	2.4 μm	~3.5 μm	~3.5 μm
	Operational Parameters			
Sec.3.4, Eq.3.5	Actuation Amplitude	2.35 μm	----------	~3.4 μm
Sec.3.6.1, Eq.3.49	Induced EMF	0.23 mV	----------	~0.25 mV
Sec.3.6.1.1, Eq.3.53	Dissipated Power	0.86 μW (rms)	----------	5.7 μW (rms)
Sec.3.4, Eq.3.11	Sense Amplitude	11 Å	----------	~9.2 Å
Sec.3.6.2, Eq.3.56	ΔC	0.33 fF p-p	----------	0.29 fF p-p
Sec.3.6.2	Detected Voltage (1 rad/sec input)	0.15 mV p-p	----------	0.14 mV p-p
Sec.6.7, Eq.6.6	Phase Delay	----------	----------	~1.83°
Sec.3.6.3, Eq.3.61	Zero-Rate-Output	----------	----------	~5.4 mV
Sec.4.3.2, Sec.6.7	Output/Input (V/rad/sec)	8.7 mV/rad/sec	----------	8.4 mV/rad/sec

TABLE 6.11: List of critical parameters that need to be considered during the design of the sensor: (a) obtained from original simulation of HSPICE model, (b) obtained from experimental results and (c) obtained from re-simulation and calculation of the model in light of the experimental results. The actuation voltage is chosen as a) V_{act}=20mV and c) V_{act}=50mV.

6.8 Chapter 6 Summary (Contributions are indicated by ✱)

. The fabrication procedure of the beams with square cross-section is explained and experimentally tested.

✱ Beams with precisely controlled dimensions, smooth vertical sidewalls, and sharp edges are fabricated using Si{100} silicon wafers, anisotropically etched in TMAH at 25wt%.

✱ Using a two step etch process the dimensions of the fabricated ~100μm-wide beams are matches within $\pm 2\mu m$ tolerance.

. The fabrication process of beams with concave corner compensated patterns is explained and experimentally tested. Several different patterns with various values of minimum feature size or safety margin are experimentally tested.

✱ Four different design patterns with various values of safety margin and minimum feature size are experimentally tested and the results are compared with the numerical simulation and graphical simulation results. A good match is found between the simulated and experimental results.

✱ A minimum flange width of ~60μm (reduction ratio of ~5.2) was experimentally obtained for a set of patterns with minimum feature size of 5μm.

✱ By allowing sufficient etch time from the time the sample is etched through ($Time_f$-$Time_{inv}$), fully formed concave corners with inverted flanges are achiev-

able.

. The fabricated beams are anodically bonded over a cavity etched in the glass substrates, coated with Aluminum and patterned to form test beam structures.

. The test beam structures are mechanically tested both under the regular atmospheric pressure and the reduced pressure. The tests are done both under the microscope and using HP4194 gain-phase analyzer.

* Several critical characteristics of the test beam structures are measured: natural frequency in horizontal and vertical directions, quality factor in horizontal and vertical directions, induced emf, non-linear hysteresis response, and natural frequency mismatch. They are satisfactorily compared with the results from theory (Chapter 3) and FEM simulation.

. Functional sensor structures are fabricated using Gold/Cr as conductors for actuation electrodes. The structures are characterized both electrically (to find the parasitic capacitances and resistances) and mechanically. The experimental results are compared with the theory.

* The zero-rate-output of the sensor is measured using a C/V converter circuit while the sensor was positioned horizontally and vertically. The values for coupling coefficient (K_c) and weight coefficient (K_w) were found by comparing the zero-rate-outputs obtained from experiment and the HSPICE model.

* The effect of concave corner compensation on the mismatch is shown both using the FEM simulation and experiment.

. The entire model of the sensor is re-adjusted in the light of the experimental results and simulated again after including all of the mechanical and electrical parameters obtained from the experiments.

CHAPTER 7

Summary of Contributions and Suggestions for Future Work

7.1 Introduction

The summaries of the contributions from each chapter are repeated here, followed by some suggestions for future research in this topic.

7.2 Summary of Contributions

7.2.1 Chapter 3

. An angular rate sensing device was designed based on a bulk-micromachined single-crystal silicon beam having square cross-section. Electromagnetic actuation using a small permanent magnet supplies the reference vibration, and the Coriolis-induced vibration is sensed by a capacitor plate in close proximity to the vibrating beam.

. The fabrication process is based on wet anisotropic etching of {100} silicon, and uses the specific anisotropy of TMAH at 25% to obtain vertical beam sidewalls, by orienting the mask-edge at 45^{o} to the wafer-flat and using a two-step etch process (at two different temperatures). The fabricated silicon beam/support is anodically bonded to glass, on which the metal sense capacitor is located.

* This design allows beams to be obtained with precisely matched dimensions, square cross-section, vertical smooth sidewalls, and sharp edges on Si{100}

wafers using this fabrication process.

. A Mass-Spring model has been provided to simulate the sensor's operation and performance.

. Several issues essential for a successful design have been considered including: actuation frequency and its effect on the output, actuation amplitude and its limitation due to the amplitude stiffening effect, sensitivity of the beam and its relation to the mismatch of horizontal and vertical resonant frequencies, spring softening effect in the sense direction and its effect on reducing the mismatch, air damping, and effect of coupling on increasing the mismatch.

* The amplitude-stiffened behavior of the beam and its effect on limiting the amplitude of the reference vibrations is discussed.
* The sensitivity of the device and its variations with different design parameters is explained.
* The spring-softening effect in the vertical direction and its possible application in tuning the mismatch between the two natural frequencies is explained.
* The damping by the air or coupling through the base is discussed and the necessity of reduced pressure environment for the operation of the device is shown.
* The effect of coupling between the two vibration modes and its effect on shifting the natural frequencies (increasing mismatch) is explained.

. The required circuitry for actuation of the beam and detection of the Coriolis induced vibrations was discussed, and some non-ideal effects, such as the effect of beam's weight and linear acceleration on the response, were presented.

* An equivalent electrical circuit model is presented for the actuation of the beam, including a tuning circuit to represent the mechanical response and the parasitic capacitors and resistors.
* Design parameters regarding the actuation system including the dissipated power in the actuation electrode, the maximum obtainable value for the induced emf in the beam, and the maximum induced stress in the beam are discussed.
* The detection circuit required to convert the variations in capacitance in the sense direction to a voltage is explained.
* The overall block diagram of the required circuitry to detect, amplify, and recover (demodulation) the coriolis induced signal at the output is explained.
* The relation between mismatch between the two natural frequencies and the bandwidth of the sensor is explained and it is shown that in an open-loop operation configuration the bandwidth is inversely proportional to the sensitivity.
* Non-ideal effects such as the effect of linear acceleration and the weight of the beam on the output signal is discussed. It is shown that a precise phase match is required at the demodulator in order to eliminate the non-ideal effects.

. A tuning fork structure was mentioned to potentially improve the performance of the sensor.

. A simulation model will be implemented in Chapter 4 based on the various principles and equations explained in this chapter. The response of the sensor and several issues such as spring softening, amplitude stiffening and the trade-off between the bandwidth and mismatch will be investigated using the developed model.

. Several experimental samples are fabricated and tested in Chapter 6 using the fabri-

cation process developed in this chapter. The samples are tested and the results are compared with the theory explained in this chapter.

7.2.2 Chapter 4

- A model is built using HSPICE to concurrently simulate both the mechanical and electrical elements of the sensor.
  - * The model includes many relevant non-linear and non-ideal effects of the mechanical behavior of the sensor and allows both the mechanical and electrical parts of the sensor to be simulated in an interrelated manner.

- A typical sensor structure is modeled and simulated using the developed model in HSPICE to find the steady state and transient response to input angular rates.

- The steady state response of the model is compared with the results from theory (Chapter 3). A sense vibration peak amplitude of ~10Å, and capacitance variation of 0.33fF p-p is obtained in response to an angular rate input of 1rad/sec.
  - * The resulting actuation amplitude, output sense vibration amplitude, induced EMF, and variations in capacitance obtained from the model match well with the theory outlined in Chapter 3.

- The non-linear behavior of the model including the spring-softening and amplitude-stiffening effects are compared with the expected results from theory.
  - * The model follows the expected behavior of the beam in the non-linear region within acceptable tolerances.

. The transient response of the sensor to a step input is investigated using the model and the results are compared for various mismatch values to show the trade-off between mismatch and settling time (bandwidth).

* The trade-off between the bandwidth and sensitivity is shown using the HSPICE model and compared with the theory.

7.2.3 Chapter 5

. The formation of flanges at the two ends of the beam during the fabrication of the beams is discussed.

* A beam with vertical sidewalls is achievable on a Si{100} wafer, but residual {111} flanges are an unavoidable side-effect at the concave corners at both ends of the beam.

* By etching from both sides of the wafer these {111} flanges can be turned inward, creating a re-entrant structure, also terminated by {111} planes.

. Concave corner compensation patterns are designed in order to reduce the size of the flanges. The design of the patterns, etch progress of the patterns, and the parameters and principles involved in successful design of such patterns is discussed in detail.

* Motivated by the need for symmetric clamping at the ends of the beam, in order to achieve a small enough mismatch between beam resonant frequencies in vertical and horizontal directions, a scheme of concave corner compensation patterns is devised, in order to substantially reduce the size of the residual {111} flanges.

* The success of the technique is sensitively dependent on the precise dimensions and placement of the rectangles, which must be designed using exact knowledge of the etch anisotropy of the particular etchant used, in this case TMAH at 25wt%. Critical parameters in designing the pattern are:
  - underetch rates of {111} ($U\{111\}$) and {100} ($U\{100\}$) planes,
  - angle of deviation, (ϕ), of fast-etch planes from the wafer flat,
  - underetch rate of fast-etch planes ($U\{\phi\}$),
  - length (L), width (W), row and column separations (S_r) and (S_c),
  - length (L_1) and width (w_1) of the last rectangle,
  - overlap (Δ) between the rectangles in adjacent columns,
  - initial distance (M) from the main etch cavity to the first closed rectangle.

* A numerical simulation program is developed to track the progress of the etch through the rectangles. Several sets of patterns were designed using the numerical simulation tool and simulated using a graphical simulation tool.

* The design principles are explained in detail and numerical simulation program is developed to track the progress of the etch fronts through the pattern of rectangles.

* The minimum obtainable flange width depends on width (w_1), Length (L, L_1), safety margin (*Margin*), and separation of rows (Sr) in the designed patterns. It also depends on the deviation angle of the fast etch planes (ϕ), and the ratio of the etch rate of {010} planes to the etch rate of fast etch planes ($U\{100\}/U\{\phi\}$) which are properties of the anisotropic etchant used.

* Several types of patterns are examined with a single set of rectangles and improved by the addition of a second set of smaller rectangles.

* The etch progress in the patterns is simulated using a graphical simulation tool and the results match very well with the numerical simulation results.

* For a beam with dimensions of ~100μm x ~100μm, a minimum flange width of ~40μm (reduction ratio ~7.25) is obtained using a single set of patterns (having a feature size of 5μm) using graphical simulation. This was improved to a minimum flange width of 18μm by using a secondary set of patterns (reduction ratio of ~16) with a feature size of 1μm.

7.2.4 Chapter 6

. Fabrication procedure of the beams with square cross-section is explained and experimentally tested.

* Beams with precisely controlled dimensions, smooth vertical sidewalls, and sharp edges are fabricated using Si{100} silicon wafers, anisotropically etched in TMAH at 25wt%.

* Using a two step etch process the dimensions of the fabricated ~100μm-wide beams are matches within ±2μ*m* tolerance.

. The fabrication process of beams with concave corner compensated patterns is explained and experimentally tested. Several different patterns with various values of minimum feature size or safety margin are experimentally tested.

* Four different design patterns with various values of safety margin and minimum feature size are experimentally tested and the results are compared with the numerical simulation and graphical simulation results. A good match is found between the simulated and experimental results.

* A minimum flange width of ~60μm (reduction ratio of ~5.2) was experimentally obtained for a set of patterns with minimum feature size of 5μm.

* By allowing sufficient etch time from the time the sample is etched through ($Time_f$-$Time_{inv}$), fully formed concave corners with inverted flanges are achievable.

. The fabricated beams are anodically bonded over a cavity etched in the glass substrates, coated with Aluminum and patterned to form test beam structures.

. The test beam structures are mechanically tested both under the regular atmospheric pressure and the reduced pressure. The tests are done both under the microscope and using HP4194 gain-phase analyzer.

* Several critical characteristics of the test beam structures are measured: natural

frequency in horizontal and vertical directions, quality factor in horizontal and vertical directions, induced emf, non-linear hysteresis response, and natural frequency mismatch. They are satisfactorily compared with the results from theory (Chapter 3) and FEM simulation.

. Functional sensor structures are fabricated using Gold/Cr as conductors for actuation electrodes. The structures are characterized both electrically (to find the parasitic capacitances and resistances) and mechanically. The experimental results are compared with the theory.

* The zero-rate-output of the sensor is measured using a C/V converter circuit while the sensor was positioned horizontally and vertically. The values for coupling coefficient (K_C) and weight coefficient (K_W) were found by comparing the zero-rate-outputs obtained from experiment and the HSPICE model.

* The effect of concave corner compensation on the mismatch is shown both using the FEM simulation and experiment.

. The entire model of the sensor is reconsidered in the light of the experimental results and simulated again after including all of the mechanical and electrical parameters obtained from the experiments.

7.3 Suggestions for Future Work

A set of proof of concept tests was done in this research. The work may be continued by design and fabrication of required circuit for actuation, detection and demodulation output signals. The sensor structure may be tested together with its circuit as a complete angular rate measurement sensor. Also, additional improvements may be done in the fabrication of the current structure. Use of other structures such as the tuning fork design, may be considered to improve the performance.

7.3.1 Actuation and Detection Circuit

The circuit required for maintaining the actuation vibrations at a precisely controlled output may be implemented as shown in Fig.3.27. Keeping a constant amplitude for the actuation vibrations precisely at the natural frequency of the beam in actuation direction is critical for the operation of the sensor.

The detection circuit has also a critical role in the operation of the sensor. The noise at the input of this stage is the limiting factor that eventually determines the minimum resolution of the sensor. Linearity and low noise operation of this block is a very important parameter in the sensor's operation. The synchronous detector or filtering may be done either in the analog or digital domain. An A/D converter would be necessary in any case to convert the analog signal to digital.

The sensor could be operated in a force-to-rebalance configuration to improve the bandwidth. The required circuit for this could be designed and tested.

7.3.2 Test of the Sensor

The sensor and its actuation and detection circuit should be placed in a reduced pressure environment (in a vacuum jar) and on a rotating table. The sensor should be rotated with various angular rates and the outputs measured and characterized.

7.3.3 Improvement in Fabrication of the Current Beam Structure

The concave corner compensation technique may be improved by using other etchants that may have a better {111}/{100} underetch ratio, which would result in a better reduction ratio especially with secondary patterns.

The dimensions of the fabricated beams may be varied (both the length, width, and thickness) to improve the performance. The weight of the beam has found to have a profound effect in limiting the minimum angular rate input detectable using the sensor structure. Smaller length, or larger thickness for the beams will greatly reduce this effect but higher actuation currents and thus higher power consumption would be required to operate the sensor. These trade-offs would have to be considered.

7.3.4 Alternative Structures

A double ended tuning fork structure is a superior structure to a single beam. More stable vibration, higher Q, and the possibility of detecting a differential capacitance output are among the most important advantages of such structure. The differential output of this structure would greatly reduce the effect of the weight of the beam and also the noise.

References

[1] M. W. Putty and K. Najafi, "A Micromachined Vibrating Ring Gyroscope," Solid-State Sensors and Actuators Workshop, Hilton Head, South California, June 13-16, 1994, pp. 213-220.

[2] A. Lawrence, "Modern Inertial Technology Navigation Guidance and Control," Springer-Verlag, NewYork, 1993, pp. 148-161.

[3] R. M. Langdon, "The Vibrating Cylinder Gyro," Marconi Rev., Vol. 45, 1982, pp. 231-249.

[4] M. Kurosawa, Y. Fukuda, M. Yakasaki, and T. Higuchi, "A Surface Acoustic Wave Gyro Sensor," Transducers 97, Chicago, Illinois, June 16-19, 1997, pp. 863-866.

[5] T. K. Tang, R. C. Gutierrez, J. Z. Wilcox, C. Stell, V. Vorperian, R. Calvet, W. J. Li, I. Charkaborty, and R. Bartman, "Silicon Bulk Micromachined Vibratory Gyroscope," Solid-State Sensors and Actuators Workshop, Hilton Head, South California, June 2-6, 1996, pp. 288-293.

[6] T. K. Tang, R. C. Gutierrez, C. B. Stell, V. Vorperian, G. A. Arakaki, J. T. Rice, W. J. Li, I. Chakraborty, K. Shcheglov, and J. Z. Wilcox, "A Packaged Silicon MEMS Vibratory Gyroscope for Microspacecraft," Proc. IEEE Micro Electro Mechanical Systems, Nagoya, Japan, Jan. 26-30, 1997, pp. 500-505.

[7] M. Lutz, W. Golderer, J. Gerstenmeier, J. Marek, B. Maihofer, S. Mahler, H. Munzel, and U. Bischof, "A Precision Yaw Rate Sensor in Silicon Micromachining," Transducers '97, Chicago, Illinois, June 16-19, 1997, pp. 847-850.

[8] H. Kuisma, T. Ryhanen, J. Lahdenpera, E. Punkka, S. Ruotsalainen, T. Sillanpaa, and H. Seppa, "A Bulk Micromachined Silicon Angular Rate Sensor," Transducers '97, Chicago, Illinois, June 16-19, 1997, pp. 875-878.

[9] R. Voss, K. Bauer, W. Ficker, T. Gleissner, W. Kupke, M. Rose, S. Sassen, J. Schalk, H. Seidel, and E. Stenzel, "Silicon Angular Rate Sensor for Automotive Applications with Piezoelectric Drive and Piezoresistive Read-Out," Transducers '97, Chicago, Illinois, June 16-19, 1997, pp. 879-882.

[10] K. Maenaka and T. Shiozawa, "A Study of Silicon Angular Rate Sensors Using Anisotropic Etching Technology," Sensors and Actuators, A43, May 1994, pp. 72-77.

[11] K. Maenaka and Yasushi Konishi, "Analysis and Design Concept of Highly Sensitive Silicon Rate Gyroscope," Transducers '95, Stockholm, Sweden, June 25-29, 1995, pp. 612-615.

[12] K. Maenaka and T. Shiozawa, "Silicon Rate Sensor Using Anisotropic Etching Technology," Transducers '93, Yokohama, Japan, June 7-10, 1993, pp. 642-645.

[13] P. Greiff, B. Boxenhorn, T. King, and L. Niles, "Silicon Monolithic Micromechanical Gyroscope," Proc. IEEE Micro Electro Mechanical Systems, Fort Lauderdale, Florida, Feb. 7-10, 1993, pp. 225-229.

[14] M. Hashimoto, C. Cabuz, K. Minami, and M. Esashi, "Silicon Resonant Angular Rate Sensor Using Electromagnetic Excitation and Capacitive Detection," Journal of Micromechanics and Microengineering, Vol. 5, Sept. 1995, pp. 219-225.

[15] J. Burdess, A. Harris, and J. Cruickshank, "A Silicon Membrane Gyroscope with Electrostatic Actuation and Sensing," Proc. SPIE, Austin, Texas, Oct. 23-24, 1995, pp. 74-83.

[16] D. R. Sparks, S. R. Zarabadi, J. D. Johnson, Q. Jiang, M. Chia, O. Larsen, W. Higdon, and P.C. Borelley, "A CMOS Integrated Surface Micromachined Angular Rate Sensor: Its Automotive Applications," Transducers '97, Chicago, Illinois, June 16-19, 1997, pp. 851-854.

[17] Y. Oh, B. Lee, S. Baek, H. Kim, J. Kim, S. kang and C. Song, "A Surface Micromachined Tunable Vibratory Gyroscope," Proc. IEEE Micro Electro Mechanical Systems, Nagoya, Japan, Jan. 26-30, 1997, pp. 272-277.

[18] T. Juneau and A. P. Pisano, "Micromachined Dual Input Axis Angular Rate Sensor," Solid-State Sensors and Actuators Workshop, Hilton Head, South California, June 2-6, 1996, pp. 299-302.

[19] W. A. Clark, R. T. Howe and R. Horowitz, "Surface Micromachined Z-Axis Vibratory Rate Gyroscope," Solid-State Sensors and Actuators Workshop, Hilton Head, South California, June 2-6, 1996, pp. 283-287.

[20] T. Fujita, T. Mizuno, R. Kenny, K. Maenaka and M. Maeda, "Two-Dimensional Micromachined Gyroscope," Transducers '97, Chicago, Illinois, June 16-19, 1997, pp. 887-890.

[21] T. Juneau, A. P. Pisano, and J. H. Smith, "Dual Axis Operation of a Micromachined Rate Gyroscope," Transducers '97, Chicago, Illinois, June 16-19, 1997, pp. 883-886.

[22] K. Y. Park, C. W. Lee, Y. S. Oh and Y. H. Cho, "Laterally Oscillated and Force Balanced Vibratory Rate Gyroscope Supported By Fish Hook Shape Springs," Proc. IEEE Micro Electro Mechanical Systems, Nagoya, Japan, Jan. 26-30, 1997, pp. 494-499.

[23] K. Tanaka, Y. Mochida, and S. Sugimoto, "A Micromachined Vibrating Gyroscope," Proc. IEEE Micro Electro Mechanical Systems, Amsterdam, Netherlands, Jan. 29 - Feb. 2, 1995, pp. 278-281.

[24] R. E. Barnaby, J. B. Chatterton and F. H. Gerring, "General Application and Operational Characteristics of the Gyrotron Angular Rate Tachometer," Aeronaut. Eng. Rev., Vol. 12, No. 11, 1953, pp. 31-36.

[25] W. D. Gates, "Vibrating Angular Rate Sensor may threaten the Gyroscope," Electronics, Vol. 41, No. 10, 1968, pp. 130-134.

[26] W. S. Watson, "Angular Rate Sensor Apparatus," Eur. Patent Applic. No. 0 084 704, Nov. 17, 1982.

[27] J. H. Staudte, "Vibratory Angular Rate Sensor," US Patent No. 4 524 619, Jan. 25, 1985.

[28] C. Song, "Commercial Vision of Silicon Based Inertial Sensors," Transducers '97, Chicago, Illinois, June 16-19, 1997, pp. 839-842.

[29] B. Barshan and H. F. Durrant-Whyte, "Evaluation of a Solid-State Gyroscope for Robotics Applications," IEEE Transactions on Instrumentation and Measurement, Vol. 44, No. 1, Feb. 1994, pp. 61-67.

[30] J. Soderkvist, "Micromachined Gyroscopes," Sensors and Actuators, A43, 1994, pp. 65-71.

[31] S. Fujishima, T. Nakamura, and K. Fujimoto, "Piezoelectric Vibratory Gyroscope Using Flexural Vibration of a Triangular Bar," Proc. 45th Symp. Frequency Control, Los Angeles, California, 1991, pp. 261-264.

[32] J. D. Nuttall, "Development of a Solid-State Gyroscope," Proc. Symp. Gyro Technology, Stuttgart, Germany, 1990, pp. 5.1-5.14.

[33] J. Bernstein, S. Cho, A. Kourepenis, P. Maciel, and M. Weinberg, "A Micromachined Comb-Drive Tuning Fork Rate Gyroscope," Proc. IEEE Micro Electro Mechanical Systems, Fort Lauderdale, Florida, Feb. 7-10, 1993, pp. 143-148.

[34] W. Tang, T. Nguyen, M. Judy, and R. Howe, "Electrostatic Comb Drive of Latheral Polisilicon Resonators," Sensors and Actuators, A21-A23, 1990, pp. 328-331.

[35] W. Tang, T. Nguyen, and R. Howe, "Laterally Driven Polysilicon Resonant Micro-

structures," Tech. Dig. IEEE Micro Electromech. Syst. Workshop, Salt Lake City, UT, Feb. 20-22, 1989, pp. 53-59.

[36] T. Hirano, T. Furuhata, K. Gabriel, and H. Fujita, "Design, Fabrication, and Operation of Submicron Gap Comb-Drive Microactuators," Journal of Microelectromechanical Systems, Vol. 1, No. 1, March 1992, pp. 52-59.

[37] K. E. Petersen, "Silicon as a Mechanical Material," Proc. IEEE, Vol. 70, No. 5, May 1982, pp. 420-457.

[38] B. Nikpour, L. M. Landsberger, B. Haroun, and M. Kahrizi, "Processes to Achieve Vibrating Beams for an Angular Rate Measurement Sensor," 1996 Canadian Conference on Electrical and Computer Engineering, Calgary, Alberta, May 26-29, 1996, pp. 76-79.

[39] S. Naseh, "Experimental Investigation of Anisotropic Etching of Silicon in Tetra-Methyl Ammonium Hydroxide," M.Sc. Thesis, Concordia University, Montreal, Quebec, 1995.

[40] W. Choi and J. G. Smits, "A Method to Etch Undoped Silicon Cantilever Beams," Journal of Microelectromecahnical Systems, Vol. 2, No. 2, June 1993, pp. 82-86.

[41] P. M. Zavracky, T. Earls, and N. L. Porkrovskiy, "Fabrication of Vertical Sidewalls by Anisotropic Etching of Silicon (100) Wafers," J. Electrochem. Soc., Vol. 141, No. 11, Nov. 1994, pp. 3182- 3188.

[42] S. Rao, "Mechanical Vibrations," Addison-Wesley, NewYork, 1990, pp. 412-413.

[43] R. A. Buster and N. F. De Rooji, "Resonant Silicon Structures," Sensors and Actuators, A17, 1989, pp. 146-153.

[44] R. A. Buser and N. F. De Rooji, "Tuning Forks in Silicon," IEEE Micro Electro Mechanical Systems Workshop, Salt Lake City, UT, Feb. 1989, pp. 94-95.

[45] S. Bouwstra and B. Geijselaers, "On the Resonance Frequencies of Micro-

Bridges," Proc. IEEE Micro Electro Mechanical Systems, Nara, Japan, 1991, pp. 538-542.

[46] C. Gui, R. Legtenberg, and H. Tilmans, "Nonlinearity and Hysteresis of Resonant Strain Gauges," Proc. IEEE Micro Electro Mechanical Systems, Amsterdam, Netherlands, Jan. 29 - Feb. 2, 1995, pp. 157-162.

[47] L. S. Fan and L. Crawford, "Spring-Softening Effect in MEMS Microstructures," Transducers '93, Yokohama, Japan, June 7-10, 1993, pp. 767-769.

[48] K. Ikeda, H. Kuwayama, T. Kobayashi, T. Watanabe, T. Nishikawa, T. Yoshida, and K. Hanada, "Study of Nonlinear Vibration in Silicon Resonant Beam Strain Gauges," Proc. of 8th Sensor Symp., Tokyo, Japan, 1989, pp. 21-24.

[49] M. V. Andres, K. W. H. Foulds and M. J. Tudor, "Nonlinear Vibrations and Hysteresis of Micromachined Silicon Resonators Designed as Frequency Out Sensors," Electronic Letters, Vol. 23, 1987, pp. 952-953.

[50] S. G. Adams, F. Bertsch, and N. MacDonald, "Independent Tuning of the Linear and Nonlinear Stiffness Coefficients of a Micromachined Device," Proc. IEEE Micro Electro Mechanical Systems, San Diego, California, 1996, pp. 32-37.

[51] T. E. Shirley and S. D. Senturia, "Frequency-Pulling Effects in Amplitude-Stiffened Resonant Sensors," Transducers '93, Yokohama, Japan, June 7-10, 1993, pp. 458-461.

[52] X. Zhang and W. C. Tang, "Viscous Air Damping in Laterally Driven Microsensors," Journal of Microelectromechanical Systems, Vol. 3, No. 2, pp. 81-87.

[53] W. E. Newell, "Miniaturization of Tunning Forks," Science, Vol. 161, 1968, pp. 1320-1326.

[54] R. A. Buser and N. F. De Rooji, "Very High Q-factor Resonators in Monocrystalline Silicon," Sensors and Actuators, A21, 1990, pp. 323-327.

[55] R. Mihailovich and N. MacDonald, "Dissipation Measurements of Vacuum-operated Single-Crystal Microactuators," Sensors and Actuators, A50, 1995, pp. 199-207.

[56] H. Hosaka, K. Itao, and S. Kuroda, "Evaluation of Energy Dissipation Mechanisms in Vibrational Microactuators," Proc. IEEE Micro Electro Mechanical Systems, 1993, pp. 193-198.

[57] H. Hosaka, K. Itao, and S. Kuroda, "Damping Characteristics of Beam-Shaped Micro-Oscillators," Sensors and Actuators, A49, 1995, pp. 87-95.

[58] J. M. Paros, "Digital Quartz Transducers for Absolute Pressure Measurement," ISA 21st Int. Instrum. Symp., Philadelphia USA, May 1975, pp. 435-439.

[59] S. S. Chuang, "Force Sensor Using Double-Ended Tuning Fork Quartz Crystals", ISA 29th Int. Instrumentation Symp., May 1983, pp. 248-254.

[60] W. J. Kass and G. S. Snow, "Double-Ended Tuning Fork Quartz Accelerometer," 40th Annual Frequency Control Symposium, 1986, pp. 230-236.

[61] J. Soderkvist, "An Equivalent Circuit Description of Two Coupled Vibrations," J. Acoust. Soc. Am., Vol. 90, No. 2, 1991, pp. 693-699.

[62] G. A. Olsen, "Elements of Mechanics of Materials," Prentice-Hall, N.J., 1982.

[63] H. B. Bakoglu, "Circuits, Interconnections, and Packaging for VLSI," Addison-Wesley, NewYork, 1990.

[64] H. J. Ahmed, "Design of a 2-Dimensional Single-Chip Accelerometer," M.Sc. Thesis, University of Concordia, Montreal, Quebec, 1995.

[65] B. Nikpour, L. M. Landsberger, T. J. Hubbard, M. Kahrizi, and A. Iftimie, "Patterns for Concave Corner Compensation Between Vertical (010)-(001) Planes on Si(100) Anisotropically Etched in TMAH," Transducers '97, Chicago, Illinois, June 16-19, 1997, pp. 691-694.

[66] B. Nikpour, L. M. Landsberger, T. J. Hubbard, M. Kahrizi, and A. Iftimie, "Concave Corner Compensation Between Vertical (010)-(001) Planes Anisotropically Etched in Si(100)," Submitted to Sensors and Actuators Journal, Oct. 1997.

[67] L. M. Landsberger, S. Naseh, M. Kahrizi, and M. Paranjape, "On Hillocks Generated During Anisotropic Etching in Si in TMAH," IEEE Journal of Microelectromechanical Systems, Vol. 5, 1996, pp. 106-116.

[68] T. J. Hubbard and E. K. Antonnson, "Emergent Faces in Silicon Micromachining," IEEE Journal of Microelectromechanical Systems, Vol. 3, 1993, pp. 19-28.

[69] T. J. Hubbard and E. K. Antonnson, "Design of MEMS via Efficient Simulation of Fabrication," 1996 ASME Design for Manufacturing Conference, Irvine, California, 96-DETC/DFM-1312.

[70] W. H. Ko, "Bonding Techniques for Micro-Sensors," Micromachining and Micropackaging of Transducers, Elesevier Science Publishers, B.V., Amsterdam, 1985, pp. 41-61.

[71] G. Wallis, "Field Assisted Glass Sealing," Electrocomponent Science and Technology, Vol. 2, No. 1, 1975, pp. 45-53.

[72] C. Ashruf, P. French, P. Sarro, M. Ngao, M. Esashi, "Fabrication of Micromechanical Structures with a New Electrodeless Electrochemical Etch Stop," Transducers '97, Chicago, Illinois, June 16-19, 1997, pp. 703-706.

[73] A. Pandy, L. M. Landsberger, B. Nikpour, M. Paranjape, M. Kahrizi, "Experimental Investigation of High Si/Al Selectivity During Anisotropic Etching in TMAH," Canadian Semiconductor Technology Conference, Ottowa, Canada, August 12-15, 1997.

APPENDIX I

HSPICE Simulation Program

```
************* Include Standard Libraries From Mitel15 Technology *************
.LIB '/project/vlsi/behrouz/icbhspice/mitel15.hspice' nominal
.LIB 'opamps.sp' opamp0

************************* Parameter Definitions ******************************
* Pi
.PARAM  pi=3.1416
* Si Young's modulus N/m^2
.PARAM  E=1.3e11
* Si Unit volume's mass Kg/m^3
.PARAM  ro=2.3e3
* Beam's Dimensions (h=height, b=width, L=Length)
.PARAM h=110e-6 b=107e-6 L=1e-2
* Quality Factor and damping
.PARAM  Q=1874
.PARAM  Zetta='1/(2*Q)'
.PARAM  Qy=900
* Series Resistance of the Beam
.PARAM  Res1=27
* Magnetic Field (Tesla)
.PARAM  BF=0.25
```

```
* Beam's Mass
.PARAM  m0='ro*b*h*L'
* Moment of Inertia of the Beam in two directions
.PARAM  Ix='(1/12)*h*b*b*b'  Iy='(1/12)*b*h*h*h'
* Spring Constant of the Beam in two directions
.PARAM  Kx='384*E*Ix/(L*L*L)'  Ky='384*E*Iy/(L*L*L)'
* Natural Frequencies along the two directions
.PARAM  wx0='(4.73/L)*(4.73/L)*sqrt(E*Ix/(ro*b*h))'
.PARAM  wy0='(4.73/L)*(4.73/L)*sqrt(E*Iy/(ro*b*h))'
.PARAM  Muy='m0*wy0/Qy'
* Effective length of the capacitor's electrode
.PARAM  Leff=8e-3
* Correction Factor for capacitance calculation
.PARAM  Ccorrect=1.1
* Effective area of detection capacitor
.PARAM  Area='b*Leff '
* Permitivity of the air
.PARAM  Epsilon=8.854e-12
* Initial distance between the detection capacitor plates
.PARAM  d=5e-6
* Initial Capacitance
.PARAM  Cap0='Epsilon*Area/d'
* Coupling between the two modes (N/m)
.PARAM  Kc=0.09
```

```
* Effect of the weight of the beam
.PARAM  Kw=0.59

* DC voltage
.PARAM Vdc=7

* Equivalent RLC tuning circuit for Beam
.PARAM   Rmech='(BF*L)*(BF*L)/(2*m0*Zetta*wx0)'
.PARAM   Cmech='m0/((BF*L)*(BF*L))'
.PARAM   Lmech='(BF*L)*(BF*L)/(m0*wx0*wx0)'

.PARAM  Coef1='-wx0*wx0'  Coef2='-wx0/Q'  Coef3='L*BF/m0'
.PARAM  Coef4='-E*b*h*pi*pi*pi*pi/(8*L*L*L*m0)'
.PARAM  Coef5='Epsilon*Area*Vdc*Vdc/(m0*d*d*d) - wy0*wy0'
.PARAM  Coef6='-wy0/Qy'
.PARAM  Coef7='Kc/m0'
.PARAM  Coef8='Epsilon*Area*Vdc*Vdc/(2*m0*d*d)'

* Actuation Voltage Source
Vact   1   0    SIN (0 0.02 'wx0/(2*pi)' 0 0)
R4     1   21   50

* Start of the mechanical model
R1    21    2   'Res1-1'
E10   2     3   VCVS  17  0  1
```

```
R3   3    0    1


E1   10   0    POLY(3)      9 0 7 0 3 0   0 Coef1 Coef2 Coef3
X3   10   11   12           add
X4   12   7    integ
X5   7    9    integ
E6   17   0    7    0       'BF*L'


* Vout=K*Vin^3
E9   11   0    POLY(1)      9    0        0 0 0 Coef4
C2   20   210  224p
C21  210  21   224p
Rp1  210  0    221
R2   17   20   27
E11  620   0    POLY(3)  7  0   30   0  60   0   0 0 0 1 0 2
E100  60   0    POLY(3)  29  0 630  7   0   Coef8 Coef5 Coef6 Coef7
X100  62   63   integ
X101  63   29   integ
Vomega     30   0   PULSE(0  1  500m 1n 1n 1 10)
Xw    30   2005 integ
Ecos  2006  0  VCVS  PWL(1)  2005   0 0,1 .5,.878 1,.54 1.5,.07 2,-.42 2.5,-.8 3.-.99
Ew     62    0   POLY(3) 2006   0      9    0   620   0   0 0 0 1 0 'Kw/m0'
E15   37     0   POLY(2)    29   0   36   0      0   'Ccorrect/(2*d)' 1e6
Vunit 36     0   1
E16   39      0  37   0   Cap0
```

```
G2    40   45  VCCAP   PWL(1)  39   0 DELTA=1e-40v,0, 1v,1u
C8    40   0    1.2p
Vdd   41   0   'Vdc/2'
Vss   45   0   '-Vdc/2'
X20   41   45    42 40   42  MITELOP1
M1    41   41    40  45   Mitelnmos L=1.5uW=10u
E21   49   0     POLY(2)    42   01   0    0 0 0 0 1e4
Xfilt 49   51     lowpass


.subckt lowpass  in  out
.PARAM  fcut=100
.PARAM  fc1='fcut*pi*2'
R1  in  7  1
L1   7  8  '0.618/fc1'
C2   8  0  '1.618/fc1'
L3   8  9  '2/fc1'
C4   9  0  '1.618/fc1'
L5   9  out  '0.618/fc1'
R2   out  0  1
.ends

.subckt  mult  in1   in2   out
Em   out   0  POLY(2)   in1  0  in2   0   0 0 0 0 1
.ends
```

```
.subckt  add  in1  in2  out
Es  out  0  POLY(2)  in1  0  in2  0  0  1  1
.ends

.subckt  integ  in  out
E1  3  0  4  0  1e9
R1  in  4  1 MEG
C1  4  3  1uF  IC=0
E2  out  0  0  3  1
.ends

.PROBE V(51)
.TRAN  0.2u  600m  START=490m
.options post interp converge=1 dcfor=1 itl1=2800 DVDT=2 LVLTIM=2
+ rmin=1e-10 relv=5e-3 newtol=1 brief probe
.END
```

Appendix II

Concave Corner Compensation Numerical Simulation Program

The following numerical simulation program is written in Matlab to predict the etch progress of the concave corner compensation patterns in TMAH. The program generates a diagram showing the timing of the main etch front reaching certain critical points. It also generates a CIF file for the designed pattern which can be directly imported into a layout design tool such as Cadence.

```
% ---------- Parameter Declaration ----------%
BoxLen=1500;  BoxHigh=1000;
Columns = [1 1 1];
Factor=cos(45*pi/180);
N=length(Columns);
Margin=85;
M=20 ;
for i=1:length(Columns)
 d(i)=35;
end;
w=10;  L=35;  w1=10;
LastL=78;  LastW=5;
s=25;  v=25;
```

```
Rate111=1.4;


%-----------------------------
%  Open the CIF file & write Header
%-----------------------------
fid = fopen('design1.cif','wt');
fprintf(fid,'\n DS 1; \n');
fprintf(fid,'9 design1; \n');
fprintf(fid,'L ACT; \n');
OriginX=0; OriginY=0;
%-------------------------------
%---------------------------------- Etch Progress Calculations ------------------------------%
zz=1;  L1=L;
K=L-(L-s)/2;
T0=0;
if M>=d(1)
  T1= sqrt(d(1)^2+M^2)*cos(22*pi/180-atan(M/d(1)))/(2.2*v) ;
else
  T1= sqrt(d(1)^2+M^2)*sin(22*pi/180+atan(M/d(1)))/(2.2*v) ;
end;
dd1= d(1)+w1/2+w+(Columns(1)-1)*(2*d(1)+w1+w);
X1=sqrt( M^2+dd1^2 - (dd1-M)^2*(cos(45*pi/180))^2 ) + (L-K)*sin(45*pi/180);
X11=X1-Margin;


Step(1)=X11;
```

```
Step1(1)=Step(1);
Time(1)=T0; Time1(1)=Time(1)+(M+(L-s)/2)*sin(22*pi/180)/(2.2*v);

Tappx=T0+T1+TT1(d(2),s,L,v);
s11=s-2*Tappx*Rate111; d11=d(2)-2*Tappx*Rate111; L11=L+2*Tappx*Rate111;
Step(2)=X11+DeltaX(L,s,d,2)+(2*d(2)+w+w1)*(Columns(2)-Columns(1))*Factor;
Step1(2)=Step(2)+sqrt(2*(Tappx*Rate111)^2)
Time(2)=T0+T1+TT1(d11,s11,L11,v);
Time1(2)=Time(2)+(w*sin(22*pi/180)+L11*sin(22*pi/180))/(2.2*v);

for i=3:N
  Tappx1=Time(i-1)+TT1(d(i-1)-2*Time(i-1)*Rate111,s-2*Time(i-1)*Rate111,L,v);
  Tappx=Tappx1+TT1(d(i)-2*Time(i-1)*Rate111,s-2*Time(i-1)*Rate111,L,v);
  s11=s-2*Tappx1*Rate111; d11=d(i-1)-2*Tappx1*Rate111;
  L11=L+2*Tappx1*Rate111;
  d12=d(i)-2*Tappx*Rate111; s12=s-2*Tappx*Rate111; L12=L+2*Tappx*Rate111;
  Step(i)=Step(i-1)+DeltaX(L,s,d,i)+(2*d(i)+w+w1)*(Columns(i)-Columns(i-1))*Factor;
  Step1(i)=Step(i)+sqrt(2*(Tappx*Rate111)^2);
  Time(i)=Time(i-1)+TT1(d11,s11,L11,v)+TT1(d12,s12,L12,v);
  Time1(i)=Time(i)+(w*sin(22*pi/180)+L12*sin(22*pi/180))/(2.2*v);
end;

dfinal=d(N)+(w1-LastW)/2;
Tappx=Time(N)+TT1(d(N)-2*Time(N)*Rate111,s-2*Time(N)*Rate111 ,
L+2*Time(N)*Rate111 ,v);
```

```
dfinal1=dfinal-2*Tappx*Rate111; s11=s-2*Tappx*Rate111; L11=L+2*Tappx*Rate111;
if s11>=dfinal1
   Tfinal=sqrt(dfinal1^2+s11^2)*cos(22*pi/180-atan(s11/dfinal1))/(2.2*v)+((L11-s11)/
2)*sin(22*pi/180)/(2.2*v);
else
   Tfinal=sqrt(dfinal1^2+s11^2)*sin(22*pi/180+atan(s11/dfinal1))/(2.2*v)+((L11-s11)/
2)*sin(22*pi/180)/(2.2*v);
end;

Time(N+1)=Time(N)+Tfinal;
LastL1=LastL+2*Time(N+1)*Rate111;  s11=s-2*Time(N+1)*Rate111;
L11=L+2*Time(N+1)*Rate111;
Time1(N+1)=Time(N+1)+(LastL1-(L11-s11)/2)*sin(22*pi/180)/(2.2*v);
Tstop = Time1(N+1);
Step_Stop= (M+L+(N-2)*(s+L)+s+LastL+Rate111*Time1(N+1))*cos(45*pi/
180)+(LastW/2)*sin(45*pi/180)-Margin;
Step(N+1)= Step_Stop;
Step1(N+1)=Step(N+1)+sqrt(2*(Time(N+1)*Rate111)^2);

Total_Length=(M+L+(N-2)*(s+L)+s+LastL+Rate111*Time1(N+1))*cos(45*pi/
180)+Margin*sin(45*pi/180)

if (s>=d)
  Critical_Factor=(2*TT1(d(1),s,L,v)-(L+s)*cos(22*pi/180)/(2.2*v))*2.2*v;
  dend=d(1)-2*Time(N)*Rate111; Send=s-2*Time(N)*Rate111;
```

```
  Critical_Factor1=(2*TT1(dend,Send,L,v)-(L+s)*cos(22*pi/180)/(2.2*v))*2.2*v
else
  Critical_Factor=(2*TT1(d(1),s,L,v)-(L+s)*cos(22*pi/180)/(2.2*v))*2.2*v
  dend=d(1)-2*Time(N)*Rate111; Send=s-2*Time(N)*Rate111;
  Critical_Factor1=(2*TT1(dend,Send,L,v)-(L+s)*cos(22*pi/180)/(2.2*v))*2.2*v
end;

for i=1:N
  UnderEtch(i)=Time1(i)*v;
end;
  UnderEtch(N+1)=Tstop*v;

Fmargin=UnderEtch(N+1)-Step1(N+1);
FinalSize=LastW+2*Rate111*Time(N+1)+2*((LastL1-(L11-s11)/2)*(cos(22*pi/180)-
sin(22*pi/180))/(2.2*sin(45*pi/180)-sin(22*pi/180)))+2*Fmargin/cos(45*pi/180);
FinalTime=(LastL1-(L11-s11)/2)*(sin(45*pi/180)*cos(22*pi/180)-sin(22*pi/180)^2/2.2)/
(1.2*v-v*sin(22*pi/180))+Time(N+1);
FlangeSize=2*FinalTime*v/sin(45*pi/180);
ReducRatio=FlangeSize/FinalSize;
TotalL=(M+L+(N-2)*(s+L)+s+LastL+Rate111*Time1(N+1));
EtchthL=TotalL-50/cos(45*pi/180)+2*50/tan(54.7*pi/180);
Concave=(FinalTime-50/v)*2.2*v-EtchthL;
ConcaveT=abs(Concave/(2.2*v))+FinalTime;
```

```
%------------------------------
% Write the pattern info. into the CIF file
%------------------------------
OriginY=OriginY+2000;
% Find the initial Cordinates & write
x1=-M*Factor; y1=x1;
xx1=x1-(w1/2)*Factor+OriginX; yy1=y1+(w1/2)*Factor+OriginY;
makebox(xx1,yy1,w1,L1,fid);
for cc=1:(Columns(1)-1)
 makebox(xx1+cc*(w1+w+2*d(1))*Factor, yy1-cc*(w1+w+2*d(1))*Factor, w1,L1,fid);
 makebox(xx1-cc*(w1+w+2*d(1))*Factor, yy1+cc*(w1+w+2*d(1))*Factor, w1,L1,fid);
end;
x2=x1+(w1/2+d(1))*cos(45*pi/180);
y2=y1-(w1/2+d(1))*cos(45*pi/180);
x3=x2+K*cos(45*pi/180);
y3=y2+K*cos(45*pi/180);
makebox(x3+OriginX,y3+OriginY,w,L,fid);
for cc=1:(Columns(1)-1)
 makebox(x3+cc*(w1+w+2*d(1))*Factor+OriginX, y3-
cc*(w1+w+2*d(1))*Factor+OriginY, w,L,fid);
end;
x4=x3-(2*d(1)+w1+w)*cos(45*pi/180);
y4=y3+(2*d(1)+w1+w)*cos(45*pi/180);
makebox(x4+OriginX,y4+OriginY,w,L,fid);
```

```
for cc=1:(Columns(1)-1)
 makebox(x4-cc*(w1+w+2*d(1))*Factor+OriginX,
y4+cc*(w1+w+2*d(1))*Factor+OriginY, w,L,fid);
end;

%find other cordinates & write
x1=x1-(w1/2)*Factor;
y1=y1+(w1/2)*Factor;

for i=2:N
 x1=x1-(L1+s)*Factor; y1=y1-(L1+s)*Factor;
if i==N
 L1=LastL;
 x1=x1+(w1/2)*Factor-(LastW/2)*Factor;
 y1=y1-(w1/2)*Factor+(LastW/2)*Factor;
 w1=LastW;
end;
 makebox(x1+OriginX,y1+OriginY,w1,L1,fid);
for cc=1:(Columns(i)-1)
 makebox(x1+cc*(w1+w+2*d(i))*Factor+OriginX, y1-cc*(w1+w+2*d(i))*Factor +
OriginY,  w1,L1,fid);
 makebox(x1-cc*(w1+w+2*d(i))*Factor+OriginX, y1+cc*(w1+w+2*d(i))*Factor+
OriginY, w1,L1,fid);
end;
 x3=x3-(L+s)*Factor-(d(i-1)-d(i))*Factor; y3=y3-(L+s)*Factor+(d(i-1)-d(i))*Factor;
```

```
 makebox(x3+OriginX,y3+OriginY,w,L,fid);
for cc=1:(Columns(i)-1)
  makebox(x3+cc*(w1+w+2*d(i))*Factor+OriginX, y3-cc*(w1+w+2*d(i))*Factor+
OriginY, w,L,fid);
end;
  x4=x4-(L+s)*Factor+(d(i-1)-d(i))*Factor; y4=y4-(L+s)*Factor-(d(i-1)-d(i))*Factor;
  makebox(x4+OriginX,y4+OriginY,w,L,fid);
for cc=1:(Columns(i)-1)
  makebox(x4-cc*(w1+w+2*d(i))*Factor+OriginX, y4+cc*(w1+w+2*d(i))*Factor+
OriginY, w,L,fid);
end;
end;

% Make the Main Box
SS=100;
y5=-Margin+OriginY; x5=Margin/tan(45*pi/180)+OriginX;
y6=Margin/tan(45*pi/180)+OriginY; x6=-Margin+OriginX;
y7=y5; x7=x5+BoxLen;
y8=y6+BoxHigh; x8=x6;
x51=round(x5*SS); y51=round(y5*SS);
x61=round(x6*SS); y61=round(y6*SS);
x71=round(x7*SS); y71=round(y7*SS);
x81=round(x8*SS); y81=round(y8*SS);
x91=x71; y91=round(BoxHigh*SS+OriginY*SS);
x101=x61; y101=y91;
```

```
fprintf(fid,'P %d,%d %d,%d %d,%d %d,%d %d,%d %d,%d %d,%d ; \n',
round(OriginX*SS),round(OriginY*SS),x51,y51,x71,y71,x91,y91,x101,y101,x61,y61);
%----------------------------------------

[P1,ErrMsg]=sprintf('%d',zz*10);
plot(Time1,Step1,'x',Time1,UnderEtch,'g-',Tstop, Step1(N+1),'ro');
text(Time,Step,P1);
xlabel('Etch time (hr)');
ylabel('Under-etch (micron)');
hold on;
end;
grid;
%---------------------------------
% Write the tail & close the CIF file
%---------------------------------

%---------------------------------- Generate the Plot ----------------------------------%
fprintf(fid,'DF; \n');
fprintf(fid,'C 1; \n');
fprintf(fid,'E \n');
fclose(fid);
%---------------------------------
hold off;
print design1.ps
```

Appendix III

Cleaning Procedure

Cleaning procedure is as follows:

1- The samples are boiled in 1:1 solution of H_2SO_4:H_2O_2 for 5 minutes, followed by rinsing in DI water.

2- The samples are boiled in 1:1:5 solution of HCL:H_2O_2:H_2O for 5 minutes, followed by rinsing in DI water.

3- The samples are placed in 1:50 solution of HF:H_2O for 20 seconds to remove the native oxide, followed by rinsing in DI water.

4- The samples are placed in hot (but not boiling) 1:1:5 solution of NH_4OH : H_2O_2 : H_2O for 5 minutes, followed by rinsing in DI water.